Mechanical properties of additively manufactured or repaired single-track thickness structures by Directed Energy Deposition.

Yanis Balit

INSTITUT POLYTECHNIQUE DE PARIS

NNT : 2019IPPAX014

Thèse de doctorat

Mechanical properties of additively manufactured or repaired single-track thickness structures by Directed Energy Deposition

Thèse de doctorat de l'Institut Polytechnique de Paris
préparée à l'École polytechnique

École doctorale n°626, École Doctorale de l'Institut Polytechnique de Paris
Spécialité de doctorat : Ingénierie, mécanique et énergétique

Thèse présentée et soutenue à Palaiseau, le 6 décembre 2019, par

YANIS BALIT

Composition du Jury :

Véronique Doquet Directrice de recherche, CNRS - École Polytechnique, LMS	Présidente
Patrick Villechaise Directeur de recherche, CNRS - ENSMA, Institut Pprime	Rapporteur
Patrice Peyre Directeur de recherche, CNRS - Arts et Métiers, PIMM	Rapporteur
Roland Logé Professeur associé, École Polytechnique Fédérale de Lausanne	Examinateur
Andrei Constantinescu Directeur de recherche, CNRS - École Polytechnique, LMS	Directeur de thèse
Eric Charkaluk Directeur de recherche, CNRS - École Polytechnique, LMS	Co-directeur de thèse
Marie-Christine Sainte Catherine Direction Générale de l'Armement (DGA)	Invitée
Louis-Romain Joly Société Nationale des Chemins de Fer français (SNCF)	Invité

Remerciments

Tout d'abord, je remercie mes directeurs de thèse Andrei Constantinescu et Eric Charkaluk pour leurs précieux conseils et leurs encadrements sans faille à mon égard. Je les remercie pour ces 3 années stimulantes pendant lesquelles j'ai muri et progressé à leurs côtés.
Ensuite, je remercie tous les membres du jury pour leurs questions très intéressantes et pour tout l'intérêt qu'ils m'ont accordé pendant cette séance. Une mention spéciale pour Patrice Peyre et Patrick Villechaise pour leurs rôles de rapporteurs et leurs retours précis et pertinents.
C'est avec une grande reconnaissance que j'écris ces quelques lignes pour remercier Simon Hallais et Alexandre Tanguy pour leurs disponibilités et leurs expertises techniques. Grâce à vous, j'ai pu réaliser des expériences d'une grande qualité.
Je suis également reconnaissant envers Pascal Marie, Sylvain Dubercq, Lahcen Cherfa, Hakim Gharbi, Jean-Christophe Eytard, Vincent de Greef et Erik Guimbretière, pour leurs soutiens techniques et leurs efficacités qui m'ont permis d'économiser un temps inestimable pendant cette thèse.
Je n'oublie pas de remercier pour leurs rapidités d'actions et leurs bonnes humeurs qui inondent notre laboratoire, mes voisines de bureau et de couloir qui œuvrent dans l'administration.
Un grand merci à tous les doctorants qui ont rendu cette aventure si agréable : Othmane, Camille, Jérémie, Nikolai, Anthony, JP, pour n'en citer que quelques-uns.
Je remercie mes parents et mon frère pour leurs soutiens indéfectibles ainsi que tous mes amis d'enfance qui se reconnaitront lorsqu'ils liront ce passage.
Je conclue en remerciant ma chère Emma pour sa relecture, sa patience et son soutien infaillible.

Merci à vous tous du fond du cœur.

Avant-propos

Cette thèse a été effectuée au Laboratoire de Mécaniques des Solides (LMS) à l'École Polytechnique. Le LMS est une unité mixte de recherche sous tutelle du Centre National de la Recherche Scientifique (CNRS) et de l'École Polytechnique. Ces travaux ont été co-financés par la Direction Générale de l'Armement (DGA) et la Société Nationale des Chemins de Fer français (SNCF).

Contents

Introduction

This thesis is dedicated to the study of additively manufactured or repaired specimens by Directed Energy Deposition (DED) and has been funded by the **Direction Générale de l'Armement** (DGA) and the **Société Nationale des Chemins de Fer français** (SNCF). The objective is to investigate the effect of the process parameters on the final properties and to associate them with the microstructure. The understanding of the underlying phenomena will demand examination at different space and time scales of the process and material. The feedstock under consideration is a standard 316L stainless steel which will be used to manufacture various single-track structure configurations. The novelty of this study is the observation of the strain localization at the grain scale during tensile loading for the very specific hierarchical microstructure inherent to this process. This experiment combined an in situ tensile test inside a Scanning Electron Microscope (SEM) with High Resolution Digital Image Correlation (HR-DIC) and an Electron Backscatter Diffraction (EBSD) map. These results permitted to give a fresh interpretation for monotonic tensile tests as well as for self-heating experiments under cyclic loading and the associated failure patterns observed at the surface of specimens.
The work is organized in 5 chapters which correspond to the following: (1) a general state of the art on metallic additive manufacturing and repair technologies, (2) a single-track analysis to define an operational process parameter window, (3) an analysis of the effect of the loading direction at the microstructure scale, (4) a study of the deformation mechanisms at the interface between the damaged part and the added material, (5) an investigation of the self-heating behavior of additively (re)manufactured specimens.

Chapter 1: State of the art is a general introduction on additive manufacturing, its inherent defects and the available types of feedstock. The discussion also adresses the problems of the repair of metallic parts and presents some current technologies used to remanufacture damaged parts.

Chapter 2: Single-track analysis starts with a quick presentation of the machine used in this study as well as the chosen material and its characteristics. Afterwards, an investigation of the effect of the process parameters on the geometry of the cross section of a single-track printed is presented. We propose an algebraic model to relate the process parameters with the observed geometry of the cross section of the track as well as the generation of an operational process parameter window. Within the complete process parameter map, the operational window contains the combinations for which the tracks have an optimal geometry. Additionally, an analysis of the microstructure and of the cellular substructure observed conducts to an optimal range of the printing

parameters and end the chapter.
Once we fixed the process parameters to one combination, single tracks were printed on top of each other and specimens were extracted in two orientations from this additively manufactured wall. Their analyses is the subject of the next chapter.

Chapter 3: Fully printed specimens proposes an investigation of the tensile properties of specimens extracted from additively manufactured single-track thickness walls. For additive manufacturing, it is well known that the process parameters are driving the microstructure and therefore the global mechanical properties of the material of the structure. In [1], it was noted that the laser energy density has a strong influence over the grain size and the part density, hence affecting the mechanical properties. The manufacturing processes, the obtained microstructure and the mechanical and wear behavior were correlated in [2]. The results showed that the highest mechanical properties, understood as yield and ultimate tensile strength, as well as the best tribological performance were obtained for 316L stainless steel specimens produced by Selective Laser Melting (SLM) when compared to hot pressing or conventional casting. The result has been explained by a finer microstructure obtained in the AM process. In [3] the effects of inter-layer dwell time interval were studied and it was found that longer dwell time intervals imposed higher cooling rates, leading to finer microstructures and therefore to higher tensile strength and lower ductility. Furthermore, in additive manufacturing, the lasing and building strategy will lead to the formation of oriented microstructures with elongated columnar grains [4]. In addition, anisotropic macroscopic properties are reported in for example [5] and [6]. In [7], several tensile behaviors for additively manufactured 316L stainless steel specimens are summarized and a clear effect of the loading direction on the mechanical properties is reported. Indeed, the authors showed that the yield and tensile strengths is superior of the specimens tested along the building direction while the elongation is greater for the specimens tested along the printing direction. Hence, the aim of this chapter is to understand the origin of the observed anisotropy. Dog-bone shaped specimens were extracted from the wall along the building and printing direction and tensile tested inside an SEM. HR-DIC combined with the microstructure map of the specimen permitted to compute the strain per grain and finally to highlight the different deformation mechanisms explaining the anisotropy.
A procedure to track the microstructural local strain is proposed and extended in the next chapter to repaired specimens.

Chapter 4: Repaired specimens investigates the capacity of the Directed Energy Depostion (DED) technology to repair components by studying the interface between the damaged part and the added material. Traditional cladding processes such as arc welding [8], thermal/plasma spraying [9, 10, 11] and cold spray [12], to name a few, have been studied for the past decades. However, they present severe limitations related to the particularities of the processes that have prevented their large scale deployment. We can mention: a large heat affected zone (HAZ), critical distortions, poor geometric accuracy and low mechanical properties as fabricated. In comparison, DED is a very promising technology thanks to its capacity to repair complex geometry and with

optimized parameters it can attenuate the HAZ, create metallurgical-bonded deposits and reduce the distortion [13, 14].
At a macroscopic scale, several research groups investigated the repair by studying the filling material, the post treatment or the repairing strategy [15, 16]. For example, in [15] promising results for the repair of an ultra-high strength AISI 4340 steel are established. However, with the same material, the authors highlighted poor tensile properties and a significantly reduced fatigue life of the repaired part. A noteworthy improvement by a factor 10 of the final properties in comparison to the repaired specimens with AISI 4340 was obtained when the cladded layer was changed to an AerMet 100 steel. Finally, for the latter specimen, the authors observed that applying a post-clad heat treatment improved the fatigue limit above the damaged part. For Inconel 718, it was shown in [16] that the geometry of the groove to be repaired as well as the printing strategy influence the final mechanical properties. The authors qualitatively observed that the trapezoidal groove generates a smooth transition of deposited materials and therefore a good bonding. Additionally, the weakest wear resistance was obtained for the specimens manufactured with a diagonal building direction.
At the microscopic scale, the material is subjected to several physical phenomena driven by the process parameters. As a consequence, hierarchical microstructures are generated [17, 5] which are significantly different from conventionally processed materials. For repair work, this implies that the original part and the repaired material can have very different microstructures which can cause different strain-fields under loading and therefore, different damage patterns and crack networks.
As a consequence of the surveyed literature, the chapter proposes an investigation of the deformation mechanisms at the interface between the damaged part and the added material. More precisely, a 316L stainless steel hot rolled sheet substrate was repaired employing DED. The dog-bone shaped repaired specimens are composed of two equal parts with an initial substrate and the added repaired part. This design permits to load the interface in tension during a tensile experiment. A fine gold pattern was deposited on an area across the interface and afterwards, the specimens were tensile tested inside an SEM. Strain full-fields were obtained through HR-DIC and we associated the results with the microstructure map. Consequently, we were able to track the local microstructural strain distribution and therefore highlight different deformation mechanisms at both sides of the interface. Additionally, the present chapter will fill the gap between microstructural strain localisation investigations performed on fully printed [18, 19, 20] and conventionally manufactured [21] specimens.

Chapter 5: Self-heating behavior proposes a study of the fatigue properties and the lifetime predictions of the fully printed and repaired specimens. These properties can be assessed at the macroscopic scale of the structure or studied at the local level of the microstructure. For metallic components, they depend on the plasticity mechanisms and the particular grain structures at the microscopic scale of the material as discussed in [22, 23]. Fatigue life in as-built metal AM materials has been discussed under different settings: (i) the influence of processing conditions and the resulting defects in structure

[24, 25], (ii) the role of the particular microstructure which has been exhibited by the anisotropic properties for static and cyclic loadings in [6, 26] and [25, 27], respectively. Studies like [28, 15] equally highlight the difficulties and the underlying cost of providing a large data-base of fatigue tests for materials that can largely vary according to the process parameters. Therefore, alternative and faster methods are required to determine such properties. One of them is based on the self-heating measurements of the specimen due to microscopic plasticity observed under cyclic loadings [29].
Here we assess a self-heating testing method for the characterization of fatigue properties of single-track thickness fully printed and repaired specimens. The critical fineness of the tested specimen was overcome and the temperature elevation versus the stress amplitude results were interpreted using the Munier self-heating model [30]. We evaluated the impact of one process parameter and also the influence of the microstructure orientation with respect to the loading direction on the dissipative behavior and the initiation of microcracks. Additionally, the results were correlated with patterns of plasticity at the grains scale observed in the chapter 3 and 4.

1 State of the art

Contents

1.1 A short introduction to Additive Manufacturing

Additive manufacturing (AM) has been defined in [31] as: "the process of joining materials to make objects from three-dimensional model data, usually layer upon layer". This unique manufacturing technique enables the production of optimized and complex parts without the need of expensive tools such as casting molds or sophisticated machining.
In the past decades, additive manufacturing has evolved from a rapid prototyping technique [32] to a manufacturing process for fully functional parts with a wide range of polymers and metallic materials [33]. Due to the low production rates and high cost per part, AM is for now a complementary technology to conventional processes and will probably never be a competitor for important series of low value components, neither for the production of very large parts. At the present moment, it is more suitable for a small number of highly complex parts and therefore, applications are the most developed in, but not limited to, aerospace [34] and biomedical industries [35]. Industries can highly benefit from the free design allowed by AM by producing "un-manufacturable" design. Furthermore, they can drastically reduce the number of components of mechanical assemblies. One of the successful examples presented by *GE Aviation* is, in October 2018, the 30000^{th} additively manufactured fuel nozzle tip [36]. This substantial technical achievement allows to additively manufacture the nozzle tip in one part instead of a mechanical assembly of 20 pieces welded together. Consequently, it permits to cut the weight by 25 % as pictured in Figure 1.1.
Additively manufactured parts can be produced on demand and are therefore extremely important for industries because it shortens the supply time for critical components and removes the financial and logistic pressure of voluminous storage.

Figure 1.1: Image of a 3D-printed fuel nozzle tip for the LEAP engine [36].

In the biomedical field, additive manufacturing is an innovation that permits patient-

specific care and revolutionizes the workflow of patient-specific orthopaedics procedures as shown in Figure 1.2 extracted from [37].
The industrialization of additive manufacturing is nevertheless complex and an expensive task because it requires an extensive understanding of the technology. More specifically, the effect of each process parameter affecting the microstructure, mechanical properties, defects and residual stress. This lack of understanding is actually the limiting issue for the certification of critical additively manufactured components. However scientists and engineers are actively investigating this technology as revealed by the number of articles per year which has multiplied by 3.6 since 2009 (see *sciencedirect.com*, keyword: Additive manufacturing).

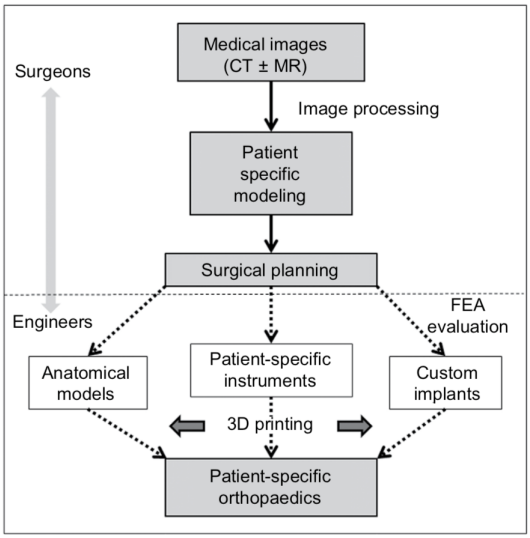

Figure 1.2: Clinical workflow of patient-specific orthopedics from image acquisition to 3D-printed models and implants [37].

1.2 Powder Bed Fusion technology

Two AM technologies have received particular attention in the past years: Powder Bed Fusion (PBF) and Directed Energy Deposition (DED). The PBF technology creates objects by sweeping a heat source over a given shape at the surface of a powder bed. As a layer of particles is fused, the powder bed descends and a fresh unfused layer of particles is distributed over the surface of the powder bed and the operations are then repeated. This technology is well known under several declinations such as Direct Metal Laser Sintering (DMLS) [38], Selective Laser Melting (SLM) [39], Electron Beam Melting (EBM) [40] etc. The heat source melting the powder is usually a laser beam but can also be an electron beam within a particular configuration as discussed later. PBF laser machines in most cases use a neodymium-doped yttrium aluminium garnet (Nd:YAG) laser with a wave of 1,06 μm permitting to develop a power

(related to the configuration, machine manufacturer etc.) between $100\,W$ to $1\,KW$. The manufacturing of the part in a PBF machine is performed in a chamber with a controlled atmosphere filled with an argon gas used as a shield to avoid oxidation. A scheme extracted from [41] and presenting the PBF technology is displayed in Figure 1.3.

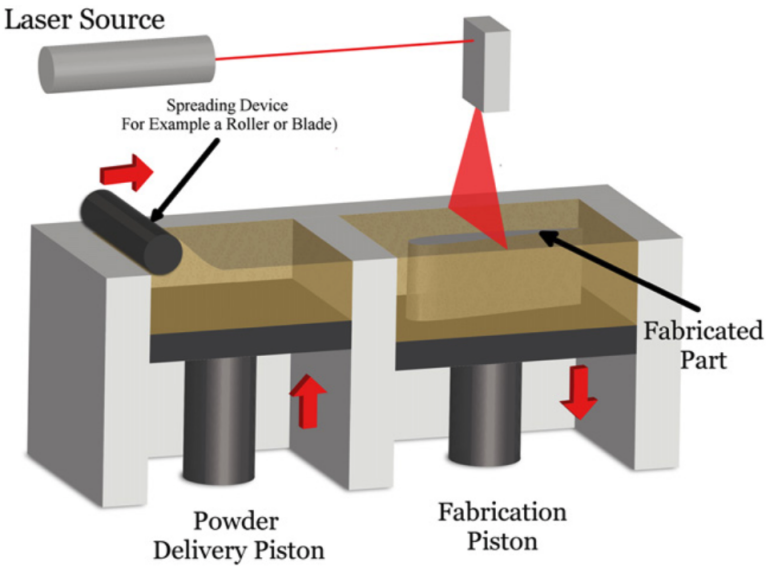

Figure 1.3: Schematic presentation of the PBF laser technology [41]

PBF electron beam machines are similar to PBF laser machines but they operate inside a vacuum chamber and the heat source is an electron beam as schemed in Figure 1.4. This different heat source consists of the acceleration of electrons creating an intense beam which is focused on an area. The melting of the powder is accomplished by transforming the kinetic energy of the bombarded electrons into a thermal one.
With a slight difference to the PBF laser machines, the PBF electron beam process relies on a two-step sequence as presented in [7]. The first step consists of a light sintering of each layer of powder in order to avoid any electro-static charging and therefore potential repulsion of the particles. Next, for the second step the electron beam finally fuses the pattern of powder to build the part layer by layer. The first step of the process is usually held on a bed at an elevated temperature permitting a relatively fast scanning speed of the beam. However, it is limited to electrically conductive powder.

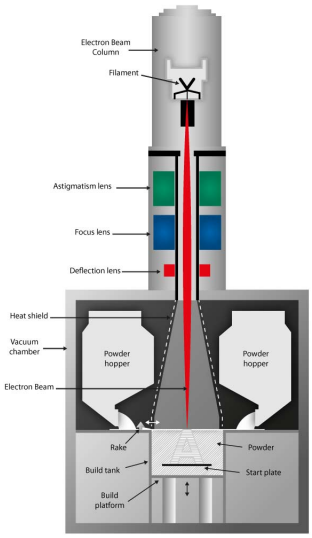

Figure 1.4: Schematic presentation of the PBF electron beam technology from Arcam [42]

1.3 Directed Energy Deposition technology

The DED technology is an additive manufacturing process in which the material is transported into a focused heat source and then deposited on the already constructed layers [43]. Particular variants of the DED process have been denoted in several ways in the literature such as: Direct Metal Deposition (DMD) [44], laser cladding [45], Laser Metal Deposition (LMD) [46], Direct Laser Deposition (DLD) [47] and Electron Beam Direct Melting (EBDM) to name a few. It has been used for various applications such as the manufacturing of complex or graded parts [48], for the deposition of coatings [49] or as a repairing technique [50].
As suggested by the various denomination, two types of heat sources can be used with this technology. Additionally, the processed materials can be either powder or wire as shown in Figure 1.5(a) and (b) respectively [7].
A common technical solution presents a depositing system (heat source + feedstock) mounted on a robotic arm or a 3 axis system (+ 2 rotation of the substrate) permitting the (re)manufacturing of complex parts. Also, the powder is most often carried by an argon gas to the melt pool with a sufficient kinetic energy allowing the powder to escape from the gravity during flight, thereby making the deposition process effective for non vertical deposition [51]. In addition, the argon gas acts as a shield protecting the melt pool from oxidation. However, for some materials such as Ti-alloys, a complete inerte chamber is required.
DED machines using an electron beam as a heating source operates in a vacuum chamber which provides a high-purity manufacturing environment. This high quality processing space is therefore particularly suitable for materials such as Ti-alloys.

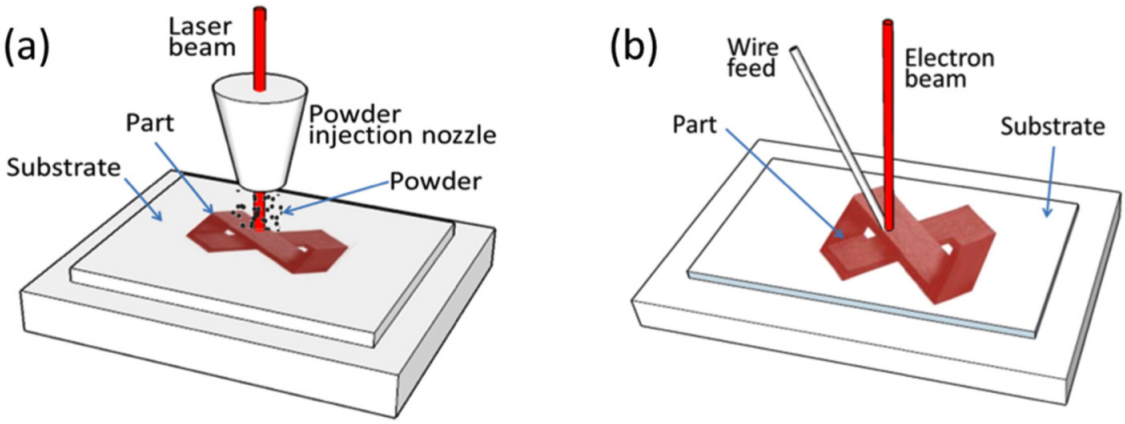

Figure 1.5: Schematic presentation of the DED technology for laser and powder in (a) and electron beam and wire in (b) [7]

As expected, the previously presented technologies have their advantages and limitations as shown in Figure 1.6 extracted from [52].
Finally, both previous technologies presented come with their respective limitations including the complexity and resolution of the technology as well as the deposition rate and part size as presented in figure 1.6 extracted from [52]. PBF and DED should be considered as complementary and used appropriately according to the application targeted.

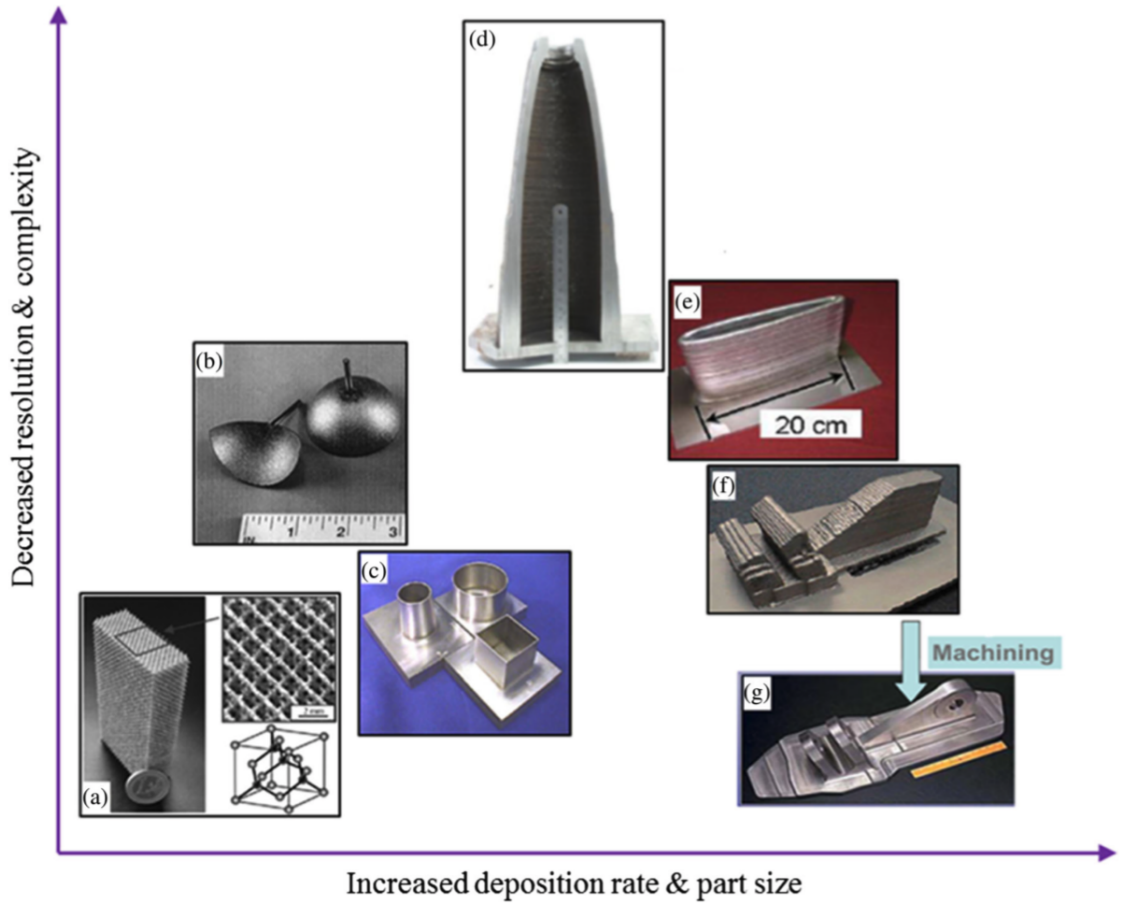

Figure 1.6: Comparison of surface finish and deposition rate between powder-feed/-bed and wire-feed technologies. a) Titanium micro lattice fabricated using powder bed electron beam melting [53]. b) A powder-feed-directed light fabrication of 316 stainless steel hemispherical shapes [54]. c) Three INC625 as built DED samples presenting a surface roughness $2\,\mu m$ [55]. d) A large structure manufactured by WAAM from Cranfield University [56]. e) 2219 Al airfoil produced by DED [57]. f) As-deposited sample made by wire-feed LAM (AeroMet) with "stair stepping" surfaces and g) shows the sample after surface machining [52]

1.4 Process parameters for the DED

DED consists of a series of various coupled physical events all taking place at different time scales. If an analysis is performed at a manufacturing instant in time, there are a few potential paths for momentum and energy transfer [58]. Immediately after deposition, the material undergoes complex melt-pool dynamics and rapid solidification ($\approx 300\,K/s$). If more layers are added, then the solidified material spends the rest of the printing time being subjected to heating-cooling thermal cycles at varying temperature rates. These physical events that can occur consecutively or in parallel are summarized and categorized in [58]. Also for each category, some specific sub-events are presented and an overview was proposed in [58].

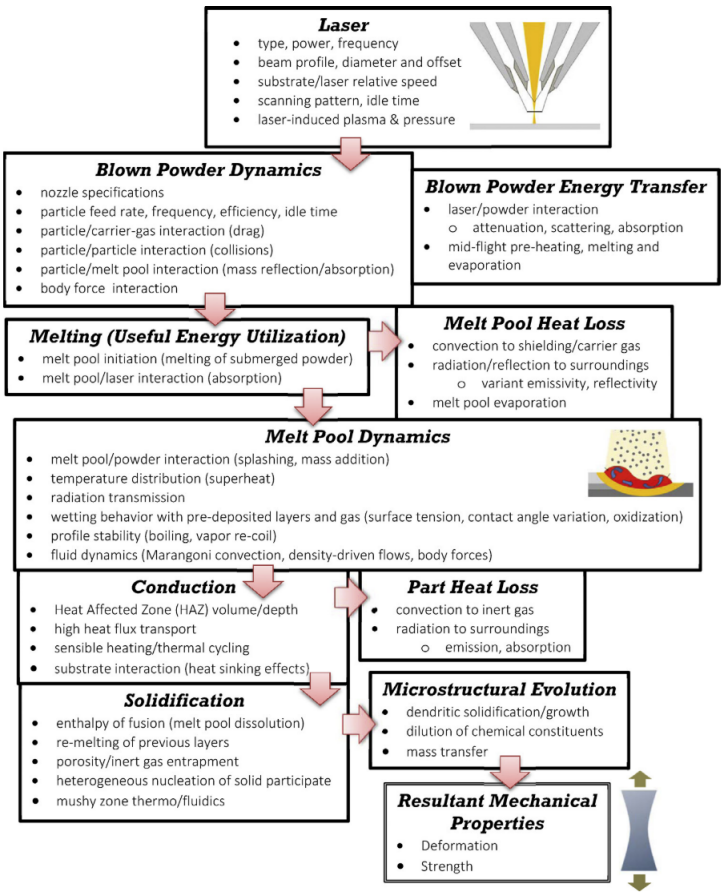

Figure 1.7: List of the physical events taking place during the manufacturing of the DED process at a given instant time. This figure is extracted from [58].

All these phenomena are directly linked to the process parameters of the DED including the deposition speed, the printing strategy, the laser power, the laser beam diameter, the powder flow, dwell time and the vertical and horizontal increment, to name some "easily

controlable" parameters. In fact, in [59], the authors listed 19 significant parameters that affect this manufacturing process and they are presented in Figure 1.8.

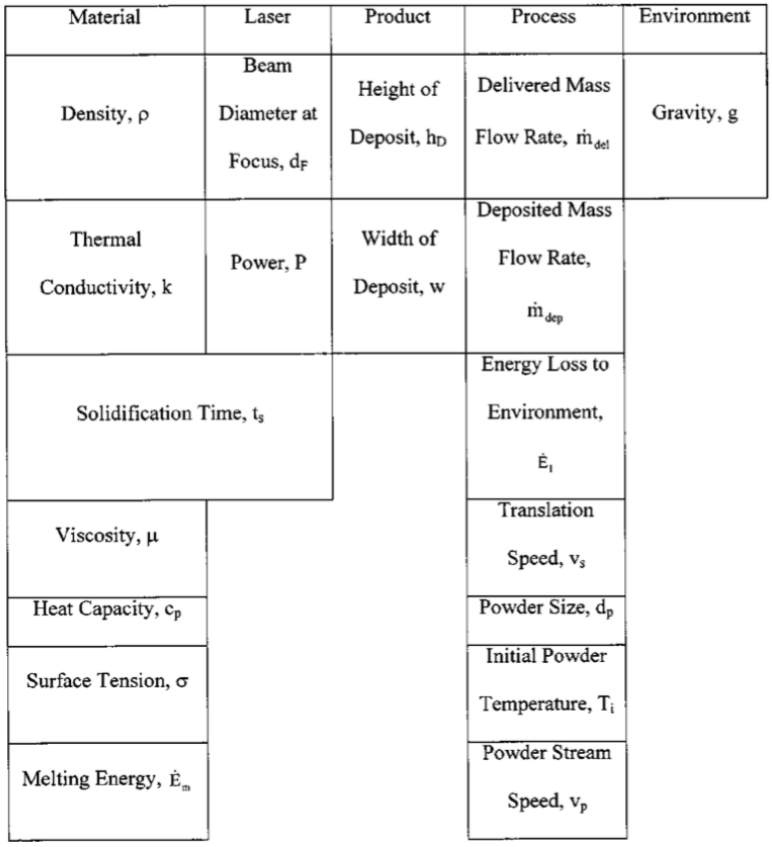

Figure 1.8: List of the various parameters that can affect the metal layer deposition process [59].

One can therefore imagine the challenges of a such process and the induced sensitivity of the final part to the process parameters. An example to illustrate this sensitivity is the effect of the printing strategy for the manufacturing of thin walls in a nickel-based superalloy [60]. In this article, the authors highlighted the difference of microstructure occurring for a unidirectional or bidirectional printing strategy as displayed in Figure 1.9(a) and (b) respectively. In fact, for the unidirectional printing strategy they observed elongated grains with a tilt angle of 60^o with respect to the horizontal axis while they found a herringbone pattern for the bidirectional printing strategy.

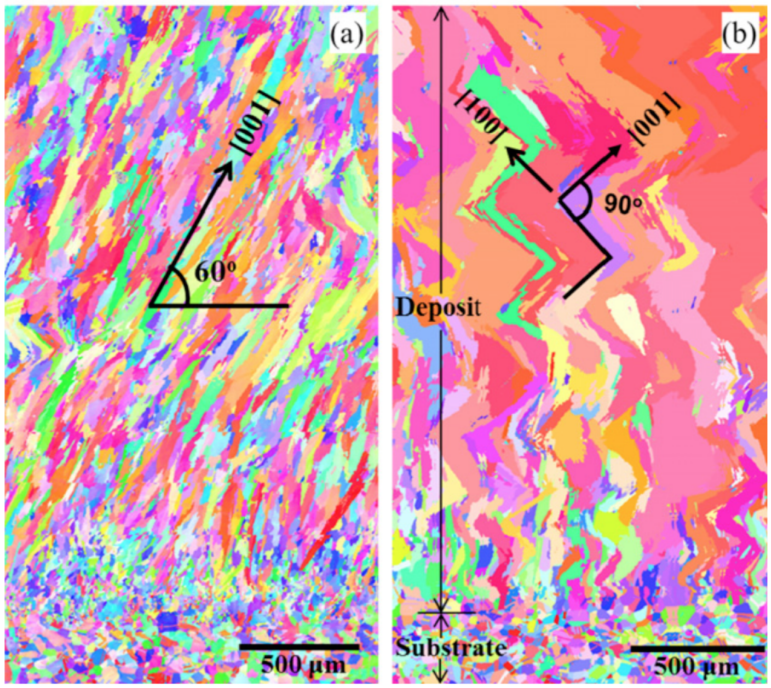

Figure 1.9: Microstructure of a nickel-based superalloy produced by a unidirectional and bidirectional printing strategy in (a) and (b) respectively. This microstructure maps are extracted from [60].

1.5 Some of the most common feedstocks for DED:

Potentially, all the weldable and castable materials can be used as feedstock materials for additive manufacturing [61]. However, the set of commercially available powders is limited even though the range of accessible materials is continuously expanding. In this section, a non exhaustive list of alloys based on the most frequently occurring feedstock in the literature, particularly for the DED process, is proposed.

Alloy Type	Aluminum	Maraging Steel	Stainless Steel	Titanium	Cobalt Chrome	Nickel Super Alloys	Precious Metals
Aerospace	X		X	X	X	X	
Medical			X	X	X		X
Energy, Oil, Gas			X				
Automotive	X		X	X			
Marine Environment			X	X		X	
Machinability Weldability	X		X	X		X	
Corrosion Resistance			X	X	X	X	
High Temperature				X		X	
Tools and Molds		X	X				
Consumer Products	X		X				X

Figure 1.10: Most common additive manufacturing alloys and application [62]. The red rectangle are the materials discussed in this section.

- **Titanium alloys:**
  Ti-alloys have been largely investigated for the aerospace and biomedical industries due to the wide spectrum of properties combining at low and high temperatures, great mechanical strength, bio compatibility, low density and corrosion resistance. Titanium alloys can be classified into 3 types namely, α-alloys, β-alloys and α-β-alloys. Specific chemical elements highly contribute to the transformation temperature of the alloy and therefore act as stabilizer of the α and β phases. Hence, solute elements such as Al, O, C, N which decrease the transformation temperature are referenced as α-stabilizers while increasing transformation temperature elements such Fe, Cr, Nb, Mo, Ta, V and W, named β-stabilizers will expend the β-phase region [63, 64, 65, 66]
  Among the large spectrum of Titanium alloys, Ti-6Al-4V in particular received

more attention thanks to its excellent ratio strength-to-weigth. This material has been extensively studied for DED and showed high sensitivity to process parameters with tensile properties usually comparable to wrought, however with a loss of ductility within 10-30% [67, 68, 69].

- **Cobalt based alloys:**
  The cobalt based alloys are particularly suitable for wear application as well as for corrosive and hot environments [70, 71, 72, 73]. Most of these properties arise from the crystallographic nature of cobalt, the solid-solution-strenghthening and anti-corrosion effect thanks alloying elements such as chromium, molybdenum and tungsten [74, 75]. Also, the chemical composition of this alloy is tailored for a particular application. For exemple, in the case of a wear application, depending if it is an abrasive, sliding or an erosive wear, the carbon, tungsten and silicon contents are adapted [75].

- **Nickel based alloys:**
  Ni-alloys are very interesting because of their ability to withstand a variety of extreme environments such as high temperature, high stress and a corrosive environment [76, 77, 78]. More specifically, the commercially available Inconel 625, 718 and Invar 36 are often used for the (re)manufacturing with AM processes for the aerospace industry [79]. In [7], many researches concerning this family of alloys are summarized, and more precisely a large comparison of the monotonic tensile behavior is proposed. No clear anisotropic behavior despite the presence of elongated and orientated grains along the building direction was found. Finally, nickel based alloys are becoming an interesting substitute to cobalt based alloys because of their mechanical properties but also because nickel is widely available and thus cheaper.

- **Stainless steels:**
  Stainless steels are an important family of materials used for diverse applications from cooking utensils to high-end application like space vehicles [80]. As suggested in the name, iron is composing the bulk of the materials usually at more than 50%. The stainless properties of this alloy are inherited from the at least 11% of chromium creating an invisible, self-healing and adherent formation of a chromium-rich oxyde surface film [81, 80]. Additional alloying elements are usually added to enhance specific properties and divides the stainless steel alloys in 5 (most common) families [82]:
  - Martensitic stainless steel [83]
  - Ferritic stainless steel [84]
  - Duplex stainless steel [85]
  - Precipitation hardening stainless steel [86]
  - Austenitic stainless steel:
    Austenitic stainless steel is the most common type of this alloy family and show exceptional corrosion resistance and equally high mechanical strength [87].

Austenitic stainless steel parts manufactured by AM include 304, 304L, 316 and 306L stainless steels. Usually these alloys present higher yield and tensile strength than conventionaly manufactured parts [88] but a lower ductility is often reported as summarized in [7].

Anisotropic behavior is observable as exhibited in Figure 1.11 showing the longitudinal versus transverse mechanical properties. In this Figure, one can note that longitudinal yield and tensile strength are slightly superior than the transverse ones as shown in (a) and (b) respectively while, in contrast in (c), the transversal elongation is superior in comparison to the longitudinal one.

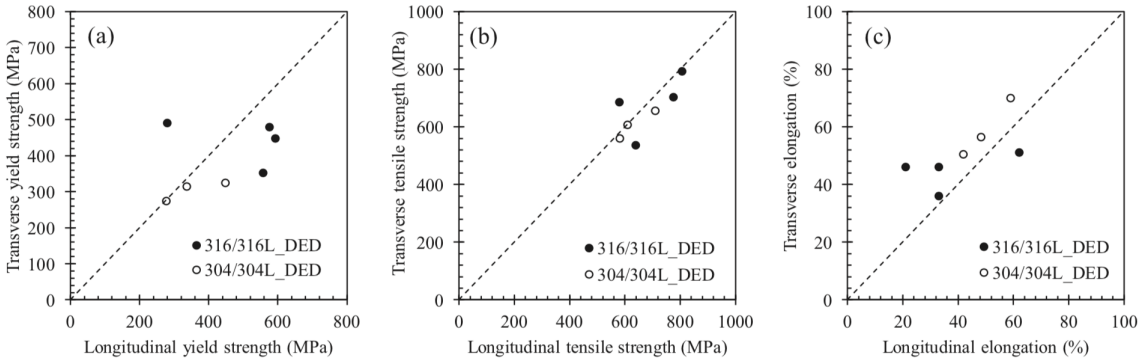

Figure 1.11: Image extracted from [7] showing that longitudinal yield and tensile strength are slightly superior than the transverse ones as shown in (a) and (b) respectively. In contrast in (c), the transversal elongation is superior in comparison to the longitudinal one.

Finally, other materials such as aluminium or copper alloys can be found in literature but their application is still challenged by the complex processing of such alloys [89].

1.6 Powder manufacturing processes

Powder is a common feedstock material used for AM processes because it is relatively convenient to transport and the melting is easy to control. However, the quality of the powder manufactured is a crucial element determining the final properties of the printed/repaired part. Indeed, characteristics including flowability, composition, shape and size distribution severely affect the properties as shown in [90, 91, 92]. These characteristics are inherited from the powder manufacturing process which can be categorized in 4 families as follows:

- **Gas atomization (GA):**
  Gas atomization is a manufacturing process where the material feedstock is melted under an air or inert gas blanket, or under vacuum as presented in Figure 1.12. The chamber is then backfilled with gas to force molten alloys through a nozzle where

high velocity air, Nitrogen (N), Helium (He) or Argon (Ar) gas impinges onto the flowing melt and breaks it up into small particles. The powder usually features spherical morphology and the presence of attached satellite particles as shown in Figure 1.13(a) and Figure 1.14(a) and (b). Inherited from the particularities of this process, the powder often contains entrapped gas bubbles creating porosity in the manufactured part as shown in Figure 1.14(c) and discussed in section 1.7.3 .

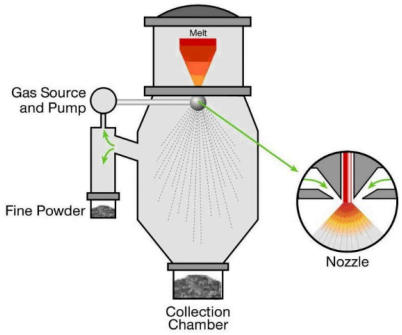

Figure 1.12: Scheme of the gas atomization process extracted from [93]

- **Water atomization (WA):**
  This manufacturing process is the same as gas atomization but with high pressure water jet instead of gas. The shape of the resulting particles is irregular and coarse in comparison to GA powder as shown in Figure 1.13. Also, this process exhibits the least uniform size distribution.

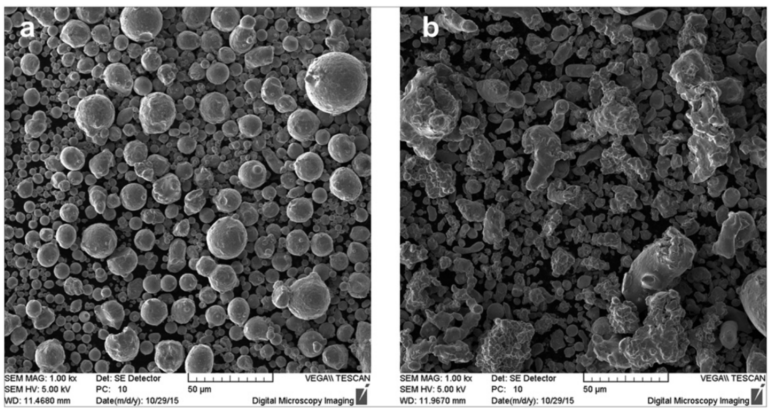

Figure 1.13: Image extracted from [94] showing SEM images of 17-4PH powder with a mean particle diameter of 20 μm produced by gas and water atomization in (a) and (b) respectively.

- **Rotary atomization (RA):**
  During this process, a molten metal is poured onto the surface of a spinning disk which ejects fine molten metal droplets that solidifies as metal powder [95]. The powder particles from the rotary atomization process exhibit smooth surfaces but the particles have an elongated aspect as shown in Figure 1.14(d) and (e).

- **Plasma rotation electrode process (PREP):**
  During this powder manufacturing technique, a bar of metal is held in rotation along its longest axe while it is melted at its free end by an electric or plasma arc creating an ejection of fine molten metal droplets that solidify as metal powder [96]. The PREP powder particles are perfectly smooth and spherical as shown in Figure 1.14 (g) and (h). Of the 4 manufacturing process, PREP show the most uniform distribution [97].

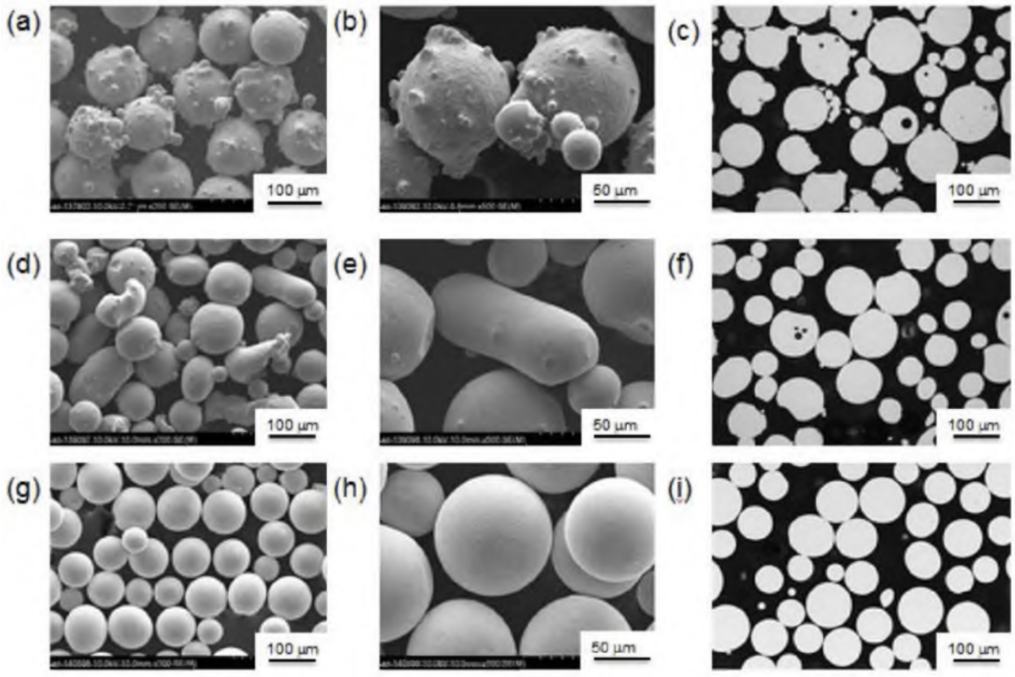

Figure 1.14: Image extracted from [97] showing a comparison of powder quality before use: (a) SEM 250x of GA, (b) SEM 500x of GA, (c) LOM of GA, (d) SEM 200x of RA, (e) SEM 500x of RA, (f) LOM of RA, (g) SEM 200x of PREP, (h) SEM 500x of PREP, (i) LOM of PREP.

1.7 Defects

Eventhough the additive manufacturing technique is promising to reshape the future of manufacturing industries, various defects inherent to AM exist and prevent the adoption of the technique to mainstream industries for now. A list of the most common defects is presented in this section.

1.7.1 Loss of alloying elements

As discussed previously, during the additive manufacturing process, the particles or wire are subjected to high temperature leading to selective vaporization. Indeed, the material to be melted is an alloy constituted of various elements that can vaporate because of their volatility resulting in additively manufactured parts with a chemical composition affected as shown in Figure 1.15. In this Figure extracted from [98], one can note the loss of aluminium and the gain of titanium with respect to the distance along the build height.

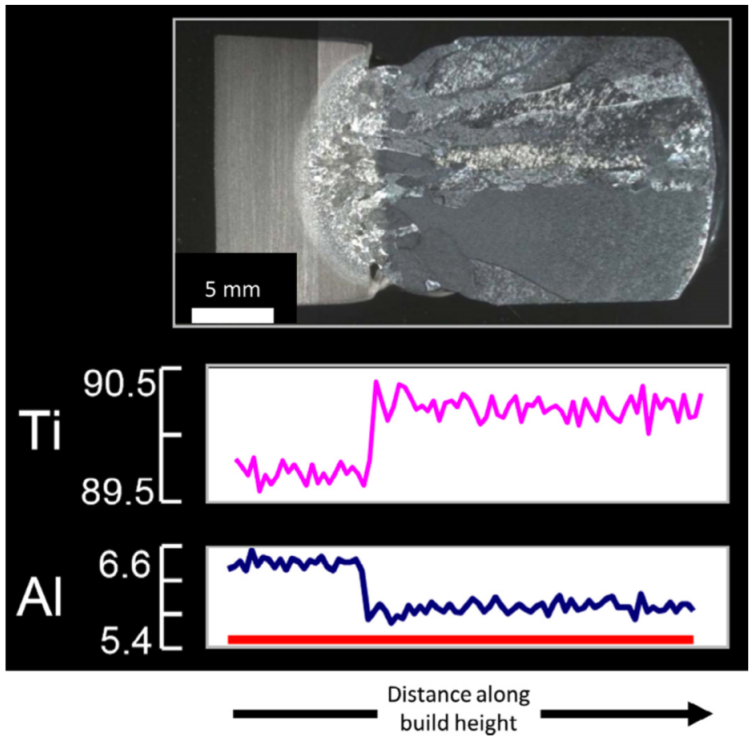

Figure 1.15: Variation of the chemical composition of a Ti-6Al-4V alloy with respect to the distance along the build heigth [98]

This variation of chemical composition is problematic because it can have several major effects on the final properties of the manufactured parts (microstructure, corrosion

resistance, mechanical strength etc.) [99, 100, 101, 102].
Therefore, it is important to measure this vaporization even though it is a complex task in the case of additive manufacturing. According to the literature, few techniques permit this kind of measure. For exemple in [103], the authors mounted a quartz tube system co-axially with the laser beam and were able to collect the vapors of certain alloying elements of an AISI 202 stainless steel.
Another way to measure this vaporization is by comparing the initial chemical compositions of the feeding materials with the final composition of the additively manufactured part. However, since AM produces highly heterogeneous microstructure and chemical segregation, a large surface of analysis is required in order to be statistically representative when non destructive analyses are performed (electron probe microanalysis, spectroscopy). However, performing destructive tests such as inductively coupled plasma mass spectrometry can greatly increase the accuracy of measurements [104].
Process parameters are driving the vaporization and should be optimized. In [105], the variation of aluminium content in a Ti-6Al-4V manufactured by DED was investigated for different process parameters. It was found that the "slow and hot" combination ensues the highest percentage of aluminium. This configuration is counter intuitive because a higher temperature facilitates the vaporization of certain alloying elements. However, the combination of process parameters expands the size of the melt pool resulting in less compositional variation i.e. it explains the higher content of aluminium. Hence one should remember that the vaporization of the alloying elements is determined by the melt pool geometry and temperature distribution i.e. directly linked to powder of the laser, deposition speed, powder rate and beam diameter.

1.7.2 Surface roughness

The surface roughness of a part is defined as the variance of the surface topology. It is directly related to a large number of interdependent parameters such as material feedstock (size of the particles, powder flow etc.), process parameters (laser powder, layer height etc.), design of the part (geometry, tilt angle), finishing etc. to name a few. This surface character of additively manufactured part is of critical importance since it will directly affect the aesthetics and mechanical properties [106, 107, 108, 109, 110, 111]. In addition, additively manufactured parts used for high end application necessitate an average surface roughness inferior to $1\,\mu m$ [112]. However, the surface roughness is usually superior to $15\,\mu m$ [113, 114], therefore limiting the direct application of parts as produced. Surface roughness can be reduced by employing several post processing techniques such as for exemple machining polishing or chemical treatment. These finishing techniques are used to limit the roughness surface of parts, however, it strongly increases the production time.
A general consensus is that optimum surface state of the additively manufactured part occurs when using thin and stable DED layers. Concerning the DED manufacturing process, 3 main phenomena are at the origin of the surface roughness and are presented next.
As described in [111], the first two causes are:

1. The sticking of the partially or non melted powder particles on the free surface as displayed in Figure 1.16

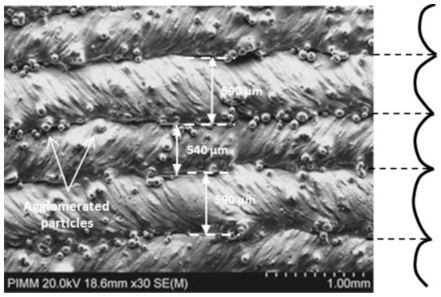

Figure 1.16: SEM image extracted from [111] showing the surface of a printed part with particles spread and agglomerated at the interlayer zones.

2. The formation of wave shapes between successive deposited layers defined as the formation of menisci with a variable curvature radii as presented in Figure 1.17

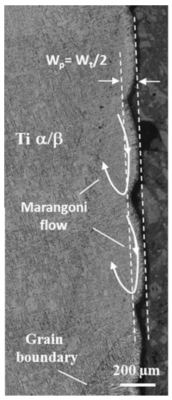

Figure 1.17: Image extracted from [111] of a transversale cut of wall where a periodic meniscus is observable.

3. The "stair case effect" presented in [115] and displayed in Figure 1.18 is a consequence of step approximation when an inclined surface is manufactured.

Other effects specific to PBF technology can be present but will not be discussed in this section.

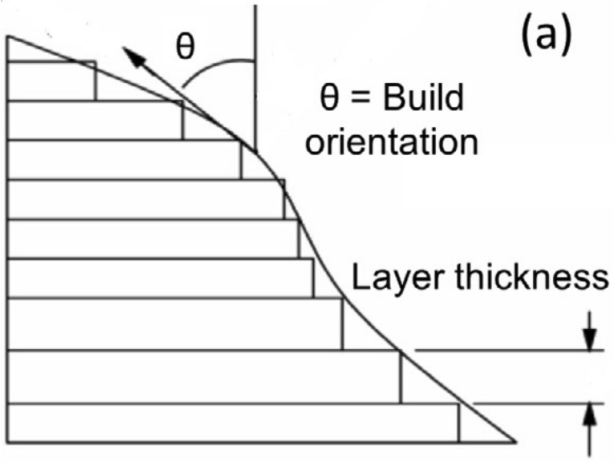

Figure 1.18: Scheme of the "stair case effect " extracted from [115] representing a transversale cut of a wall where a periodic meniscus is observable.

1.7.3 Porosity and lack of fusion defects

One of the challenges of additive manufacturing is to eliminate the presence of lack of fusion and porosity. Indeed, these common phenomena negatively affects the mechanical properties [116] and can be classified as follows:

- **Keyhole induced porosity:**
  As explained in [117], under certains conditions, the molten pool depth is driven by the evaporation of the metal ensuing very deep dilution (defined later in equation 2.4). Additionally, a punctual collapse of the vapor cavity formed by the evaporation of the metal can create holes at the bottom of the dilution of the track as presented in Figure 1.19.

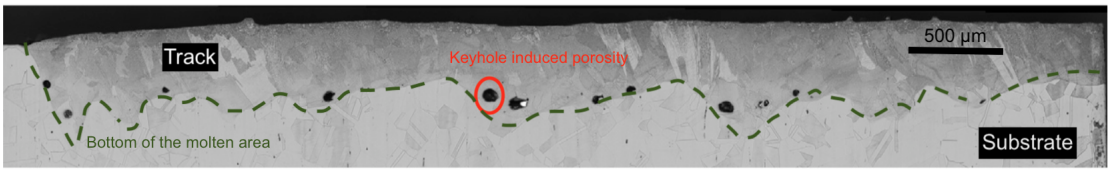

Figure 1.19: Longitudinal cross section of a track with the presence of keyhole induced porosity at the bottom of the molten area. We annotated the figure but the original was extracted from [117]

- **Intralayer porosity:** This phenomenon is often characterized by spherical porosity within a deposited layer due to gas entrapped as shown in Figure 1.20. These porosity can be due to: (i) the already present gas in the particle inherent from the

manufacturing process, (ii) the shielding gas or vapor in the melt pool entrapped during the solidification.

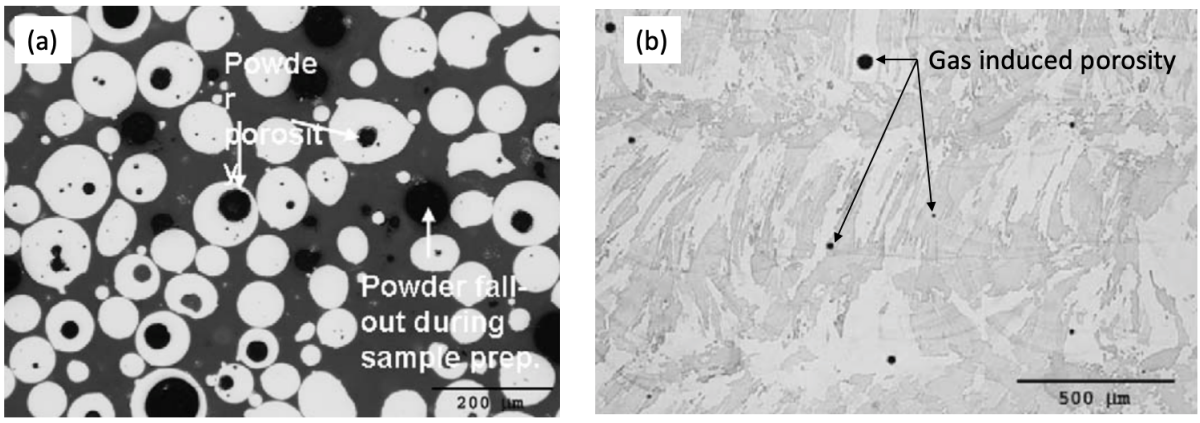

Figure 1.20: Photomicrographs of as-polished 17-4PH in (a) revealing porosity in the powder particle and in (b), image of a manufactured part showing gas induced porosity. The figure (b) was annotated by our mean and original (a) and (b) were extracted from [118].

- **Interlayer porosity or lack of fusion:** When there is an incomplete bonding (penetration of the melt pool) with the substrate or previously deposited layers, fusion defects can be observed as shown in Figure 1.21.

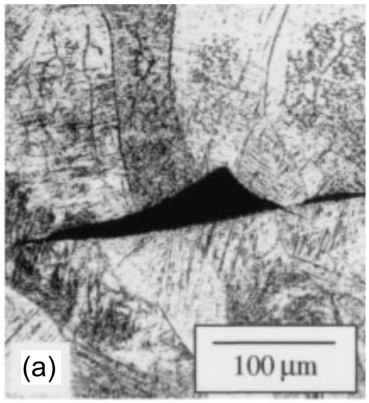

Figure 1.21: Image extracted from [119] of a metallographic observation of a lack-of-fusion porosity for laser-deposited Ti-6Al-4V

- **inter-run porosity or geometry induced porosity:** The geometry induced porosity is caused by the horizontally aligned or offset tracks of incompatible aspect ratios and forms near the base of deposited tracks [120] as schemed in the figure 1.22 extracted from [121].

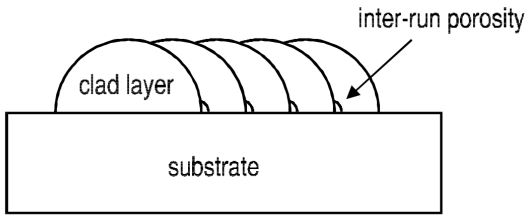

Figure 1.22: Scheme extracted from [121] of the inter-run porosity which is caused by the horizontally aligned or offset tracks of incompatible aspect ratios and forms near the base of deposited tracks

1.7.4 Cracking and delamination

Additively manufactured components are subject to 3 main types of cracking as detailed next:

1. The first type of cracking is usually referred to a delamination. This kind of phenomenon is pictured in Figure 1.23 and corresponds to the separation of two consecutive layers (or with the substrate) because of residual stresses. Indeed, when such a development is happening, the residual stress at the interlayer is superior to the yield strength of the material as explained in [122]. The origin and effect of residual stress will be discussed later in section 1.7.5

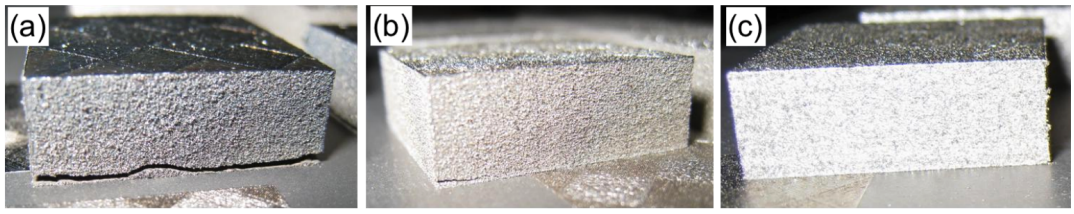

Figure 1.23: M2 High speed steel parts are produced by Selective Laser Melting and the effect of the substrate preheating on the delamination for 90^{o}C 150^{o}C and 200^{o}C is respectively displayed in (a), (b) and (c). The images are from [123] and one can note that pre-heating the substrate lowers the thermal gradient during the process and is therefore limiting the delamination.

2. The second type of cracking is the solidification cracking or hot cracking and can be observed in the deposited layer. More precisely, during the deposition, the difference of temperature between the depositing layer and deposited layers/substrate results in a difference of thermal contraction. Hence, the solidifying layer is limited creating a tensile strength and if the magnitude of this stress is higher than the solidifying track, cracking may occur in the solidifying layer and along grain boundaries or phases [124, 125].

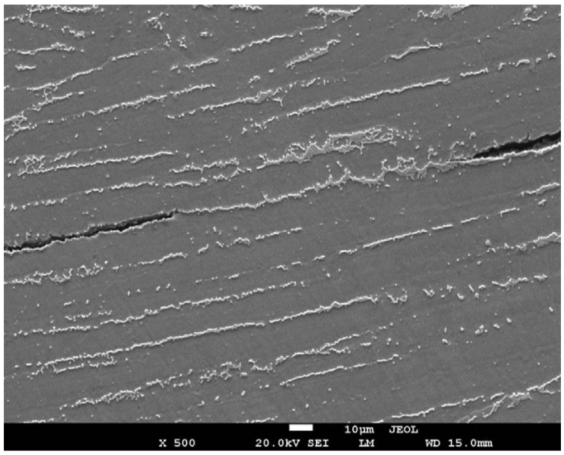

Figure 1.24: Image extracted from [125] showing a hot crack in the 718 coating with long chain morphology Laves phase.

3. Finally the liquidation cracking can be noticed in the partially melted zone. In this zone, certain low melting temperature precipitate phases present at the boundary of the grains are liquid during the cooling down when the deposited layer contracts and shrinks, this liquid zone might act like as a crack site [124, 126]

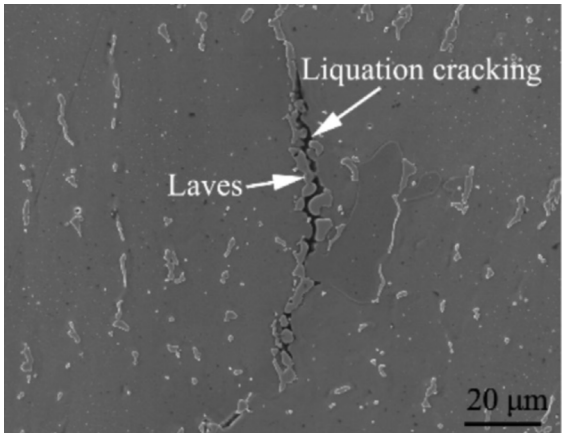

Figure 1.25: Image extracted from [126] showing the liquidation cracking an Inconel manufactured by laser additive manufactured system.

1.7.5 Residual stresses and distortion

During additive manufacturing, a liquid material is deposited onto cooler layers or substrate resulting in a unique thermal cycle with rapid heating and cooling down. This quick variation of temperature leads to several physical and mechanical phenomena and

residual stress is one of them. The origin of the residual stress (RS) is therefore multi-factorial and the key physical phenomena governing (RS) includes: i) the effect of the spatial temperature gradient as a consequence of the localised and in-motion heated zone, ii) the thermal match between the expansion and contraction of the material, iii) The uneven elastic strain distribution. Many of these phenomena are shared by the welding science since AM is very similar[124]. Finally, residual stress is very important because it can dramatically deteriorate the final properties by ensuing distortion [127] of the part as shown in Figure 1.26, as well as crack and delamination as discussed in section 1.7.4. However, several methods to reduce the RS is investigated and the most common one is preheating the substrate in order to reduce the thermal gradient [128, 129].

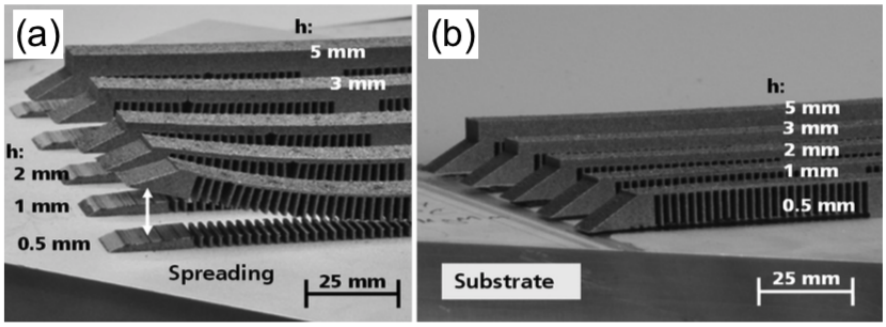

Figure 1.26: Image extracted from [128] showing the beneficial effects of preheating. In (a) and (b) aluminium components manufactured by selective laser melting with no preheating and a preheating of 200^{o}C are displayed respectively.

1.8 Repair of metallic parts

Repairing metallic parts with additive manufacturing is ambitious because it combines the challenges known and inherent to AM and the effects on the repaired part (bonding, heat affected zone, residual stress etc.). However, the benefits from a successful repair are profoundly attractive with important environmental and economic gains. Independently from the nature of the repairing technology, the purpose was always either to correct a default following the manufacturing procedure or to extend the life of the part by adding materials to the damaged zone. There are nevertheless still scientific challenges that need to be solved before it can be applied to critical aerospace parts such as the blades of the aircraft engine. However, for parts with a lower criticality, several repaired parts are already in use as illustrated in Figure 1.27 with the successful repair of a F/A-18 Rudder Anti-Rotation Bracket [130]. This component is often replaced because of extreme localizing wear damage. The price of the replacement operation with a new component is relatively cheap (300 USD) but the supply time can dramatically affect the availability of the aircraft up to 18 months which is critical during military operations. The component was successfully repaired by laser cladding and was certified as having

low risk permitting to provide operational components in few days (more details in [130]).

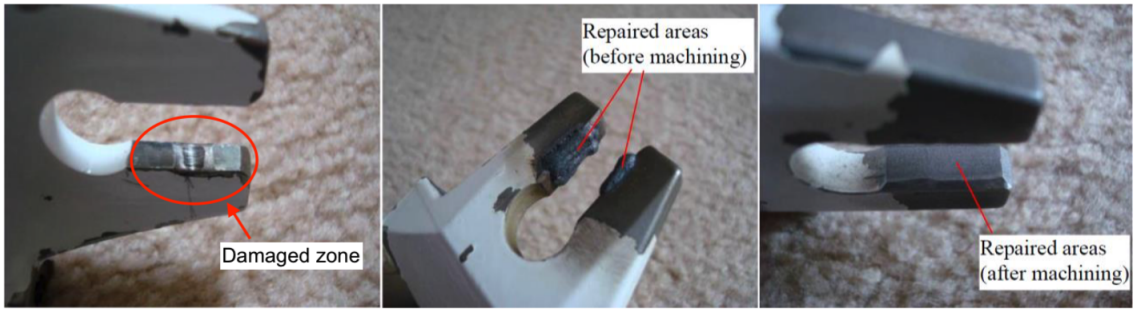

Figure 1.27: Image of the repairing procedure of a F/A-18 Rudder Anti-Rotation Bracket extracted from [130]

Next in this section, a non exhaustive list of the most common conventional repairing techniques will be presented with their advantages and inconveniences and finally an opening of the DED technology used as a repairing method will be proposed.

1.8.1 Conventional repairing methods

1.8.1.1 Thermal spray technology

The thermal spray process gathers different shades of technology such as arc spray, flame spray, plasma spray etc. [131] but the fundamental principles are the same. For a such process, a heat source is used to create molten or semi molten droplets from wire or powder and they are carried by a subsonic or supersonic gas on the damaged area of the substrate as schemed in Figure 1.29.
As the droplets impact the zone of interest, they quickly solidify and form the particular deposit called "splat" [132]. The splats randomly stack up on each other and form the lamellar microstructure characteristics of the thermal spray process. A typical microstructure is displayed in Figure 1.29.
The advantages of thermal spray [132] are:

- The deposition of potentially all the materials having a stable molten phase i.e. metals, alloys, ceramic, glass and some polymers at high deposition rates.
- An even greater number of suitable materials as substrates can be used because in this process, temperature-sensitive substrate are not subject to excessive heat because of the limited thermal energy of the droplet.

The limitations of thermal spray are [134, 132]:

- The presence of porosity (Figure 1.29) which varies greatly according to the processing conditions and heating source. Nevertheless it is generally between 3 to 15%.

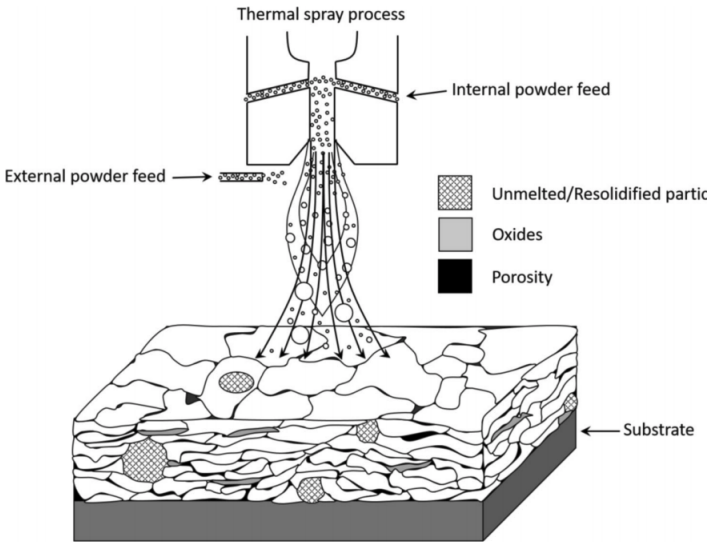

Figure 1.28: Schematic representation of a thermal spraying process with the two main components, a heat source and a jet, and the main features of the produced coatings extracted from [131]

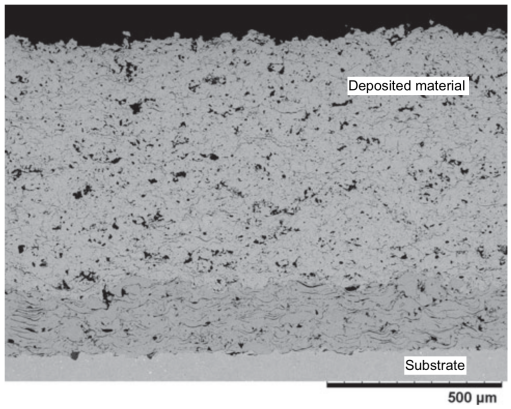

Figure 1.29: Typical microstructure obtained by thermal spray [133]

- During the spraying of the metals, the molten or semi molten particles are in contact with air resulting in the formation of metal oxide in the repaired deposit. The quantity of oxide depends directly on the process, parameters and materials and is in the order of few percent. Finally, the plasma spray technology operates in a vacuum atmosphere limiting the oxidation. However the magnitude of temperature is higher and some change in the alloy chemistry is more likely to occur.

- Residual stress is present as a consequence of the solidifying droplet on a colder material which is subject to thermal contraction. This residual stress increases as

the amount of material is increased and consequently the residual tensile stress rises to the point that the repaired deposit will crack or separate from the substrate. Therefore, generally, deposits with large thickness are not suitable for this process unless the powder sprayed is a high ductility material with low melting temperature.

- The deposition is limited to directly accessible surface to the spray stream.

1.8.1.2 Cold spray

Cold spray is a low temperature, solid-state material deposition process whereby metal particles (5 to 100 μm) are accelerated by a high-velocity gas (usually nitrogen, air) and projected onto the damaged substrate as schemed in Figure 1.30. As the particles impact the zone of interest, they intensively and plastically deform and create a high strength bond without thermally damaging the repaired components [135, 136]. In comparison to thermal spray, cold spray enables a higher thickness of deposit. Furthermore, this deposit benefits of compressive residual stresses [132].

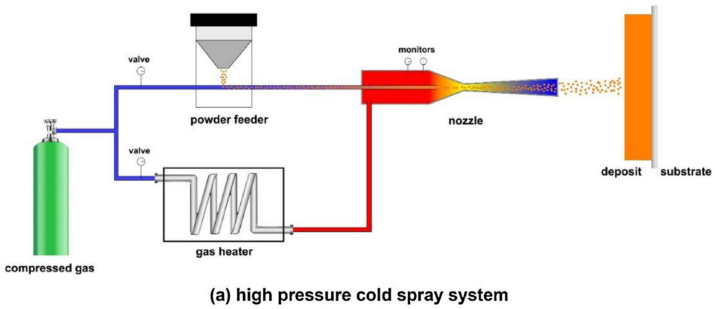

Figure 1.30: Scheme of the cold spray technology extracted from [12].

The advantages are [132, 12, 135, 136]:

- Higher density than thermal spray.
- Flexibility of materials.
- Minimum thermal input.
- High bond strength.
- Ultra-thick coatings with compressive residual stresses.
- No phase changes.
- No oxidation.

However strong disadvantages are present [132]:

- Near zero ductility of the deposited material.

- Hard materials cannot be projected and ductile substrates are preferred.
- The deposition on complex geometry is extremely complicated.

1.8.1.3 Arc welding

The arc welding is the most common welding technology and was originally used to join metals [137]. It is also well suitable to repair cracks can be declined into two families:

- The Tungesten inert gas (TIG) welding or the gas tungsten arc welding (GTAW)
- The plasma or microplasma transferred arc welding (PTAW)

GTAW, also referred as TIG is one of the most used technology for repair. As schemed in Figure 1.31. The process consists of maintaining an arc between the part to repair and the tungsten electrode generating heat by ionizing a gas and therefore creating a weld pool around 2500^{o}C. These operations are taking place while a filler metal is brought to the zone of fusion. During the operation, an inert gas is present to sustain the arc and protect the molten metal from contamination [138]. This shielding gas can be balanced depending on the application / material [139] as follows:

- Argon: The most commonly-used for a wide range of materials including steels, aluminium, titanium and stainless steel.
- Argon + 2 to 5 H_2 : Constricts and increases the temperature of the arc and permits higher welding speed and reduces the surface oxidation. However hydrogen cracking and porosity can be present for carbon steels and aluminium respectively.
- Helium + mixtures of helium/argon: Helium also has an increasing temperature effect resulting in faster and deeper welding. The higher price per m^3 of helium is limiting.
- Other elements such as oxygen and carbon dioxide can be added with respect to the effect desired.

PTAW is very similar to GTAW in the technology of the process, however, the fundamental difference is that PTAW comprises constriction of the arc thanks to an assembly around the electrode producing a higher amount of plasma resulting in higher arc temperatures. However for both processes, this high heat input is at the origin of inevitable cracks and a large heat affected zone is present [138].

1.8.2 Repairing with Directed Energy Deposition

The previous quick overview of the different technologies enable to picture how directed energy deposition used as a repair method could be promising. Indeed, with optimized parameters, this process could overcome the severe limitations to repair critical components requiring fine and complex deposition as well as a metallurgical bonding with very limited heat affected zone. It will be detailed in chapter 4

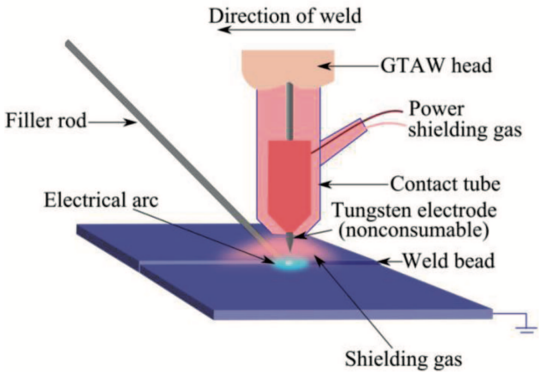

Figure 1.31: Scheme of the GTAW technology extracted from [140]

1.9 Conclusion

This chapter permits to understand what is additive manufacturing and more specifically Directed Energy Deposition. Moreover, the complexity of this unique process and the sensitivity to process parameters of the final properties are addressed. A list of defects occurring during the additive manufacturing process as well as the most common types the feedstock are proposed. This brief introduction permits to list the challenges of additive manufacturing and the necessity to understand all the main physical events in order to produce complex parts with great final properties.
Additionally, DED allow the repair of complex geometry. Some of the most common repair technologies such as cold spray, arc welding and thermal spray are compared and their limitations are listed. Consequently, the reasons why these traditional repair technologies are not suitable for critical, complex and fine components were highlighted. With optimized parameters DED can overcome all these limitations.
In the next chapters, DED walls will be used to manufacture fully printed specimens and then repair thin 316L stainless steel thin substrate. We will show that DED is a promising technology.

2 Analysis of the process parameters

Overview

The analysis of the process parameters begins with the presentation of the machine and the materials used in this study. Starting from an experimental database, we explore the shape of the cross section of a single-track and propose a model to predict the relation between process parameters and geometric parameters of the cross section of the track. Afterwards, we use these relations to: (i) predict the geometry of the track cross section thanks to an algebraic model, (ii) define a window of parameters for which the tracks have desired geometry. Finally, a satisfying combination of parameters was proposed and the microstructure was analysed at two different scales.

Contents

2.1 Objective

The objectives of this chapter are to:

- Propose relations between the process parameters and the track geometry.
- Predict the track geometry thanks to an algebraic model.
- Define a window of process parameters in which the geometry of the tracks satisfy manufacturing and repair applications.
- Analyze the microstructure of a "good track".
- Propose a combination of parameters that will be used for the rest of the thesis.

2.2 BeAM *mobile* machine

The 3D printer used in this study is the DED machine *mobile* from the manufacturer *BeAM* [141] shown in Figure 5.14. The machine is equipped with a 500W YLR-fiber laser and the powder is delivered to the deposition region through coaxial nozzles positioned approximately 3.5 mm above the substrate surface. The laser beam was delivered to the collimator through a $200\,\mu m$ optic fiber and was focused via a lens (focal length of 300 mm) on the substrate to a spot with a diameter of $0.8\,mm$. The operating wavelength of the laser is $1070\,nm$ and can offer a power up to $500\,W$. The powder is delivered by an argon gas flow which is also acting as a shielding gas around the melt pool. The amount of delivered particles is not directly chosen by the operator, but rather the powder flow is controlled by the speed of a rotating system for which a quantity of powder proportional to the rotation speed fall in a fumer and is carried by the gas previously presented. The powder flow is thus delicate to fully master. The gas flow was kept constant at 6 liters per minute and a measured powder flow of $6.5\,g/min$ is equivalent to a rotating speed of 3.3 round per minute. Finally, the transformation of the 3D designed geometry into a printing code accessible for the machine is done in PowerClad [142]. For simple geometry such as tracks or walls, the G-Code was directly coded.

Figure 2.1: Photo of the DED machine at the *Laboratoire de Mécanique des Solides* of École Polytechnique.

2.3 316L stainless steel: material of this study

Austenitic stainless steels are an interesting family of materials used in a diverse range of applications. We decided to work with 316L stainless steel (SS316L) for the following reasons:

- The great properties such as its weldability (primordial for AM), corrosion resistance and relatively high mechanical performances.
- A strong interest from a wide range of industries and therefore a great number of researches on this material additively or conventionally manufactured.
- The availability of this material on the market.

The commercially available SS316L powder used in this study was produced through gas atomization by Höganäs AB [143]. The atomization process was reminded in the chapter 1, and a SEM image of the powder is proposed in Figure 2.2. One can observe mostly spherical particles but also the satellites inherent to gas atomization.
The powder particles had a size lying within $45 - 90\,\mu m$ and its chemical and physical properties are presented in the tables 2.1 and 2.2 respectively. These informations were not measured in this study but extracted from the certificate of the powder delivered by the manufacturer. Additional details can be retrieved from the website of the manufacturer [143].
SS316L is after iron, primarily constituted by chromium (between 17–20%), nickel (9–14%) and molybdenum (2–4.5%) [144]. This material is composed by an Iron-Chromium-Nickel austenitic matrix i.e. a face-centered cubic (fcc) crystallographic structure and some of its minor constituents such as molybdenum, silicium, manganese act as substitutionable atoms while carbon and azote act as interstitial ones. The chromium is

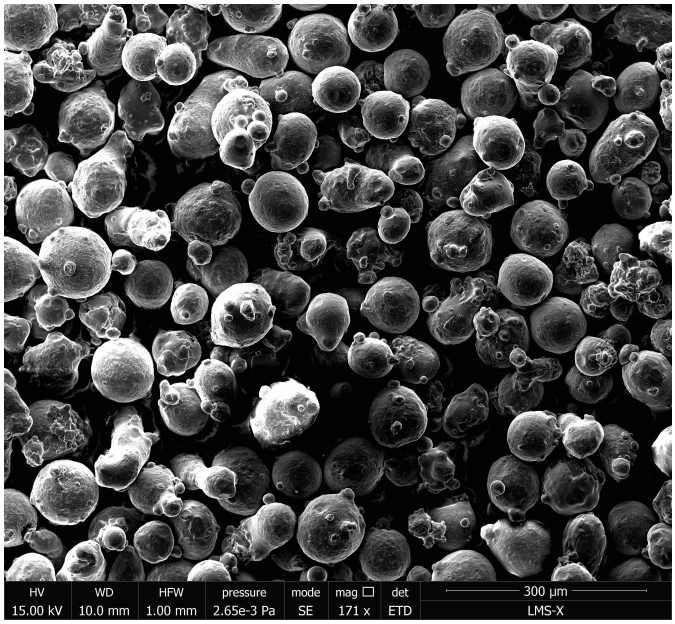

Figure 2.2: SEM image of the 316L stainless steel powder

at the origin of the good corrosion resistance and the fcc structure induces a high ductility and is permitted at ambiant temperature by the presence of "Gammagenic" elements such as Ni, N and Mn that expand the domain of stabilized austenite. At the opposite, other elements such as Cr and Mo are "Alphagenic" i.e. resulting in a body-centered cubic crystallographic structure.
Therefore the quantity of "Gammagenic" and "Alphagenic" elements are important for the final properties as they define the crystallographic structure of the alloy. A method to predict the phase balance was proposed in [145] where a "nickel equivalent" (Ni_{eq}) is calculated for the austenite stabilizing elements and compared to a "chromium equivalent"(Cr_{eq}) representing the ferrite stabilizing elements. By knowing the chemical composition of the alloy used in this study, the determination of the phases is possible. Ni_{eq} and Cr_{eq} are defined by the following equations:

$$Ni_{eq} = 15\% + 30 \cdot \%C + 30 \cdot \%N + 0{,}5 \cdot \%Mn \approx 16{,}1 \tag{2.1}$$

$$Cr_{eq} = \%Cr + \%Mo + 1{,}5 \cdot \%Si + 0{,}5 \cdot \%Cb \approx 20{,}45 \tag{2.2}$$

Finally, the position of the 316L is plotted in the phase diagram in Figure 2.3 and one can conclude that the processed material should be almost fully austenitic with some residual ferrite.

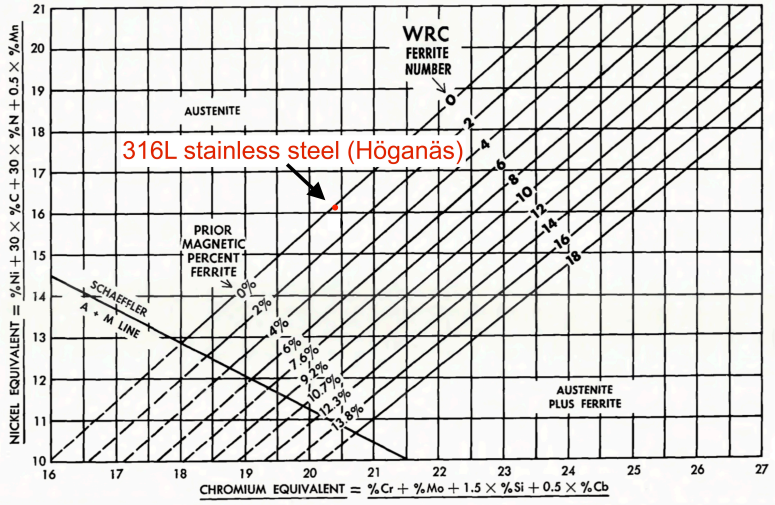

Figure 2.3: Position of the 316L powder (red dot) in the constitution diagram expressed as nickel versus chromium equivalent respectively. The diagram was extracted from [145].

Elements	C	Mo	Ni	Fe	Mn	Cr	Si
Weight (%)	0.011	2.5	12.7	balance	1.5	16.9	0.7

Table 2.1: Chemical properties of the 316L stainless steel powder.

Apparent density (Hall)	Flowrate (Hall)
3.96 g/cm^3	18.1 $sec/50g$

Table 2.2: Physical properties of the 316L stainless steel powder.

2.4 State of the art

As introduced previously, additive manufacturing is a manufacturing process whereby the final properties of the additively (re)manufactured component are directly dependant on the manufacturing parameters including the process parameters and the feedstock characteristics. Before printing a part and without any knowledge about the optimal process parameters, a process parameter map is defined. This map corresponds to all the combinations of parameters that are tested. The challenge is to define in the map, the combinations that we call the operational process parameter window, for which the tracks have an optimal geometry. This good geometry (detailed further) is a necessary condition to ensure the printability of a part, even though it is not sufficient to guarantee satisfying mechanical properties. The objective is to find a point in this window to reach targeted microstructure / materials properties.
In the case of DED, there is usually a consensus on 3 user accessible parameters

- the power of the laser - P (W)
- the deposition speed (scanning speed, printing speed etc.) - V (mm/min)
- the powder flow - Q (g/min)

Other parameters such as laser beam spot size, gas flow, laser beam energy density etc. will not be studied here but details can be found in [146, 147, 148]. The later are related to the machine construction and are difficult to access.
Understanding the effect of these 3 interconnected parameters on the geometry of the track is therefore fundamental. This preliminary study is performed with an experimental approach consisting of evaluating the effect of the variation of P,V and Q on the geometric parameters of the track defined in Figure 2.4 with W the width of the track, H the height of the track, A_c the surface of the track, A_m the surface of the molten area, h_d the depth of the track and α the track angles.
An arbitrary window of parameter values (i.e the process parameter map) is defined for the chosen parameters and tracks sweeping a series of the combination possibilities are printed and studied. Subsequently, we can evaluate the quality of each combination of parameters by analyzing the geometric characteristics of the track cross section and the microstructure. Finally, it is possible to create algebraic models fitted on the data of the shape, with for inputs P, Q and V and with the geometry of the track as result. Determining these relationships is the first step toward process parameter development and high quality tracks that are only reachable by working within a particular processing window. Similar discussions on the correlation between the processing parameters for a DED machine and the resulting geometry of the printed tracks have already been studied in [149, 150, 151, 152, 153, 154, 155]. We will emphasize the results in [150] where a mathematical formulae describing the relations between a geometrical characteristic and the machine parameters has been proposed under the following form:

$$Geometric\ \ parameter = a + (Q^{\alpha} \cdot P^{\gamma} \cdot V^{\beta}) + b \tag{2.3}$$

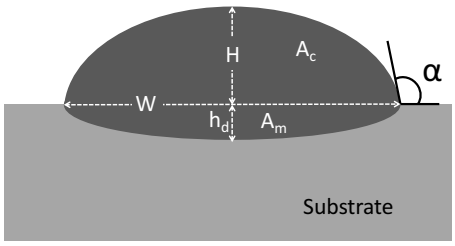

Figure 2.4: Scheme of the cross section of a single track deposition on a substrate. Its main geometric characteristics are: track height H, track width W, track area A_c, molten area A_m, track depth h_d, track angle α.

Where "geometric parameters" stands for any of the parameters (H, W, A_c etc.) displayed in Figure 2.4. We recall that Q, P and V denote the powder flow, the laser power and the deposition speed respectively. Also, a and b are model constants and α, γ and β are exponents calculated from experimental measures. The term $(Q^\alpha \cdot P^\gamma \cdot V^\beta)$ was originally named "complex parameters" but in the newer literature the term "combined parameters" is more established and will therefore be used in this study. This method has found a wide acceptance in the community [156, 154, 151, 155] and permits the creation of an operational process parameter window within the process parameter map as shown in Figure 2.5. In this Figure, one can see a process parameter map which takes into account the track angle and the track dilution with the power of the laser for the vertical axis and the ratio of the deposition speed over the powder flow on the horizontal axis. The algebraic relationships enable the definition for an operational window within the process parameter map where an optimal single-track can be formed (area shaded in grey).
Let us remark that non-geometric parameters such as building rates or powder efficiency can be added to refine the operational process parameters window. For example in [155], in addition to geometrical characteristics, the authors proposed to take into account industrial issues. Indeed economic issues can be tackled through building rate and powder efficiency which correspond to the volume of material deposited per hour and the amount of powder melted over the powder flow, respectively. A cross section track analysis of the geometry was performed as shown in Figure 2.6(a) in order to determine process parameters / track geometry relationships. From these equations, the authors were able to plot a processing map which highlights an operational window with boundary conditions such as a track dilution between $[10 - 30\%]$, a building rate of $100\,cm^3/h$ and a powder efficiency of 90% as plotted in Figure 2.6(b).

Inspired by these previous studies and by the particular objectives of repair, the two geometric parameters that will be of interest are: (i) the dilution D for the metallurgical

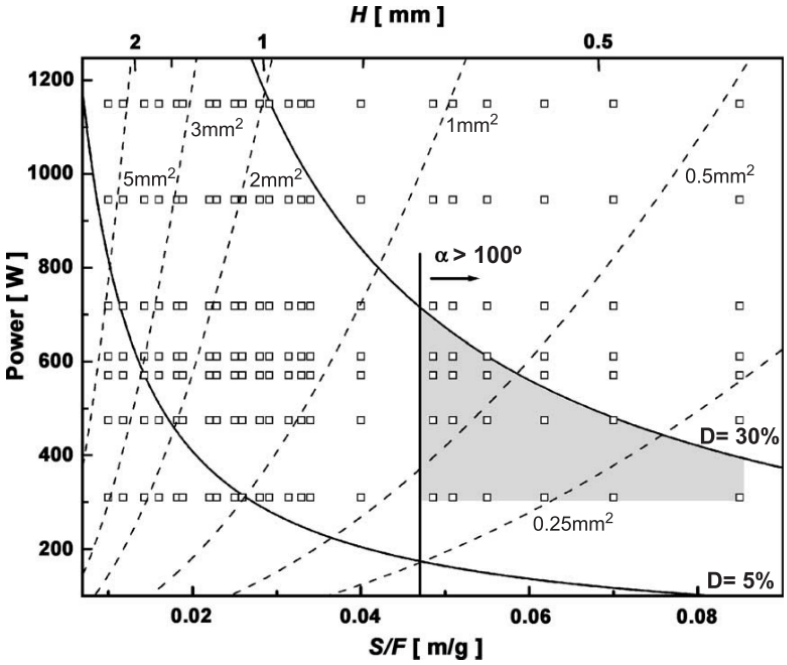

Figure 2.5: Process parameter map for single track of Ni-based alloy on a steel substrate extracted from [156]. The operation window in which the dilution is inferior to 30% and a track angle superior to 100^o is shaded in grey.

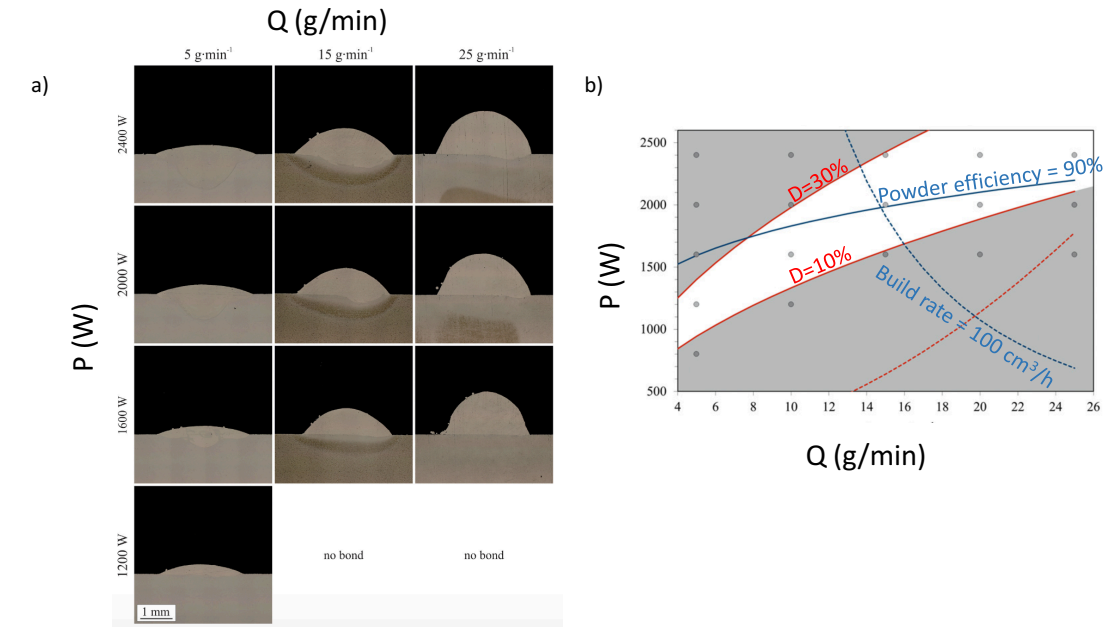

Figure 2.6: (a): Variation of the cross section geometry of an Inconel 718 track printed on mild steel with a deposition speed of 1000 mm/min. (b): 2d process parameter maps for a deposition speed of 1000 mm/min. The grey dots represent the data set in their work, the red lines are dilution boundaries, the dashed and continuous blue lines correspond to a build rate of 100 cm^3/h and a powder efficiency of 90% respectively.

bonding and, (ii) the track angle α. The latter permits to avoid inter-run porosity in case of a multi-track thickness repair. The dilution D is a dimensionless parameter that can be defined as: (i) the ratio of the the molten area (A_m) over the sum of the molten area and the track area (A_c) [156], or (ii) by the ratio of the track depth (h_d) and the track height (H) [157]. Next, we will use the definition of the dilution formulated in [157] and it is formulated in equation 2.4.

$$D = \frac{h_d}{H} \tag{2.4}$$

There is not a particular value of dilution that should be targeted, however, it seems that there is a consensus for a range between 10 to 30 %[151, 155]. In fact, in [158] the effect of the amount of dilution for a Ni-Cr-B-Si-C hardfacing alloy cladded is investigated. The authors observed a diminution of the Ni-Si-B eutectics which is one of the main strengthening components as the dilution increased resulting in the degradation of hardness. Hence, dilution is a critical parameter which has to be controlled.

2.5 Single track analysis

2.5.1 Influence of the machine parameters on a track

As mentioned previously, DED machines have a process parameter map defined by 3 interconnected machine parameters; the power of the laser P (W), the speed deposition or scanning deposition V (mm/min), and the powder flow rate Q (g/min). Variation of these parameters have an effect on the geometry of the printed track and will be quantified through the analysis of the cross section geometry of 36 tracks with the possible combinations presented in table 2.3.

Powder flow rate - Q (g/min)	Laser power -P (W)	Deposition speed - V (mm/min)
5.5	125	500
6.5	225	1000
8.5	325	2000
		3000

Table 2.3: Combination of the three operational parameters.The parameter ranges were estimated from [159] in order to sweep values around a combination of parameters offering an interesting geometry.

6 cm length tracks were deposited on a $15cm \times 20cm \times 0.5cm$ SS316L substrate with printing parameters in table 2.3 as presented in Figure 2.4 (a). Then, an orthogonal cross section cut was performed employing a *Labotom-5* machine [160] as shown in Figure 2.4 (b). Afterwards, the tracks were separated into different mountings to facilitate the polishing as pictured in Figure 2.4(c). Finally, the tracks were extracted from the mountings and a chemical attack consisting of soaking the tracks for 5 seconds in solution (detailed in section 2.5.5) permits to reveal the molten area, microstructure and chemical segregations. The cross section images used to measure the different geometric parameters were acquired by a numerical microscope *Keyence VHX-1000* and are displayed with respect to the powder flow during the manufacturing in Figure 2.8, 2.9 and 2.10 respectively. The different geometric parameters measured from the sections are listed in Table 2.4 and will first be qualitatively analyzed.

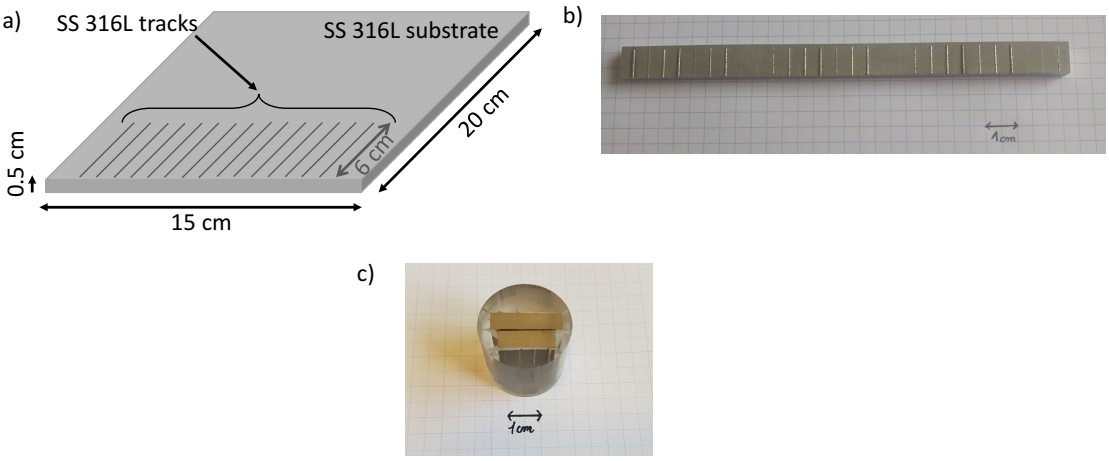

Figure 2.7: (a): Scheme of the printing procedure of SS316L tracks additively manufactured by DED on SS316L substrate with a unique combination of the manufacturing parameters. A transverse cut was performed and tracks were separated into different mountings to perform a fine polishing as pictured in (b) and (c) respectively.

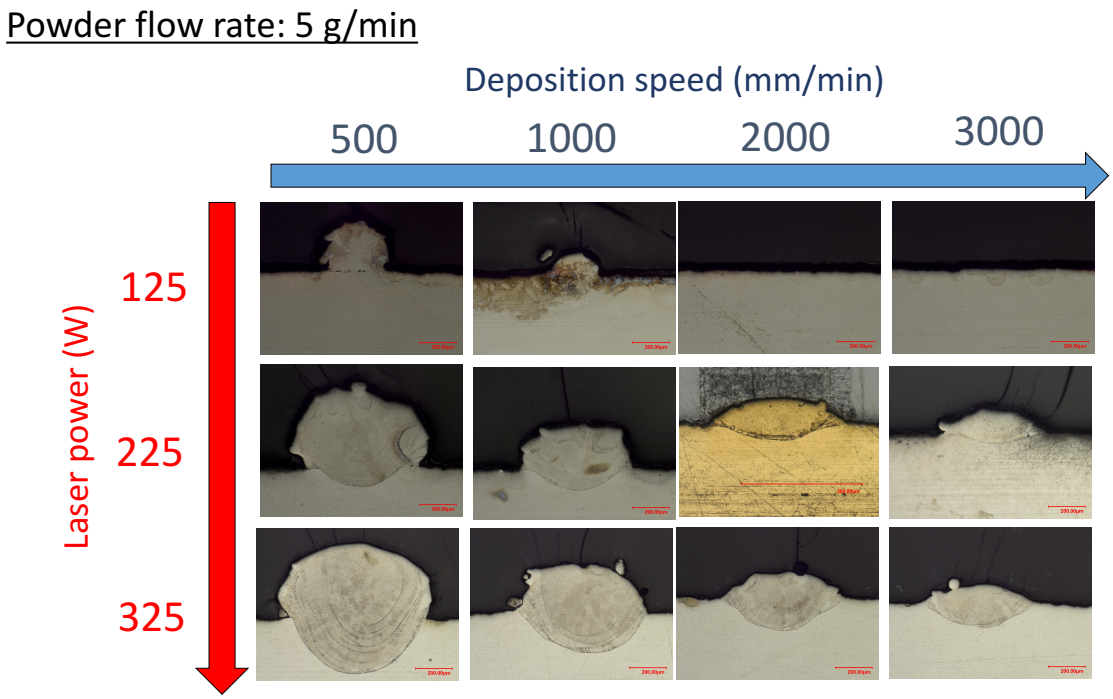

Figure 2.8: Cross-section map of SS316L tracks manufactured by DED on SS316L substrate for a powder flow rate of $5g/min$. The deposition speed and the laser power are the horizontal and vertical axes respectively.

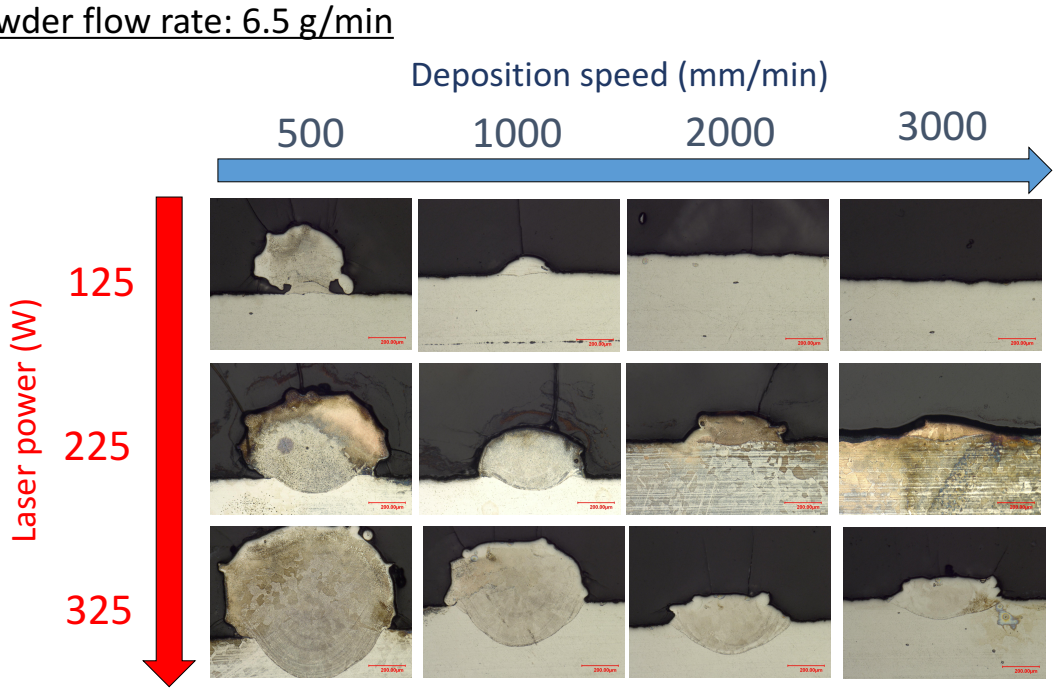

Figure 2.9: Same as 2.8 for a powder flow rate of $6.5 g/min$.

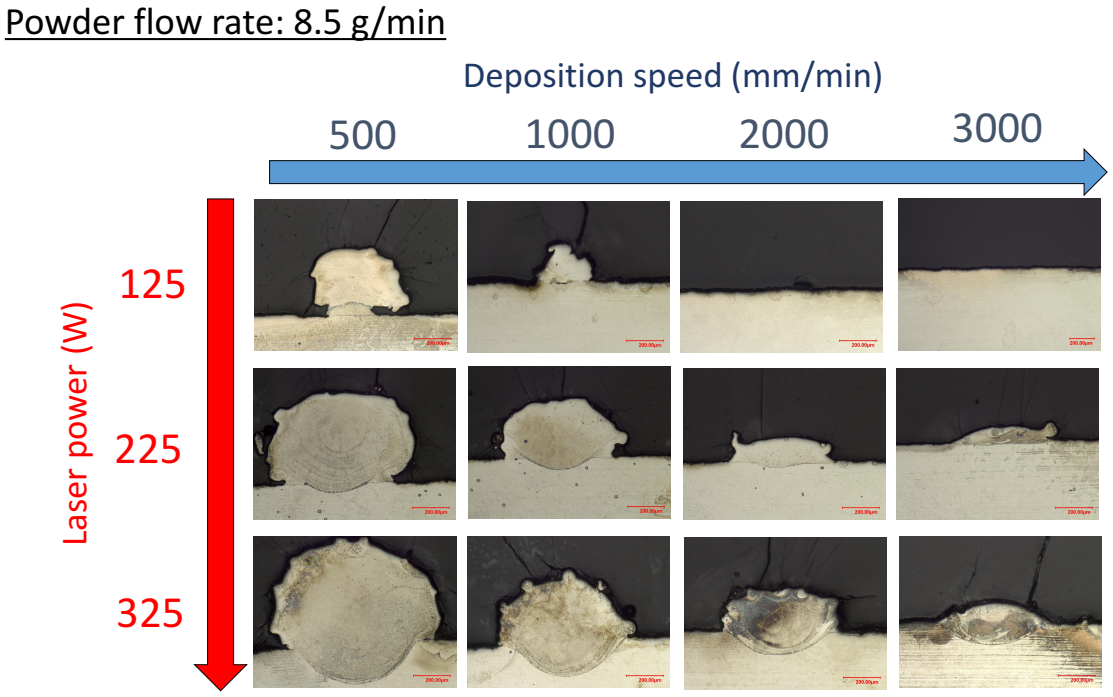

Figure 2.10: Same as 2.8 for a powder flow rate of $8.5 g/min$

Powder flow rate (g/min)	Laser power (W)	Deposition speed (mm/min)	Track Height (mm)	Track Width (mm)	Dilution height (mm)	Track surface (mm^2)	Molten area (mm^2)	Track angle (°)	Id
5	125	500	270	308	0	65646	0	94	1
		1000	110	250	16	19219	963	108	2
		2000	0	0	0	0	0	0	3
		3000	0	0	0	0	0	0	4
	225	500	420	606	105	238893	29939	66	5
		1000	218	597	111	110689	37308	113.5	6
		2000	127	620	46	52709	21173	145	7
		3000	126	569	59	51634	16218		8
	325	500	393	732	286	268935	150845	64	9
		1000	248	710	204	142973	105294	125	10
		2000	128	675	159	65264	73222	130.5	11
		3000	127	564	112	48682	47030	144	12
6.5	125	500	366	267	0	131503	0	60.5	13
		1000	88	325	15	17968	1435	145	14
		2000	0	0	0	0	0	0	15
		3000	0	0	0	0	0	0	16
	225	500	451	598	92	386339	28635	54	17
		1000	259	566	71	127213	21332	92.5	18
		2000	143	536	20	64699	3950	121.5	19
		3000	68	478	35	19956	8594	157.5	20
	325	500	571	733	245	464620	117550	32	21
		1000	329	723	220	202120	105879	102.5	22
		2000	156	672	170	78946	74200	134.5	23
		3000	125	647	103	49346	43209	142.5	24
8.5	125	500	493	257	0	152224	0	0	25
		1000	203	287	0	44149	0	0	26
		2000	0	0	0	0	0	0	27
		3000	0	0	0	0	0	0	28
	225	500	489	590	37	330798	11867	18	29
		1000	312	583	56	164198	10057	89.5	30
		2000	137	564	27	59504	7156	133.5	31
		3000	85	556	12	32723	1639	155.5	32
	325	500	563	775	211	476716	94247	40	33
		1000	350	695	124	204517	78101	91.5	34
		2000	219	616	126	90731	50073	98.5	35
		3000	100	617	111	37288	46137	150.5	36

Table 2.4: Table representing the measured geometric parameters with respect to the printing parameters.

2.5.1.1 Qualitative analysis

The effect of P, Q and V on the track geometry will be investigated and compared with the results from [161] where a similar analysis for a SS316L tracks cladded on a SS316L substrate has been performed.
The observations regarding the track height H are presented in Figure 2.11. One can remark in Figure 2.11(a) that the track height increases as the power augments. This effect is thought to be a consequence of a larger amount of powder melts as the power increases resulting in higher tracks. In contrast in [161], the authors found a very limited effect of the power of the laser on the height. In Figure 2.11(b), one can observe the diminishing effect of increasing the deposition speed on the track height. This effect is due to the fact that faster deposition brings less energy and powder per length unit ensuing a smaller track. Similar conclusions were drawn from [161]. Finally, one can note in Figure 2.11(c) that increasing the powder flow leads to a slight increase in the track height. This result can be explained by the fact that the available powder to be melted is increased leading to higher deposit. This trend was also shared in [161].
Figure 2.12(a) highlights some important properties regarding the track width. The plotted trend shows that increasing the power contributes to the augmentation of the track width. We explain this observation as a consequence of a larger melt pool is created as more power is provided. Consequently, the larger melt pool results in a larger track once solidified. A similar result was also shared in [161]. An opposite effect was noticed concerning the influence of the deposition speed as displayed in Figure 2.12(b). Indeed, a slight width decrease when the nozzle goes faster was observed. This is a consequence of the reduced power absorbed per length unit resulting in a smaller melt pool and therefore thinner tracks. This conclusion was also reported in [161]. Finally, the variation of the powder flow does not really affect the width as expressed by the curves in Figure 2.12(c).This observation was also shared in [161].
The measurements regarding the track depth h_d are displayed in Figure 2.13. It can be noticed in Figure 2.13(a) that increasing the power results in a deeper track. This is a consequence of the power increase for a given surface of application, which will consequently increase the penetration depth and therefore the corresponding track depth. Similar observation and results were also shared in [161]. Also by increasing the speed, one can see on Figure 2.13(b) that the track depth is diminishing because a faster nozzle reduces the amount of power per length unit. One can finally see on Figure 2.13(c) that increasing the powder flow results in reducing h_d. Indeed, more powder has the effect of attenuating the power penetrating the substate thus reducing the penetration of the laser in the substrate.

All theses analyses showed the direct effect of the power of the laser, speed deposition and powder flow on the track deposited from a qualitative point of view, but also how these parameters are interconnected. However, this type of analyses cannot capture the complexity of the relation between the parameters and the additively manufactured track. It is therefore necessary to investigate these complex associations with a finer and quantitative approach.

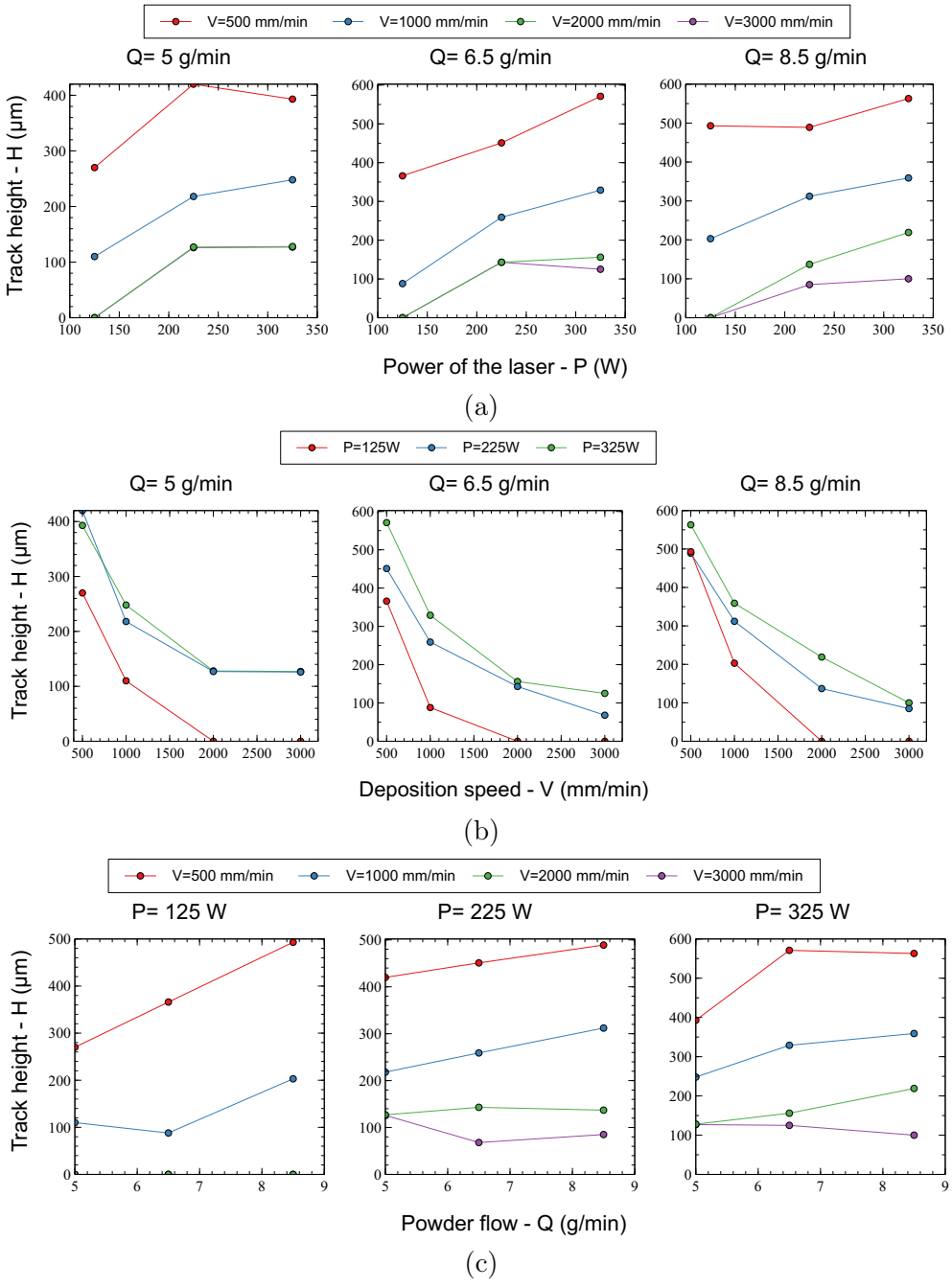

Figure 2.11: Evolution of the measured track height with respect to the laser power (P), deposition speed (V) and powder flow (Q) in (a), (b) and (c) respectively.

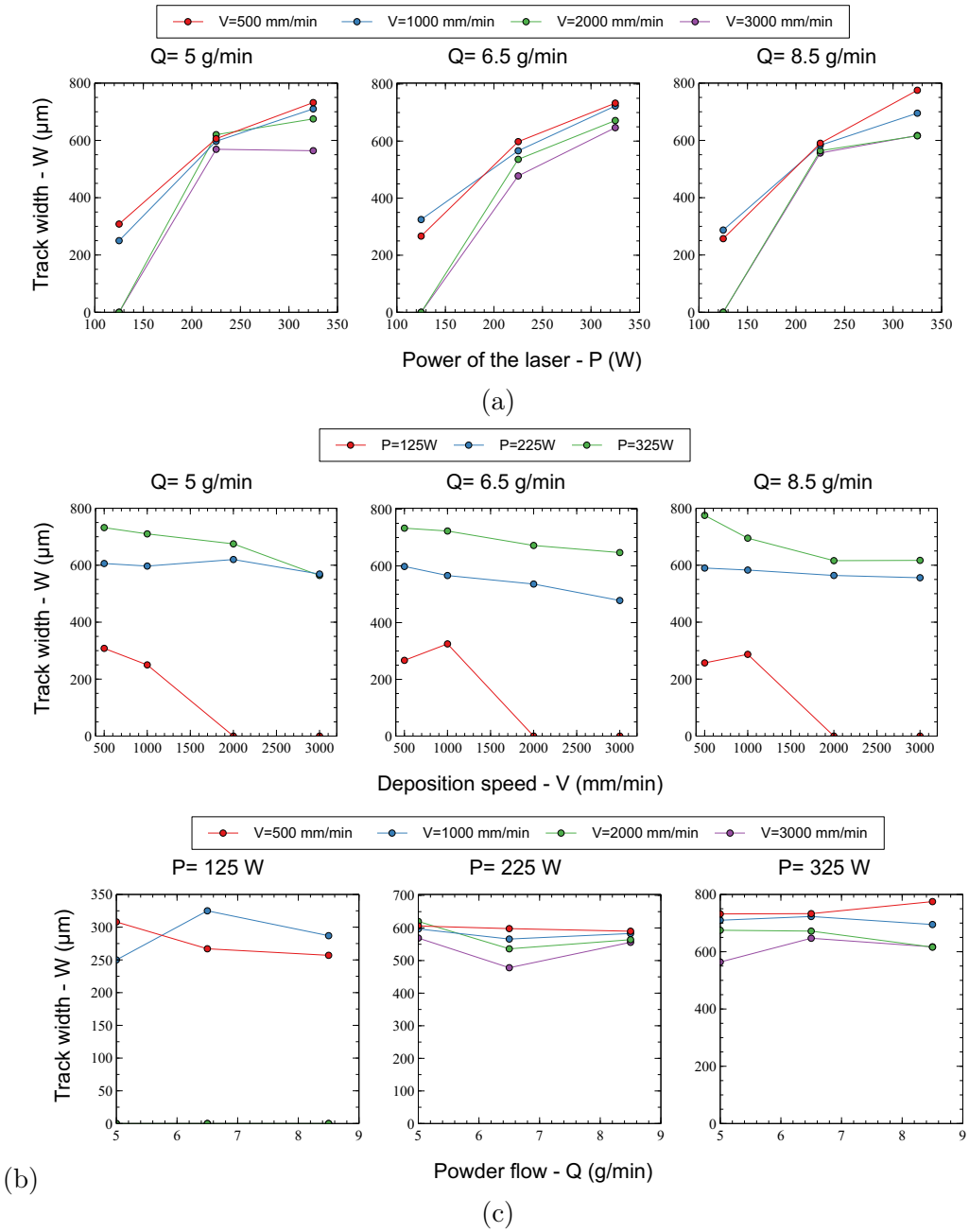

Figure 2.12: Evolution of the measured track width with respect to the laser power (P), deposition speed (V) and powder flow (Q) in (a), (b) and (c) respectively.

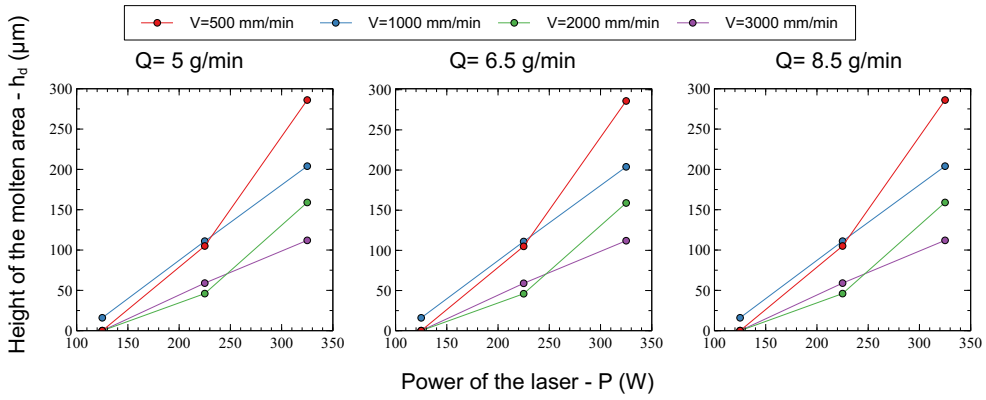

(a)

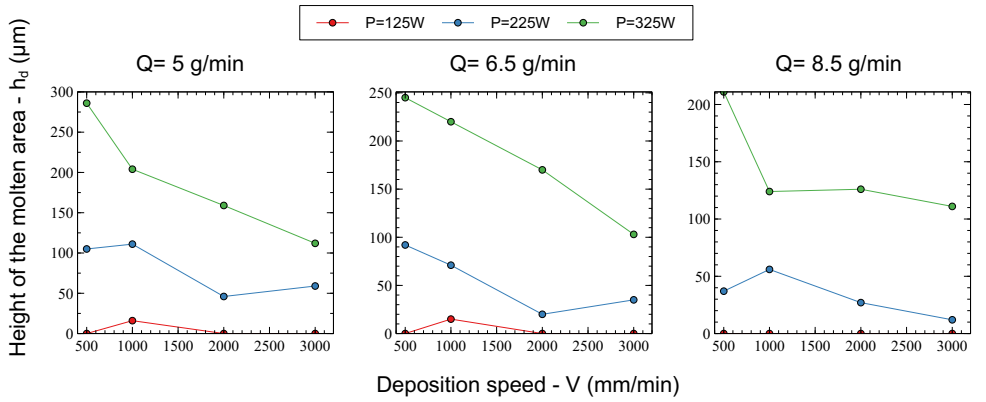

(b)

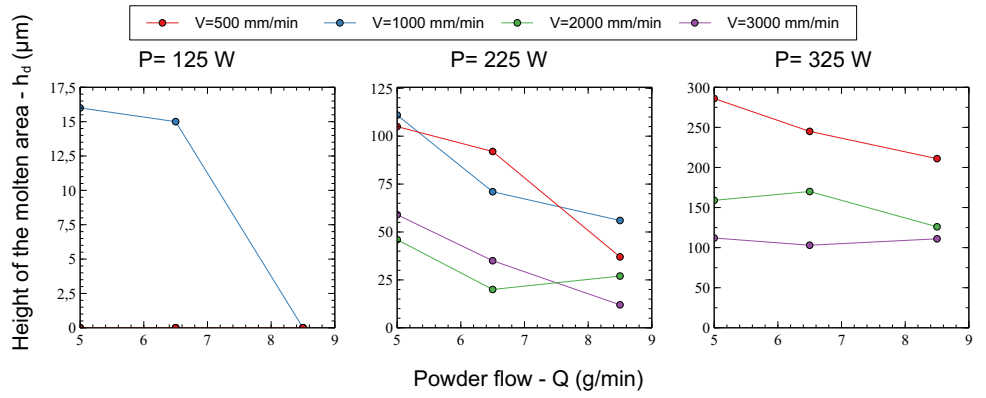

(c)

Figure 2.13: Evolution of the measured molten area height with respect to the laser power (P), deposition speed (V) and powder flow (Q) in (a), (b) and (c) respectively.

2.5.1.2 Parametric analysis

The measured geometric data of a single-track as a function of the process parameters Q, P and V will be used next to construct a parametric model for the observations. The parametric analysis is based on a procedure established in [150]. It permits the determination of a mathematical formulae describing the relations between a geometrical characteristic of the track cross section and the machine parameters as exhibited in equation 2.3. The proposed results and mathematic formulae will be compared to homologous results obtained in [151, 156, 159, 154]. Finally we will implement our results in a model predicting the geometry of the track.

The height of the track is one of the important geometric characteristics during the manufacturing of a part because the nozzle has to be elevated by a vertical increment to deposit the successive layer. A vertical spacing that is too large can lead to a loss of distance between the nozzle and the track conducting in the failure of the manufacturing after few layers. A vertical spacing that is too small would greatly increase the manufacturing time and the loss of powder which are economic issues that industries face. Therefore, the parametric model permits an accurate control of the vertical increment based on the prediction of the track height. The determination of the coefficient α, β, γ, a and b in equation 2.3 was done on Matlab and the relation for the track height H as well as its corresponding model are expressed in equation 2.5 and plotted in Figure 2.14, respectively.

$$H = 0{,}84 \cdot (Q^{0{,}58} \cdot P^{1{,}72} \cdot V^{-0{,}75}) + 42{,}19 \tag{2.5}$$

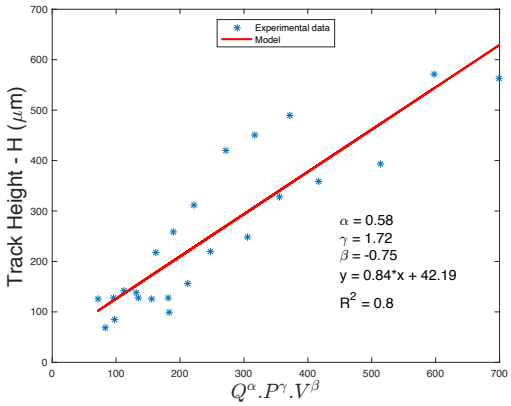

Figure 2.14: Parametric model for the track heigth.

The linear squares fitting conducted to a parameter set with a correlation coefficient $R = 0{,}89$ ($R^2 = 0{,}8$). We consider the result as a good correlation between the track

height and the combination of parameters.
A close inspection of the obtained parameters, more precisely the exponents of Q, P and V permit to draw some conclusions. The negative value of the exponent of the deposition speed V states that the height diminishes for an increasing speed. One can also note the important increasing effect of the laser power as it has the highest positive exponent. The same increasing effect with a lower magnitude can be observed for the powder flow. These results are consistent with the observations made in the qualitative analysis.
The corresponding expressions of the track height for [151, 156, 159, 154] are proposed in table 2.5. In [151, 156], the track height is only proportionate to the ratio $\frac{Q}{V}$ corresponding to the mass of powder deposited per meter. In [159, 154], a relation similar to ours is proposed. We believe that the power should have an important effect in the track height equation as it is responsible for the amount of powder melted and therefore the height.

The width of a track is also a parameter of great importance since it is a necessary information for the overlapping of the tracks in the case of a a multi-track thickness part. It is also primordial in the case of a single-track repair of a thin part as the width should fill the complete area. The model of the track width is expressed in equation 2.6 and plotted in Figure 2.15.

$$W = 0{,}73 \cdot (Q^{0{,}15} \cdot P^{1{,}11} \cdot V^{-0{,}01}) + 146{,}01 \tag{2.6}$$

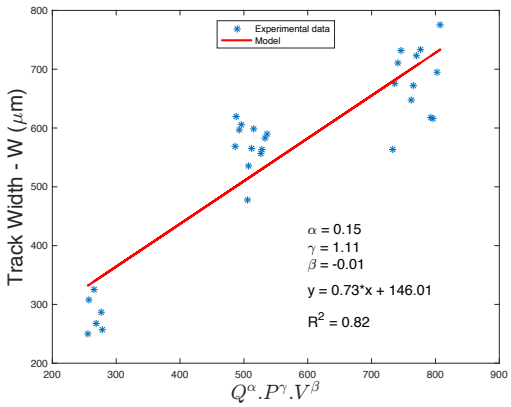

Figure 2.15: Parametric model for the track width.

The linear squares fitting conducted to a parameter set with a correlation coefficient of $R = 0{,}91$ ($R^2 = 0{,}82$). We believe the results to be a good agreement between the parametric model and the measured value of the width. One can notice that the

exponents of the deposition speed and powder flow are small in comparison to the one of the power, i.e. the power mainly drives the width of the track. These observations were also shared in the qualitative analysis of the width. In contrast, other research groups show relations with a track width only depending on the ratio $\frac{P}{Q}$ as shown in table 2.5. Their relationship therefore expresses that the track is exclusively a consequence of thermal effect i.e, the power and the deposition speed are both interconnected and impact the amount of energy brought per meter in the substrate and therefore on the size of the melt pool. We completely agree with the preceding observation supported by a physical interpretation, however our data did not support this conclusion.

The area of the track, A_c is of significant interest as it will be useful in the prediction of the geometry of a track (detailed in section 2.5.2). The model for this geometric parameter is exhibited and plotted in equation 2.7 and Figure 2.16 respectively.

$$A_c = 0{,}74 \cdot (Q^{0{,}88} \cdot P^{3{,}07} \cdot V^{-1{,}01}) + 37945{,}15 \tag{2.7}$$

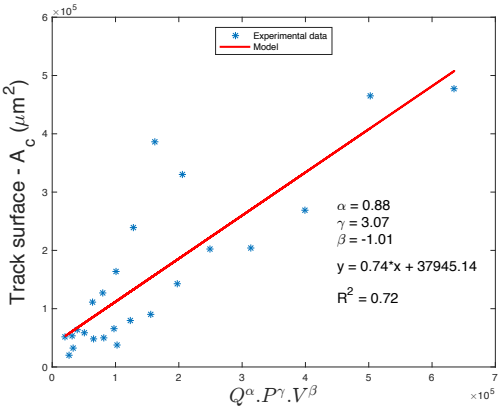

Figure 2.16: Parametric model for the track surface.

The linear squares fitting conducted to a parameter set with a correlation coefficient of $R = 0{,}84$ ($R^2 = 0{,}78$). We consider the result as a good correlation between the molten area and the combination of parameters. For this models, a similar conclusion to the track height can be drawn for the effects of Q, P and V. In addition, the equation is similar in terms of trend to the one proposed by [151] , [156] and [153] in table 2.5.

Finally, the same analysis can be made for other geometric parameters, and their respective model and comparison to [151, 156, 159, 154] are available in Figure 2.17 and table 2.5 respectively.

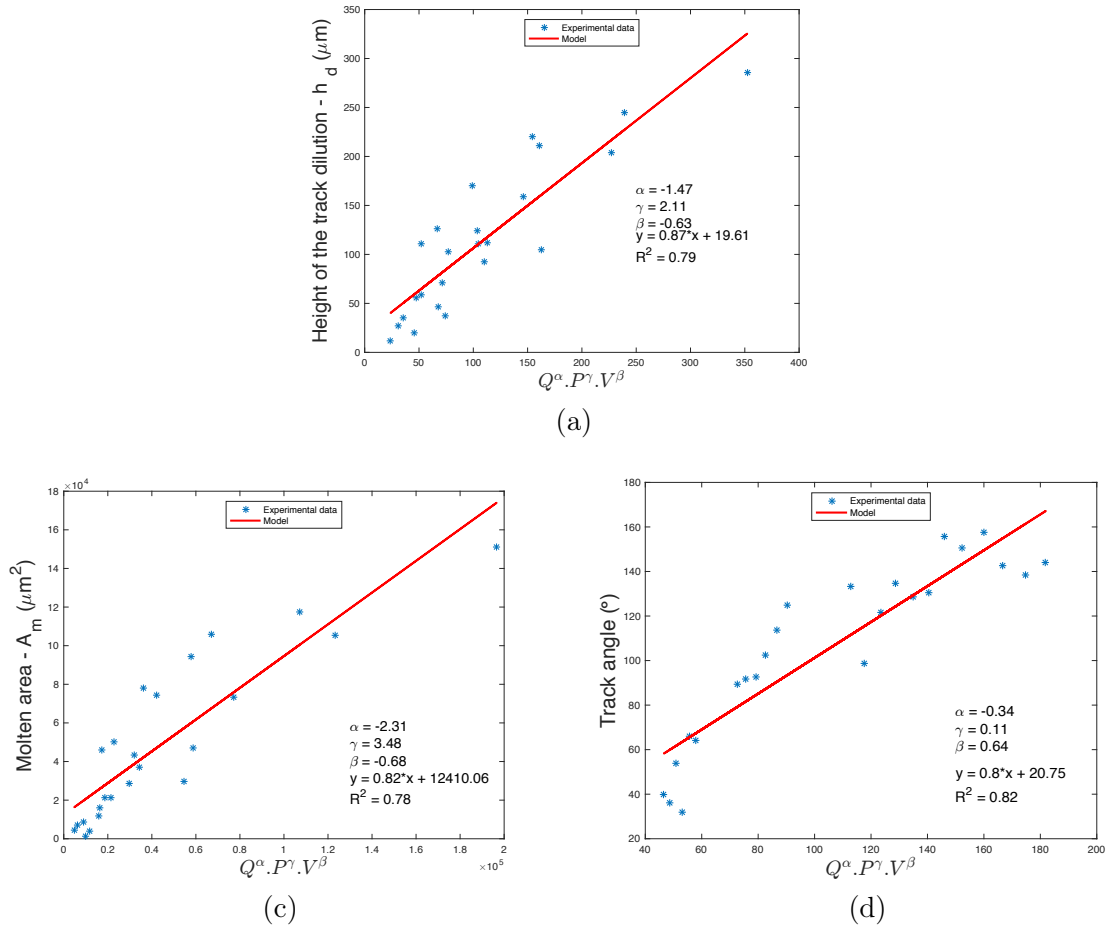

Figure 2.17: Parametric models for the height of the track dilution, the molten area and the track angle in (a), (b) and (c) respectively.

	[151]	CR	[156]	CR	[159]	CR	[154]	CR	This work	CR
H	Q/V	0.97	as in [151]		$P^{1/4}.Q^{3/4}/V$	0.6	$P^2.Q/V^{3/2}$	0.6	$Q^{0,56}.P^{1,72}/V^{3/4}$	0.8
W	$P/V^{1/2}$	0.90	as in [151]		$P^{3/4}.V^{1/4}$	0.92	$P^{3/2}/V^{1/3}$	0.73	$Q^{0,15}.P^{1,11}/V^{0,01}$	0.82
A_c	$P^{1/2}.Q/V$	0.98	as in [151]		$P.Q/V^{3/2}$	0.91			$Q^{0,88}.P^{3,07}/V^{1,01}$	0.72
A_m	$P/(Q.V)^{1/3}$	0.9	$P^2/V^{1/2}$	0.67	$ln(P^{4/5}/Q^{1/4})$	0.39			$P^{3,48}/(Q^{2,31}.V^{0,68})$	0.78
α	V/Q	0.66	$Q/(P.V)^{1/2}$	0.74			$P.Q^{1/2}/V$	0.56	$Q^{0,11}.V^{0,64}/P^{0,34}$	0.82
h_d									$V^{2,11}/(Q^{1,47}.P^{0,63})$	0.79
D	$(P.V/Q)^{1/2}$	0.28	$\ln(P.(V.Q)^{1/2})$	0.50			V/Q	0.39		

Table 2.5: Parametric models for the different geometric parameters of a track cross section and their respective correlation coefficient (CR).

2.5.2 Statistical prediction of the geometry

The shape of a single-track is characterized by the superior and inferior shape defining the part in contact with the air and the substrate respectively. The objective of this subsection is to predict the complete superior geometry of the cross section using a model proposed in [153]. Such a tool would allow the machine operator to produce tracks with a targeted geometry in order to (i) specify the vertical increment between two layers, (ii) avoid inter-run porosity for multi-track thickness (re)manufacturing and (iii) target a specific track width in case of a single-track thickness repair. This model named "disk model" proposes a circular arc for the superior shape. This choice is justified by Figure 2.8, 2.9 and 2.10 where one can see that the part of the track above the substrate can be approximate to a section of a disk which is centered either under or above the substrate as shown in Figure 2.18(1) and (2) respectively. Such geometry can be explained by the surface tension effect [162] and provides successful prediction with a limited uncertainty [153].

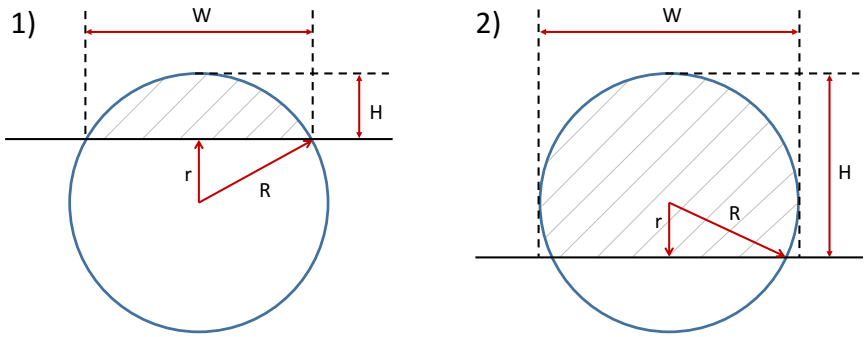

Figure 2.18: Scheme of the two types of cross-section geometry of the single track. In 1) and 2), the center of the circle is under and above the substrate line respectively.

To determine between the configuration (1) or (2) of Figure 2.18, we compare the track surface A_c to the half surface of a disk with a diameter W. If $A_c < \frac{pi \cdot W^2}{8}$, the track will have the targeted type (1) geometry whereas if $A_c > \frac{pi \cdot W^2}{8}$, the track will have a type (2) geometry which is unacceptable in case of multi-track thickness manufacturing (inter-run porosity). Finally if $A_c = \frac{pi \cdot W^2}{8}$, the track will be a half disk with a diameter W.

- Type (1): For this geometry, $A_c < \frac{pi \cdot W^2}{8}$. From Figure 2.18(1), the center of the circle under the substrate surface ($Center - Type1$) is located at a distance :

$$Center - Type1 = \sqrt{R^2 - (\frac{W}{2})^2} \tag{2.8}$$

In addition, it was demonstrated in [163] that the area of the disk segment above the chord (corresponding the to track area A_c) can be expressed with a high accuracy as:

$$A_c = \frac{2}{3}W \cdot D + \frac{H^3}{2W} = \frac{H}{6W}(4W^2 + 3H^2) \tag{2.9}$$

Further, from the figure 2.18, we can also express the track height as:

$$H = R\left(1 - \sqrt{1 - (\frac{W}{2R})^2}\right) \tag{2.10}$$

Finally by replacing H into equation 2.9, we have:

$$A_c = \frac{1}{6W}(R(1 - \sqrt{1 - (\frac{W}{2R})^2})(3R^2\left(1 - \sqrt{1 - (\frac{W}{2R})^2}\right)^2 + 4W^2) \tag{2.11}$$

- Type (2): For this geometry, $A_c > \frac{pi \cdot W^2}{8}$. With the same procedure, the radius of the circle is determined by solving the following equation:

$$A_c = \pi R^2 - \frac{1}{6W}(R(1 - \sqrt{1 - (\frac{W}{2R})^2})(3R^2\left(1 - \sqrt{1 - (\frac{W}{2R})^2}\right)^2 + 4W^2) \tag{2.12}$$

Finally, the value of R, the disk radius can be calculated from equation 2.11 and 2.12. Indeed, A_c and W can be predicted from a set of process parameters thanks to their respective models in equation 2.7 and 2.5 and therefore, the tracks can be simulated just from these inputs.
A detailed example of the simulation of the track geometry is plotted in blue in Figure 2.19 for the following set of process parameters: Q= 6.5 g/min, V= 500 mm/min and P= 325W. As a comparison, we plotted in orange the disk model having A_c and W measured directly on the track. A difference of $\approx 11\%$ between the blue (parametric inputs) and orange (experimental inputs) is observed. This difference is a consequence of the scatter of the data and the measurements coming from the uncertainties.

Next, a comparison of the track cross section with the geometry simulated is proposed in Figure 2.20, 2.21 and 2.22. First of all, one can notice that the type of simulated geometry ((1) or (2), see Figure 2.18) is always in accordance with the geometry of the real track cross section. In addition, one can remark that the orange model i.e. the geometry

simulated with experimental measure inputs is for most of the printed tracks respecting with a fair accuracy the dimensions and shape. Hence, the assumptions concerning the geometry of the track cross section induced by surface tension effect is confirmed. Nevertheless, one can see that the blue model i.e. the geometry simulated with parametric inputs is less accurate. It is a consequence of the scattering measurements for A_c and W affecting the precision of their relative parametric model. If these relations are now compared with the ones in [151, 156, 159] (displayed in Table 2.5), one can remark that the correlation coefficient for A_c and W are $\approx 13\%$ and $\approx 31\%$ lower respectively than the ones from the literature. This lack of accuracy is thought to be mainly due to the powder flow. Indeed, a variability of the flow particularly at the beginning of the printing was observed and could explain the previous results.
Finally, the presented disk model is a phenemological model and therefore its accuracy is driven by the quantity of data the parameters used in the model. One way to improve the model is to introduce an analytical relation of A_c and W function of the process parameters.

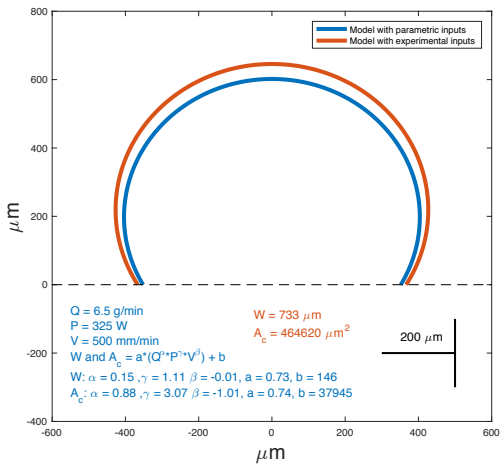

Figure 2.19: Prediction of the superior shape of the track by a model with imputs coming from the parametric and experimental measures in blue and orange respectively.

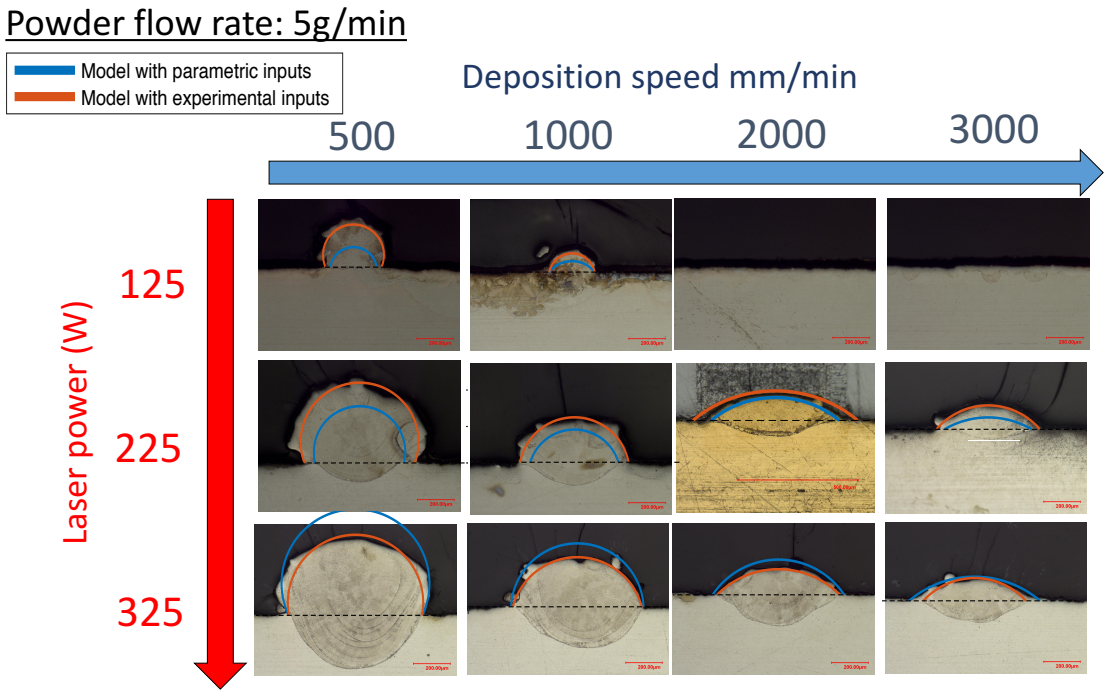

Figure 2.20: Cross-section map of SS316L tracks manufactured by DED on SS316L substrate for a powder flow rate of $5\,g/min$ and its geometric prediction coming from parametric and experimental inputs. The deposition speed and the laser power are the horizontal and vertical axis respectively.

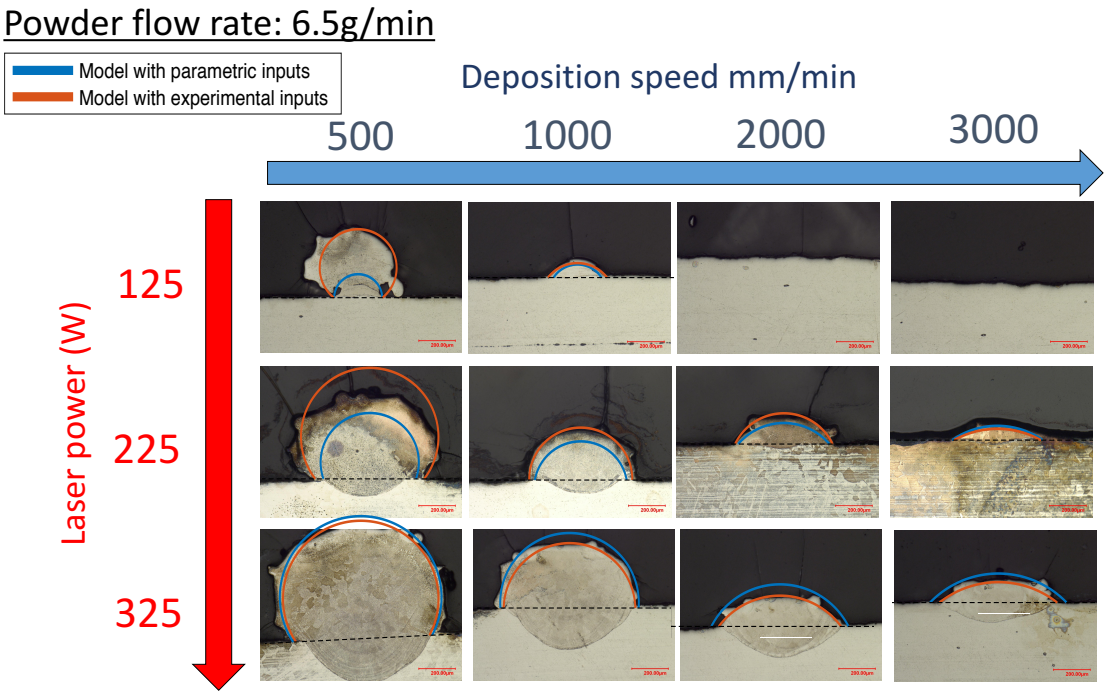

Figure 2.21: Same as 2.20 for a powder flow rate of 6.5 g/min

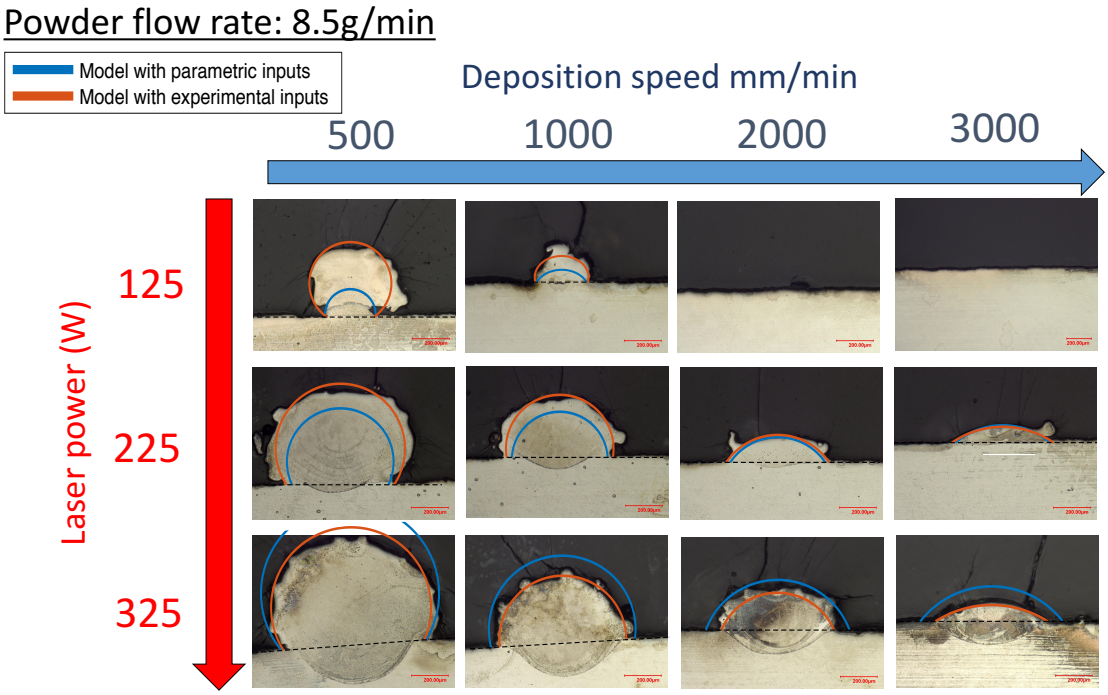

Figure 2.22: Same as 2.20 for a powder flow rate of 8.5 g/min

2.5.3 Generation of an operational process parameter window

As discussed previously, an optimal track defined by its geometric characteristics can only be printed in a small operational window within the process parameter map. Additionally, constraints such as powder efficiency and building rates can be added to narrow the operational window as shown in Figure 2.6. In this study, for a repair purpose, only the dilution D defined in equation 2.4 and track angle α will be taken into account. The dilution permits a metallurgical bonding with the damaged part. However the dilution should not be too great as it can deteriorate the chemical composition and thus affect the chemical composition and the properties [164]. Hence, a dilution included in the interval $[10\% - 50\%]$ will be targeted. Finally, even though all the printed specimens in the thesis have a single-track thickness, a track angle superior to 100° was chosen in order to have an operational process parameters window ready for multi-track thickness repair.
In Figure 2.23 a process parameter map for which the blue points correspond to combinations of process parameters (Q,V and P) defined in table 2.3 is plotted. Furthermore, the previous parametric models serve as boundaries of the operational window in the process parameter map. In fact, in this map a surface for which the process parameter combination will ensure a track with an angle of 100° is plotted in green. The parametric model of α is available in table 2.5. In addition, with the same procedure, the red and and blue surfaces are plotted and correspond to a dilution of 10% and 50% respectively. The equations of the parametric model of h_d and H are available in table 2.5. These three surfaces added to the process parameter map permit the definition of an operational window. Within this window, as detailed in Figure 2.23 the tracks will have a track angle superior to 100° for process parameters above the green surface. In addition, the tracks will have a dilution superior to 10% and inferior to 50% for process parameters above the red and under the dark blue surfaces respectively.
Finally, this theoretical operational process parameter window for which tracks should fulfill the dilution and track angle requirements is compared with tracks really fulfilling these requirements. These tracks had their angle and dilution measured and their process parameter combinations are marked with a yellow cross as shown in Figure 2.23. One can see that the operational window is overestimated and this is due to the lack of certainty from the parametric model as already discussed.
To conclude, an operational process parameter window was proposed and even though there is a lack of accuracy of our parametric model, it is thought to be a friendly way to represent the process parameter map and its operational window. For future work, a more precise parametric model as well as additional limitations such as powder efficiency should be investigated. Potentially, many other parameters can be added at the convenience of the operator.

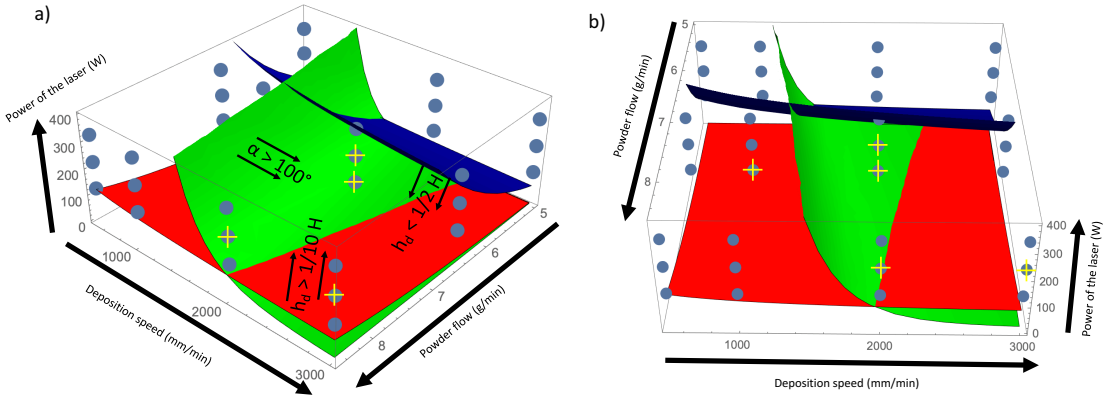

Figure 2.23: 3D process parameter map with 2 different point of view in (a) and (b). The blue points correspond to the combinations of parameters tested. The operational window is delimitated by the three colored surfaces. Above the green surface and the red surface, the tracks have an angle superior to 100^o and a dilution superior to 10% respectively. Under the blue surface, the dilution is inferior to 50%. The yellow crosses correspond to the real combination of process parameters satisfying the requirement of geometry.

2.5.4 Microstructure of a track

The preceding analysis proposed a model. Next we will make a choice of a combination of parameters that generates a track satisfying the dilution and track angle requirements for both repair and manufacturing. The two shortlisted combinations are the following: (i) $P = 225\,W$, $V = 2000\,mm/min$, $Q = 5$ (C1) and (ii) $P = 225\,W$, $V = 2000\,mm/min$, $Q = 6.5$ (C2). (C1) and (C2) present a dilution of 36% and 14% respectively and also a track angle of 121.5^o and 145^o respectively.
A scanning electron microscope (SEM) image and its complementary view obtained by Electron Backscatter Diffraction (EBSD) of a track printed with the (C1) configuration is shown in figure in 2.24 (a) and (b) respectively. In this Figure, one can notice an epitaxial growth of elongated grains from the interface. These grains are perpendicular to the melt pool and oriented toward the center of the track. Also, one can notice the presence of small grains located close to the surface in contact with the air. These smaller grains can be the product of residual or partially melted powder [165] or a consequence of high convective cooling [166]. We decided to work with (C2) even though the dilution is smaller. This choice was motivated by the fact that during the manufacturing of the wall, an increasing of the molten area in the substrate was expected as a consequence of the remelting effect during the first deposited layers. We expected this combination to be more adapted for the repair of thin and small substrate. A figure showing the cross section of a single track and two walls manufactured with 5 and 10 back and forth are

displayed in Figure 2.25(1), (2) and (3) respectively. One can notice that between (1) and (2), the height of the track dilution increased from $20\mu m$ to $52\mu m$ respectively. In contrast, it is same the depth of the dilution is constant between (2) and (3). This is due to the very local remelting during the manufacturing and has therefore no effect after a few layers. More details on the microstructure will be available in the chapter 4.

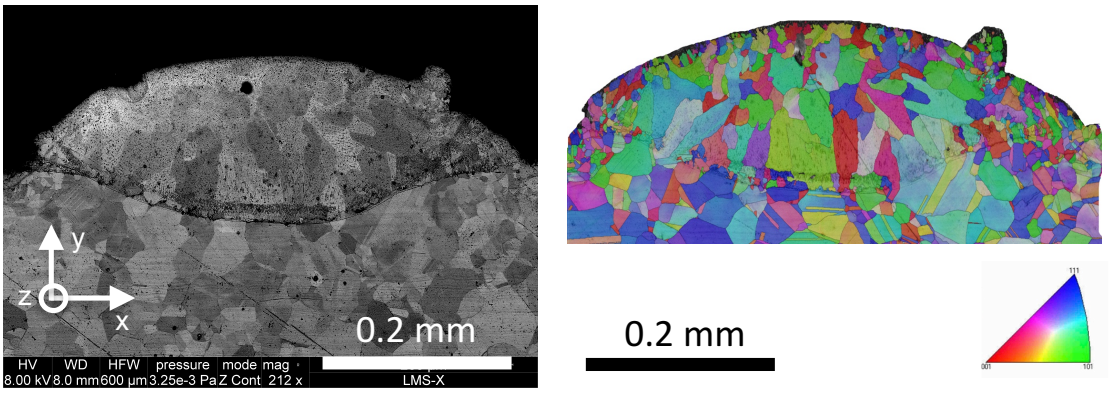

Figure 2.24: SEM image of the cross section of a track its correspond ESBD map (IPF X). The track is printed with $P = 225\,W$, $V = 2000\,mm/min$, $Q = 5$. One can remark the epitaxial growth of long grains from the substrate and a layer of small grains on the superior contour.

2.5.5 Investigation of the lower scales of the microstructure

The preceding section reveals a first rapid analysis of the microstructure at the level of the grains ($\approx 25\,\mu m$). We shall now make a rapid incursion in lower scales. To our knowledge, a very limited number of articles dealing with the substructure in the grains were published so far at the moment of the investigation. Now, some works on their formation and roles have been shared and they will be discussed further.
The cellular substructure were revealed by a chemical attack ($80\,ml\ HCl$, $80\,ml\ H_2O$ and $14\,g\ CuSO_4$) on the surface of the cross section of the track. While the presence of these cellular sub-structures is commonly reported for additively manufactured specimens, very few research groups have investigated their chemical composition [167, 168].

The track printed with $P = 325\,W$, $V = 2000\,mm/min$, $Q = 6.5\,g/min$ was analyzed under an SEM and a back-scattered electrons image is presented in Figure 2.26. One can notice the presence of cellular sub-structures. Moreover back-scattered electrons are sensitive to the atomic number i.e. the heavy elements appear brighter in the image, therefore, the sub-structure should be composed of heavier elements. To elucidate this interrogation, we performed at first a SEM dispersive X-ray spectrometry analysis as portrayed in Figure 2.27. More precisely, a linear chemical analysis corresponding to

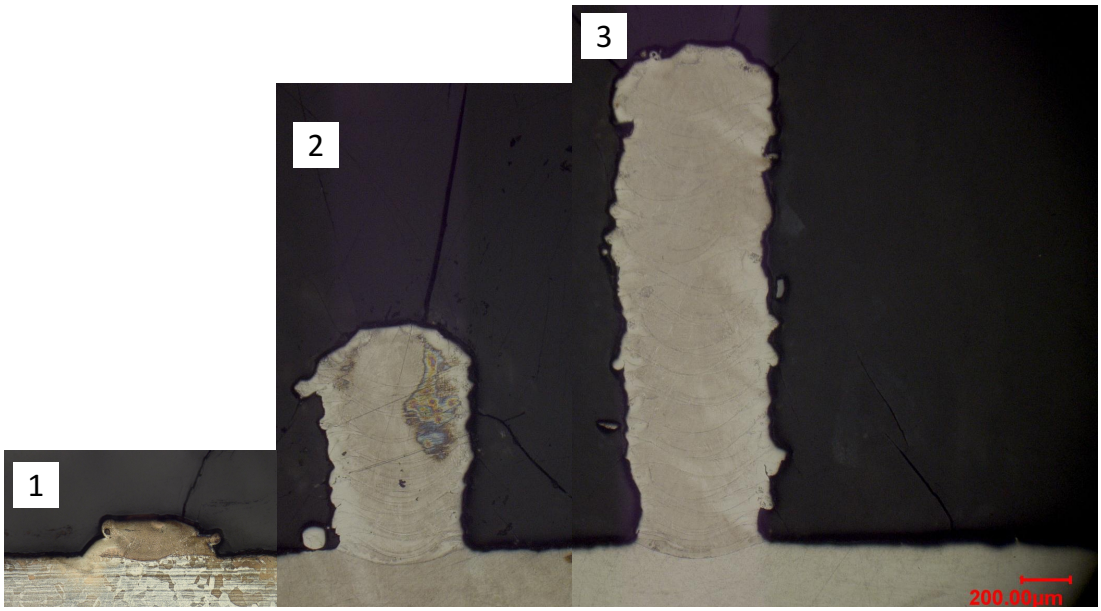

Figure 2.25: Cross section of a single track printed with $P = 225\,W$, $V = 2000\,mm/min$, $Q = 6.5$ (C1). in 2) and 3) is pictured the cross section of walls printed with 5 and 10 back-and-forth respectively and with a vertical increment of 0.2mm. One can observe an increase of the height of dilution between 1) and 2).

the yellow zone of interest being located half out of the cell and half in the cell (bright part) was performed. This first analysis was unfortunately not precise enough due to a $1\,\mu m^3$ resolution while the bright lines thickness is inferior to $200\,nm$. Nevertheless, we were able to capture the decrease of iron (Fe) content, the main element. Next, a Transmission Electron Microscopy dispersive X-ray spectrometry analysis to benefit from the nanometric resolution of this technology was done. A thin foil perpendicular to the cell (red segment) was extracted by FIB at École Centrale de Paris and the result of this analysis is plotted on Figure 2.28. One can observe a similar trend concerning Fe but also an increase of Molybdenum and Chromium which could explain the brightness of the cells.
Similar results were observed in [167, 168, 169]. In [168], the authors proposed that these substructures are a consequence of the chemical segregation due to the slow kinetic of homogeneous alloying elements such as Molybden and Chromium during the fast solidification. In addition, in [167, 169], the authors associated the cell walls with the presence of dense dislocation tangles and as an explanation of the enhanced strength and ductility observed during a monotonic test.

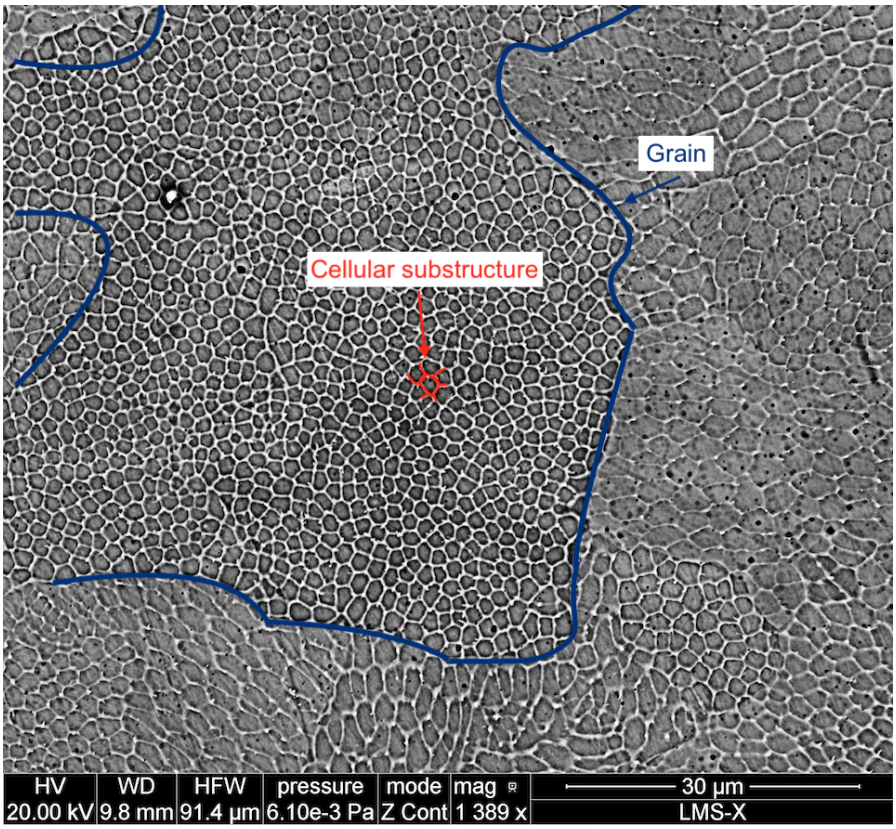

Figure 2.26: SEM image of a cross section of a track attacked by a chemical solution which highlight the presence of the cellular substructures in the grains.

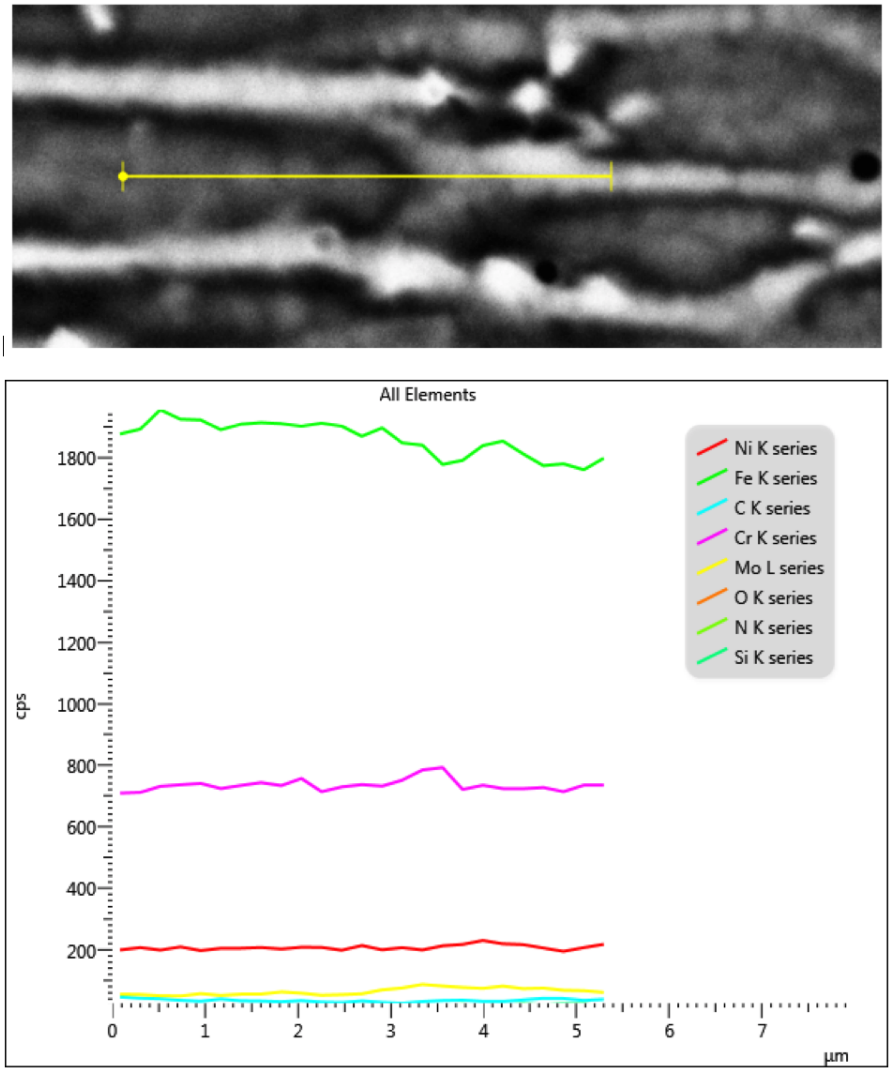

Figure 2.27: SEM EDS analysis on the yellow line being half in the sub-structure. One can note a slight decreasing of Fer.

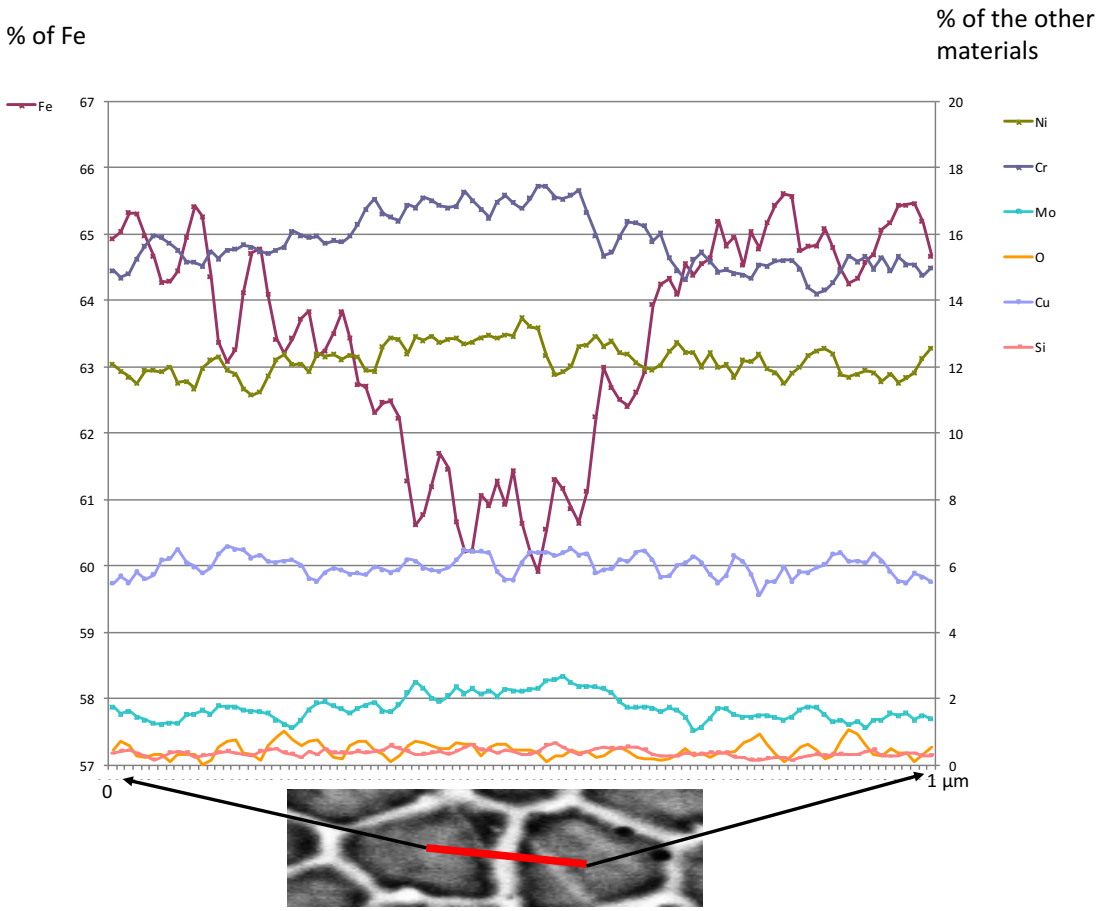

Figure 2.28: TEM Chemical analysis showing a finer state of the chemical segregation. The analysis was performed on a thin foil perpendicular to the segregation as presenter in red.

2.6 Conclusion

This chapter presented an analysis of the effect of the process parameters on the geometry of the cross section of a track. Based on an experimental data base, parametric models between geometric parameters of the track and equations such as $(Q^{\alpha} \cdot P^{\gamma} \cdot V^{\beta})$ with, Q the powder flow, P the laser power and V the deposition speed were established. These relations were used to predict the shape of the track above the surface and also to define an operational process parameter window in which the tracks have an optimal shape. This window was constrained by two geometric parameters: (i) the dilution included in the interval $[10\% - 50\%]$ and (ii) a track angle superior to $100°$. A combination of parameters was selected and an analysis of the microstructure at the grain and subgrain scales was performed. Grains were found to grow by epitaxy from the substrate with an elongated shape. At a smaller scale, substructures were observed and a chemical analysis showed a chemical segregation with a loss of Iron and a gain of Molybdenum and Chromium. In the literature, these cells were associated with the presence of dense dislocation tangles and were an explanation of the enhanced strength and ductility observed during monotonic test of additively manufactured specimen.
Extended work could refine the understanding of certain phenomena. For example the analysis of the effect of the laser power (P), powder flow (Q) and deposition speed (V) on the geometry of the track could be tackled through dimensionless numbers. Also, we could use new parameters such as the amount of powder deposited par meter $(\frac{Q}{V})$ in order to facilitate the comparison with other work. Finally, the present study showed a lack of accuracy of the parametric models. It can be solved by: (i) a finer experimental protocole with for example more tracks or a longer time to stabilize the powder flow or (ii) more elaborated models.

3 Fully printed specimens

Overview

In additive manufacturing, the process parameters have a direct impact on the microstructure of the material and consequently on the mechanical properties of the manufactured parts. The purpose of this chapter is to explore this relation by characterizing the local microstructural response via in situ tensile tests under a scanning electron microscope (SEM) combined with high resolution digital image correlation (HR-DIC) and electron backscatter diffraction (EBSD) maps. The specimens under scrutiny were extracted from bidirectionally printed single-track thickness 316L stainless steel walls built by directed energy deposition. The morphologic and crystallographic textures of the grains were characterized by statistical analysis and associated with the particular heat flow pattern of the process. Grains were sorted according to their size into *large* columnar grains located within the printed layer and *small* equiaxed grains located at the interfaces between successive layers. In situ tensile experiments were performed with a loading direction either perpendicular or along the printing direction and exhibit different mechanisms of deformation. A statistical analysis of the average deformation per grain indicates that for a tensile loading along the building direction, *small* grains deform less than the *large* ones. In addition, HR-DIC combined with EBSD maps showed strain localization situated at the interface between layers in the absence of *small* grains either individual or in clusters. For tensile loads along the printing direction, the strain localization was present in several particular *large* grains. These observations permit to justify the differences in yield and ultimate strength noticed during macroscopic tensile tests for both configurations. Moreover, they indicate that an optimization of the process parameters could trigger the control of microstructure and consequently the macroscopic mechanical behavior.

Contents

3.1 Introduction

The well known AISI 316L stainless steel is a suitable material for AM due to its welding capacity, its relatively high mechanical properties and for its high-temperature performance. In the last decade meaningful efforts were deployed by various groups to investigate the AM process for this steel and its inherent special mechanical properties. For example, the impact of the size and morphology of the powder was studied in [170] and it was found that over a certain particle diameter, the mechanical properties decrease. The influence of the process parameters, i.e. laser scanning speed and preheating temperature on the geometry and microstructure of a single-track metal deposition, were investigated in [171]. The conclusion was that the contact angle and the track height were controlled by the preheating temperature while the track width and the contact zone characteristics were governed by the scanning speed.In [172], the authors showed that the best precision of large-scale parts produced by DED was obtained combining a small laser spot with high scanning velocity. Last but not least, the improvement of the surface finish of stainless steel thin walls was explored in [173], and it was noticed that by adjusting the scanning speed to a certain value of temperature in the melt pool, the layer's thickness reduces resulting in a better surface finishing.The quality of the printed part depends on the process parameters. For DED, the powder flow, the speed deposition, the laser power and the lasing strategy have been defined as the main parameters steering the growth of the microstructure and therefore controlling the mechanical properties as reported in [156, 174, 159].
The microstructure of the 316L stainless steel and their influence on the mechanical performance were studied by various research groups at different material scales and through different investigation methods. In [1], it was noted that the laser energy density has a strong influence over the grain size and the part density, hence affecting the mechanical properties. The manufacturing processes, the obtained microstructure and the mechanical and wear behavior were correlated in [2]. The results showed that the highest mechanical properties, understood as yield and ultimate tensile strength, as well as the best tribological performance were obtained for 316L stainless steel specimens produced by Selective Laser Melting (SLM) when compared to hot pressing or conventional casting. The result has been explained by a finer microstructure obtained in the AM process. In [3] is studied the effects of inter-layer dwell time interval and found that longer dwell time intervals imposed higher cooling rates, leading to finer microstructures and therefore to higher tensile strength and lower ductility. Other efforts [6, 175] tried to elucidate the direct relation between microstructure and observed mechanical properties, but due to the complexity of the phenomena and the large number of parameters involved, additional insights are needed to solve these questions. Indeed, it is well known that polycrystalline materials reveal microstructural strain heterogeneities due to the particular grain size, texture and morphology. These heterogeneities lead to strain localization, accumulation of local plastic strain [176, 177] and are the precursors of crack initiation and propagation [178, 179]. Furthermore, in additive manufacturing, the lasing and building strategy will encourage the formation of oriented microstructures with elongated columnar grains

[4]. In addition, anisotropic macroscopic properties are reported for example in [5] and [6]. In order to understand the anisotropic material behavior during tensile loading, it is necessary to unveil the particular deformation of the microstructure of AM materials and the underlying strain localization. Advanced characterization techniques have emerged in the last decades, enabling the tracking of the deformation fields at the grain scale with applied loading by simultaneously combining digital image correlation (DIC) and Electron Backscatter Diffraction (EBSD) analysis [180]. Few investigations were performed at the scale of the grains for AM materials. For Ti-6Al-4V manufactured by DED, the authors of [18] observed areas of high strain localisation at the interfaces of the layers. This accumulation was associated to the material anisotropy. The authors in [19] investigated the anisotropy of two INC718 specimens tested along and orthogonal to the building direction under tensile load. The associated strain maps at the grain scale of the specimens produced by SLM exhibited different patterns of deformation.
The goal of this chapter is to investigate the strain heterogeneity and the strain localisation in the microstructure of 316L specimens manufactured by DED during a tensile test. The observations are performed in situ under a scanning electron microscope (SEM) and combined simultaneously DIC and EBSD observations.
The chapter is organized as follows. It starts with the presentation of the specimens and the experimental techniques. Afterwards, the characterization of the microstructure is discussed and the macroscopic mechanical properties are exhibited. Next, a procedure to compute the statistics of deformation of the microstructure at the grain scale is presented and the results are analyzed and discussed. Finally, several remarks will conclude this study.

3.2 Materials and experiments

A series of 316L stainless steel walls with a single-track thickness have been manufactured by Directed Energy Deposition (DED). The commercially available powder used in this study was produced through gas atomization by Höganäs AB and its main characteristics can be retrieved in the section 2.3. The 3D printer is a DED *Mobile* machine from BeAM [141] equipped with a 500W YLR-fiber laser. The powder is transported by argon gas flux and delivered to the deposition region through coaxial nozzles positioned approximately 3,5 mm above the substrate surface. The powder flow was directly measured by averaging the weight of the powder sent to the nozzle during 1 minute. The single-track thickness walls were built employing a back-and-forth laser scanning strategy in the printing direction. In the building direction, the vertical spacing between the successive deposited layers was of 0.2 mm. A schematic representation is proposed in Figure 3.1(a). Finally, the walls with the dimensions of 100 $mm \times 30\,mm \times 0{,}8\,mm$ were printed on a 150 $mm \times 5\,mm \times 200mm$ 316L stainless steel substrate plate as displayed in Figure 3.2.
The calibration of the main writing parameters of the machine i.e. laser power, deposition speed and powder flow, were optimised using a parametric study as detailed in section 2.5. It led to the following optimal set of parameters: (i) a laser power of 225 W, (ii) a powder flow of 6.5 g/min and (iii) a deposition speed of 2000 mm/min.

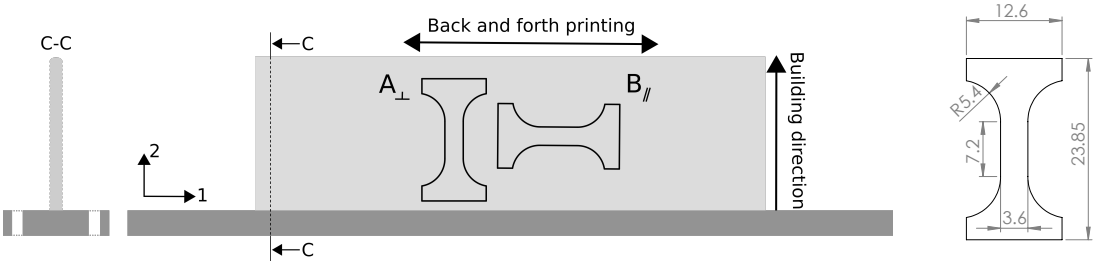

Figure 3.1: (a): Side view (C-C) of the single-track thickness wall printed on the substrate and position of the specimens $A_{\perp}$ and $B_{/\!/}$, orthogonal and along the printing direction respectively. (b): Dimensions in minimeter (mm) of the dogbone shaped specimens extracted from the wall.

Dogbone shaped specimens used for observation and testing were extracted from the single-track walls by water jet cutting with a *Mach 2b waterjet* [181].
Their precise positions and geometry in the wall is displayed in Figure 3.1(a) and (b). The distortion of the wall is negligible, i.e. the differences with a straight ruler are of the order of the magnitude of the roughness. Furthermore, the specimens are polished on the both side removing roughness and any potential distortion. Finally, the residual stress of the polished specimens were measured by X-ray diffraction and it was found that low compressive residual stress was present 75 MPa ± 31. Let us further remark that larger

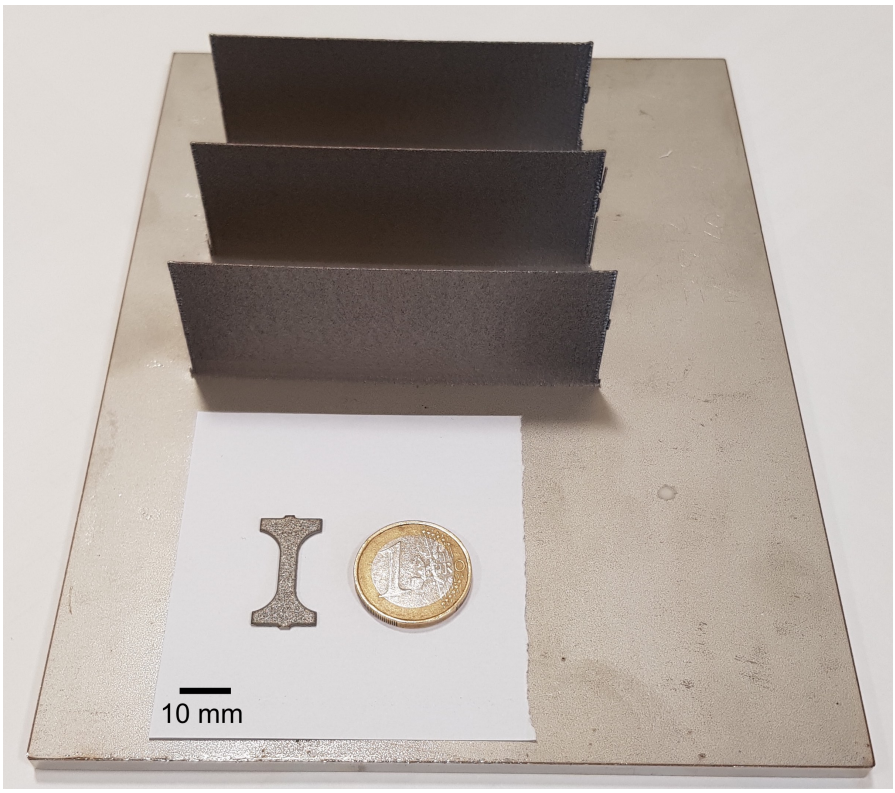

Figure 3.2: The printed wall on the substrate and a specimen after waterjet cutting.

.

residual stresses and stronger distortion have only been observed when higher walls have been build. The dogbone geometry does not adhere to any standards and was imposed by pratical limitations such as the size of the ion polisher chamber or compatibility requirements with the homemade SEM in situ tensile tests machine. However, a prior finite element study confirmed a homogeneous macroscopic strain in the zone of interest. The dimensions of the specimens were defined by the compatibility with the homemade SEM in situ tensile tests machine. Two orientations were defined for the specimens in order to apply tensile loading along the building and printing direction i.e, perpendicular and parallel with respect to the printing direction. Next, we denote the specimen with a tensile direction perpendicular and parallel to the printing direction as $A_{\perp}$ and $B_{/\!/}$ respectively, as represented in Figure 3.1(a).

The specimens were mechanically polished after the extraction in order to obtain a mirror surface adequate for SEM observations. As such, the specimens lost their surface roughness inherited from the manufacturing process. However, this will only affect final failure or fatigue properties but not the ones discussed next. The polishing was performed with silicon carbide abrasive papers with successive grit values from 400 to 4000 and finished with a $1\,\mu m$ diamond paste. The specimens were finally ion polished during one hour

with the following parameters: 6° polishing angle, 6 keV electron beam power, 6 rpm specimen angular velocity in a *PECS II* machine from *Gatan* [182].

The microstructure of the specimens was examined by EBSD (Electron Backscatter Diffraction) on a FEI QUANTA 600F SEM (Scanning Electron Microscopy) apparatus. Data was collected and analyzed using the Aztec and Channel 5 software respectively. EBSD maps were collected on a central area of $1.8 \times 1.9\, mm^2$ for specimen $A_{\perp}$ and $1.8 \times 1.85\, mm^2$ for the specimen $B_{/\!/}$ using a step size of $1\, \mu m$ in both cases.

In order to record displacement and strain fields at different scales by Digital Image Correlation (DIC), a multi-scale lithography grid was performed on each specimen in a $3 \times 3\, mm^2$ central area. The lithography preparation consists of applying a drop of PMMA 5 % (i.e. Poly(methyl methacrylate) on the polished specimen surface and to spread it by spin coating (2000 rpm) during 70 seconds. The specimens with the transparent thermoplastic coating are then put into an oven at 170°C during 30 minutes (polymerizing conditions). Subsequently, the electron beam of the SEM is driven on the surface of the specimen by the software Raith Elphy Quantum to reproduce the PMMA designed pattern by irradiating the resin. After this step, the specimens are bathed during 90 seconds in a solution (1/4 methyl-ethal-cetone and 3/4 propanol) to dissolve the irradiated resin. Then, gold is firstly deposited by sputtering ($1\, nm$) and by vacuum vaporization ($12\, nm$). Finally, the non-irradiated resin is removed by ultrasonic cleaning during 1 minute with ethyl-acetate.

The specimens were tested in SEM under a tensile load in order to observe the strain field at the microstructure scale and to associate it with EBSD maps. The strain rate was fixed at $2 \times 10^{-4}\, s^{-1}$ and the loading steps 1, 2, 3, 4 and 5 were respectively defined by the macroscopic strain levels corresponding to $1\%, 6\%, 12\%, 16\%$ and 20% . The loading steps were imposed based on a real-time strain computation based on DIC on the larger grid, with a cross spacing of $100\, \mu m$ (blue grid on Figure 3.3). At each strain step, an elastic unloading is performed and an image of the smaller grid area, with a $3\, \mu m$ cross spacing (red grid on Figure 3.3) is recorded. The comparison of this image with the initial one provided a high resolution strain full-fields and permits to analyse the deformation process at the grain scale, highlighting the zones with a high plastic strain.

In order to compare the obtained mechanical properties with other experiments, an additional monotonic tensile test, i.e. in the absence of the unloading steps, was equally performed on the same tensile machine. The in situ machine was associated with a $4\, KN$ load cell and the strain rate was fixed at $10^{-3} s^{-1}$.

Digital image correlation (DIC) for strain fields computation based on successive images of deformed specimens is now a conventional technique for the measurement of strain fields as discussed in [183] and [184]. However as different algorithms and assumptions are covered by software and literature, we shall summarize the procedure used next. Displacement full-fields are computed using *Correlation Manual Value*, a homemade software [176, 185, 186].

The correlation starts from a set of non-overlapping points located on the grid crosses of the reference image, $CD_n(X_n, Y_n)$, on Figure 3.4(a). This set of points, also denoted as

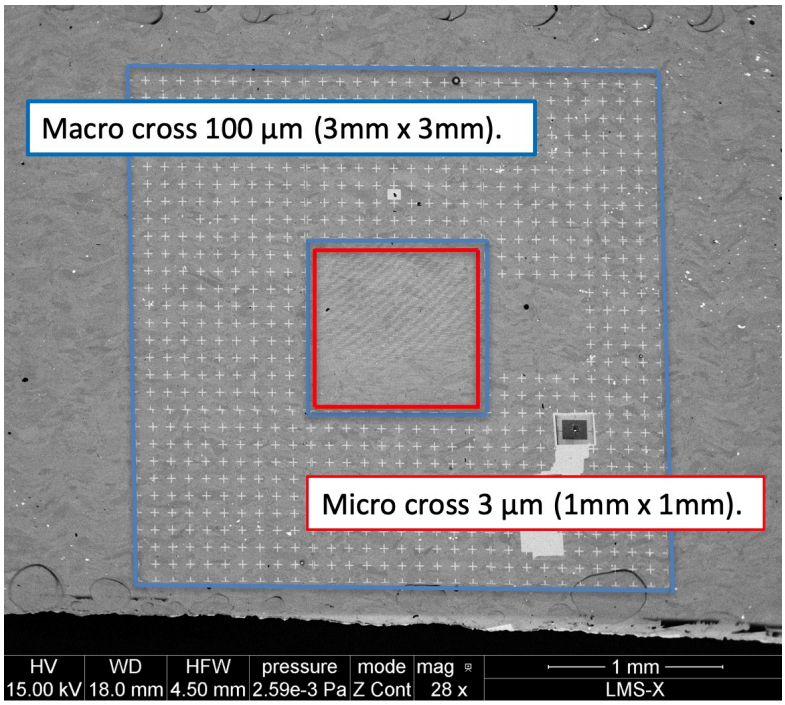

Figure 3.3: Image of the multiscale grids on the tensile specimen. Blue area of $3 \times 3mm^2$ with macro crosses with a pitch of $100\,\mu m$ was designed for macroscopic deformation patterns while the red area of $1 \times 1mm^2$ was designed to capture high resolution images needed for the DIC and thus to determine the deformation pattern at the microstructure scale.

correlation domains, is then tracked in its new position ($CD_n(y_n, y_n)$) through the images at different deformation steps, see the deformed configuration on Figure 3.4(b). The tracking is done by minimization of the correlation coefficient, which measures closeness of the distribution of grey levels between reference and deformed images.

The local in-plain Green-Lagrange $\mathbf{E}_\Omega$ tensor for each correlation point is calculated over an integration domain Ω, defined by the neighboring correlation points as displayed in Figure 3.4 (c). The average displacement gradient $\langle \mathbf{F} \rangle_\Omega$ over the domain Ω, is computed as detailed in [185].

The representation of the average displacement gradient $\langle \mathbf{F} \rangle_\Omega$ in Cartesian components is:

$$\langle \mathbf{F} \rangle_\Omega = F_{ij} \mathbf{e}_i \otimes \mathbf{e}_j \tag{3.1}$$

where $\mathbf{e}_i$ are the unit vectors of the Cartesian coordinates. Its components oriented along

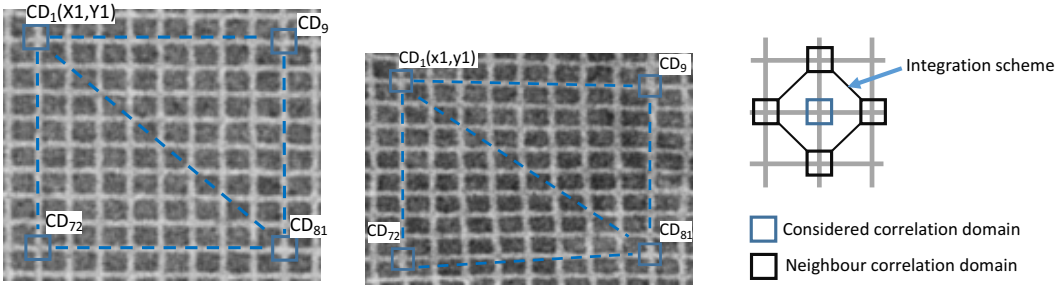

(a) (b) (c)

Figure 3.4: Layout of the correlation domain (a) in the reference image, (b) in the deformed image and (c): scheme of the integration domains for computation of the Green-Lagrange strain tensor.

the X and Y axes are expressed as:

$$F_{XX} = \frac{1}{2\,S}\sum_{n=1}^{N}(x^n + x^{n+1})(Y^{n+1} - Y^n) \tag{3.2}$$

$$F_{XY} = \frac{1}{2\,S}\sum_{n=1}^{N} -(x^n + x^{n+1})(X^{n+1} - X^n) \tag{3.3}$$

$$F_{YX} = \frac{1}{2\,S}\sum_{n=1}^{N}(y^n + y^{n+1})(Y^{n+1} - Y^n) \tag{3.4}$$

$$F_{YY} = \frac{1}{2\,S}\sum_{n=1}^{N} -(y^n + y^{n+1})(X^{n+1} - X^n) \tag{3.5}$$

where S denotes the area of the integration domain and N the number of correlation domains. (x^n, y^n) and (X^n, Y^n) are the coordinates of the control points in the actual and initial configuration respectively.

From the displacement gradient, the Green-Lagrange strain tensor is computed using the convential formula:

$$\mathbf{E}_\Omega = \frac{1}{2}(\langle\mathbf{F}\rangle_\Omega^T \cdot \langle\mathbf{F}\rangle_\Omega - \mathbf{I}) \tag{3.6}$$

Next, the experiments will be performed under a small strain assumption and therefore:

$$\varepsilon \approx \mathbf{E}_\Omega \tag{3.7}$$

The correlation errors of this method, see [185], can be reduced significantly by increasing the size of the integration domain (at the expense of local informations). In this work, as we are interested in the mean deformation of a grain, this implies that the larger the grain is, the smaller the error will be. More precisely, the estimated maximum absolute

error for the ε_{11} strain component is 26×10^{-4} for a $8 \times 8\mu\, m^2$ area corresponding to an average *small* grain and 36×10^{-5} for a $32 \times 32\mu m^2$ area which is equivalent to an average *large* grain. The terms *small* and *large* grain will be explained further. Moreover, the errors are also related to the noise of the recorded images by the SEM and can be reduced by decreasing the acquisition speed [187]. In the cases studied here, we had to balance the dwell time with the image resolution, because a longer exposition time would enhance the image quality but will distort the acquisition. To ensure a reasonable grey-scale contrast for the DIC, it was necessary to fix the resolution to 8192×7168 pixels i.e. the smallest resolution still allowing a few pixels within the micro crosses of the red area in case of a Horizontal Field Width (HFW) $= 1750\,\mu m$.

3.3 Results and discussion

3.3.1 Grain morphology and texture analysis

The microstructure was analyzed qualitatively and quantitatively in terms of grain size, shape and distribution from the EBSD data.
The statistical analysis of grain sizes and shapes conducted to similar results for both specimens irrespective of their orientations as displayed in table 3.1. This result was expected as a consequence of the following factors: (i) both specimens were extracted in the middle section of the wall, i.e. away from the extreme free edges and at the same height of the wall, thus avoiding the eventual variation of spatial and temporal characteristic of the temperature, (ii) they have the same level of polishing, i.e same thickness and (iii) the areas where EBSD analyses are performed are large enough to contain a statistically representative number of grains. As a consequence, in order to simplify the discussion, only the microstructural analysis conducted on the specimen $B_{/\!/}$ will be reported here in the sequel.
The microstructural texture, in terms of both morphology and crystallographic orientations is determined by the local heat flow during solidification and cooling. The history will guide the preferred growth directions of the grains. The particular heat flow pattern depends on both the geometry and heat exchange coefficients as well as on a given set of printing parameters such as the power of the laser, the printing speed, the scanning pattern strategy etc. which are driving the position of the heat source in the transient heat flow problem. Direct relations between the printing parameters and the microstructural texture are discussed in [188, 44, 17], but will not be presented in detail in this chapter.
A typical microstructure at the center of the wall is displayed in Figure 3.5(a). For the given vertical build step of $0{,}2\,mm$ one layer of grains has an average height equal to $0{,}12\,mm$ and its grains have an average orientation of 29^o with respect to the printing direction (more precisely $\alpha_1 = 31{,}4^o$ and $\alpha_2 = 26{,}4^o$ as shown on Figure 3.5(b). The noticeable zigzag pattern is a consequence of the alternating movement of the laser head during the manufacturing, which controls the local thermal history and the direction of maximum heat flow in different layers [188].
The crystallographic texture obtained from the EBSD analysis was plotted in Figure 5.9

using three pole figures corresponding to different areas of focus. Two subsets of grains corresponding to two successive layers were extracted, one relative to the layers printed from left-to-right and the other one relative to layers printed from right-to-left. Both are represented in blue and red respectively in Figure 5.9(a). In Figure 5.9(b), the pole figure of the complete set of grains is plotted while, in Figure 5.9(c) and (d) the two subsets of grains are displayed. In Figure 5.9(c), the crystallographic texture of the layers printed from left-to right is represented and one can remark a hotspot close to the Building Direction (BD) axis which illustrates a slight texture of the crystallographic plane {100}. A similar observation can be made in Figure 5.9(d) for the layers printed from right-to-left. By firstly analyzing the subsets, it is easier to understand the whole EBSD texture as the sum of two fiber textures. The distance of the two hotspots from the BD axis corresponds to a tilt angle of 30^o toward the printing direction i.e. the crystallographic and morphologic texture are both aligned. It is known that the texture is determined during solidification and in the case of centered cubic alloys [188], it is defined by the preferred crystallographic direction which is closely aligned with the maximum heat flow. The precise direction of the heat flow was not measured during printing, but the observed textures gave a clear idea of the heat flow pattern in this case.

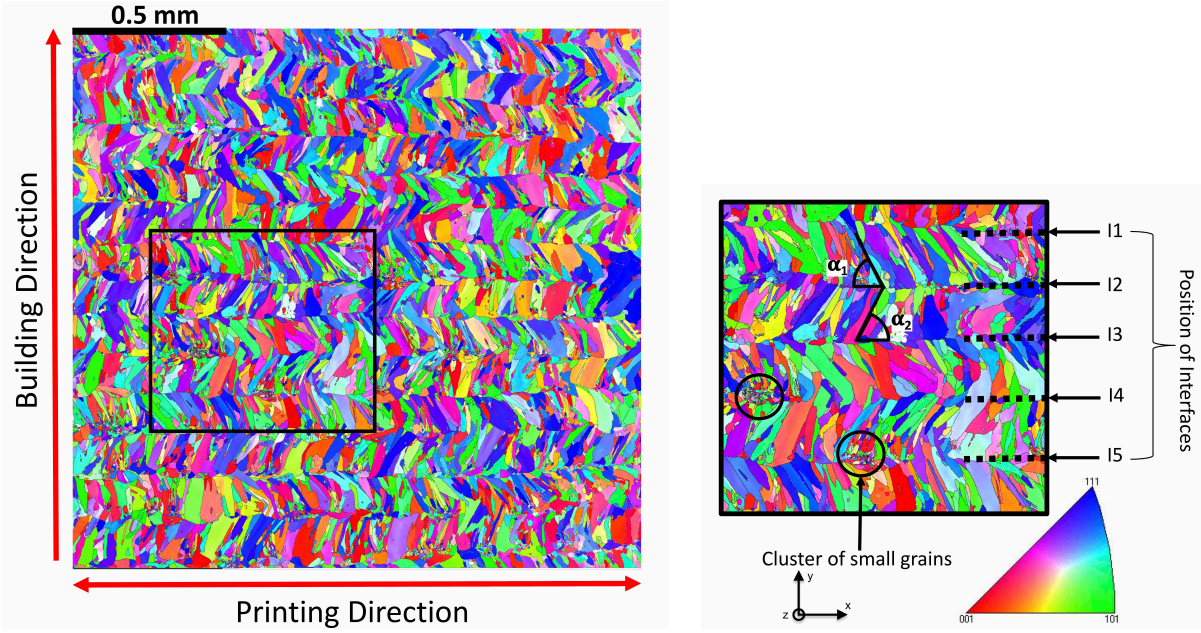

(a) (b)

Figure 3.5: (a): EBSD map (IPF X) of the specimen $B_{/\!/}$. (b): Zoom on the EBSD map showing in detail the interfaces between layers, cluster of *small* grains present at interfaces and the morphological grain angles for both directions of printing.

A precise observation of the Figure 3.5(a) exhibits an important surface covered by large

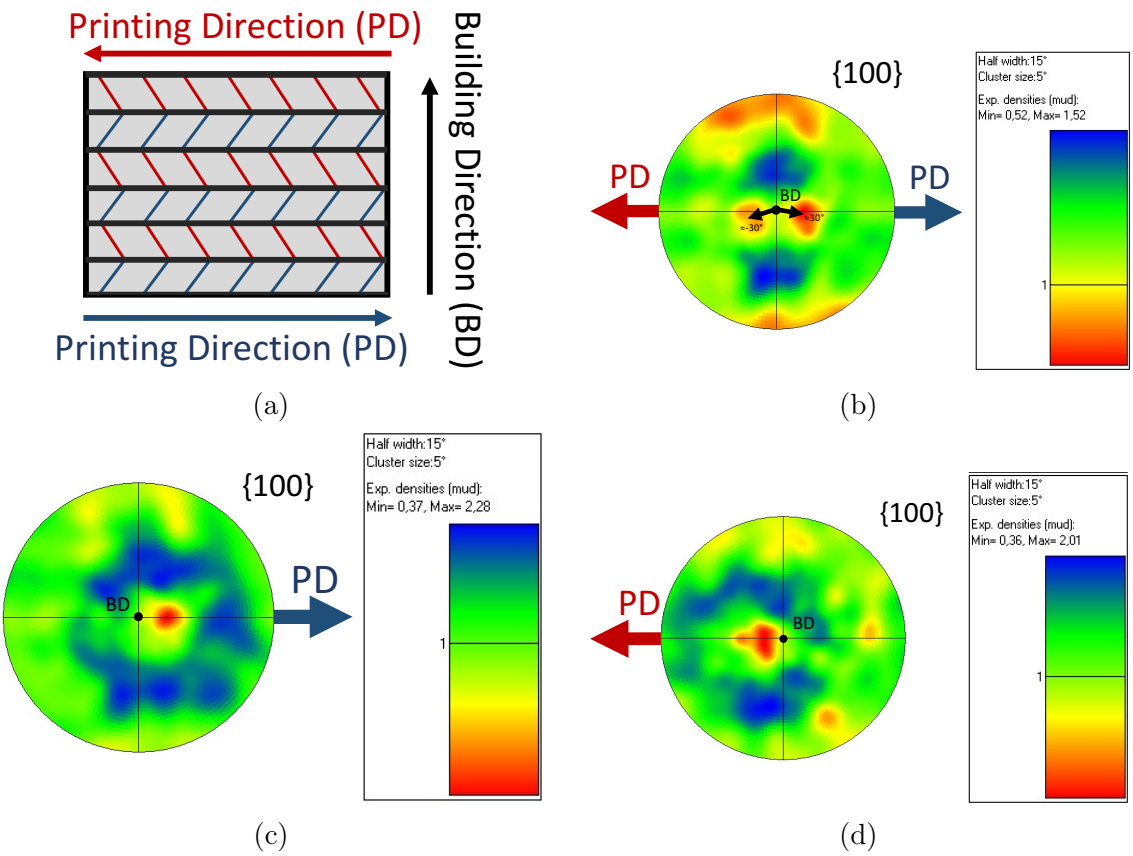

Figure 3.6: The texture of the microstructure: (a) Schematic representation of the printed layers and their relative morphological grain angles associated by color to the printing direction. Pole Figure for the whole EBSD, for the layers printed from left to right the one printed from right to left diplayed in (b), (c) and (d) respectively

grains. They mainly form the printed layers while smaller grains will cover the interface between the layers. The smaller grains will equally cluster between layers as illustrated in Figure 3.5(b). However a repetitive pattern of the *small* grain clusters could not be found. For example, clusters are present in interfaces I5 and I4, while absent in I1, I2 and I3. Similar observations on the presence of *small* grains and their clustering between layers was also reported in [17]. More precisely, the authors related this type of microstructure to particular values of the solidification rate and the thermal gradient associated with the heat suction from the substrate and the printing parameters. They reported that after a specific building height, the fine grains tend to disappear because of the heat accumulation in the built part, which corresponds to our observations. It has also been previously reported in [5], that grains at the top of the wall are larger than the ones at the bottom. This was associated to a faster cooling closer to the substrate.

However, this was not observed in the present work as the studied surface was too small and positioned at the center of the wall.

Next, we propose to sort the grains in two families with respect to their surface area, i.e. *small* and *large* grains. This threshold value between the two families correspond to the surface of the biggest grain found in a cluster of small grains and is equal to an area of $176\,\mu m^2$. This area approximately corresponds to a circle with a $15\,\mu m$ diameter.

This separation will allow to better apprehend the role of different grains in the deformation process and asses from a statistical point of view the differences in term of size, quantity and surface occupied by grains, as resumed in the table 3.1. One can easily note that there are more *small* grains, 61% of total number, than *large* ones, 39%, while the *small* ones occupy only 8% of the total surface. We have a ratio of 4 between the average diameters of *large* and *small* grains.

	Specimen A		Specimen B	
	small grains	*large* grains	*small* grains	*large* grains
Average diameter	7.6 ± 3.3 μm	31.6± 16.8 μm	7.2 ± 3.4μm	29.6 ± 15.4 μm
Mediane of diameter	7μm	26.3μm	6.5μm	24.4μm
Numbers of grains	61%	39%	67%	33%
Surface occupied	8%	92%	11%	89%
Average of the aspect ratio	2.4± 1.4	3.4± 2.1	2.6 ± 1.6	3.8 ± 3.2
Mediane of the aspect ratio	2	2.8	2.1	3.2
EBSD surface	3.3 mm^2		3.4 mm^2	

Table 3.1: Grains size statistics.

The aspect ratio of the grain was defined as the ratio of principal axes of the smallest circumscribed ellipse, implying that an aspect ratio of 1 indicates an equiaxed grain. Ellipses fitting the *small* grains have an average aspect ratio of 2,4 ± 1,4 while ellipses fitting the *large* grains have a an average aspect ratio of 3,4 ± 2,1 (complete data set is available in table 3.1). The distribution of the grain sizes is depicted in Figure 3.7 by the plot of the continuous probability density function (PDF) of frequency as a function of aspect ratio for *small* and *large* grains. The continuous distribution was fitted from the discrete measured distribution using [189]. Moreover, one can see that, the PDF of the aspect ratio of *small* grains is narrow attaining its peak value at an aspect ratio of 1,8 which is smaller than 2,4, its average aspect ratio. The distribution of aspect ratios for the *large* grains is more spread, it attains its peak at an aspect ratio of 2,2 which is also smaller than 3.4, the average aspect ratio for *large* grains. Moreover, we recall that the total surface of *small* grains is far smaller than the surface occupied by *large* grains while the *small* grains are superior in terms of quantity.

As a closure remark regarding sizes and shapes, we can state that *large* grains have a columnar shape while *small* grains have a more equiaxial one.

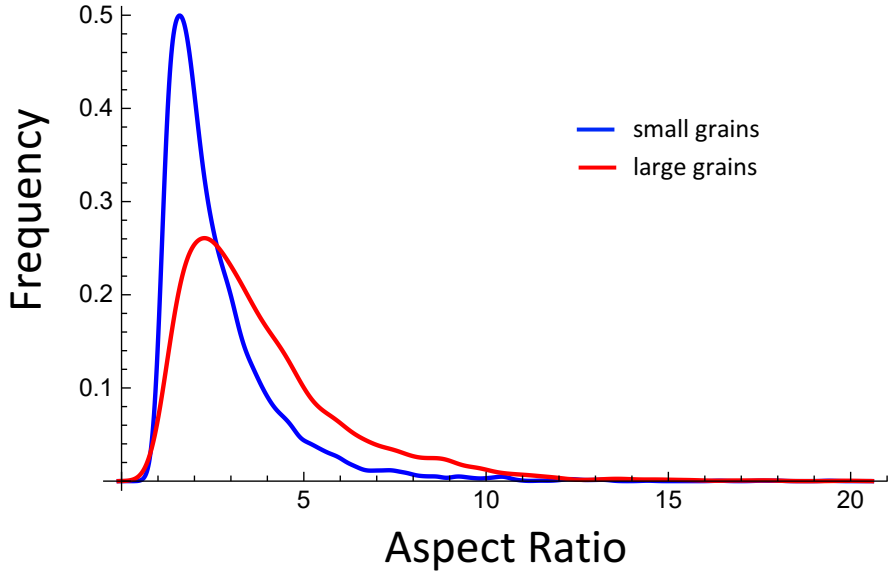

Figure 3.7: Probability density function of grain ellipticity, i.e. frequency in terms of ratio between the large and small axes of the ellipse fitting the grain by its surface and shape.

3.3.2 Mechanical properties

The tensile engineering stress versus strain curve of the specimens $A_{\perp}$ or $B_{/\!/}$ are compared in Figure 3.8. In order to provide a precise quantitative comparison of the tensile response differences, we provide standard material parameters such as the yield stress at 0,2% (YS), ultimate strength (UTS) and the ductility (D). To facilitate the analysis, the ratio R of the material parameters of $B_{/\!/}$ over $A_{\perp}$ is compared to values from literature [26, 6, 190]. If the ductility is almost similar for the specimen $A_{\perp}$ or $B_{/\!/}$ with a ratio of 1, the value of the ultimate strength of specimen $B_{/\!/}$ is higher with a ratio attaining 1,18 and a similar trend is observed for the yield strength with a ratio of 1,4. One can therefore notice an anisotropy for the yield and the ultimate strength of the two specimens.

Previous publications [6, 191, 192] on stainless steel employing DED as a manufacturing technology present similar trends regarding the mechanical behavior under uniaxial tensile test. The tensile engineering stress versus strain curve of the present specimens $A_{\perp}$ or $B_{/\!/}$ are compared with the curves of their homologous ones extracted from a multi-track thickness volume in 316L obtained by DED [26]. One can notice that the differences between the tensile properties for both sets of configurations are comparable, in the sense that one obtains higher yield and ultimate strength for the type $A_{\perp}$ specimens and larger ductility for the type $B_{/\!/}$ specimens. Nevertheless, it can be noted that intrinsic values are different. Even tough the nature of the feedstock (316L stainless steel) and printing technology (DED) are the same, the size and chemical composition of the powder as well as the machine's parameters (laser power, speed deposition, printing strategy etc.) for

both compared studies are different. In [7], the authors summarized the tensile properties of 316L specimens manufactured by DED from different research groups permitting to highlight the scatter of the properties and the large spectrum of tensile strength. In addition, it was also noted that specimens manufactured with lower linear heat inputs have smaller melt pools, thus faster cooling rate leading to a finer microstructure and therefore higher yield and ultimate tensile strengths in comparison to the ones produced with higher linear inputs. Also, it was reported that even for the same linear heat inputs, the type of laser has an influence on the energy absorbed by the substrate or deposited layers and thus on the final properties. In addition, the chemical composition [193] and particle size [194] of the powder affect the mechanical properties as well as the printing parameters as mentionned in the introduction. Therefore, one can perceive the sensitivity of the mechanical properties to process/machine's parameters and can consequently understand the difference observed in Figure 3.8 and more generally between studies of the same type of materials additively manufactured.
Furthermore, the material parameters of table 3.2 are compared with the ones of a hot rolled and annealed 316L. The hot rolled and annealed material present isotropic properties with a higher ductility but lower yield and ultimate strength in comparison to 316L obtained by DED. An explanation for the anisotropy in the case of DED was proposed in [5] who analyzed a material manufactured in similar conditions as our specimen. A specimen of type $A_{\perp}$ has long and narrow columnar grains oriented along the building direction. Therefore, under uniaxial test along the building direction, dislocations are required to meet fewer grain boundaries to elongate the sample than specimen in the configuration of $B_{/\!/}$ where dislocations will meet more boundaries. This can explain the difference between the UTS and YS. It was also noticed in [6] that interlayer in case of a tensile direction orthogonal to the printing direction are ideal crack initiation sites. In order to validate such assumptions, it is therefore important to investigate the strain localization process at the microstructure scale as proposed in the next section.

Technology	YS (MPa)			UTS (MPa)			D (%)		
Printing versus tensile direction	$\perp$	$/\!/$	R	$\perp$	$/\!/$	R	$\perp$	$/\!/$	R
DED (our results)-from wall	272 ± 8	381±5	1.4	621.7 ± 9.4	734.1 ± 12.8	1.18	46.4 ± 2	44.4 ± 3.8	0.96
LENS [26] from bulk	479	576	1.2	703	776	1.1	46	33	0.72
LMDS[6] from wall	352	558	1.6	536	639	1.19	46	21	0.46
Hot rolled and annealed [190]	302	307	1.01	595	600	1	57	59	1.03

Table 3.2: Mechanical properties of 316L from the present tests and from the literature [26, 6, 190]. R is the ratio of the material parameters of the specimen $B_{/\!/}$ over the specimen $A_{\perp}$

3.3.3 Combined strain and EBSD analysis

Next, a combined DIC-EBSD analysis is proposed to reveal and to understand the observed differences between the mechanical properties in tensile test, depending on the orientation of the loading with respect to the printing direction, i.e. along or orthogonal to the printing direction. The analysis is split in several steps: (i) an initial EBSD

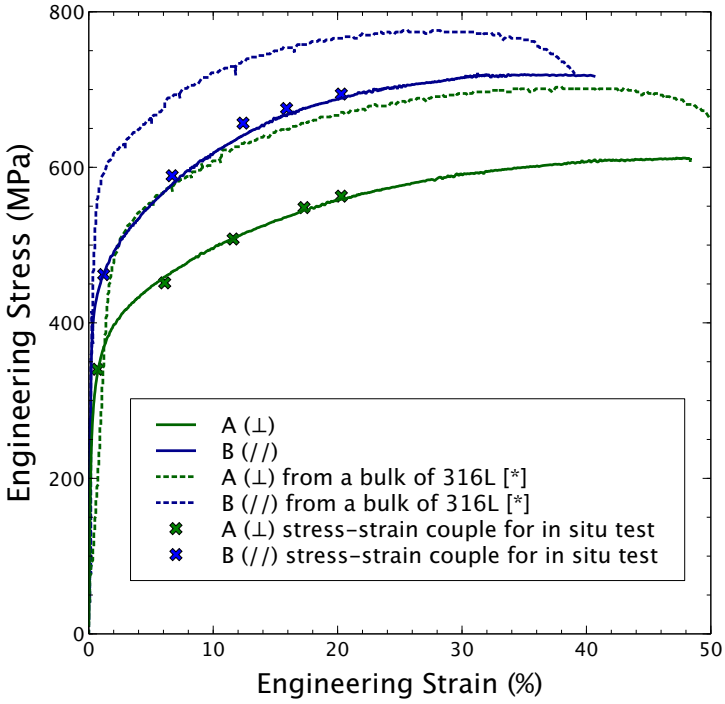

Figure 3.8: Monotonic tensile stress-strain curves of the specimen $A_{\perp}$ and $B_{/\!/}$ extracted from a DED 316L wall and their counterparts extracted from DED 316L bulk. *=[26].The stress-strain position data for the in situ tests of specimen $A_{\perp}$ and $B_{/\!/}$ are represented by green and blue crosses respectively.

analysis of the central part of the specimen as described in Figure 3.3, (ii) a SEM in situ tensile test combined with DIC described in section 3.2, (iii) a projection of DIC results on EBSD which will be described in this section and (iv) a statistical analysis of mean strain value per grain associated to a study of the local strain patterns.

As stated previously, DIC full-fields were projected on EBSD maps: this enables us to determine the correlation points included in each grain. To perform this overlapping, we had to correct the non-linear distortion of the EBSD coming from several factors such as the beam drift, the stability of the specimen etc. The procedure is detailed in [195] and the code used for this correction was adapted from the Matlab procedure available in [196]. This image correction procedure will distort the initial image shape from rectangular to an arbitrary shape as already reported in [195]. It is important to notice that the distortion is image specific and therefore the exact transformation will be different for each image. A Matlab routine was programmed to reconstruct the EBSD map with a unique RGB color averaged for each grain based on its euler angle in order to determine the contour of the grain and thus, the correlation points included. Then,

as presented previously, from the average transformation gradient, it was possible to compute the mean value of the Green-Lagrange tensor components in each grain. The precise procedure is schematized in Figure 3.9.

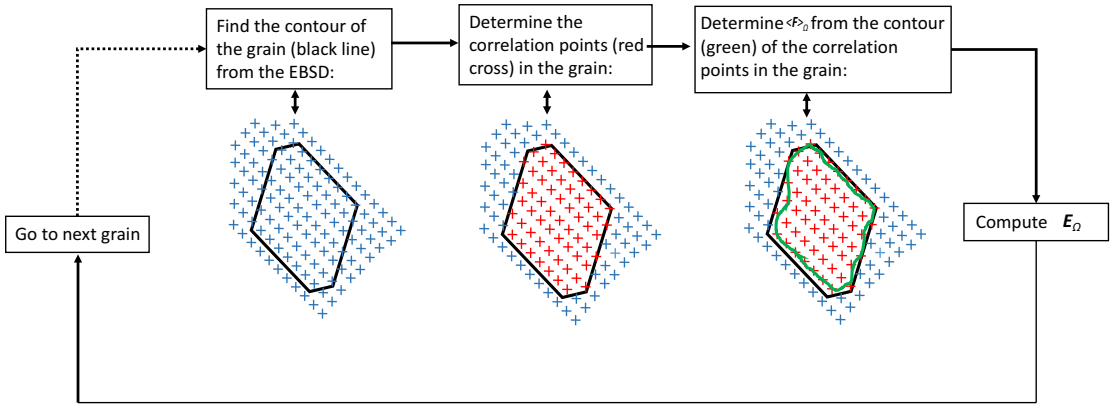

Figure 3.9: Algorithmic scheme of the implemented procedure for the determination of the mean value of the Green-Lagrange tensor components in each grain.

First of all, a comparative study of the two grain families (*small* and *large*) for specimens $A_\perp$ and $B_{/\!/}$ is proposed. Let us mention that the deformation patterns/deformation statistics are defined starting with the first applied strain step and evolve afterwards mainly in terms of strain amplitude. Therefore, only the data for the step 2, corresponding to a global strain of $\approx 6\%$ will be discussed.

	Specimen $A_\perp$		Specimen $B_{/\!/}$	
	small grains	*large* grains	*small* grains	*large* grains
Average of the strains	0.052 ± 0.025	0.06 ± 0.019	0.072 ± 0.031	0.074 ± 0.026
Mediane of the strains	0.048	0.06	0.069	0.072

Table 3.3: Grains size statistics.

In Figure 3.10, the PDF of the ε_{11} strain component relative to the grain's family (red for *large* grains and blue for *small* grains) is plotted in case of a global applied strain of $\approx 6\%$ (purple line). For the specimen $A_\perp$, the two distributions are quite different with, for the *large* grains, a peak aligned with the global strain whereas for the *small* grains a peak of frequency centered around $4,8\%$. In addition, the strain average of the *small* grain is $5,2\%$ with a median at $4,8\%$ while for the *large* grains, the average and median were $6,9\%$ and $7,2\%$ respectively. Thus, one can note that when the tensile test is perpendicular to the printing direction, the mechanical behavior is not the same for *small* and *large* grains: *small* grains deform less than *large* grains.
The same investigation for specimen $B_{/\!/}$ led us to a different conclusion. One can remark on Figure 3.10(b) that both peaks are aligned on the global mean strain. More precisely, the average strain of the *small* grain is 7,2% with a median at 6,9% while for the *large*

grains, the average and median were values 7,4% and 7,2% respectively. One can therefore conclude that when the tensile load is parallel to the printing direction, the mechanical behavior is almost the same for *small* and *large* grains.

In order to get a precise understanding of the relation between grain size and average grain deformation, we propose to analyze the probability density function of the grain surface versus average grain strain over the ε_{11} strain component (2D PDF). This representation will permit to highlight where the maximum deformation is concentrated and will indicate where strain localization and/or failure will probably occur. The corresponding colored histograms are displayed in Figure 3.11. In Figure 3.11(a) and (c), one can see the 2D PDF for the *small* and *large* grain of the specimen $A_{\perp}$ respectively at the same step of deformation as previously. From these plots, we cannot add additional details to the conclusion made in Figure 3.10(a). Nevertheless, for the specimen $B_{/\!/}$, particular areas are observable in the 2D PDF of the *large* grains as shown in Figure 3.11(d). These areas are circled by white dots and they correspond to particular *large* grains that deform more than the others. This was hidden in the figure 3.10(b), where just from this plot, deformation could have been thought uniform. As a first step into the investigation to determine the difference observed during the tensile tests, one can infer that for the specimen $A_{\perp}$, there is a difference of the tensile behavior between *small* and *large* grains while for the specimen $B_{/\!/}$, some particular *large* grains are highly localizing.

It is now necessary to investigate the spatial localization (i.e the deformation patterns) from the strain field obtained by the DIC overlapped on the EBSD in order to qualify and explain the previous statistical observations. In Figure 3.12(a) and (b), the local ε_{11} strain component obtained by DIC for specimen $A_{\perp}$ and $B_{/\!/}$ is displayed in the case of a global strain of 6,1% and 6,7% respectively. One can remark in Figure 3.12(a) that the strain is very localized in some areas while on the Figure 3.12(b), the strain localisation is more spread in some columnar shapes allowing to recognize the zig-zag pattern of the microstructure. For the step of deformation 2, the DIC full-fields for $A_{\perp}$ and $B_{/\!/}$ were respectively overlapped on their relative EBSD map in Figure 3.13(a) and (b) in order to associate the strain pattern with the microstructure. One can see in Figure 3.13(a) that the strain localisations actually correspond to interfaces between the layers. Nevertheless, it can also be noted that not all interfaces show such localization and one can observe that these areas correspond to zones where there is the presence of *small* grains and clusters of *small* grains. One can remember that for specimen $A_{\perp}$, the statistical analysis showed that *small* grains deform less. Therefore, it is reasonable that no strain localisation is observed at the interface in the presence of clusters of *small* grains. Finally, this confirms the results of [6] which noticed that interlayer is a crack initiation area when the tensile direction is orthogonal to the printing direction.

A similar investigation of the DIC overlapped on the EBSD for the specimen $B_{/\!/}$ is plotted in Figure 3.13(b); in this case, the strain localization follows a zig-zag pattern of particular *large* grains. In addition, there are no singularities at interfaces and this makes sense considering the previous results showing that *small* and *large* grains present the same strain distribution. The strong localization in some particular *large* grains shown in 3.13(b) was also expected since it was highlighted by the 2D PDF in Figure 3.10(d). A

complementary graph is proposed in Figure 3.14 where the average ϵ_{11} per grain is plotted and confirmed the presence of particular large grains with higher localisation. Finally, the same trend of localisation for higher deformation steps is observable as displayed in Figure 3.13(c), (d), (e) and (f). It can also be noted that for $A_{\perp}$, localization seems to be more present at the boundaries of the grains while for $B_{/\!/}$, it is more diffuse.
In conclusion, in the case of a tensile load orthogonal to the printing direction, the *small* grains deform less than the *large* ones. It was also observed that the strain localization is mainly situated at the interface between layers in the absence of *small* grains either individual or in clusters. In the other case of a tensile load along the printing direction, we found that *small* and *large* grains deform the same. We also observed that the strain localization was present in some particular *large* grains.

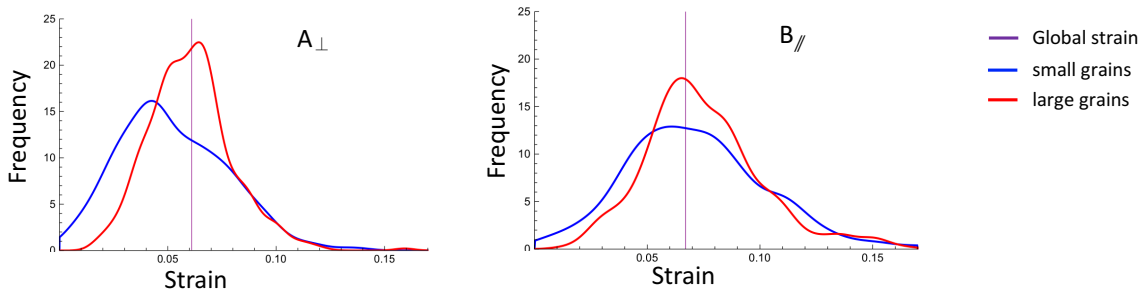

(a) (b)

Figure 3.10: Probality density function of the strain associated for the *small* and *large* grains of specimen $A_{\perp}$ and $B_{/\!/}$ in (a) and (b) respectively.

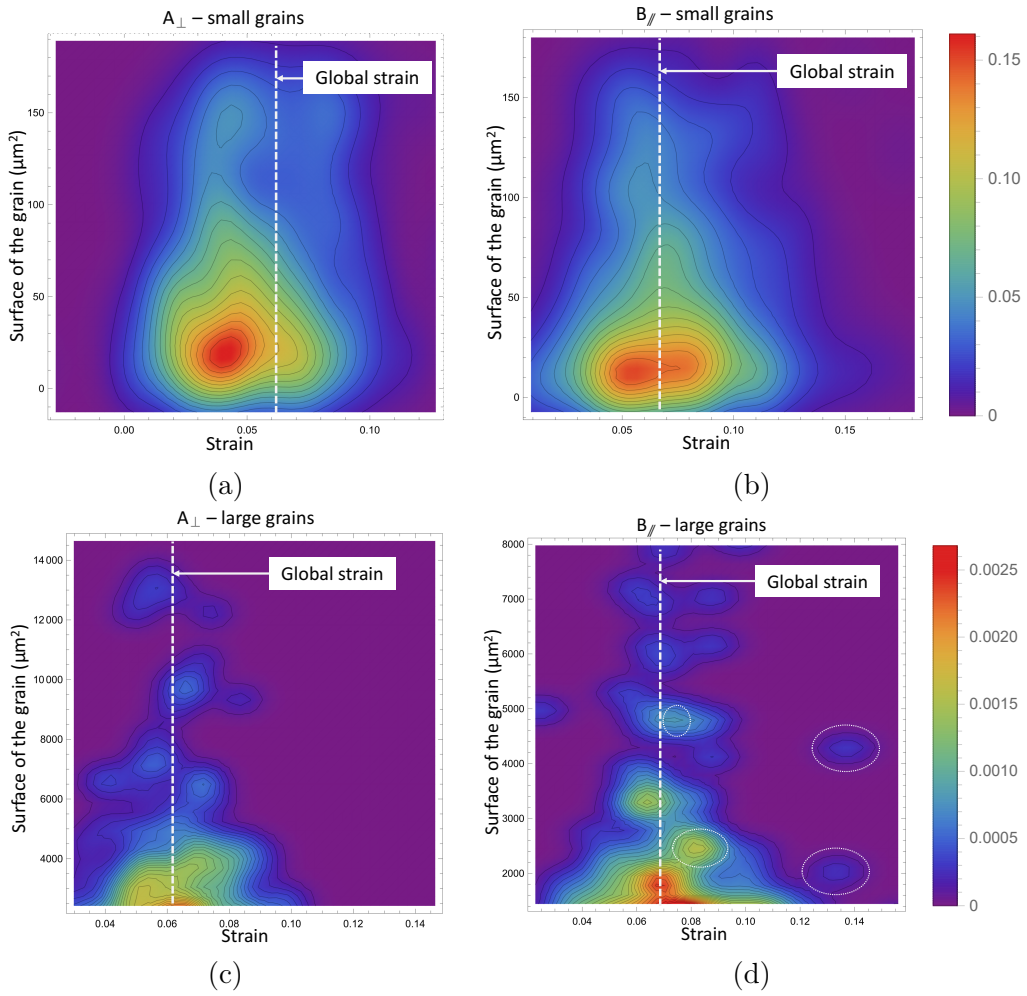

Figure 3.11: 2D Probality density function of the strain for the *small* grains of specimen $A_{\perp}$ and $B_{/\!/}$ in (a) and (b) respectively and for their *large* grains in (c) and (d).

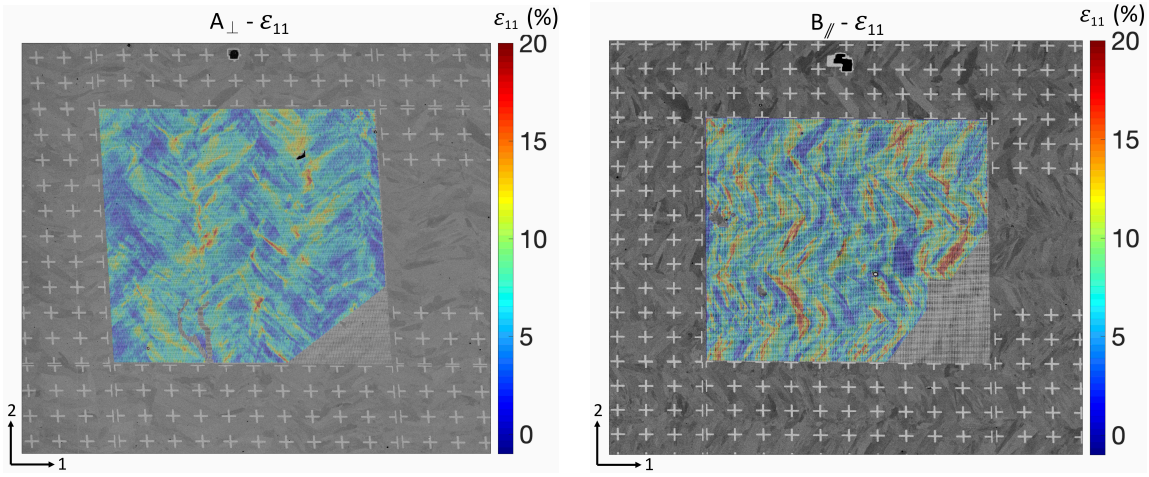

(a) (b)

Figure 3.12: Evolution of the horizontal deformation ε_{11} obtained by digitial image correlation for the specimen $A_{\perp}$ and $B_{/\!/}$ in (a) and (b) respectively.

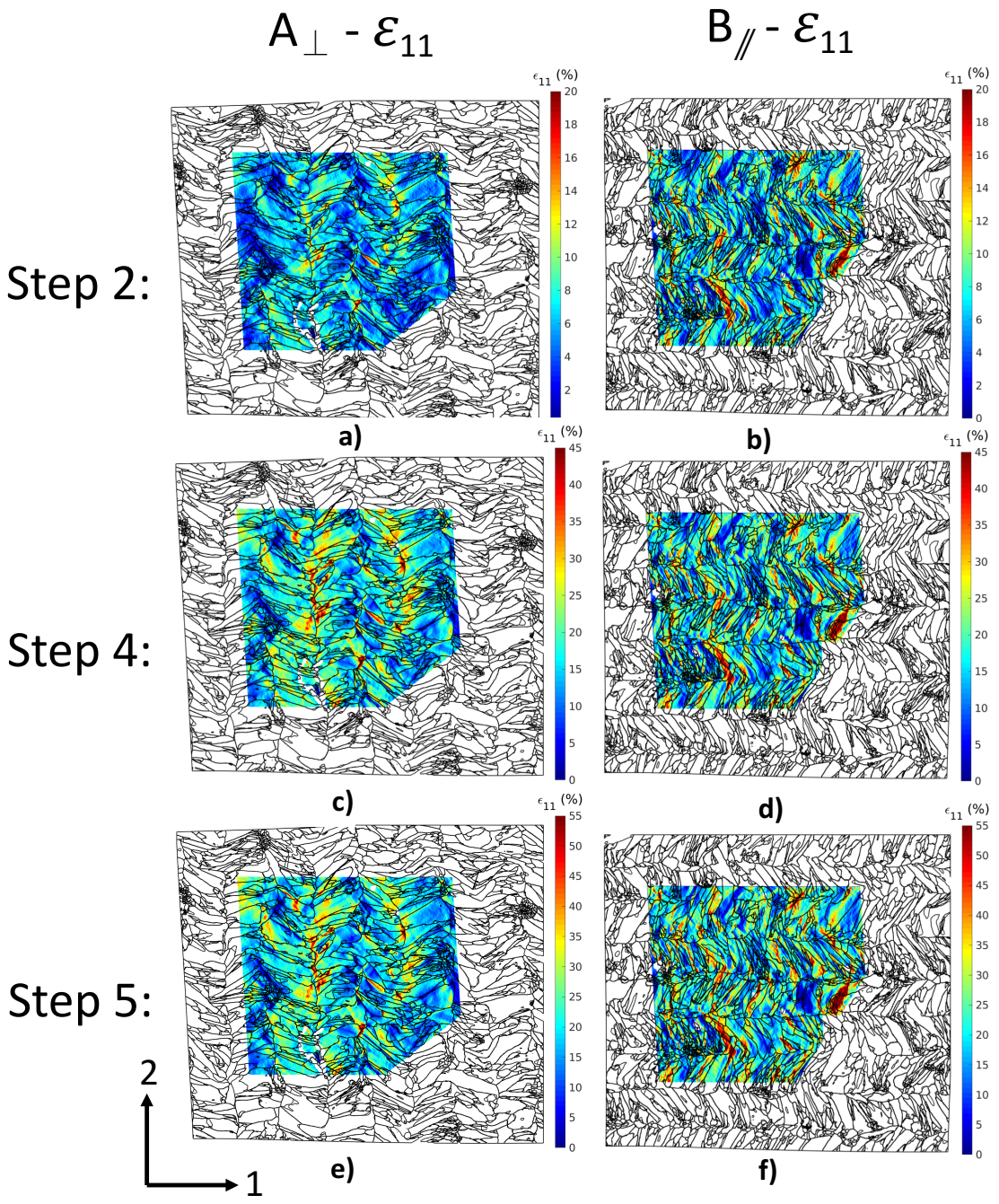

Figure 3.13: DIC overlapped for $A_{\perp}$ and $B_{/\!/}$ on their respective corrected EBSD maps at the step of deformation 2, 4 and 5 corresponding to macroscopic strain of 6%, 16% and 20% respectively.

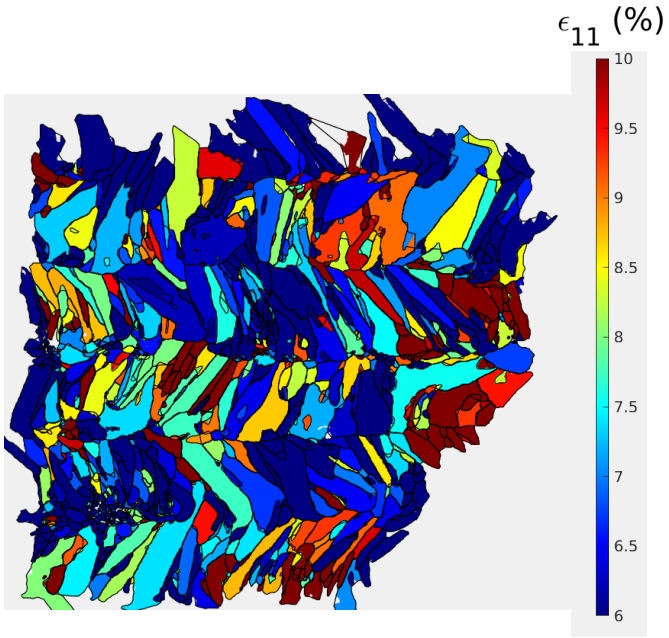

Figure 3.14: Average ϵ_{11} per grains for the specimen $B_{/\!/}$ at the deformation step 2.

3.4 Conclusion and perspectives

In this study, we associated the observed mechanical anisotropy of specimens produced by additive manufacturing with the anisotropic and heterogeneous microstructure and the induced microscopical strain localization. Specimens were extracted from 316L stainless steel single-track thickness walls built by DED. Firstly, we investigated microstructure through morphologic and texture analysis. Then, we performed tensile tests that revealed anisotropy. Finally, in situ tensile tests under an SEM combined with HR-DIC and EBSD maps enabled the qualification and quantification of the mechanisms of deformation. The conclusions are the following:

- The morphologic and crystallographic textures are aligned and can be associated with the heat flow pattern induced by the printing strategy.
- The grain morphology is characterized by *small* equiaxed grains present as isolated or in clusters at the interface between printed layers and *large* columnar grains within the layer.
- Anisotropy was detected during tensile tests. Specimens tested along the printing direction ($B_{/\!/}$) exhibited higher mechanical properties in terms of yield strength (YS) and ultimate tensile strength (UTS) than the specimens tested perpendicularly to the printing direction ($A_{\perp}$). A similar trend was reported in literature.
- In the case of a tensile load perpendicular to the printing direction, *small* grains deform less than *large* ones. Moreover, strain localization is mainly situated at the interface between layers in the absence of *small* grains.
- In the case of a tensile load along the printing direction, the strain localization was observed in some particular *large* grains.

There are several natural extensions of this work such as a precise investigation of the slip systems of the grains exhibiting strong deformations, and the observations of the mechanisms of deformation under cyclic loadings and their relations with the fatigue phenomena. A study of the effect of the cellular substructure should also be performed.

4 Repaired specimens

Overview

Directed Energy Deposition, a metal additive manufacturing process, was employed to repair 316L stainless steel substrates. The dog-bone repaired specimens are composed of two equal parts with an initial substrate and the added repaired part. This design permits to load the interface in tension during a tensile experiment and to analyze how the loading is distributed at the interface where a strong microstructural gradient was observed.
First, the microstructure was investigated and a clear difference between the two halves was observed. The substrate exhibits small equiaxed grains while the printed half presents larger and elongated grains. The effect of the vertical increment also plays an important role on the microstructure and was highlighted in this chapter.
Second, under monotonic tensile loading, the overall mechanical properties of the repaired specimen was found to lie between the tensile properties of the fully printed and substrate specimens.
Finally, an in situ tensile test under a scanning electron microscope combined with High Resolution Digital Image Correlation (HR-DIC) was performed. Additionally, the HR-DIC was associated to the microstructure map allowing to track the local microstructural strain distribution. While homogeneous strain was observed in the substrate half, the printed half showed a strain heterogeneity, with the highest localization found at some interlayers. A zone of low deformation was observed at the interface and was associated with higher hardness.

Contents

4.1 Introduction

One of the growing application areas of AM, particularly for DED, is the repair of costly industrial parts such as aircraft engines, gas turbine, train structure etc. The questions in repair are:

- How should the damaged zone be prepared before the repair?
- What is the necessary quality of the bonding between the damaged part and the added material? With another material?
- What are the effects of post-treatment?
- How is the load distributed in the repair area where a strong microstructural gradient can be observed?
- How is the repaired part thermally affected?
- What are the final properties?

There has been extensive research regarding these questions over several time and length scales [15, 16, 18, 19].
At a macroscopic scale, several research groups investigated the repairing strategy by studying the filling material, post treatment or groove shape. For example, in [15] promising results for the repairing of a ultra-high strength AISI 4340 steel with another material are established. The authors highlighted a noteworthy improvement of the tensile and fatigue properties of the specimen repaired with AerMet 100 steel in comparison to the ones repaired with AISI 4340. Additionally, the authors observed that applying a post-clad heat treatment improved the fatigue limit for all the repaired specimens and placed the limit of the ones repaired with AerMet 100 steel above the fatigue limit of the damaged specimens. For Inconel 718, it was proven in [16] that both the geometry of the groove and the printing strategy influence the final mechanical properties. The authors obtained an optimal bonding with a smooth transition of materials between the repaired part and the added material for a trapezoidal groove. Additionally, the authors observed that the strategy with the diagonal building results with the weakest wear resistance.
At the microscopic scale, the molten material undergoes complex melt-pool dynamics, rapid solidification and then rapid cooling in the solid state. The deposited material volume will undergo several cycles as successive layer will further be deposited. The temperature interval surpasses phase transition and the cycles will act as thermal treatment. These phenomena driven by process parameters generate a hierarchical microstructure [17, 5] that is very different from conventionally processed materials. In the particular configuration of repair, this implies that the original part and the repaired material might end up with significantly different microstructures. Moreover, under mechanical loading, the difference in microstructure and subsequently the global material properties will conduct to different load distribution and strain localisation as one would

expect in a homogenous part. Microstructural strain localisation investigations on fully printed [18, 19, 20] and conventionally manufactured [21] specimens have already been performed but the link between them is missing.
The present chapter aims to contribute to (i) the analysis of the microstructure of repaired specimens by describing the local gradient of microstructural properties and (ii) to propose an investigation of the deformation mechanisms. For (ii), we investigated exclusively the interface zone between the repaired substrate and the added material. More precisely, strain full-fields were obtained through High Resolution Digital Image Correlation (HR-DIC) during an in situ tensile test inside a Scanning Electron Micrsocope (SEM). Additionally, the HR-DIC was associated to the microstructure map allowing to track the local microstructural strain distribution.

4.2 Materials and methods

The design of the repaired specimen is presented in Figure 4.1(a). More precisely, this dog-bone specimen is composed along the vertical axis of two equal parts: (i) an initial substrate and (ii) the added repaired part. This design permits to load the interface in tension during a tensile experiment which is a fundamental repair question. Also, a groove is not required in the configuration of specimen and this design finds many application and is particularly representative of the repair of turbine blades [197]. The specimens were extracted by water jet cutting from the single-track thickness walls manufactured with a back-and-forth printing strategy. The thin 316L stainless steel (SS316L) hot rolled sheet substrate had the dimensions $55 \times 40 \times 0{,}7\,mm$. The $50 \times 15 \times 0{,}7\,mm$ thin walls were additively manufactured by a DED machine from BeAM [141] using a SS316L powder with particles size lying within $45 - 90\,\mu m$ [143]. Additional details concerning the 3D printer and the powder are available in section 2.2 and 2.3 respectively. The process parameters were the following: laser power of $225\,W$, deposition speed of $2000\,mm/min$, powder flow of $6.5\,g/min$ and for a first set of specimens, a vertical spacing between layer of $0.12\,mm$ and for the second, $0.2\,mm$. Finally a pause of $1\,s$ between each layer was necessary for comparative purpose with the fully printed specimens as explained in the section 5.2.1.
After being extracted by water-jet cutting, the specimens were mirror polished with silicon carbide abrasive papers with successive grit values from 400 to 4000 and then finished by ion polishing in order to acquire the electron backscatter diffraction (EBSD) maps.
A first set of ex situ monotonic tensile tests was performed for a repaired, fully printed and substrate specimen. Then, another repaired specimen prepared with a two-scale gold pattern on its surface was loaded with a tensile machine inside a scanning electron microscope (SEM). This gold pattern was deposited using lithography on an area extended across the interface and used to determine the strain localization. In order to reach targeted macroscopic deformations, real-time strain computation was performed using a "macro crosses" grid with a pitch of $15\mu m$ (see Figure 4.1(b), blue area). Once reached, the specimen was unloaded in its elastic regime and images of the 3
mum grids (see Figure 4.1(b), red area) were captured in order to compute high resolution strain full-fields. The strain maps were computed using the *Correlation Manual Value* (CMV) DIC software [185, 186] and the HR-DIC data were overlapped on a distortion corrected EBSD map [195] in order to associate strain localisation patterns with the microstructure.

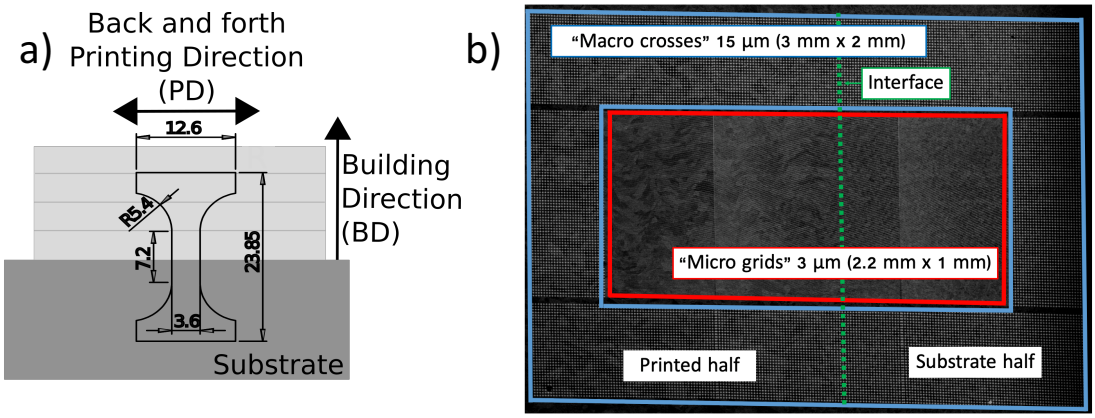

Figure 4.1: (a): Design scheme of the repaired specimen. (b): Image of the multiscale grids on the tensile specimen. Blue area of $3 \times 2mm^2$ with macro crosses with a pitch of $15\,\mu m$ was designed for macroscopic deformation while the red area of $2{,}2 \times 1mm^2$ with a pitch of $3\,\mu m$ was used to capture high resolution images to determine the deformation pattern at the microstructure scale.

4.3 Result and discussion

4.3.1 Microstructure

The microstructure of the repaired specimens with a vertical increment of $0{,}12\,mm$ and $0{,}2\,mm$ are displayed in Figure 4.2(a) and (b) respectively with, at the bottom, the substrate with a fine microstructure and above the printed part with larger grains. For both vertical increments, the walls were able to be printed i.e. $0{,}12\,mm$ and $0{,}2\,mm$ are suitable vertical increments for repair. Let us notice that the difference of vertical spacing generates a difference of thermal history of the complete wall and on the local level because 5/3 more back-and-forth scans were necessary for the $0{,}12\,mm$ vertical increment. We shall observe differences on the pattern of the microstructure and only the morphologic aspect will be reported in this chapter. The crystallographic texture will be presented in section 5.3.1.
In addition, because of the back and forth printing strategy leading to an alternating solidification front for each layer[17, 198], a herringbone pattern, more pronounced for $0{,}2\,mm$ than for $0{,}12\,mm$ can be observed in Figure 4.2(a) and (b) respectively. Also, at the interface, one can remark an epitaxial growth from the substrate of some grains that proves the good metallurgical bonding between the two materials [199].

For both vertical increments, the evolution of the equivalent grain diameter from Figure 4.2, corresponding to the diameter of a circle fitting the grain by its surface is plotted with respect to its distance from the interface in Figure 4.4(a) and (b) respectively. The grains

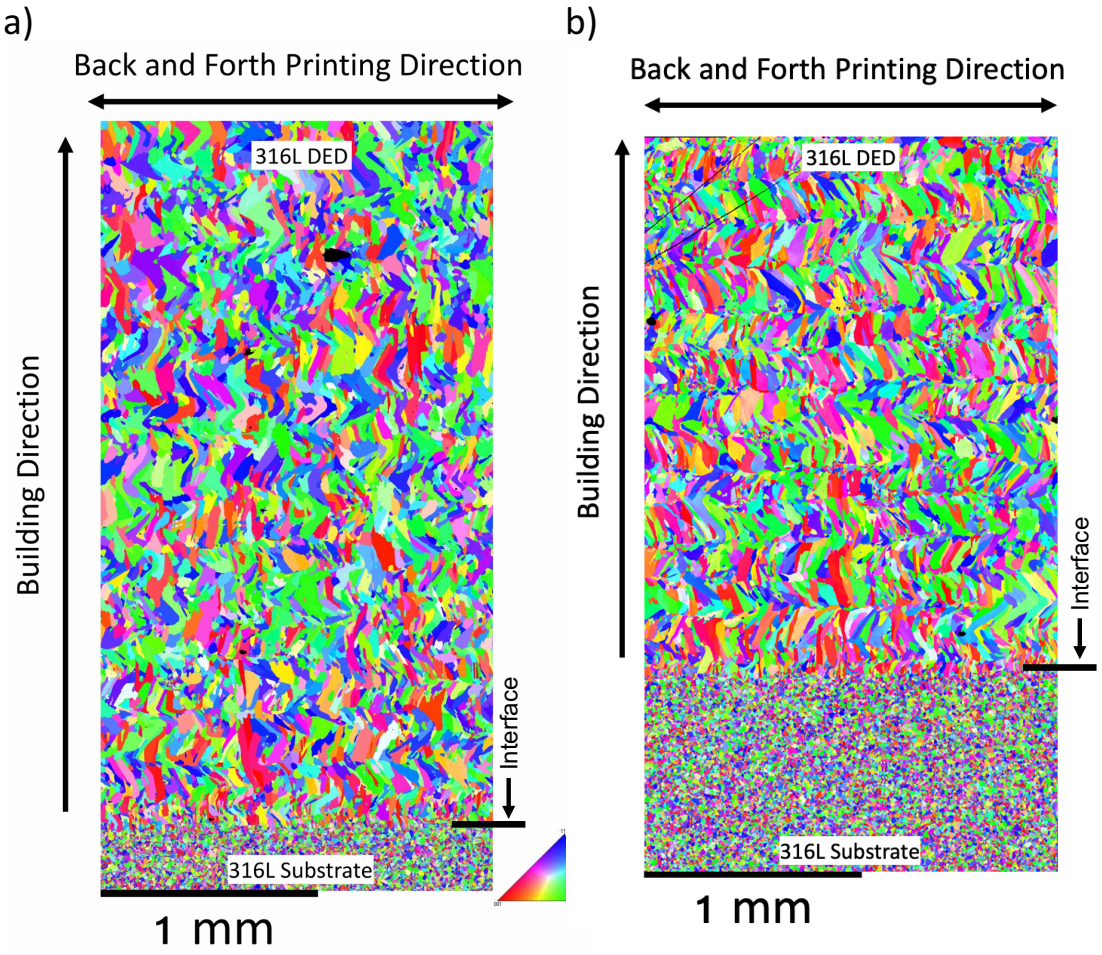

Figure 4.2: EBSD map (IPF X) of the repaired specimen manufactured with a vertical increment of 0,12 mm and 0,2 mm in (a) and (b) respectively.

were gathered into bins with respect to the distance to the interface of their respective center of gravity. The black line links the average equivalent grain diameter of each bins and the blue lines correspond to the standard deviation of the bin. Three regimes can be noticed for 0,12 mm in Figure 4.2(a): (i) the substrate domain $[0\,\mu m\ ;\ 1200\,\mu m[$ where the grain size is small and constant, (ii) the first deposited layers $[-400\,\mu m\ ;\ 0\,\mu m[$ where the steep slope corresponds to the transition between equiaxed to elongated grains, (iii) the printed material $[-3800\,\mu m\ ;\ -400\,\mu m\ [$ with a more moderate slope. The slowly increasing size of the grain with respect to its distance to the interface is a consequence of the heat accumulation in the wall due to poor heat absorption of the substrate resulting in more energy for the grain to grow [5]. For 0,2 mm in Figure 4.2(b), the same analysis can be made for the first two regimes. However, for the printed material $[-2600\,\mu m\ ;$

$-300\,\mu m$ [, the slope is constant due to less heat accumulation in the wall.

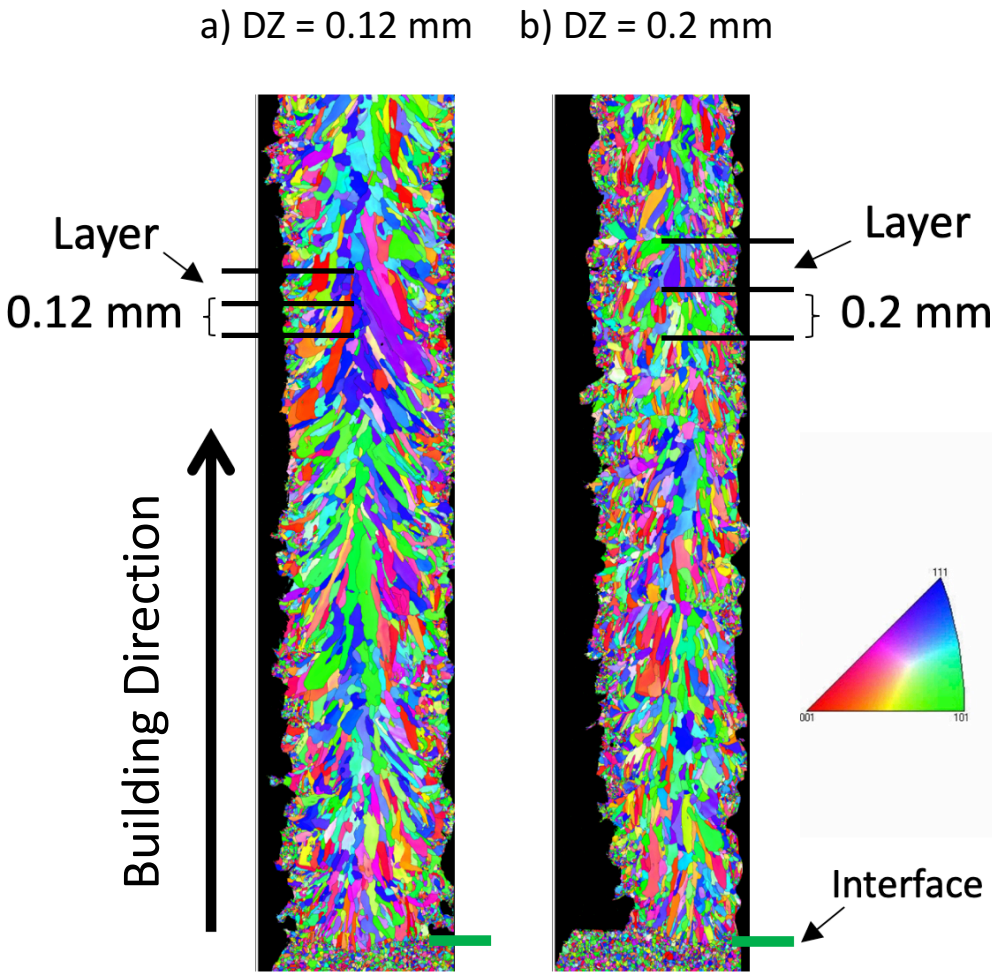

Figure 4.3: EBSD map (IPF X) of the cross section of the repaired specimen manufactured with a vertical increment of 0,12 mm and 0,2 mm in (a) and (b) respectively.

Additionally, the microstructure of the transverse cross section for a vertical increment of 0,12 mm and 0,2 mm is presented in Figure 4.3 (a) and (b) respectively. On both maps, a small layer on both sides of the wall can be distinguished with small grains while in the kernel region, the grains are larger. The variation of the grain size along the thickness of the wall can be a consequence of different mechanisms: convection dominates conduction mechanisms near the surfaces of the wall [200]. These small grains near the surfaces could also be unmelted powder. A clear difference is observable for the kernel grains with respect to the vertical increment. Indeed, for the 0,12 mm vertical increment,

grains are larger and a "christmas tree" shape is noticeable. In contrast, for the 0,2 mm vertical increment, the kernel grains are smaller and have a slope more aligned with the building direction axis. Also for the 0,12 mm configuration, the kernel grains can cross several layers while for the 0,2 mm, they are essentially present in only one layer. The inclination angle is defined as the angle between the longest axis of the fitting ellipse and the building direction axis. This difference of angle was quantified by plotting the probability density function of the slope of the kernel grains with respect to the building grains in Figure 4.4(c) and (d). In (c) one can see that the inclination angle of the kernel grains have a slope at $\approx \pm 60^o$ with respect to the building axis. In (d) the kernel grains are more aligned with the building axis with a slope at $\approx \pm 75^o$. This difference is mostly a consequence of the different thermal history. Indeed for the 0,12 mm vertical increment, more layers are required, therefore the wall is subjected to more heat accumulation. Consequently, it affects the heat flow direction and therefore the solidification direction and crystallographic orientation. This explains the grains oriented toward the free surface of the wall for 0,12 mm vertical increment and the difference of crystallographic texture between 0,12 mm and 0,2 mm observed in the next chapter, section 5.3.1. In addition, one can remark that the distribution in Figure 4.4(c) is symmetric while is not in Figure 4.4(d). This disimetry is thought to be a consequence of the non perfect orthogonal cross section on which the microstructure data were acquired.
Next, the microstructure of the printed part and substrate is compared by their shape and size. For the printed part, the grains were sorted in two families, *small* and *large* grains, according to their respective equivalent grain diameter. The threshold value between the two families of grains is 15μm and it will allow for finer description during the analysis of the morphological texture. These *small* grains are found disseminated at interlayers and especially in clusters at interlayers. The shape of the grain is described by its aspect ratio (AR) defined as the ratio of principal axes of the smallest circumscribed ellipse, implying that an aspect ratio of 1 indicates an equiaxed grain. One can see in table 5.1 that *small* and *large* grains in the 0,12 mm configuration have an average equivalent diameter of 8,5 $\mu m \pm$ 3,5 and 36 $\mu m \pm$ 20,9 respectively. For a vertical increment of 0,2 mm, the average equivalent diameter for *small* and *large* grains are 7,6 $\mu m \pm$ 3,5 and 31 $\mu m \pm$ 16,8 respectively. Additionally, for both vertical increments, *large* grains are more elongated with a larger AR than for the *small* grains. Moreover, the amount of *small* grains highly decreases with a smaller vertical increment and this is due to more heat accumulation in the wall giving more energy for the grains to grow. Finally, the substrate has an average grain size of 7,2 $\pm$ 3,9 and an AR of 1,8 $\pm$ 0,8. This difference of morphology as well as the crystallographic texture (presented in in chapter 5) results in different mechanical properties and will be presented next.

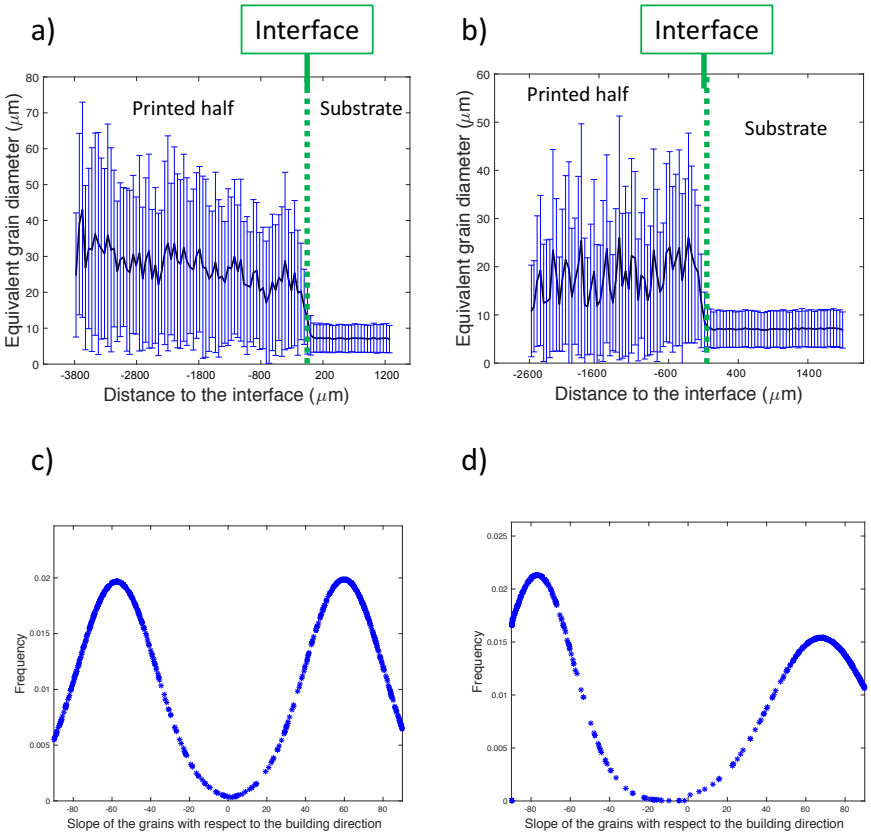

Figure 4.4: Evolution of the equivalent grain diameter with respect to its distance from the interface for the 0,12 mm and 0,2 mm configuration in (a) and (b) respectively. In (c) and (d) is displayed the angle of the inclination angle of the grain in the kernel with respect to the building direction axis for the 0,12 mm and 0,2 mm configuration respectively.

	Printed part - 0,12 mm			Printed part - 0,2 mm			Substrate part
	All grains	*small* grains	*large* grains	All grains	*small* grains	*large* grains	All grains
Diameter average (μm)	$25{,}2 \pm 21{,}2$	$8{,}5 \pm 3{,}5$	$36 \pm 20{,}9$	$16{,}5 \pm 15{,}6$	$7{,}6 \pm 3{,}5$	$31 \pm 16{,}8$	$7{,}2 \pm 3{,}9$
Diameter Median (μm)	19,3	8,4	29,5	11,2	7	25,5	6,2
Aspect ratio average	$2{,}4 \pm 1{,}3$	$2{,}3 \pm 1{,}3$	$2{,}7 \pm 1{,}6$	$2{,}4 \pm 1{,}4$	$2{,}1 \pm 1$	$2{,}9 \pm 1{,}7$	$1{,}8 \pm 0{,}6$
Aspect ratio Median	2	2	2,2	2	1,8	2,4	1,6
Quantity of grains (%)		39,3	60,7		62,2	37,8	
Surface occupied (%)		13,3	86,7		28,7	71,3	
Surface of study (mm^2)	$3{,}8 \times 2$			$2{,}2 \times 1{,}6$			$1{,}6 \times 2$

Table 4.1: Grain size and shape statistic.

4.3.2 Mechanical properties

The tensile behavior under monotonic loading for the fully printed, repaired and substrate specimens are compared in Figure 4.5. One can notice for 0,12 mm configuration in (a) that the tensile strength of the repaired specimen falls between the two other ones. In addition it is less ductile, a similar result was also shared in [201, 202]. The same trend was observed for the 0,2 mm configuration in (b). Finally, all the repaired specimens tested fractured in the printed part, away from the interface, which indicates that the bonding zone is not a limiting weak area during uniaxial loadings.

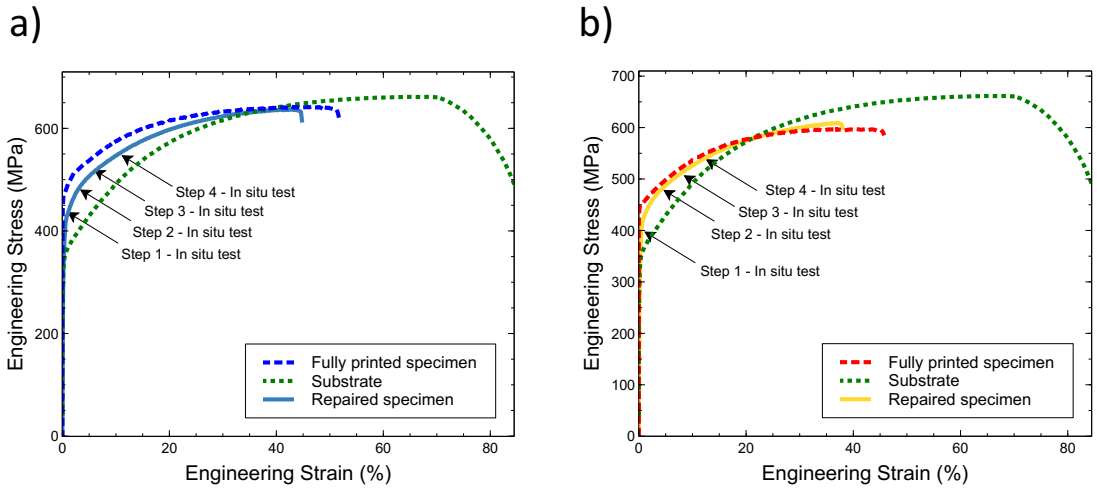

Figure 4.5: Tensile engineering stress-strain curves for the 0,12 mm and 0,2 mm configuration in (a) and (b) respectively.

Next, for the 0,12 mm configuration, an analysis combining HR-DIC and EBSD map is proposed to reveal the microstructural strain localisation near the interface. The image (a), (b) and (c) in Figure 4.6 are showing the strain localisation ϵ_{11} (aligned with the tensile direction) for the deformation step 1 ($\simeq 2\,\%$), 3 ($\simeq 6\,\%$) and 4 ($\simeq 15\,\%$) defined in Figure 4.5(a) respectively. In addition, the average values of ϵ_{11} on a line parallel to the interface is proposed in order to obtain a finer analysis. At the step 1, the strain localisation only occurs in the substrate as shown in Figure 4.6(a). Further, the deformation is homogeneous and this behavior will be the same for all the other steps studied. At the step 2, heterogeneous strain localisations in the printed half start to appear and they are located at some interlayer zones as shown in Figure 4.6(b). As the tensile loading increases, the strain magnitude increases and particularly in the printed part. More precisely, the previous zones of heterogeneous localisation at the interlayer zones are becoming the highest local strain localisation of the entire specimen as shown in Figure 4.6(c). This is consistent with the results presented in [6] where the authors reported that for a fully printed specimen, the interlayer is a crack initiation area when

the tensile direction is orthogonal to the printing direction. It also recalls the localisation observed at interlayers for a fully printed specimen tested along the building direction in the chapter 3.
Finally, close to both sides of the interface, a zone with low deformation was observed. This area is associated with the microhardness of the materials in Figure 4.6(d). One can see that this zone in the substrate or printed half represented in pink is harder than their respective half ($\approx 25\%$). This is a consequence of the heat affected zone in the substrate with strengthening effect [203] and the finer grains present in the first deposited layers in the printed part leading to Hall-petch effect [200]. Additionally, one can remark that the hardness is higher in the printed half than in the substrate. It is compelling with the fact that the yield strength is higher for the fully printed specimen than for the substrate's one as one can see in Figure 4.5(a).
The same results and deformation mechanisms are obtained for the $0{,}2\,mm$ configuration. They are not discussed but they are exhibited in figure 4.7.
Finally to conclude, the microstructural gradient observed has a clear effect on the strain localization and it should be optimized to increase the final properties of repaired specimens.

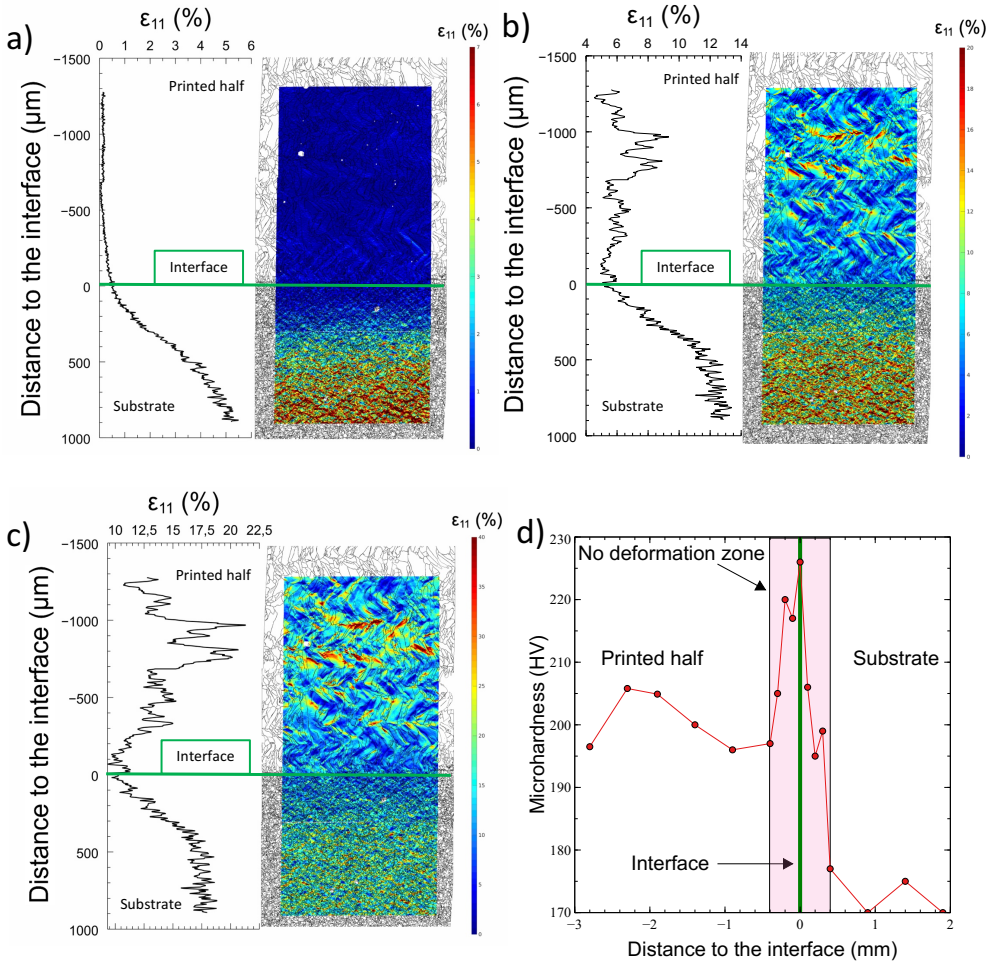

Figure 4.6: For the 0,12 *mm* configuration: evolution of the strain along the tensile direction at the deformation step 1, 3 and 4 respectively in (a) (b) and (c). The deformation ϵ_{11} obtained by DIC is overlapped on the microstructure obtained by EBSD and a complementary plot of the evolution of ϵ_{11} with respect to the distance to the interface is proposed. (d): Microhardness map showing higher hardness around the interface of the repaired zone corresponding to a no deformation area.

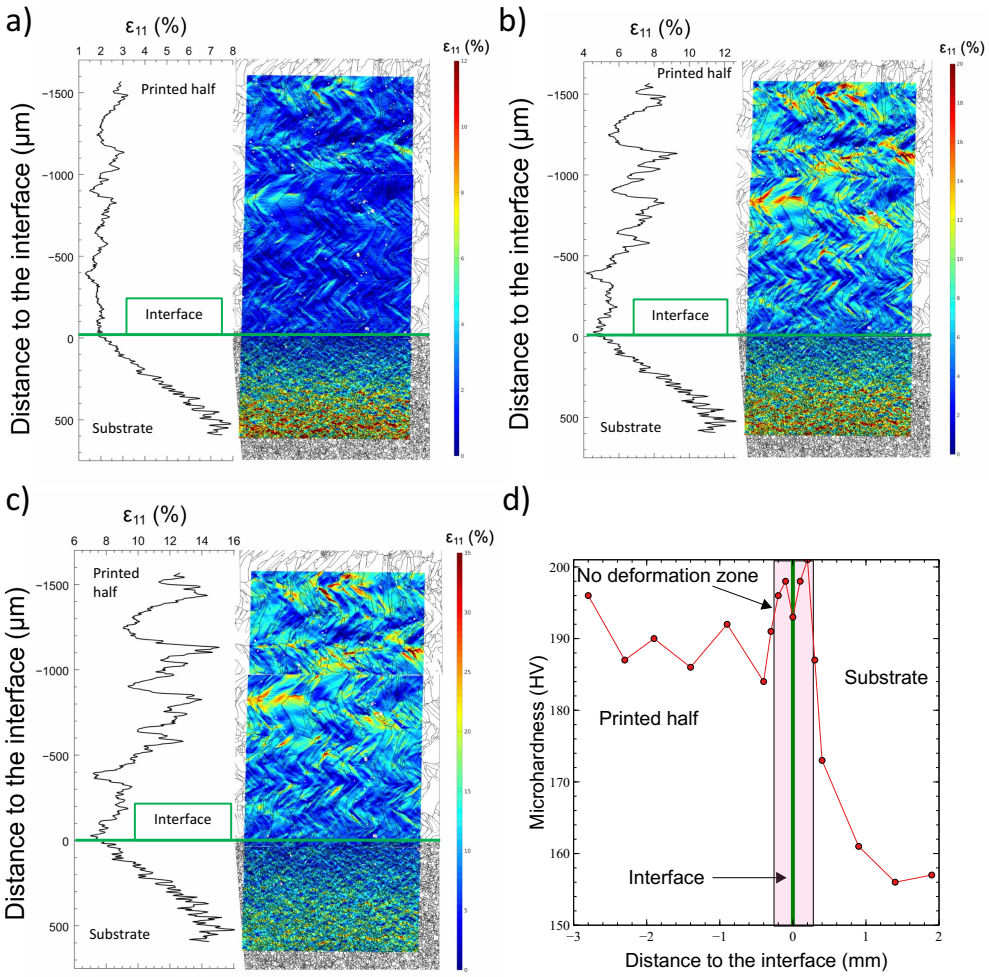

Figure 4.7: For the 0,2 mm configuration: evolution of the strain along the tensile direction at the deformation step 2, 3 and 4 respectively in (a) (b) and (c). The deformation ϵ_{11} obtained by DIC is overlapped on the microstructure obtained by EBSD and a complementary plot of the evolution of ϵ_{11} with respect to the distance to the interface is proposed. (d): Microhardness map showing higher hardness around the interface of the repaired zone corresponding to a no deformation area.

4.4 Conclusion

The microstructure and mechanical properties of repaired specimens by Directed Energy Deposition was investigated in this chapter. The microstructure of the repaired half featured a particular morphology with larger and elongated grains in comparison to the small equiaxed grains in the substrate half. In addition, it appears that the interface was not a weak area during uniaxial static tests, since all specimens fractured in the printed part away from the interface. In situ tensile tests performed under an SEM combined with high resolution digital image correlation and electron backscatter diffraction map enable the tracking of the local microstructural strain localisation. While homogeneous strain was observed in the substrate half, the printed half showed a strain heterogeneity, with the highest localization found at some interlayers. A zone of low deformation was observed at the interface and was associated with higher hardness.

5 Self-heating behavior

Overview

The purpose of this chapter is to assess a self-heating testing method for the characterization of fatigue properties of single-track thickness specimens additively manufactured. It also evaluates the impact of the microstructure orientation with respect to the loading direction on the dissipative behavior and the initiation of microcracks. The 316L stainless steel specimens under scrutiny were manufactured by Directed Energy Deposition in two configurations: (i) fully printed specimens (2 orientations) (ii) repaired specimens. The chapter first presents a morphologic and crystallographic texture analysis and second, a series of self-heating tests under cyclic loading. The microstructural analysis revealed elongated grains with their sizes, shapes and preferred orientations prescribed by process parameters. The self-heating measurements under cyclic tensile loading proved that the infrared dissipation measurements can be performed on small scale thin specimens. The self-heating curves could successfully be represented by the Munier model. Moreover, several links between the printing parameters and self-heating results could be established. For example, a smaller vertical increment between successively deposited layers leads to higher mean endurance limits in all configurations. Repaired specimens had a lower mean endurance limit when compared with fully printed or conventionally manufactured substrate specimens. Finally, anisotropy was highlighted during these cyclic tests: specimens loaded orthogonally to the Printing Direction (PD) showed higher fatigue limits when compared with the ones tested along the PD. Additionally, post-mortem observations revealed characteristic microcracking patterns initiated during the self-heating experiments. Loading along the printing direction induced a classical dominating crack, whereas orthogonal loading generated a network of microcracks along the writing direction suggesting the damage and opening of the the interlayers. Additionally these patterns can be correlated with patterns of plasticity at the grains scale observed in chapter 3 and 4.

Contents

5.1 Introduction

As introduced in the state of the art, traditional cladding processes used as repairing techniques with the same or different materials have been investigated for the past decades. To name a few, arc welding [8], thermal/plasma spraying [9, 10, 11] and cold spray [12] have been studied, however severe limitations related to the particularities of the processes such as a large heat affected zone (HAZ), critical distortions, poor accuracy and poor mechanical properties as built have prevented the deployment of these technologies. Directed Energy Deposition (DED), one of the two main metallic Additive Manufacturing (AM) technologies received a particular attention as an alternative repairing technique in the past years. The DED technology is an additive manufacturing process in which the material is transported into a focused heat source and then deposited on the already constructed layers [43]. Particular variants of the DED process have been denoted in several ways in the literature such as: Direct Metal Deposition (DMD), 3D laser cladding, Laser Metal Deposition (LMD) and Direct Laser Deposition (DLD) to name a few. One of the key advantages of the technology is its manufacturing ability on non-planar substrates, which permits to construct coatings [204] or to repair complex geometries [205, 50]. However, it does not reach the performances of Powder Bed Fusion (PBF), the other main metallic AM technology, in fineness or complexity of the manufacturing parts [206].
Manufacturing or repairing with a DED technology is a task requiring the understanding of the particular microstructure inherent to such a process and its effect on the mechanical properties. In fact, several research groups investigated the effects of the process parameters such as the power of the laser, powder flow, deposition speed etc. on additively manufactured parts and highlighted the presence of oriented microstructure with elongated grains as well as anisotropic macroscopic properties [20, 26, 207]. A discussion in [208] of the microstructure for a Vanadis 4 metallic substrate repaired by LMD with two different powders CPM 10V and Vanadis 4 showed that microstructure of the resulting repaired part was similar to a quenched alloy tool steel, which indicated the suitability of this technology for repair work. With optimized parameters, DED can attenuate the HAZ, create metallurgical-bonded deposits and reduce the distortion i.e. it can solve the above mentioned problems [13, 14], and thus, is particularly interesting for the repairing of high-value components [209, 210]. As an example, a comparison of laser-cladding and gas metal arc welding of gray cast iron repair is presented in [211]. It revealed a larger heat affected zone and lower ultimate elongations for the gas metal arc welding repaired components, highlighting the superior properties for components repaired by laser-cladding. The quantity of repairing as well as the lasing strategy and shape of the slot to fill were found to also be of high importance for the properties of the repaired specimens. The polycrystalline microstructures of 316L stainless steel used for the repair of tools have been discussed in [203]. The study underlines a complex dendritic structures growth as a consequence of irregular nucleation. The focus on simulated damage of different sizes repaired by laser-cladding showed that cracks occurred around the repair only for the deepest ones and explained their occurrences by the presence of thermal stresses and oxide inclusions. The authors finally reported that tensile proper-

ties exhibited a 5% degradation for the repaired specimens with a depth of damage of 0.5mm. In [16], the authors noticed that a trapezoidal shape of slot allows for a porosity free bonding in comparison to a rectangular slot. In addition, the authors observed that the scanning strategy, more particularly the diagonal pattern, had an influence on the friction coefficient and the wear resistance.
Another important aspect of additively manufactured metallic parts are the fatigue properties and lifetime predictions. These properties can be assessed at the macroscopic scale of the structure, however for metallic components, they depend on the plasticity mechanisms and the particular grain structures at the microscopic scale of the material as discussed for example in [22, 23]. Fatigue life in as-built metal AM materials has been assessed and discussed under different settings: the influence of processing conditions and the resulting defect structure is highlighted in [24, 25] whether the role of the particular microstructure has been underscored by exhibiting anisotropy properties for static and cyclic loadings in [6, 26] and [25, 27], respectively. More precisely, a study in [25] focused on Direct Metal Laser Sintering of 316L stainless steel and found that the measured fatigue strength was close to the wrought material's one when subjected to uniaxial stress parallel to the layers. However, when the loading direction was perpendicular to the printed layers, fatigue fractures often occured prematurely by separation of the material. In the case of 304L stainless steel manufactured by DED, it was reported in [27] that specimens loaded perpendicularly to the layers manifested an improvement in the intermediate fatigue regime (10^4-10^6) of 25% and performed identical to wrought in the high cycle fatigue regime. For the latter regime, a decrease of 7% of the fatigue limit for the specimens tested parallely to the layers in comparison to the wrought was measured.
The fatigue properties of DED repaired structures was less investigated. A study reported in [15] showed that repairing a AISI 4340 substrate with the same material brought very poor tensile properties and a significantly reduced fatigue life. Nevertheless, the replacement of the cladded layer with AerMet 100 steel improved the fatigue life by a factor 10 and additionally applying a post-clad heat treatment improved the fatigue slightly above the grind-out substrate's one. In [28], the authors investigated the printing strategy for Ti-6Al-4V specimens repaired by DED and more precisely the inter-track pause effect. They observed a clear difference of microstructure and 50% more tensile residual stress for the specimen manufactured with inter-track pause. For the latter, shorter fatigue life was mostly attributed to geometrical defects. These studies equally highlight the difficulties and the underlying cost of providing a large data-base of fatigue test for materials that can largely vary according to the process parameters. Therefore, alternative and faster methods are required to determine such properties. One of them is based on the self-heating measurements of the specimen due to microscopic plasticity observed under cyclic loadings. This method was firstly used by Stromeyer in 1914 [29] to perform a rapid determination of the mean fatigue limit defined as the minimum level of alternating stress which will generate heat in the tested specimen. Over the years, this method was refined and applied to various materials and configurations [212, 213, 214, 215, 216, 217, 218]. More recently in [30], the authors proposed a two scale probabilistic model with two dissipative mechanisms taking into account the dissipation of the primary and secondary

regime in order to analyse the self-heating phenomenon. To our knowledge, this method has not been yet used to analyse fatigue of repaired parts by DED. This could enable a fast determination of fatigue properties in AM parts allowing a parametric analysis.
The objective of this chapter is therefore to apply the self-heating testing method to assess the damage evolution for single-track thickness specimens and to evaluate the applicability of the method in thin small scale fully printed and repaired specimens. The chapter is organized as follows: It starts with the presentation of the specimens and the experimental techniques. Afterwards, the characterization of the microstructure of the specimens is discussed and macroscopic mechanical properties during uniaxial tensile tests are exhibited. Next, measurements of the self-heating phenomenon during increasing cyclic loadings will be analyzed and discussed.

5.2 Materials and experiments

5.2.1 Manufacturing of the specimens

As presented in Figure 5.1, a series of bidirectionally-printed single-track thickness walls were built by Directed Energy Deposition (DED) in two configurations. A first set of $100\,mm \times 30\,mm \times 0{,}7\,mm$ walls was printed on a horizontal 316L stainless steel substrate, in which fully printed specimens were extracted in two orientations with respect to the printing direction. A second set of $50\,mm \times 15\,mm \times 0{,}7\,mm$ walls was printed on a vertical substrate in which "repaired" specimens being half substrate half printed were extracted. For both configurations, the specimens were extracted at the center of the walls by water jet cutting with a *Mach 2b water jet* [181]. The two orientations for the fully printed specimens were defined in order to apply a perpendicular or parallel tensile loading with respect to the Printing Direction (PD).
The precise shape of the dogbone specimens does not adhere to any standards but was governed by compatibility requirements such as for example the size of the ion polisher chamber. However, prior to the start of experiments, a finite element analysis of the elastic model of the geometry confirmed a homogeneous macroscopic strain in the zone of interest.
In addition, because of practical limitations, the manufacturing of the walls for the repaired configuration had to have a length twice shorter. Also, it is known that the thermal history during a repairing operation is of great importance for the microstructure, residual stresses and therefore mechanical properties [28]. Since the walls for both configurations had a ratio of 2 in terms of length, a pause time of $1\,s$ for the laser between each layer was necessary for the repaired walls in order to compensate for the smaller length and therefore replicate the same thermal history at the center of the wall. However, the difference of size of the substrates for the fully printed specimens ($150\,mm \times 5\,mm \times 200\,mm$) and for the repaired ones ($55\,mm \times 40\,mm \times 0{,}7\,mm$) and its effect on their respective capacity of heat absorbtion was not quantified in this study.
316L stainless steel gas atomised powder from Höganäs AB [143] with a particles size within 45-90 μm was used in this study for its weldability and mechanical properties. For both configurations, walls were printed with the following parameters of the machine: (i) a powder flow of $6{,}5\,g/min$, (ii) a deposition speed of $2000\,mm/min$ and (iii) a laser power of $225\,W$. Additional information concerning the powder, the additive manufacturing machine Mobile from BeAM [141] as well as the process calibration are available in the chapter 2. For both configurations, the effect of process parameters on microstructure and mechanical behavior was studied through the effect of two different vertical increments i.e. the vertical spacing between the successive deposited layers. For $0{,}12\,mm$ and $0{,}2\,mm$ of vertical increments, the walls were able to be manufactured with targeted dimensions i.e. both vertical increment are suitable for repairing. However, the difference of vertical spacing for the same configuration brought a different thermal history during the manufacturing i.e. a ratio of $5/3$ of back-and-forth scans were necessary for a vertical increment of $0{,}12\,mm$ in comparison to the $0{,}2\,mm$ one to print the same height wall, resulting in a difference of properties and microstructure as analysed next.

Next, we denote the latter specimens manufactured with a vertical increment of 0,12 mm and a perpendicular or parallel tensile direction to the PD as $A_{\perp\,0,12}$ and $B_{/\!/\,0,12}$ respectively, as represented in Figure 5.1. For a vertical increment of 0,2 mm, they are denoted as $A_{\perp\,0,2}$ and $B_{/\!/\,0,2}$ respectively. Finally, the repaired specimens manufactured with a vertical spacing of 0,12 mm and 0,2 mm are named $R_{0,12}$ and $R_{0,2}$ and their dimensions in mm (common to the fully printed ones) are shown in Figure 5.1.

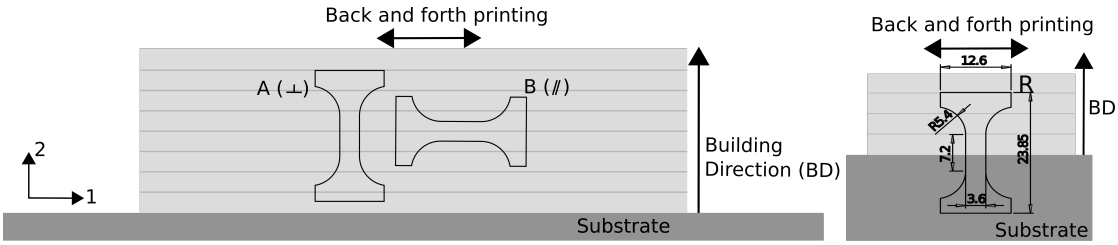

Figure 5.1: Schemes of the 316L single-track thickness walls where fully printed in both orientation and repaired specimens were extracted by water jet cutting. The common dimensions for all the specimens are presented on the scheme of the repaired specimens (right).

5.2.2 Specimen preparation and observation

The specimens were all mechanically polished after the extraction in order to obtain a mirror surface and were additionally ion polished for Electron Backscatter Diffraction (EBSD) maps acquisition. The precise procedure and parameters are available in section 3.2. This mirror surface state was necessary for the self-heating tests in order to override the surface roughness incurred during the manufacturing process and more particularly because the specimens were only one single-track thickness meaning that the roughness effect would affect in first order the final failure or fatigue properties.The authors noticed indeed in [203], that the fatigue properties of Ti-6Al-4V samples, produced by direct metal laser sintering and electron beam melting, are dominated by surface roughness effects.

The microstructure was analyzed qualitatively and quantitatively in terms of grain size, shape and distribution from the EBSD data. In order to compare the microstructures and the influence of the vertical spacing between layers, it was necessary to respect the following protocol: (i) the specimens fully additively manufactured were extracted from the middle and at the same height of the wall, i.e. away from the edges that could have brought a different microstructure as a consequence of the back-and-forth printing strategy, (ii) the repaired specimens were manufactured with a pause time between layers to imitate the manufacturing conditions of the fully printed one, (iii) the EBSD analyses were performed after the same level of polishing, i.e same depth for the final specimen, (iv) EBSD maps are large enough to contain a statistically representative number of grains with a step size of 1 μm. Therefore, in order to simplify the discussion and avoid

redundancy, only the following configurations will be reported next: $A_{\perp\,0,12}$, $B_{/\!/\,0,2}$, $R_{0,12}$, $R_{0,2}$.

5.2.3 Mechanical testing

Tensile tests were first conducted under a static monotonic loading on an electro-mechanical *Instron ElectroPulsTM E3000* machine [219]. The tests were performed under a $3\,kN$ load cell at a strain rate fixed at $2.10^{-2}\,s^{-1}$. The deformation field was obtained by Digital Image Correlation (DIC) from a homemade software *Correl Manu* [185, 220] on a coarse speckle made by white and black paintings. For comparative purpose, the specimens had the same surface preparation as the ones used for the fatigue tests.
Following these monotonic tests, self-heating tests were performed. This experiment consists in applying a successive series of cycles for different increasing stress amplitude Σ_0 while keeping the same stress ratio as represented in Figure 5.2(a). Thermal effects result from the dissipation due the microplasticity and are recorded for each cycling block. More precisely, the temperature elevation for a cycles block is defined as the difference between the average temperature recorded during a cycles block and the average temperature during the pause time (t) of 3 minutes. This pause time permits to dissipate the heat accumulated during the cycles block. A graph corresponding to the couples stress amplitude and temperature elevation is plotted in Figure 5.2(b) and one can notice the presence of two regimes. The primary regime corresponds to a very limited dissipation regime while the secondary regime appears beyond a Σ_0 with an increased slope. This change of slope generally occurs near to the fatigue limit [221]. Thermal measurements have been carried out using the *FLIR X6580sc* camera [222] at the recording frequency of $10\,Hz$ which was focused on the specimen's surface using a G1 lens allowing a resolution of $15\,\mu m/pixel$ on a $3 \times 4mm^2$ area.

Usually, for this type of test, the elevation temperature requires to also take into account the influence of the temperature of the hot oil circulating in the hydraulic press which can be conducted to the specimen through the machine's jaws and therefore affect the recorded temperature [30]. However, the machine used in the present case is an oil-free machine based on a linear motor technology which enables us to only focus on the variation of the specimen's temperature due to the microscopic plasticity during the cyclic loadings. Moreover, it was observed in [223], that taking into account the effects of the jaws mostly matters for the low stress amplitudes (primary regimes) while for the secondary regime, the effect is negligible.
To experiment in the best conditions, the specimens were painted in black to obtain an emissivity close to 1 and the experimental set up was covered by a protective enclosure to limit the thermal noise from the surroundings as pictured in Figure 5.3 . The specimens were tested at the frequency of $30Hz$ during 20000 cycles per block and a constant loading ratio R_Σ, was chosen to be positive and equal to 0,1 to prevent the buckling of the thin specimens. R_Σ is defined as follows:

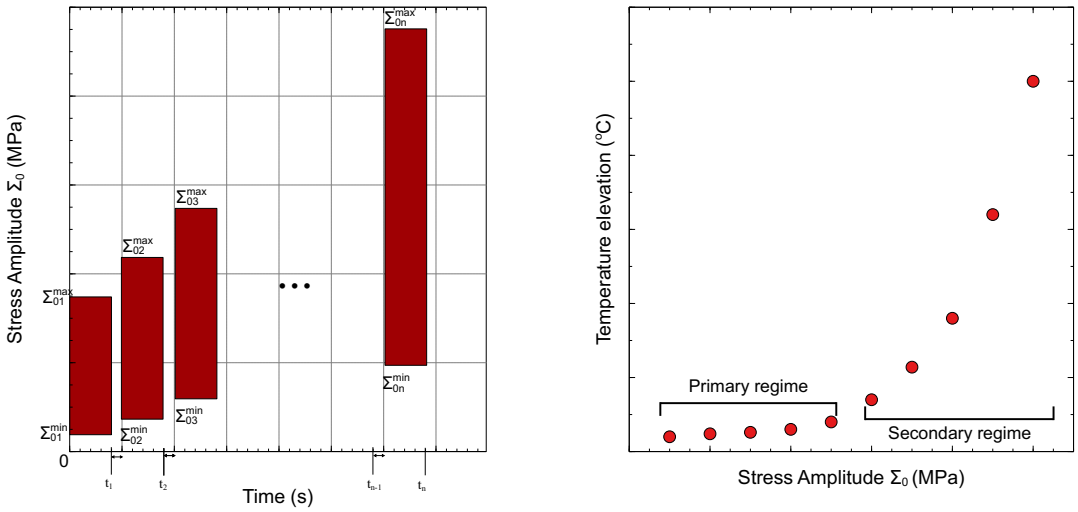

(a) (b)

Figure 5.2: (a): Successive series of cyclic loadings with increasing at the same ratio, the stress amplitudes Σ_0 used for self-heating tests. Between the cyclic blocks, a rest period r_n is made to cool down the specimens. (b): Evolution of the temperature elevation during several series of cyclic loadings.

$$R_\Sigma = \frac{\sigma_{min}}{\sigma_{max}} = 0{,}1, \tag{5.1}$$

with σ_{min} and σ_{max} respectively the minimum and the maximum stress for each block. Finally, for each printed configuration, the tests were performed 2 times, fitted by Munier's model [30] (detailed further) and compared between themselves and the literature.

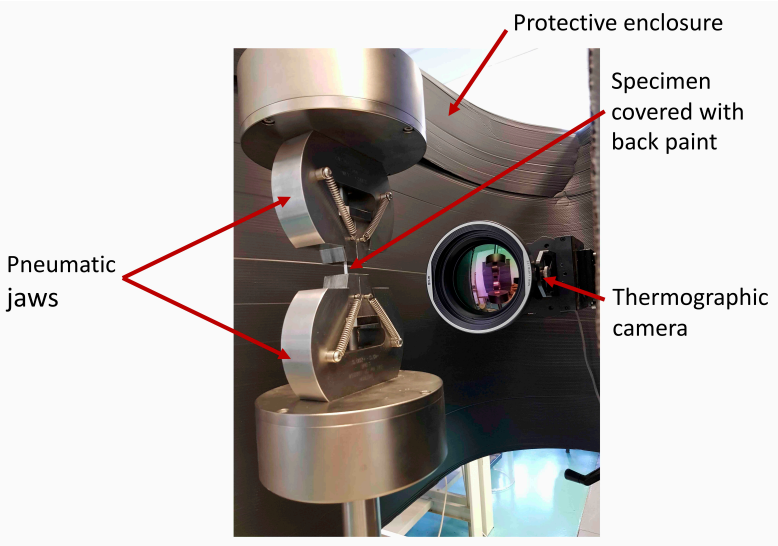

Figure 5.3: Experimental setup to measure the self-heating of the specimen during cyclic loadings.

5.3 Result and discussion

5.3.1 Microstructure

Let us mention again that to simplify the discussion only the following configurations will be reported in this section:$A_{\perp\,0,12}$, $B_{/\!/\,0,2}$, $R_{0,12}$, $R_{0,2}$.

Typical microstructures of specimens fully printed or repaired with a vertical increment of $0{,}2mm$ are presented in Figure 5.4 and 5.5, respectively. On these two EBSD data maps corresponding to the microstructure of the specimen $B_{/\!/\,0,2}$ and $R_{0,2}$, one can observe similarities in terms of morphological aspects. Indeed, a clear ziz-zag pattern of the grains showing the direction of deposition of the layers during the back and forth scanning is observable. A zoom on both microstructures is proposed on the same figures and it can be noticed that layers are mainly composed by large grains while there is the presence of smaller grains, which can be in clusters and are located between the printed layers. Next, the grains were sorted in two families with respect to their equivalent grain diameters, i.e. *small* and *large* grains. The threshold value between the two families of grains is $15\mu m$ which corresponds to the equivalent diameter of a disk matching by surface the biggest grain found in a cluster of *small* grains.
In the case of the specimens fully printed or repaired with a vertical increment of $0{,}12mm$ represented in Figure 5.7 and 5.8 respectively, one can note that for $A_{\perp\,0,12}$ and $R_{0,12}$, it is difficult to determine the deposited layers and their respective printing direction. Furthermore, it can be noticed that clusters of small grains are absent eventhough *small*

grains are still present.

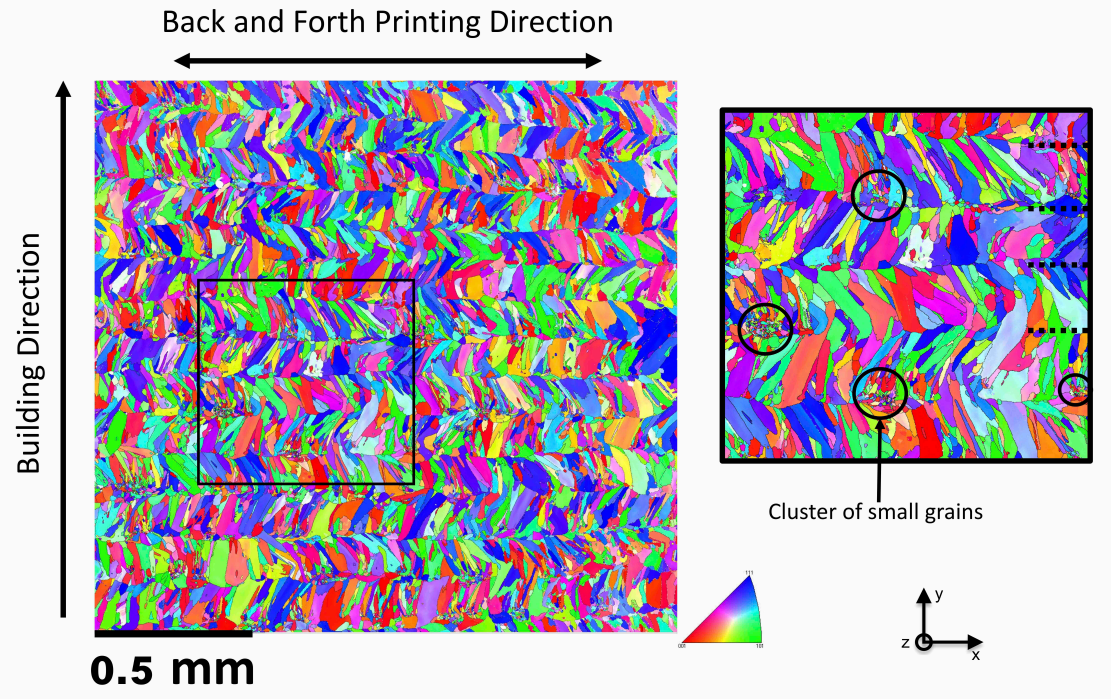

Figure 5.4: EBSD map (IPF X) of the specimen $B_{/\!/}$. A zoom is proposed to show the microstructure in detail and the presence of clusters of small grains between some layers.

Next, the aspect ratio of the grain is defined as the ratio of principal axes of the smallest circumscribed ellipse, implying that an aspect ratio of 1 indicates an equiaxed grain. The aspect ratio will be used to describe the shape of the grain. For all specimens, the distribution of the grain sizes and shapes are illustrated in Figure 5.6 by the probability density function (PDF) of the equivalent grain diameter and of the aspect ratio. In addition, all the shape and size data such as the equivalent diameter average, aspect ratio median etc. are available in table 5.1.

First, the analysis of the comparative plot of the equivalent grain diameter distributions is displayed in Figure 5.6(a) pointing out the influence of the vertical increment for the fully printed specimens. In this plot, the manufacturing with a $0{,}12mm$ and $0{,}2mm$ vertical increment are represented by $A_{\perp\,0{,}12}$ in blue and $B_{/\!/\,0{,}2}$ in red and the continuous, dashed and dotted lines, illustrate the data of the whole EBSD map, the *large* grains and the *small* grains respectively. One can see that the distribution of all the grains is more spread for $A_{\perp\,0{,}12}$ than for $B_{/\!/\,0{,}2}$ with an average equivalent grain diameter of $26{,}8\,\mu m \pm 20{,}8\,\mu m$ (median of $22\,\mu m$) and $14{,}7\,\mu m \pm 14\,\mu m$ (median of $9\mu m$), respectively. A focus on the two families of grains previously presented shows that for $A_{\perp\,0{,}12}$,

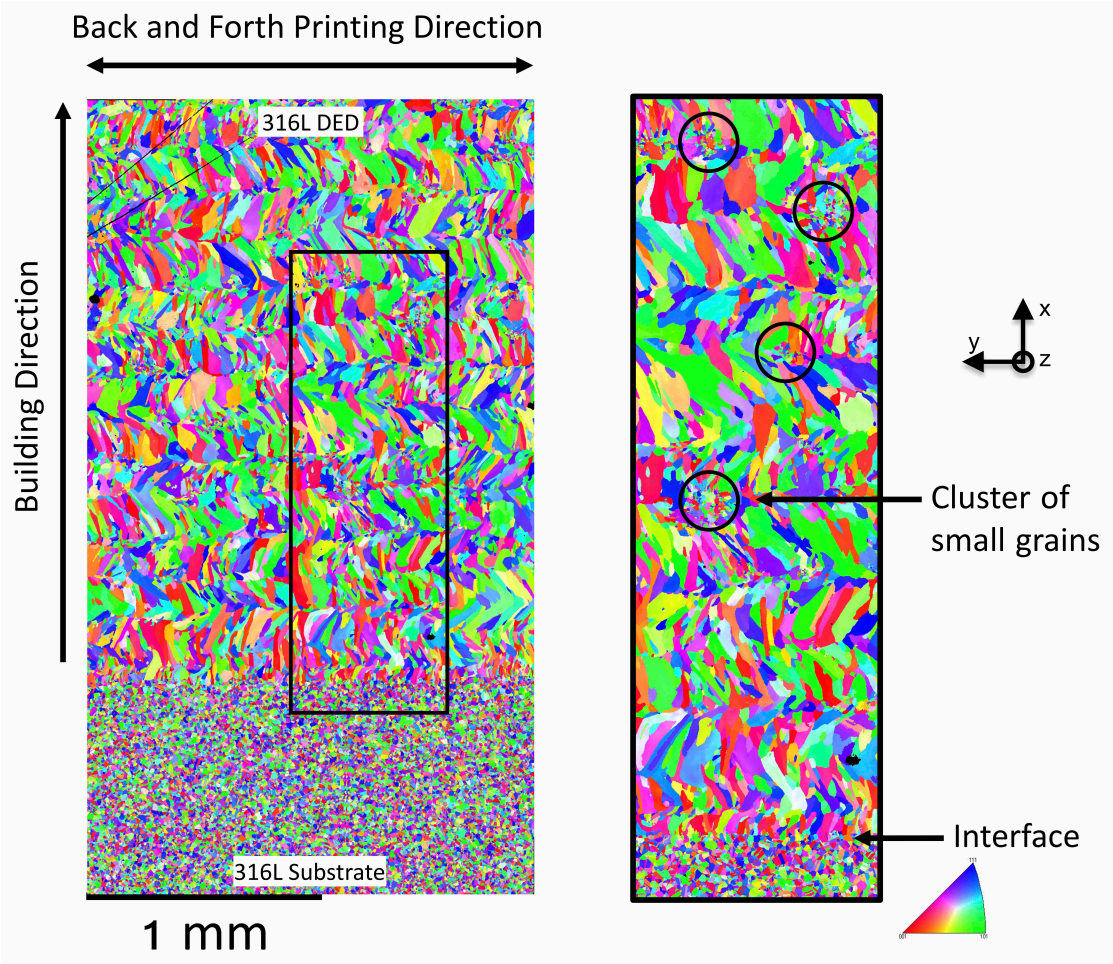

Figure 5.5: EBSD map (IPF X) of the specimen R_{02}. A zoom is proposed to show in details the zigzag pattern of the microstructure, the presence of cluster of small grains between some layers and the epitaxial growth from the substrate.

the distribution for *large* grains is more spread with a higher equivalent diameter of $35{,}2\,\mu m \pm 19{,}3\,\mu m$ and a spread expressed by a median of $29{,}9\,\mu m$ than for $B_{/\!/\,0,2}$ which has an equivalent diameter of $29{,}6\,\mu m \pm 15{,}3\,\mu m$ and a median value of $24{,}4\,\mu m$. The same scrutiny for the *small* grains shows similar distribution trends with a slight offset for their respective peaks. Same as for the *large* grains, the *small* ones show higher equivalent diameter of $8{,}9\,\mu m \pm 3{,}6\,\mu m$ (median of $9{,}9\,\mu m$) for $A_{\perp\,0,12}$ than for $B_{/\!/\,0,2}$ which has an equivalent diameter of $7{,}2\,\mu m \pm 3{,}4\,\mu m$ (median of $6{,}5\,\mu m$). Also one can note that for the specimens $A_{\perp\,0,12}$, the *small* grains represent 32,7% of the microstructure although occupying 10,5% of the surface while for the specimen $B_{/\!/\,0,2}$, they represent 65,6% of the microstructure despite occupying 31,4% of the surface. The same analysis

and trend concerning the equivalent grain diameter can be observed for the specimens $R_{0,12}$ and $R_{0,2}$ on figure 5.6(c).
Concerning the aspect ratio, one shall focus on the Figure 5.6(b) portraying the distribution for the fully printed specimens. For $B_{/\!/\,0,2}$ in blue, the aspect ratio curves present distinct PDF for the two families of grains where the *large* grains have a spread distribution with an aspect ratio average of $3{,}3 \pm 2$ (median of 2,8) whereas a narrow distribution for the *small* ones is present with an aspect ratio average of $2{,}4 \pm 1{,}4$ (median of 2). For $A_{\perp\,0,12}$ in red, the same trend but lessened is observable with an aspect ratio average of $2{,}4 \pm 1{,}2$ (median of 2,1) and $2{,}3 \pm 1{,}3$ (median of 2) for the *large* and *small* grains, respectively.

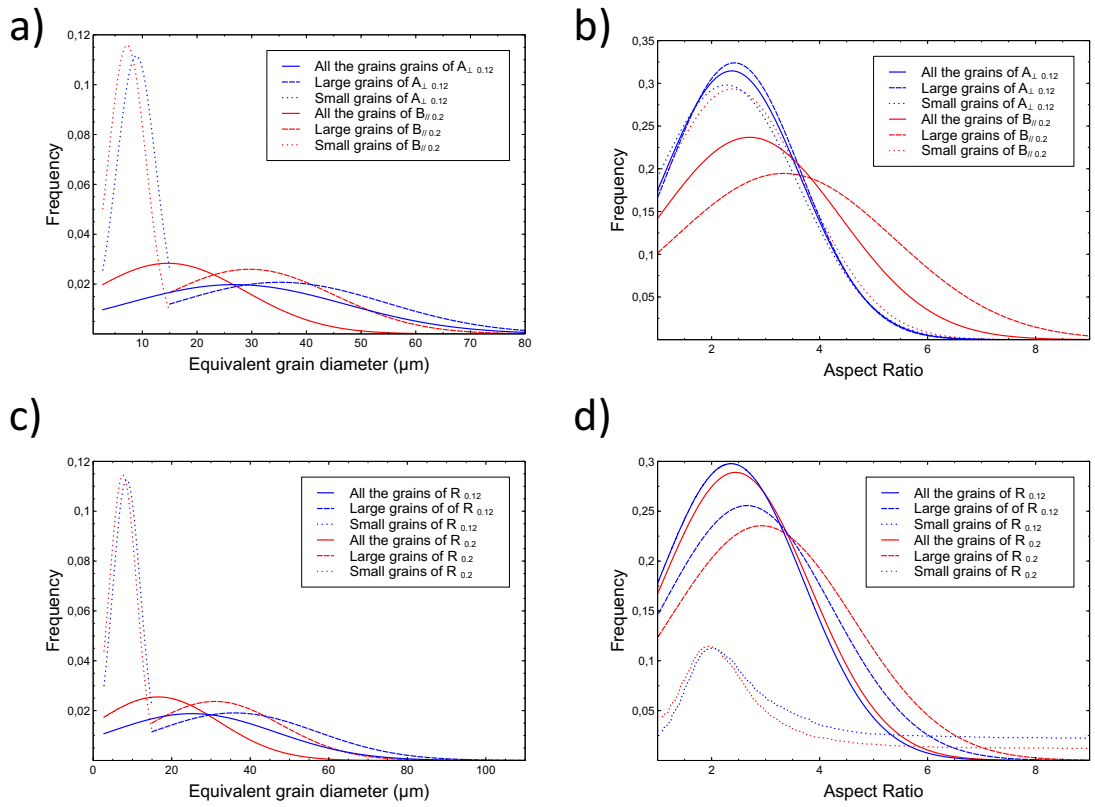

Figure 5.6: Probability density function of grain equivalent diameter, i.e. the diameter of a circle fitting the grain by its surface, for the fully printed and repaired specimens in (a) and (c) respectively. Probability density function of grain ellipticity, i.e. frequency in terms of ratio between the large and small axes of the ellipse fitting the grain by its surface and shape in (b) and (d) respectively.

The microstructural texture, in terms of both morphology and crystallographic orientations is determined by the local heat flow during solidification and cooling [17, 44, 224].

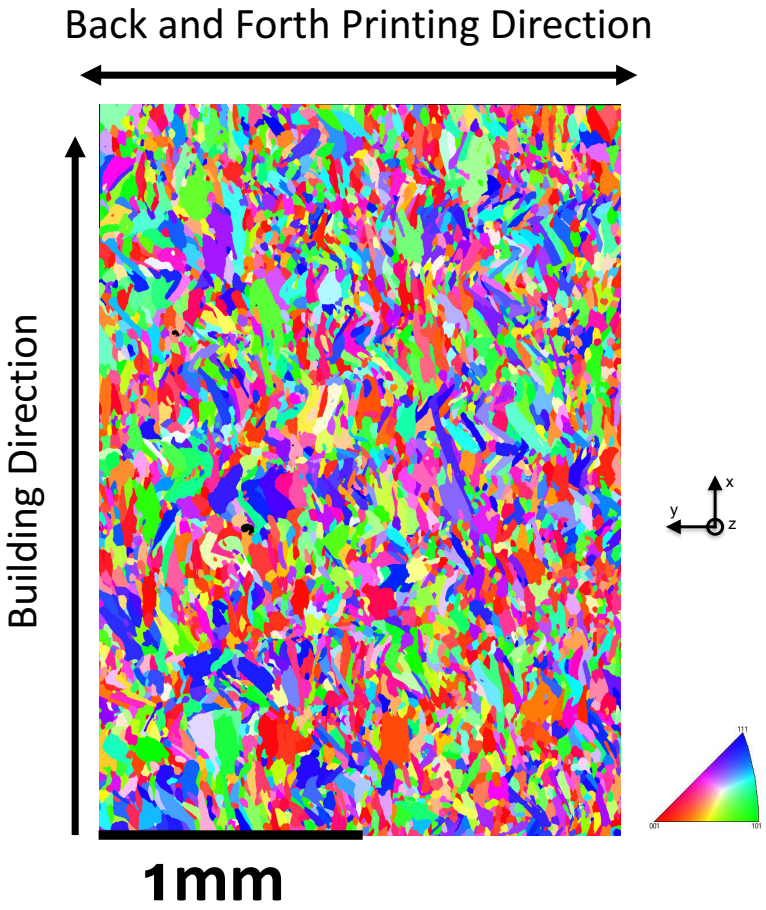

Figure 5.7: EBSD map (IPF X) of the specimen $A_{\perp 012}$.

The history will guide the preferred growth directions of the grains. The particular heat flow pattern depends on both the geometry and heat exchange coefficients as well as of a given set of printing parameters such as the power of the laser, the printing speed, the scanning pattern strategy and in our case the vertical spacing, which are driving the position of the heat source in the transient heat flow problem. Therefore for the $0{,}2mm$ specimens, the zig-zag pattern is inherited from the thermal flow due to the manufacturing conditions as it was also reported by [17]. Also, printing with the vertical increment of $0{,}12mm$ results in a different thermal history during the manufacturing

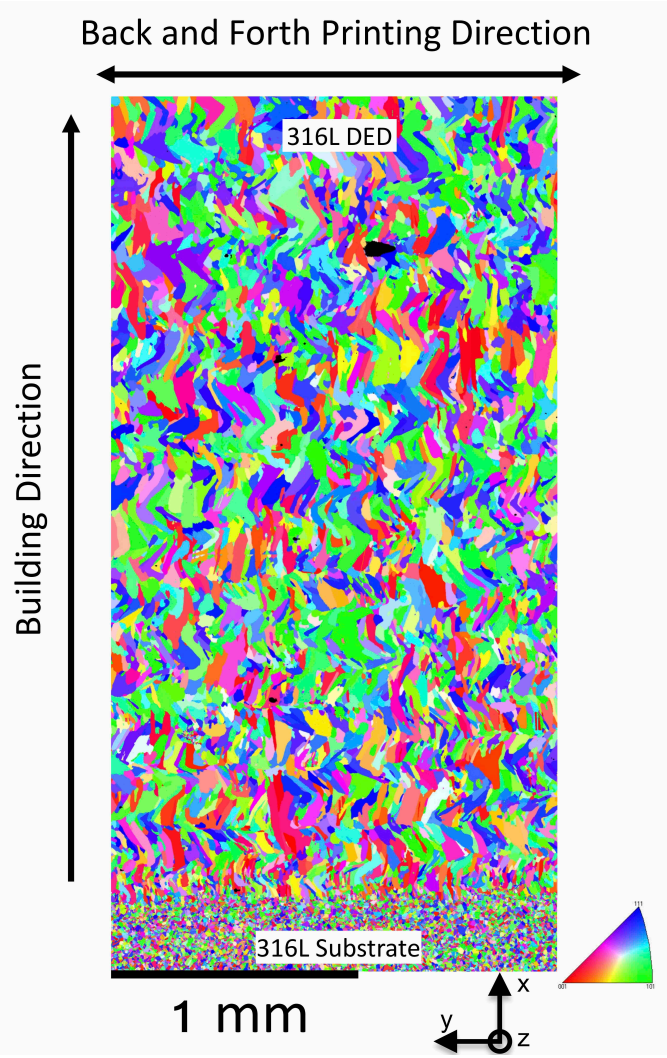

Figure 5.8: EBSD map (IPF X) of the specimen R_{012} showing an epitaxial growth, a zigzag pattern of microstructure less clear than for R_{012} and the almost absence of cluster of small grains at interfaces between layers

process impacting on the energy the grains were able to obtain from the laser (driving the size) and the cooling rate/direction (driving the shape and orientation). Therefore with more heat in the wall for the 0,12mm, grains will have more energy to grow and it explains the difference of size remarked as well as smaller quantity *small* grains.

Finally, one can conclude from the previous results that: (i) A zig-zag pattern is evident for the 0,2mm vertical increment in contrast to the specimen manufactured with a 0,12mm vertical increment, (ii) *large* grains are more columnar than the *small* ones

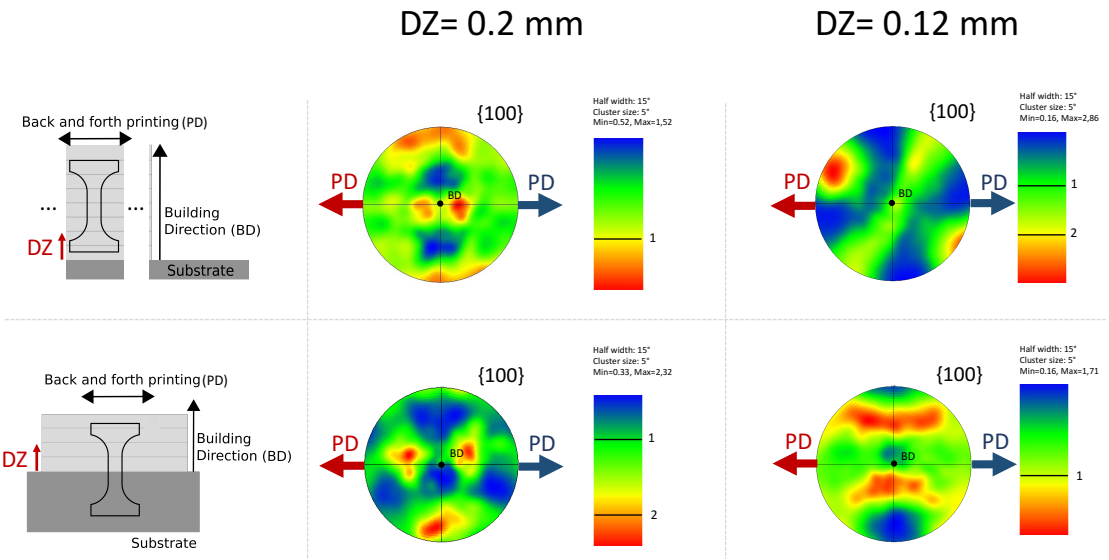

Figure 5.9: Pole figures of the crystallographic texture of the fully printed and repaired specimens in respect to their vertical increment.

which can be described as more equiaxis, (iii) the aspect ratio difference between *small* and *large* grains is more distinct for the 0.2 *mm* vertical spacing than for the 0.12 *mm* specimens due the different temperature gradient.

It is well known from solidification theory [225] that face-centered cubic (FCC) have a preferred growth in the <001> direction. This is a consequence of being an axis involving the least atoms resulting in the fastest growing direction during the solidification, and it was notably remarked for the additive manufacturing process in [226, 227]. Therefore the crystallographic texture was analyzed in Figure 5.9 by plotting the pole figure of the crystallographic family plane {100} for both types of tensile specimens (exclusively in the printed half for the repaired ones) with respect to their vertical increment. For the 0,2*mm* configuration, one can note that independently from the type of specimens (repaired or fully printed), a similar texture with two red hotspots from either side of the Building Direction (BD) axis is available. This texture is the sum of two fiber textures that can be associated to the layers printed from left-to-right and right-to-left for the right and left hotspot, respectively. The distance between the BD axis and each one of the two hotspots is equivalent to a tilt angle of $\approx \pm 30°$. In addition, the layers printed from left-to-right and the opposite have morphologic orientation corresponding to the tilt angle between the longest axis of ellipse defined earlier with respect to the BD axe. This morphologic angle is of $\approx \pm 30°$ and therefore, one can note that for this configuration, the morphologic and crystallographic orientation can be associated. Moreover, during solidification, the preferred crystallographic direction is closely aligned with the maximum heat flow [224]. The precise

direction of the heat flow was not measured during printing, but the observed crystallographic and morphologic textures gave a clear idea of the heat flow pattern in this case.

An analysis of the Figure 5.9 for the 0,12mm configurations shows that the preferred orientation is not the same as for the 0.2mm ones. Indeed, one can recognize in the case of the 0,12mm fully printed specimen, a fiber texture corresponding to a tilt half way toward the Normal Direction (ND) and Printing Direction (PD). For the 0,12mm vertical spacing, the printing nozzle had to do 5/3 more times the number of back-and-forth to manufacture the same wall resulting in differences of heat accumulation and flow direction in the wall. Knowing that crystallographic texture orientation is dependent of the heat flow direction, the previous fiber texture enable us to associate this orientation to a different direction of heat flow (compared to the 0,2mm) which is a consequence of the heat accumulation in the wall due to the manufacturing conditions and a poor absorption from the substrate. This tilt toward the surface of the wall in contact with the air can be understood as the fact that conduction by the layers and substrate is not anymore the main heat dissipation system, convection seems to be privileged.

Last but not least, in contrast to the 0,2mm configuration where the fully printed and repaired specimens have the same crystallographic texture, a different preferred orientation is observable for the 0,12mm repaired specimens. Indeed, one can see a texture corresponding to a tilt of the {100} from the Building Direction axis toward the Normal Direction axis and rotating around a vector aligned with the Normal Direction. This particular texture is thought to be influenced by the substrate's texture especially because it was found that the preferred orientation of the grains is evolving as the zone of study is further from the interface. The turning point corresponding to a certain distance from the interface for which the preferred orientation of $R_{0,12}$ becomes the one present in $A_{\perp\,0,12}$ is assumed to exist but was not found.

To sum up, changing the vertical spacing affects thermal phenomenon and therefore results in differences of crystallographic textures. More precisely, we found that for the fully printed and repaired specimens with a vertical spacing of 0,2mm, the texture is to be associated with the back-and-forth printing strategy and the ensuing heat flow pattern. Reducing the vertical spacing to manufacture the same wall accrues the heat in the wall and the heat absorption capacity of the substrate was not able to accommodate. Because of this poor absorption, for the fully printed specimens, the preferred orientation is toward the wall's surface in contact with the air. For the repaired specimens, the texture is thought to be mainly influenced by the substrate.

	$A_{\perp\,0,12}$			$B_{/\!/\,0,2}$			$R_{0,12}$			$R_{0,2}$		
	All grains	*small* grains	*large* grains	All grains	*small* grains	*large* grains	All grains	*small* grains	*large* grains	All grains	*small* grains	*large* grains
Diameter average (μm)	$26{,}6 \pm 20{,}2$	$8{,}9 \pm 3{,}6$	$35{,}2 \pm 19{,}3$	$14{,}7 \pm 14$	$7{,}2 \pm 3{,}4$	$29{,}6 \pm 15{,}3$	$25{,}2 \pm 21{,}2$	$8{,}5 \pm 3{,}5$	$36 \pm 20{,}9$	$16{,}5 \pm 15{,}6$	$7{,}6 \pm 3{,}5$	$31 \pm 16{,}8$
Diameter Median (μm)	22	96	29,9	9,8	6,5	24,4	19,3	8,4	29,5	11,2	7	25,5
Aspect ratio average	$2{,}4 \pm 1{,}3$	$2{,}3 \pm 1{,}3$	$2{,}4 \pm 1{,}2$	$2{,}7 \pm 1{,}7$	$2{,}4 \pm 2{,}4$	$3{,}3 \pm 2$	$2{,}4 \pm 1{,}3$	$2{,}3 \pm 1{,}3$	$2{,}7 \pm 1{,}6$	$2{,}4 \pm 1{,}4$	$2{,}1 \pm 1$	$2{,}9 \pm 1{,}7$
Aspect ratio Median	2	2	2,1	2,2	2	2,8	2	2	2,2	2	1,8	2,4
Quantity of grains (%)		32,7	67,3		65,6	34,4		39,3	60,7		62,2	37,8
Surface occupied (%)		10,5	89,5		31,4	68,6		13,3	86,7		28,7	71,3
Surface of study (mm^2)	$2{,}9 \times 2{,}1$			$1{,}9 \times 1{,}8$			$3{,}8 \times 2$			$2{,}2 \times 1{,}6$		

Table 5.1: Grains size statistics.

5.3.2 Tensile properties

First, for both vertical increment, 3 monotonic tests were performed for the repaired specimens and for the fully printed specimens in both orientation with respect to the printing direction, and their respective mechanical properties were determined. In order to provide a precise quantitative comparison of the tensile properties, we provide standard material parameters such as the yield stress (σ_y), ultimate tensile strength (UTS) and the ductility (D). To facilitate the analysis, the ratio, $r_{/\!//\perp}$ of each material parameters corresponding to the value obtained for the configurations parallel to the printing direction over the value measured for the perpendicular ones is compared to data extracted from literature [26, 6, 228]; they are all listed in table 5.2. One can remark that even if the ductility is almost similar for the specimen $A_{\perp\,0,2}$ and $B_{/\!/\,0,2}$ with a ratio of 0,98, higher ratio values of 1,14 and 1,15 are observable for the yield and ultimate strength respectively. Thus, an anisotropy is noticeable between the two specimens. For $A_{\perp\,0,12}$ and $B_{/\!/\,0,12}$, a less pronounced but similar trend can also be noticed for the yield and the ultimate strength, with ratio of 1,06 and 1,05 respectively. Previous publications on stainless steel employing DED as a manufacturing technology presented similar results regarding the mechanical behavior under uniaxial tensile test [6, 191, 192, 26, 228]. Higher σ_y and UTS for the specimens parallel to the Printing Direction were found as shown in table 5.2. However, in these cases, specimens tested perpendicularly to the Printed Direction had higher ductility while in this study, the ductility were found almost similar for both orientations. The difference of geometries can explain this difference but this aspect was not investigated. The particular elongated microstructure induced by this additive manufacturing process is at the origin of this particular anisotropy. Indeed, grains are columnar i.e. depending on the tensile orientation, dislocation are required to meet more or fewer boundaries resulting in a difference of properties [229]. Also, a less marked anisotropy observed for the smaller vertical increment is due to a less columnar microstructure than for the 0,2mm configuration as demonstrated earlier.

Technology	σ_y (MPa)			UTS (MPa)			D (%)		
Printing versus tensile direction	$\perp$	$/\!/$	$r_{/\!/}$	$\perp$	$/\!/$	$r_{/\!/}$	$\perp$	$/\!/$	$r_{/\!/}$
0,12mm configuration	445 ± 6.2	475±5.3	1.06	639 ± 8.4	667 ± 11.4	1.05	51 ± 3.2	50 ± 3.8	0.98
0,2mm configuration	420 ± 7.3	480 ±8.5	1.14	597 ± 6.7	688 ± 10.3	1.15	46 ± 3.1	47 ± 4.2	1.02
R_0,12 configuration	418 ± 9.2	/	/	638± 7.6	/	/	45± 4.3	/	/
R_0,2 configuration	414 ± 6.7	/	/	602± 9.8	/	/	41± 3.6	/	/
Substrate	360 ± 14.5	/	/	660 ± 8.7	/	/	85± 8.1	/	/
316L - LENS [26] from bulk	479	576	1.2	703	776	1.1	46	33	0.72
316L LMDS [6] from wall	352	558	1.6	536	639	1.19	46	21	0.46
304L DED [228] from bulk	440	552	1.3	670	730	1.09	70	51	0.73

Table 5.2: Mechanical properties of 316L from the present tests and from the literature [26, 6]. R is the ratio of the material parameters of the specimen $B_{/\!/}$ over the specimen $A_\perp$

Finally, one can remark that even though the trends are similar, the intrinsic values are spread as also summarized in [7]. The scattering of the mechanical properties

are directly due the different machines, specimen geometries, process parameters and material composition used as shown in [7, 193, 194] and is also illustrated in this work by the difference due to the vertical building increment.
The corresponding tensile engineering stress versus strain curve of all the specimens tested in this study are plotted in Figure 5.10. One can remark in this Figure that the tensile strength of the repaired specimens falls between those of the the substrate and $A_{\perp}$ ones for their respective vertical increment. In addition, the ductility is more limited than the two joined materials tested separately and these results were also shared by [201, 202]. An improvement of the properties by reducing the vertical increment is still present for the repaired specimens as exhibited for the fully specimens $A_{\perp 0,12}$. Finally, one can observe that all the repaired specimens fractured in the printed parted, far away from the interface, which indicates that the bonding zone is not a limiting weak zone during uniaxial static loadings.

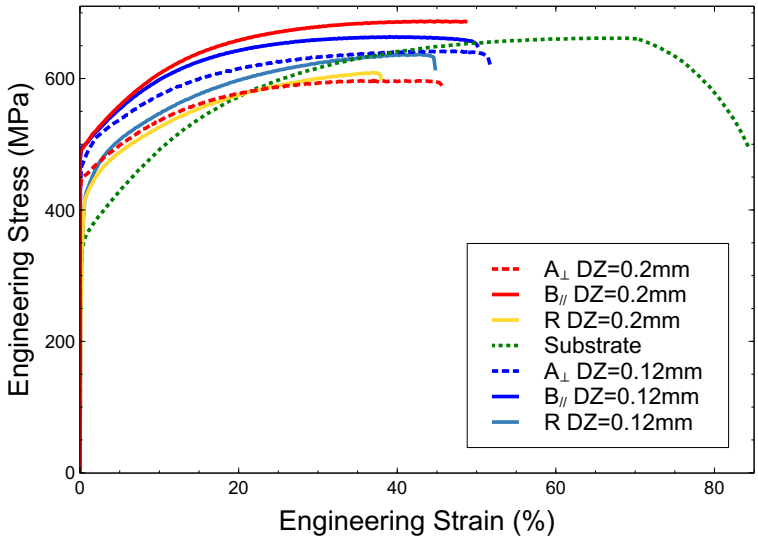

Figure 5.10: Tensile stress-strain curves of all the specimens.

5.3.3 Comparison of the self-heating curves

During self-heating test, two regimes of the temperature elevation with respect to the stress amplitude are observable. Indeed, beyond a certain stress amplitude, a greater slope due to more microscopic plasticity is noticeable. This steeper slope is denoted as the secondary regime while the first part of the curve as the primary regime. Usually, for the determination of the fatigue limit from self-heating tests, the mean endurance limit is determined by a linear regression of the three last points of the secondary regime

[230, 231, 232]. In fact, it has been shown that the intersection between this straight line and the stress amplitude axis is a good estimation of the mean endurance limit at 2 millions of cycles. The validity of this empirical knowledge was investigated in [30] for several steel grades with various microstructures and the comparison between the mean endurance limit obtained from self-heating curves and by using a standard stair-case showed an error lower than 2% for the majority of the tested specimens. The success of a self-heating experiment is directly associated to the capacity to measure the thermal dissipation due to the microscopic plasticity. Therefore, the bigger the volume of the specimen is, the more accurate the self-heating curves and the more reliable the 3 points rule will be. Hence, in this study, capturing without important scatter, the small temperature elevation was challenging because of to the small tested volume. Therefore, using the 3 points rules to determine the mean endurance is not reliable. Nevertheless, we used an analytical model fitting self-heating curves developed in [30] to bypass this limitation. The model is presented in equation 5.2 and is based on energy balance. The temperature elevation is equal to the sum of two terms related to the intensity of the primary and secondary regime, respectively.

$$\Omega = \alpha(\frac{\Sigma_0}{\Sigma_{max}})^2 + \delta(\frac{\Sigma_0}{\Sigma_{max}})^{m+2} \tag{5.2}$$

In this equation, the temperature elevation Ω, the maximal stress amplitude before failure Σ_{max} and the stress amplitude per block Σ_0 are known from experimental data and a linear fit was performed to determine the unknown coefficient α, δ and m. During the fitting process, boundaries conditions on α and δ were applied in order to have physical meaning i.e. they are respectively related to heat dissipation during the primary and secondary regime and should be positive or equal to 0. The fitting of the experimental data for all the configurations and their respective secondary regime tangent determining the mean endurance are plotted in Figure 5.11. The coefficients and mean endurance limits are listed in table 5.3. One can see in this table that the parameter α corresponding to the primary regime, is a null value for most of the configurations. However in [30], the values of α are higher and lie between 0.4 and 4.54. This difference is due to the fact that our specimens being very small, during the first blocks with low stress amplitude, the thermography camera could not be precise enough to capture the heat coming from the micro plastification. Nevertheless, from this model, we were able to plot an average self heating curve for all our specimens and plot the tangent of the secondary regime which intersects the stress amplitude axis at the mean endurance(Σ_∞). Vertical increment and orientation effect have identifiable trends concerning Σ_∞.

The ratio $r_{\Sigma_\infty \frac{0,12}{0,2}}$, corresponding to the ratio of mean endurance (Σ_∞) for specimen manufactured with a vertical increment of 0,12mm over 0,2mm, is first listed in the table 5.4. One can note that the 0,12mm specimens always exhibit higher fatigue limit with an improvement of 8%, 6% and 13% for the configuration $A_\perp$, $B_{/\!/}$ and R, respectively. The improvement was expected for $A_\perp$ and R since it was shown for monotonic tests, however it is also the case for $B_{/\!/}$. Finally, the repaired specimens showed the lowest mean endurance in comparison to the substrate limit with a decrease of 11% and 21%

for the 0,12mm and 0,2mm repaired configurations.

Specimens	α	δ	m	Σ_∞	$r_{\Sigma_\infty \frac{0,12}{0,2}}$
$A_{\perp 0,12}$	0	2.84	5.58	373	1.08
$A_{\perp 0,2}$	0.28	2.38	10.59	345	
$B_{/\!/ 0,12}$	0	2.87	3.86	339	1.06
$B_{/\!/ 0,2}$	0	2.94	3.58	319	
$R_{0,12}$	0	2.08	2.6	293	1.13
$R_{0,2}$	0	1.13	3.24	259	
Substrate	0.17	2.54	6.22	328	/

Table 5.3: Values of the fitting parameters from Munier's model [30] and other relative value such as the mean endurance Σ_∞, the ratio of the mean endurance on the yield strenght $\frac{\Sigma_\infty}{\sigma_y}$ and the ratio highlighting the effect of the vertical increment for a comparable configuration $r_{\Sigma_\infty \frac{0,12}{0,2}}$.

Let us denote by $r_{\Sigma_\infty \frac{\perp}{/\!/}}$ the ratio of the mean endurance limit of the specimens tested perpendicularly and parallely with respect to the printing direction. As detailed in table 5.4, one can notice that specimens fully printed and tested perpendicularly to the printing direction have a higher Σ_∞ than for specimens tested parallely to the printed direction. This anisotropy was also shared in [228] and [27] in the case of 304L manufactured by DED and WAAM respectively but also in [233] for 316L printed by SLM. We shall remind that during uniaxial static tensile tests for additively manufactured specimens, mechanical anisotropy is also present. In fact, the specimens tested perpendicularly to the Printing Direction (PD) exhibit lower σ_y and UTS than the specimen tested along the PD [26, 6]. Anisotropy is also present during cyclic tests but in this case, perpendicular configuration shows higher fatigue limits than parallel one [228, 27] i.e the orientation effects is being inverted for cyclic tests compared to the monotonic ones.
This favorable orientation in terms of $r_{\Sigma_\infty \frac{\perp}{/\!/}}$ was quantified at 10% for the 0,12mm configuration, 8% for the 0,2mm configuration and are in the same magnitude as the ones found in the literature.
The reason of this anisotropic behavior is explained in [234] as the consequence of the particular microstructure obtained by additive manufacturing. More exactly, the difference observed for the two orientations is associated to the presence of long grains oriented along the building direction inducing a crack growth with a tortuous path in the case of a test perpendicular to the printing direction. A more forward and less tortuous crack path with fatigue cracks predominantly growing along grain boundaries was noticed in the case of a specimen tested along the printing direction. Also in [235] in addition to the highly tortuous crack observed in the case of a perpendicular specimens, local mixed-mode fracture was also highlighted with the crack path often changing directions. Therefore, these explanations could be a key to understand the anisotropy that was highlighted during cyclic tests conducting a favorable perpendicular

Specimens	$r_{\Sigma_\infty \frac{\perp}{/\!/}}$
$A_{\perp\,0,12}$ $B_{/\!/\,0,12}$	1.1
$A_{\perp\,0,2}$ $B_{/\!/\,0,2}$	1.08
$\perp$ [228]	> 1
$/\!/$ [228]	
$\perp$ [27]	1.07
$/\!/$ [27]	
$\perp$ [233]	1.17
$/\!/$ [233]	

Table 5.4: Anisotropic behavior of our specimens highlighted by the ratio of the mean endurance of the specimens perpendicular to the printing direction on the specimens parallel $r_{\Sigma_\infty \frac{\perp}{/\!/}}$. These values are compared with SS304 specimens manufactured by DED and WAAM in [228] and [27] respectively but also with SS316L specimens manufactured by SLM in [233]

configuration.
However, during self-heating tests, the cyclic loadings are performed at lower stress than the yield strength and during a very limited number of cycles per block. Therefore mostly micro-plasticity phenomena are generated [30] rather than crack growth. Post mortem SEM images of specimens $A_\perp$ and $B_{/\!/}$ after the self-heating test are proposed in Figure 5.12(a) and (b) respectively. For these 2 images, the printed layers are vertical for $A_\perp$ and horizontal for $B_{/\!/}$ i.e. the loading direction is perpendicular and parallel to the printing direction for $A_\perp$and $B_{/\!/}$ respectively. One can notice in (a), the presence of multiple vertical cracks (b) the presence of only two large crack with one that led to the failure of the specimen. For both specimens, the cracks initiated for the highest stress amplitude i.e. at the end of the test. In addition, these two post mortem images were investigated under the scope of the distribution of the crack sites. Therefore, images were cropped to the white frame and binarized in order to have black pixels exclusively in the crack sites. One can observe the distribution of the black pixels for $A_\perp$ and $B_{/\!/}$ above their respective post mortem images in Figure 5.12(a) and (b). In addition, a gaussian filter was applied to smooth and clarify the trends. For the specimen $A_\perp$, one can notice the recurrence of the gaussian filter peaks to a distance corresponding to 2-4 layers. A very contrasted trend is noticeable for specimen $B_{/\!/}$. Indeed, except for the two large cracks, no peaks are observable. Therefore one can conclude a different crack growth/failure mechanisms for both specimens. Next a comparison with strain localisation during monotonic tensile test of these specimens is proposed in order to understand the two post mortem images. The complete procedure permitting to obtain high resolution strain full-fields overlapped on microstructure maps is available in [20]. In Figure 5.13, one can see that for specimen $A_\perp$, the strain localisation is

heterogeneous with localisation at some interlayers while for $B_{/\!/}$, the deformation is more homogeneously distributed. In addition in [20], it was observed that for $A_{\perp}$, cluster of small grains present at interlayers deform less and therefore explain why some interlayers are not localizing. Moreover, it was observed that the strain localisation is the same at low or high macroscopic deformation, only the magnitude of strain evolves. For specimen $B_{/\!/}$, the authors found that the strain localisation was located in particular large grains. Finally by taking into account the microplasticity observations during monotonic tensile test, the self-heating behavior and the final microcracks observations, it suggests that the microdamage mechanisms are different for the specimens $A_{\perp}$ and $B_{/\!/}$. One can propose the following scenario: a tensile load perpendicular to the printing direction, specimen $A_{\perp}$, will initiate a large number of extended dissipation zones located at intense plastic sites i.e. interlayers. Afterwards, these zones of high strain localization will generate a network of microcracks. Additionally, a crack shielding mechanism as proposed in [236] could also account for the network of cracks observed for $A_{\perp}$. In contrat, for specimen $B_{/\!/}$, a more classical fatigue scenario happens. The plasticity is distributed over a small number of grains due to their orientations regarding the loading. One of the grain will fail generating localized plasticity. Afterwards, a large crack will initiate from this grain and will conduct later the specimen failure.
Therefore, extended dissipation zones at the interlayers for $A_{\perp}$ and a localized dissipation for $B_{/\!/}$ can explain why the transition between the primary regime and secondary regime happens at a higher stress amplitude for $A_{\perp}$.

Complementary investigations with a study of the strain localisation for the $A_{\perp}$ during self-heating is under progress in order to understand: (i) when the crack sites initiate with respect to the stress amplitude, (ii) a finer explanation of the mechanisms arresting the cracks growth.

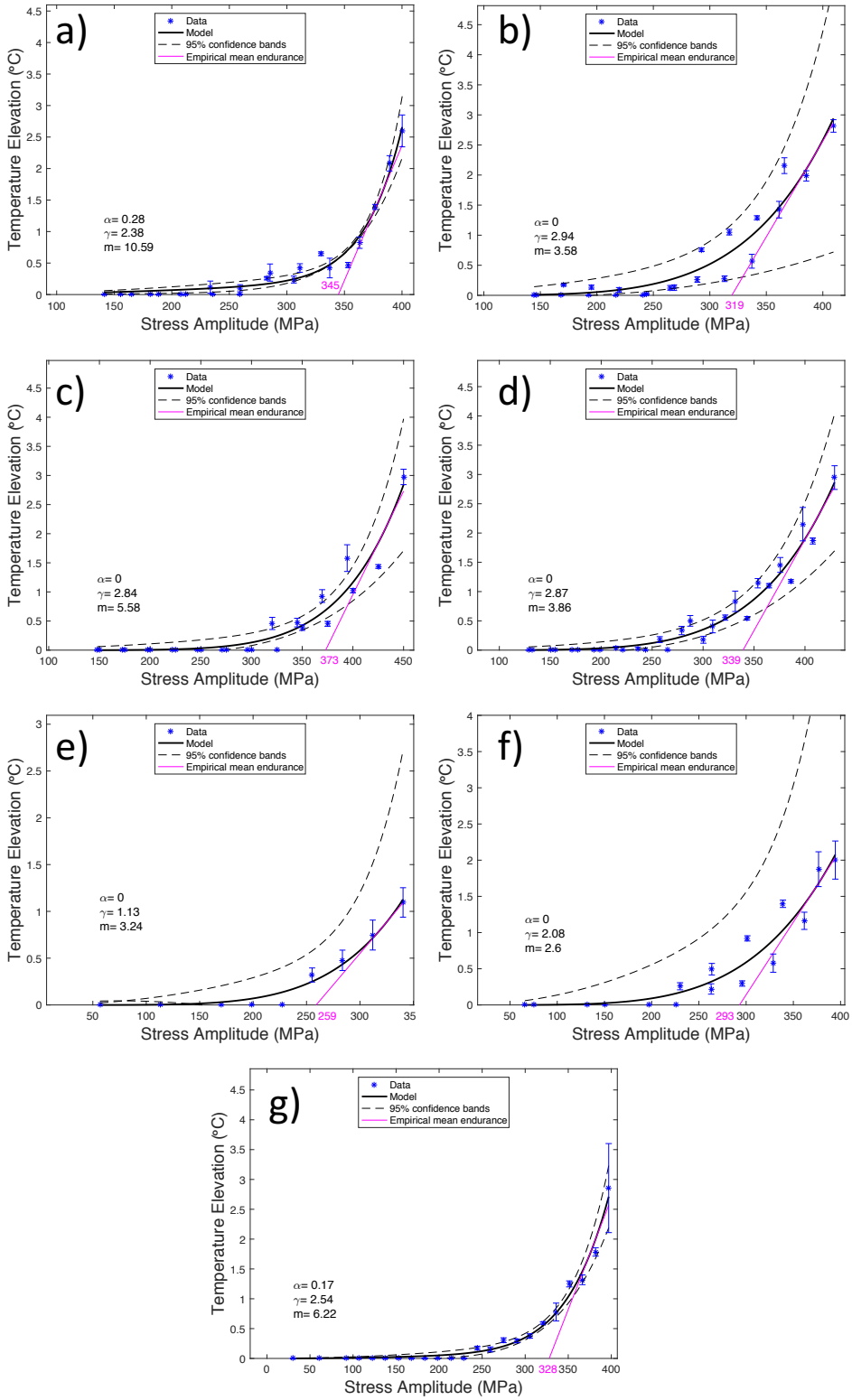

Figure 5.11: Evolution of the temperature elevation of the specimen associated with a level of stress amplitude for specimens $A_{\perp\,0,2}$, $B_{/\!/\,0,2}$, $A_{\perp\,0,12}$, $B_{/\!/\,0,12}$, $R_{0,2}$, $R_{0,12}$ and the substrate in (a), (b), (c), (d), (e), (f) and (g) respectively. A self-heating model proposed in [30] is fitted on the experimental data and used to determine the mean endurance limit (pink).

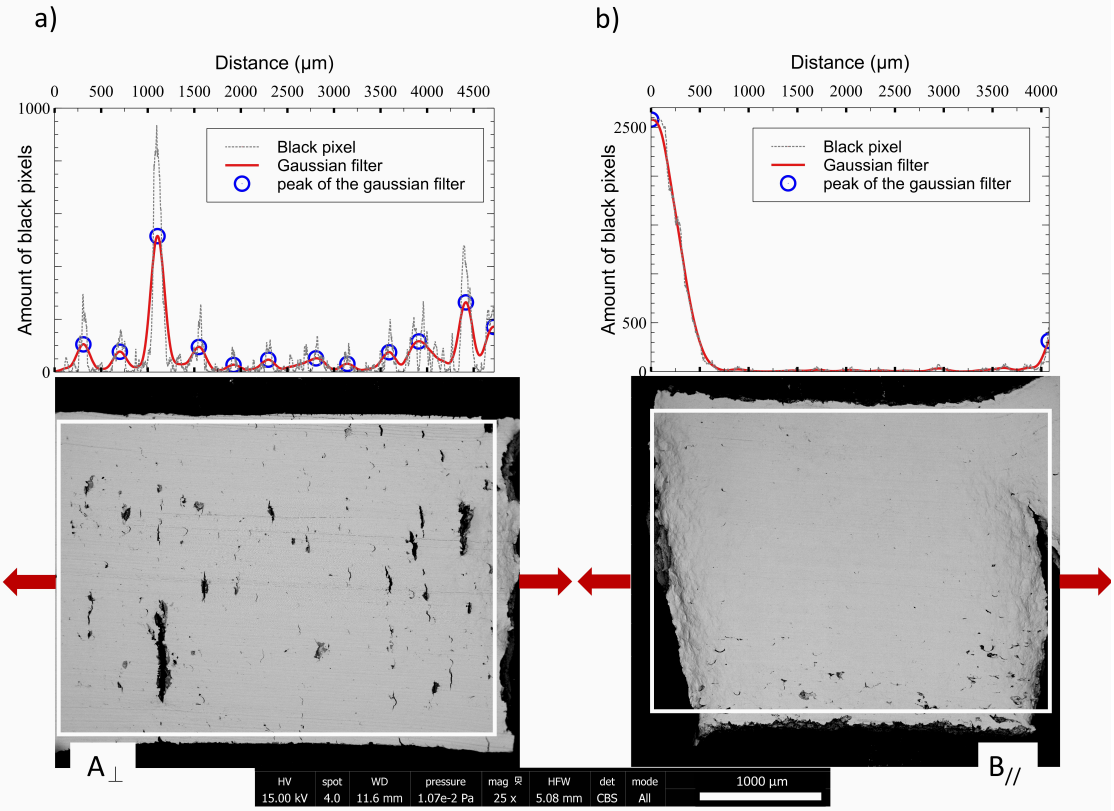

Figure 5.12: Post mortem SEM images after self-heating test for specimens $A_{\perp}$ and $B_{/\!/}$ in (a) and (b) respectively. The lower images represent the raw SEM observation and one can remark two distinct patterns of the onset of crack initiation sites. The tensile loading is direction of the red arrows. The upper images represent the sum of black pixels on each vertical line of the SEM image. The maximal values obtained after MovingAverage filtering and a detection of the local maxima exhibit the location of the cracks.

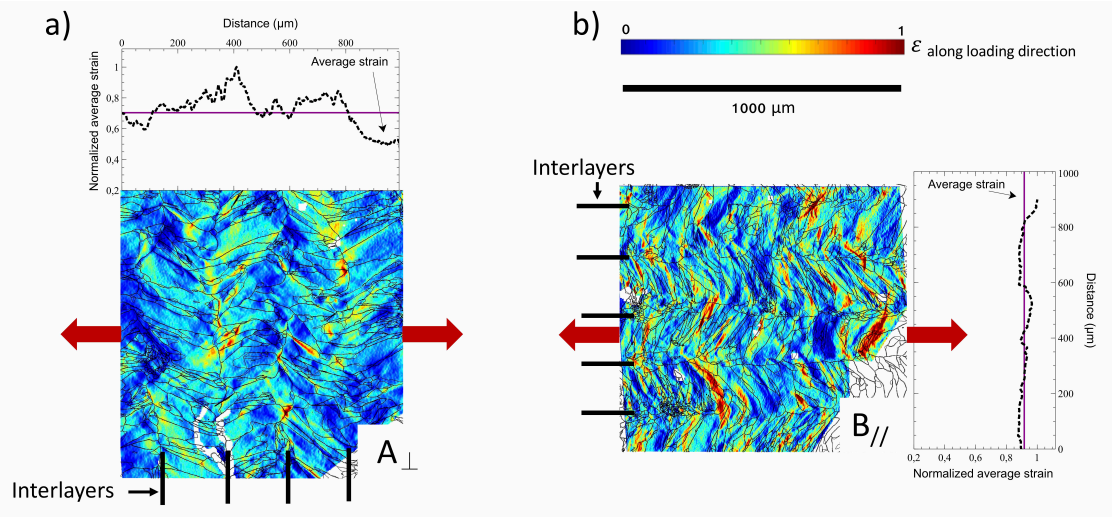

Figure 5.13: Strain localisation along the loading direction, indicated by the red arrows, for specimens $A_{\perp}$ and $B_{/\!/}$ in (a) and (b) respectively. The strain is heterogeneously distributed for $A_{\perp}$ and localized at some interlayers. For $B_{/\!/}$, the strain is more homogeneously distributed. The complete experiment and results is available in chapter 3

5.4 Conclusion

In this study, we investigated the self-heating behavior during cyclic loadings of 316L stainless steel specimens manufactured or repaired by DED. Specimens were extracted from bidirectionally-printed single-track thickness walls in different orientations and configurations and then compared.
Firstly, we investigated the microstructure of the different configurations through morphologic and crystallographical textures. We noticed that changing the vertical increment from $0.2mm$ to $0.12mm$ had a strong effect on the microstructure. For the morphological texture, we remarked that a zig-zag pattern is more evident for the $0.2mm$ vertical increment than for the $0{,}12mm$. We also found that the *large* grains are more columnar than the *small* ones. Finally we noticed that the aspect ratio difference between *small* and *large* grains is more distinct for the $0{,}2mm$ vertical spacing than for the $0{,}12mm$. Concerning the crystallographic texture, we noted that changing the vertical increment affects the preferred grains orientation. More precisely, we found that for the fully printed and repaired specimens with a vertical spacing of $0{,}2mm$, the texture could be associated with the back-and-forth printing strategy. For the $0{,}12mm$ vertical increment, we found a different texture for the repaired and fully printed specimens. This difference is due to the substrate influence and heat accumulation after a certain height in the wall. Secondly, we investigated the mechanical properties during monotonic tensile tests and anisotropy was detected for the fully printed specimens. The specimens $B_{/\!/}$ exhibited higher mechanical properties in terms of yield strength (YS) and ultimate tensile strength (UTS) than specimen $A_{\perp}$. We also found that the tensile strength of the repaired specimens falls between those of the the substrate and $A_{\perp}$ ones. The self-heating tests showed that the $0{,}12mm$ specimens always exhibit higher fatigue limits with an improvement of 8%, 6% and 13% for the configurations $A_{\perp}$, $B_{/\!/}$ and R, respectively. In addition, repaired specimens had a $\approx 11-21\%$ lower mean endurance limit when compared with the substrate manufactured by standard procedure. Finally, anisotropy was highlighted during these cyclic tests: specimens tested perpendicularly to the Printing Direction (PD) showed higher fatigue limits ($\approx 8-10\%$) in comparison to the ones tested along the printing direction. Post mortem analysis revealed a multitude of cracks at interlayers for the specimens tested perpendicularly to the PD creating several sites of heat diffusion. For the specimens tested along the PD, a more classical fatigue scenario was observed with one dominating crack and thus a localized heat dissipation. This difference explains why the transition between the primary regime and secondary regime of self-heating curves happen at a higher stress amplitude for the specimen tested perpendicularly to the PD.

Conclusion and perspectives

This thesis was dedicated to the study of 316L stainless steel additively manufactured or repaired specimens by Directed Energy Deposition (DED). The different configurations were manufactured using a *BeAM mobile* machine under optimal process parameters. The novelty of this work is the observation of the microstructural strain localization un such specimens. These experiments combined in situ tensile tests inside a Scanning Electron Microscope (SEM) with High Resolution Digital Image Correlation (HR-DIC) and an Electron Backscatter Diffraction (EBSD) map. Their results allowed for a fresh interpretation of monotonic tensile tests as well as of self-heating experiments under cyclic loading and the failure patterns observed at the surface of specimens.
The core of this work can be split into 4 complementary studies: (1) the microstructure and the effect of the process parameters for the fully printed and repaired specimens, (2) the microstructural strain localization with respect to the loading direction for fully printed specimens, (3) the deformation mechanisms at the interface of a repaired specimen under tensile loading and (4) the self-heating behavior under cyclic loading to study the fatigue properties and the lifetime predictions for both configurations of specimens.

(1) Microstructure and process parameters:
The first objective was to assess the microstructural properties of fully printed and repaired specimens fabricated using back and forth printing strategy and a vertical increment of either $0{,}12\,mm$ or $0{,}2\,mm$. Their microstructures at the scale of the grain presented the following features:

- For the $0{,}2\,mm$ configuration: a herringbone pattern can be observed. The morphologic and crystallographic textures are aligned and can be associated with the heat flow pattern induced by the bidirectional printing strategy for the fully printed specimen. Similar results can be found in the printed half of the repaired specimen.
- For the $0{,}12\,mm$ configuration: the herringbone pattern is less evident and the crystallographic texture consists of grains with a preferred orientation toward the surfaces of the wall in contact with air. It is a consequence of the heat accumulated in the wall and consequently a heat flow direction dominated by convective phenomena. A different crystallographic texture was found in the printed half of the repaired specimen which is believed to be influenced by the texture of the substrate.
- For both vertical increments: the grain morphology is characterized by *small* equiaxed grains present as isolated or in clusters at the interface between printed layers and *large* columnar grains within the layer. However, there are less *small*

grains for the 0,12 mm configuration. Similar results can be observed in the printed half of the repaired specimens.

(2) Microstructural strain localization:
The second objective was to understand the deformation mechanisms at the grain scale which could explain the observed macroscopic anisotropy of the tensile properties as reported in literature. Two loading directions, along and orthogonal, were considered with respect to the printing direction for fully printed specimens. The conclusions of the microscale analysis are the following:

- Specimens tested along the printing direction ($B_{/\!/}$) exhibited higher mechanical properties in terms of yield strength (YS) and ultimate tensile strength (UTS) compared to the specimen tested orthogonally to the printing direction ($A_{\perp}$). The observed anisotropy is consistent with the literature.

- For a tensile load perpendicular to the printing direction, *small* grains deform less than *large* grains. Moreover, strain localization is mainly situated at the interlayers in the absence of *small* grains.

- For a tensile load along the printing direction, the strain localization was observed in some particular *large* grains.

(3) Deformation mechanisms at the interface of a repaired specimen:
The third objective was the assessment of DED as a repair technology. We showed that the technology not only permits the filling of grooves which is the traditional application, but also the direct addition of material on a preexisting thin wall. The repaired specimens exhibited an important hierarchical microstructural gradient. We investigated the distribution of the strain at the interface between the damaged part and the added material. The conclusions are the following:

- The tensile strength of the repaired specimens falls between those of the substrate and fully printed specimens.

- The interface is not a weak area during a monotonic tensile test.

- While homogeneous strain was observed in the substrate half, the printed half showed a strain heterogeneity, with the highest localization found at some interlayers.

- A zone of low deformation was observed at both sides of the interface and was associated with higher hardness.

(4) Self-heating behavior under cyclic loading:
The fourth objective was to evaluate the fatigue properties by self-heating tests. The experiment has proven that the difficulties due to the small dimensions of the single-track thickness specimens can be overcome by careful construction of the experimental set-up.

We were not able to track the dissipative mechanism at the scale of the grain, however the results revealed certain correlation between the pattern of the microstructure, the deformation pattern at this scale and the self-heating results. The main conclusions are:

- The self-heating tests showed that the $0{,}12mm$ specimens always exhibit a higher fatigue limit with an improvement of 8%, 6% and 13% for the configuration $A_{\perp}$, $B_{/\!/}$ and the repaired specimens respectively. Repaired specimens had a $\approx 11-21\%$ lower mean endurance limit when compared with the substrate manufactured by standard procedures.

- Anisotropy was highlighted during these cyclic tests where specimens tested perpendicularly to the printing direction showed higher fatigue limits ($\approx 8-10\%$) in comparison to the ones tested along the printing direction. A similar favorable orientation of the specimen was shared in literature.

- Post mortem analysis revealed a multitude of cracks at interlayers for the specimens tested perpendicularly to the printing direction creating several sites of heat diffusion. For the specimens tested along the printing direction, a more classical fatigue scenario was observed with one dominating crack and thus a localized heat dissipation.

The advancements established in this work open up a series of natural extensions that could improve the accuracy of the work done in this thesis. A first series of extensions concern the analysis of the microstructure. A detailed investigation of the origin of the clusters of *small* grains should be performed as a different mechanical behavior was highlighted when compared with the rest of the microstructure. For the specimens tested along the printing direction, the HR-DIC associated with the microstructure map revealed that the strain was localized in some particular *large* grains. A detailed morphologic and crystallographic analysis of these regions should be performed. Eventually, FEM computation in the regions with these *large* grains could bring additional arguments and enable the prediction of failure in case of a monotonic or cyclic loading.
A second series of supplements can be done around the question of process parameters and the effect of post-manufacturing treatments. In particular, the effect of the latter on the metallurgical bonding between the damaged part and the added material should be examined.
The third series of perspectives are the natural extensions dealing with the fatigue. The results obtained by self-heating tests should be compared to the fatigue limits obtained by classical testing method. Additionally, the relation between the self-heating and the deformation localization under small strain cyclic loadings should be established. The validation of this fast method to determine the fatigue properties would permit to tremendously facilitate the analysis of process parameters and post-manufacturing treatment on the final fatigue properties.

Resumé de thèse en français

Introduction

Cette thèse est consacrée à l'étude de pièces métalliques fabriquées ou réparées par la technologie de fabrication additive **Directed Energy Deposition** (DED). Ce projet de recherche a été co-financé par la Direction Générale de l'Armement (DGA) et la Société Nationale des Chemins de Fer français (SNCF).
L'objectif est d'étudier l'effet des paramètres du procédé DED sur les propriétés mécaniques des pièces fabriquées ou réparées tout en associant ces dernières avec leurs microstructures respectives. La compréhension des différents phénomènes en jeu nécessite une étude à différentes échelles, allant des paramètres du procédé, jusqu'aux champs de déformation locaux sous sollicitation. Le matériau d'étude est un acier inoxydable 316L qui est utilisé pour la fabrication de différentes structures ayant toutes une épaisseur d'un seul cordon. La nouveauté de cette étude réside dans l'observation de la localisation des déformations à l'échelle de la microstructure. Pour ce faire, un test de traction in situ dans un microscope électronique à balayage (MEB) est effectué, puis associé avec de la corrélation d'image numérique à haute résolution (HR-DIC) et une carte de la microstructure obtenue par diffraction des électrons rétrodiffusés (EBSD). Les résultats permettent de donner une nouvelle interprétation des essais de traction monotones, ainsi qu'une compréhension des schémas de fissuration observés à la surface des éprouvettes lors d'essais d'auto-échauffement sous chargement cyclique. Le résumé est organisé en quatre parties qui correspondent aux éléments suivants: (1) présentation de la technologie DED, (2) analyse de l'influence de la direction du chargement à l'échelle de la microstructure, (3) étude des mécanismes de déformation à l'interface entre la pièce endommagée et le matériau ajouté, (4) étude du comportement d'auto-échauffement sous chargements cycliques des éprouvettes réparées ou fabriquées par DED.

La technologie Directed Energy Deposition

La fabrication additive (FA) se définit comme un procédé pour lequel la fabrication d'une pièce s'effectue par ajout de matière couche après couche à partir d'un modèle numérique. Cette technique de fabrication unique permet de créer des pièces complexes sans avoir recours à des outils coûteux tels que des moules de fonderie ou un usinage sophistiqué. Au cours des dernières décennies, la fabrication additive est passée d'une technique de prototypage rapide [32] à un processus de fabrication de pièces entièrement fonctionnelles constituées d'une large gamme de polymères et de matériaux métalliques [34]. Dans le cas de ces dernières, en raison des faibles taux de production et du coût élevé par pièce, la FA est pour le moment une technologie complémentaire aux procédés classiques et est principalement employée dans les secteurs de l'aérospatial et du médical.
Deux technologies de FA ont fait l'objet d'une attention particulière au cours de ces dernières années: (i) la fusion sur lit de poudre et (ii) la fusion de poudre projetée (= Directed Energy Deposition, DED).
La technologie DED, utilisée dans cette thèse, est un processus de fabrication durant lequel le matériau (poudre ou fil) est directement transporté dans une source de chaleur focalisée qui est générée par un laser. En mettant en mouvement la tête d'impression, le bain de fusion se déplace et par conséquent un cordon est fabriqué. La machine utilisée dans cette étude est le modèle *mobile* du fabricant français BeAM (Figure 5.14). La tête d'impression peut se déplacer selon les axes X,Y et Z, quant au substrat fixé sur le berceau, deux rotations selon X et Z sont possibles. En plus de la fabrication, ces degrés de libertés permettent la réparation de pièces métalliques complexes en ajoutant directement du matériau dans les zones d'intérêt.

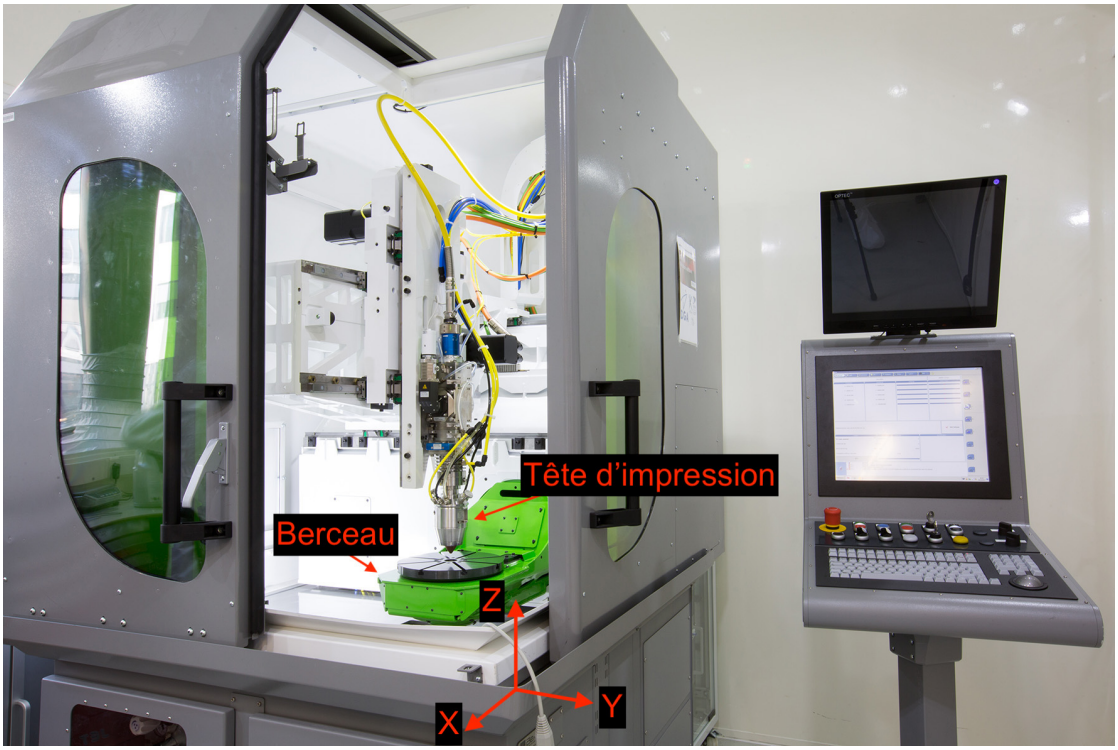

Figure 5.14: Photo de la machine *mobile* de chez **BeAM** au *Laboratoire de Mécanique des Solides* de l'École Polytechnique.

Éprouvettes imprimées

Il est bien connu que pour la FA, les paramètres du procédé déterminent la microstructure et donc les propriétés mécaniques générales du matériau et de la structure. Dans [1], il a été noté que la densité d'énergie du laser a une forte influence sur la taille des grains et sur la densité de la pièce, affectant ainsi les propriétés mécaniques. Les paramètres du procédé, la microstructure obtenue et le comportement mécanique sont mis en relation dans [2]. Les résultats ont montré que les meilleures propriétés mécaniques i.e. la résistance à la traction, ainsi que les meilleures performances tribologiques ont été obtenues pour des éprouvettes en acier inoxydable 316L produites par Selective Laser Melting (SLM) en comparaison de celles issues de procédés conventionnels tel que le pressage à chaud ou la fonderie. Ces meilleures propriétés ont été expliquées en partie par la présence une microstructure plus fine obtenue pour le SLM.
Pour la FA, la stratégie de fabrication conduit généralement à la formation de microstructures orientées avec des grains allongés [17]. Des propriétés macroscopiques anisotropes sont souvent rapportées comme par exemple dans [6] et [4]. Dans [7], le comportement en traction d'éprouvettes en acier inoxydable 316L fabriquées par FA issu des résultats de plusieurs groupes de recherche sont présentés et un effet clair de la direction de chargement est mis en lumière. En effet, les auteurs ont montré que la limite élastique et la résistance à la rupture sont supérieures pour les éprouvettes testées parallèlement au sens d'impression ($B_{//}$, Figure 5.15), tandis que l'allongement maximum est plus grand pour les éprouvettes testées perpendiculairement à la direction d'impression ($A_{\perp}$, Figure 5.15). Le but de cette partie est de comprendre l'origine de l'anisotropie observée. Des éprouvettes plates ont été extraites d'un mur mono-cordon imprimé selon deux directions comme schématisée dans la Figure 5.15. L'analyse de la microstructure de ces éprouvettes présentée dans la Figure 5.16 révèle des grains allongés dans les couches et la présence d'ilots de plus petits grains equiaxes aux intercouches. Le même comportement anisotrope mis en lumière dans la littérature lors d'essai de traction a été observé dans nos essais. Les essais de traction in situ dans un MEB ont été réalisés et la HR-DIC associée à la microstructure des éprouvettes a permis de calculer la déformation moyenne par grain et enfin de mettre en évidence les différents mécanismes de déformation expliquant l'anisotropie observée. Comme le montre la Figure 5.17(a), dans le cas de l'éprouvettes $A_{\perp}$, la localisation des contraintes se situe au niveau de certaines intercouches alors que pour $B_{//}$, la déformation est plus homogène et se trouve notamment dans certains gros grains comme le montre la Figure 5.17(b).
Pour cette microstructure architecturée bien particulière, on observe donc deux différent mécanismes de déformation en fonction de la direction de sollicitation

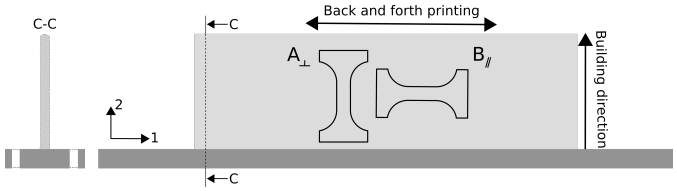

Figure 5.15: Schéma des éprouvettes $A_{\perp}$ et $B_{//}$ extraites de murs mono-cordon.

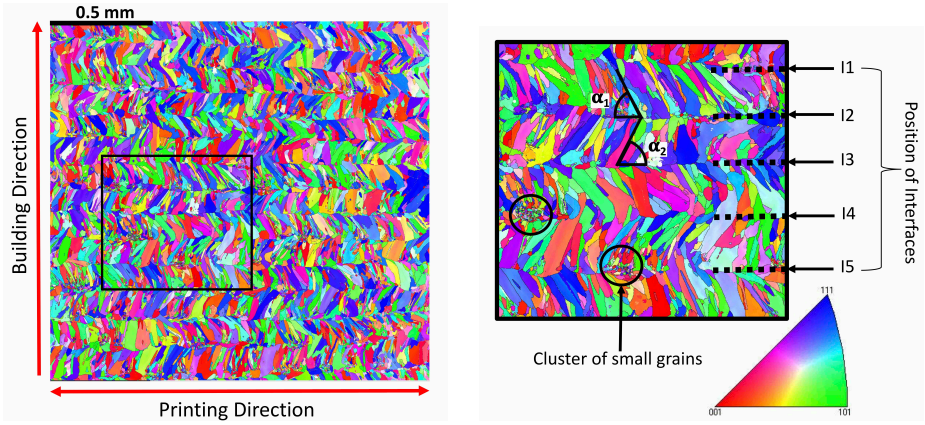

(a) (b)

Figure 5.16: (a): EBSD de l'éprouvette $B_{//}$. (b): Zoom sur l'EBSD montrant en détail la microstructure et la présence d'ilots de petits grains au niveaux des intercouches.

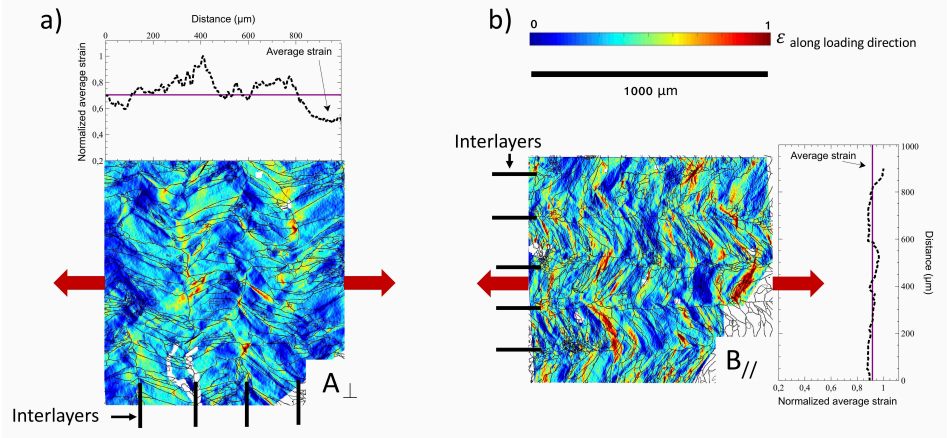

Figure 5.17: Déformation microstructurale locale alignée avec la direction de sollicitation (flèche rouge) pour les éprouvettes $A_{\perp}$ et $B_{//}$ en (a) et (b) respectivement.

Éprouvettes réparées

Dans cette partie, la capacité de la technologie DED à réparer des composants est présentée en étudiant l'interface entre la pièce endommagée et le matériau ajouté. Les procédés de réparations traditionnels tels que le soudage à l'arc [8], la projection thermique/au plasma [10, 9, 11] et la projection à froid [12] ont été étudiés au cours des dernières décennies. Cependant, ces technologies de réparations présentent des limitations sévères liées à leurs particularités qui ont empêché leurs déploiements à grande échelle. De manière non exhaustive, on peut citer comme limitation : une grande zone affectée thermiquement (ZAT), des distorsions critiques, une précision géométrique médiocre et de faibles propriétés mécaniques sans post-traitement. En comparaison, le DED est une technologie très prometteuse grâce à sa capacité à réparer des géométries complexes mais aussi par le fait qu'avec des paramètres optimisés, la ZAT et les distorsions peuvent être minimisées [13, 14]. À l'échelle microscopique, le matériau est soumis à plusieurs phénomènes physiques déterminés par les paramètres du procédé. En conséquence, des microstructures architecturées sont générées [229, 17] et qui sont significativement différentes des matériaux fabriqués de manière conventionnelle. Cela implique que la pièce d'origine et le matériau réparé peuvent avoir des microstructures très différentes pouvant induirent différents champs de déformations sous chargement et, par conséquent, différents types de dommages.
Cette partie propose une étude des mécanismes de déformation à l'interface entre la pièce endommagée et le matériau ajouté. Plus précisément, un substrat en tôle laminée à chaud en acier inoxydable 316L a été réparé par DED. Les éprouvettes plates sont composées de deux parties égales comme le montre la Figure 5.18(a). Cette conception permet de charger l'interface en tension lors d'une expérience de traction. L'analyse de la microstructure de ses éprouvettes présentée dans la Figure 5.18(b) révèle des gros grains allongés dans la partie imprimée alors que dans le matériau initial de la tôle, des petits grains equiaxes peuvent être observés. Ces éprouvettes ont ensuite été soumises à un essai de traction in situ dans un MEB. Les champs de déformation ont été obtenus via HR-DIC et les résultats ont été associés à la carte de microstructure. Par conséquent, nous avons pu suivre la distribution de déformation microstructurale locale et mettre en évidence différents mécanismes de déformation des deux côtés de l'interface.
Les images (a), (b) et (c) de la Figure 5.19 montrent la localisation de la contrainte ϵ_{11} (aligner avec la direction de traction) pour les niveaux de déformation 1 ($\approx 2\%$), 3 ($\approx 6\%$) et 4. ($\approx 15\%$). Pour le niveau 1, la localisation de la déformation se produit exclusivement dans le substrat comme illustré dans la Figure 5.19(a). De plus, la déformation est homogène et ce comportement sera le même pour toutes les autres niveaux étudiés. Pour le niveau 2, une localisation hétérogènes des déformations dans la moitié imprimée commencent à apparaître. Ces déformations se situent au niveau de certaines zones intercouches comme montrées dans la Figure 5.19(b). À mesure que la contrainte de traction augmente, l'amplitude de la déformation augmente et en particulier dans la partie imprimée. Plus précisément, certaines intercouches deviennent alors les zones les plus déformées de la zone d'étude comme présentéés sur la Figure 5.19(c). Enfin, de part

et d'autre de l'interface, une zone de faible déformation peut être observée. Cette zone est associée à la microdureté des matériaux comme proposé dans la Figure 5.19(d). On peut voir que cette zone de faible déformation représentée en rose est plus dure. Ceci est une conséquence de la mise en solution de certains éléments dans la zone affectée thermiquement et des grains plus fins présents dans les premières couches déposées dans la partie imprimée conduisant à un effet de Hall-Petch.

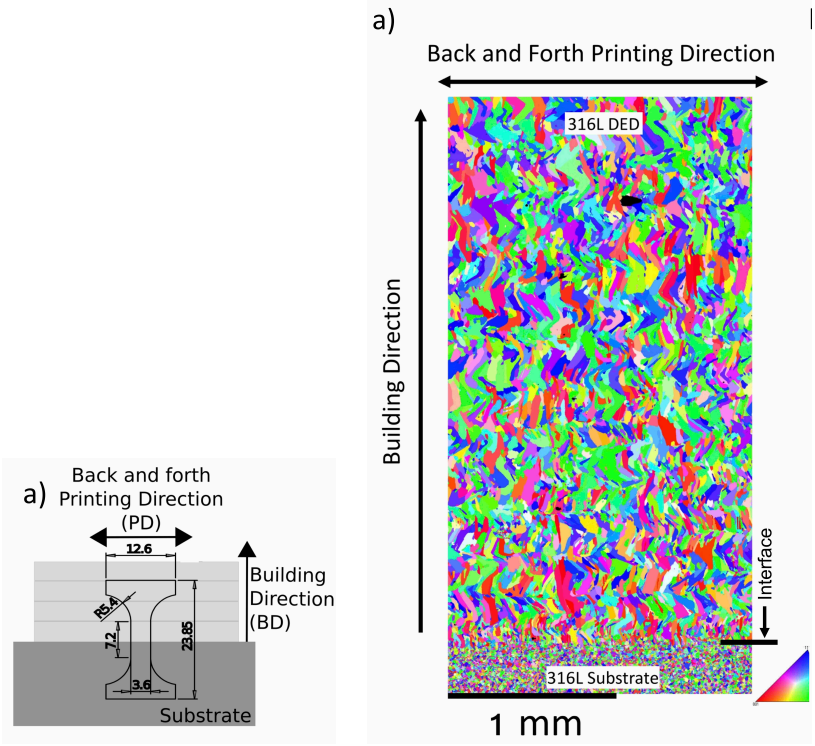

(a) (b)

Figure 5.18: (a): schéma de l'éprouvette réparée. Ce design permet de tester l'interface en traction qui est un point critique d'une réparation. (b): EBSD de l'éprouvette réparée.

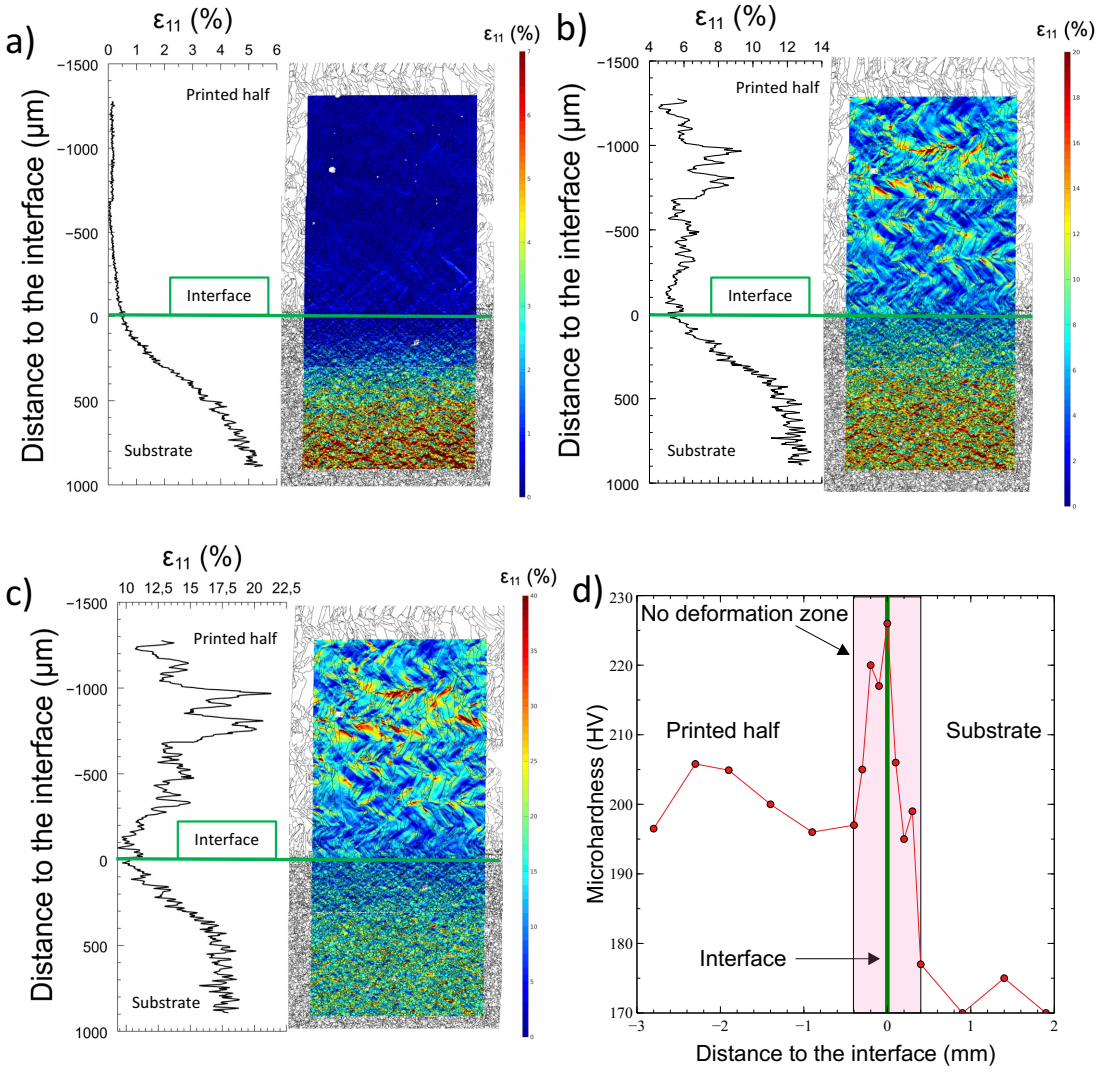

Figure 5.19: Localisation de la contrainte ϵ_{11} (alignée avec la direction de traction) pour les niveaux de déformation 1 ($\approx 2\%$), 3 ($\approx 6\%$) et 4. ($\approx 15\%$). (d) : Carte de la microdureté montrant une zone plus dure de part et d'autre de l'interface.

Comportements d'auto-échauffement

Les propriétés de fatigue et les prévisions de durée de vie de pièces entièrement imprimées et réparées sont primordiales. Ces propriétés peuvent être évaluées à l'échelle macroscopique de la structure ou étudiées au niveau local de la microstructure à travers les mécanismes de plasticité comme proposé dans [22, 23]. La durée de vie en fatigue de pièces métalliques issus de la FA a été abordée sous différents angles: (i) influence des paramètres du procédé et des défauts qui en résultent [24, 25], (ii) rôle de la microstructure particulière conduisant à des propriétés anisotropes sous des chargements monotones ou cycliques dans [6, 26] et [25, 27], respectivement. Des études telles que [28, 15] soulignent également les difficultés de la constitution d'une vaste base de données d'essais de fatigue pour ces matériaux. En effet, ces propriétés varient considérablement en fonction des paramètres de fabrication. Par conséquent, des méthodes alternatives plus rapides sont nécessaires pour déterminer ces propriétés. L'une d'entre elles est basée sur les mesures d'auto-échauffement de l'échantillon dues à la plasticité microscopique observée sous des chargements cycliques [30]. L'experience consiste à soumettre une éprouvette à une séquence de chargement cyclique par blocs pendant que l'évolution de sa température est enregistrée. D'un bloc à l'autre, l'amplitude de contrainte augmente et une fois un certain chargement dépassé, l'auto-échauffement augmente de manière significative. Cette transition peut être reliée à la limite d'endurance [214].
Nous avons évalué dans cette partie une méthode d'essai d'auto-échauffement pour la caractérisation des propriétés de fatigue de pièces minces entièrement imprimées ou réparées. La faible épaisseur ($\approx 300\,\mu m$) des échantillons testés a été surmontée par un protocole bien maitrisé. Les éprouvettes réparées ont montré les limites d'endurances les plus faibles. De plus, un comportement anisotrope a été observé durant ces essais cycliques avec des éprouvettes perpendiculaires au sens d'impression ($A_{\perp}$) montrant une plus grande limite d'endurance par rapport aux éprouvettes parallèles ($B_{//}$) comme schématisé par les courbes d'auto-échauffement dans la Figure 5.20. Pour ces dernières, des analyses post-mortem exposées dans la Figure 5.21(b) ont montré un scénario de fatigue classique avec une fissure dominante et donc une source de dissipation de chaleur localisée. À l'inverse, une multitude de fissures aux intercouches a été constatée a été constatée dans le cas des éprouvettes testées perpendiculairement (voir Figure 5.21(a)). Cela crée alors de nombreux sites de dissipation et un comportement à l'autoéchauffement différent.

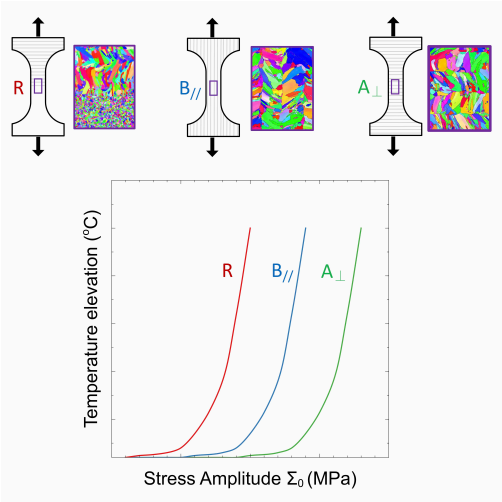

Figure 5.20: Schéma des courbes d'auto-échauffement pour les éprouvettes réparées (R), parallèles ($B_{//}$) et perpendiculaires ($A_{\perp}$) au sens d'impression.

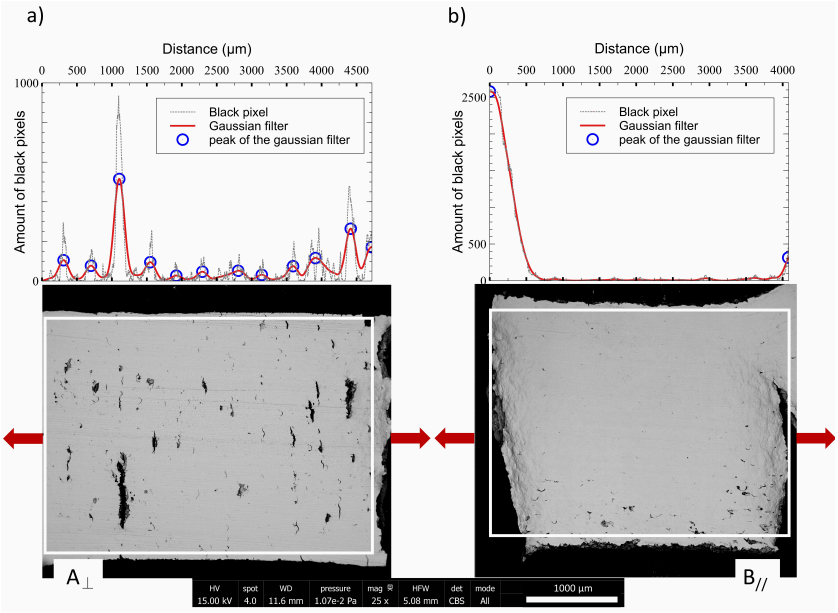

Figure 5.21: Analyse post mortem des essais d'auto-échauffement pour les éprouvettes $A_{\perp}$ et $B_{//}$ en (a) et (b) respectivement. Les images MEB permettent de voir deux mécanismes de fissuration différents en fonction de l'orientation. Les graphiques associés représentent la quantité de pixels noir correspondant aux fissures dans le cadre blanc.

Conclusion

Les travaux de cette thèse ont été dédiés à l'étude de pièces minces en acier inoxydable 316L fabriquées ou réparées par Directed Energy Deposition (DED). La nouveauté princpale est l'observation de la déformation à l'échelle de la microstructure. Pour ce faire, une expérience associant un essai de traction in situ dans un microscope électronique à balayage, de la corrélation d'images à haute résolution et une carte EBSD de la microstructure ont été réalisés. Les résultats obtenus permettent alors de mieux appréhender les différentes propriétés en traction ainsi que les comportements d'autoéchauffement lors d'essais cycliques. Le premier objectif a été de qualifier et quantifier les mécanismes de déformation à l'échelle de la microstructure pour expliquer le comportent anisotrope révélé lors d'essais de traction. Par conséquent, deux orientations de sollicitation permettant d'effectuer un chargement perpendiculaire ou parallèle à la direction d'impression ont été définies. Dans le premier cas, la localisation de deformation s'effectue au niveau de certaines intercouches. Pour le second, une localisation dans certaines régions correspondant à de gros grains particuliers a été observée. Le deuxième objectif a été d'évaluer la capacité du DED à réparer. Pour ce faire, des éprouvettes moitié tôle / moitié imprimées ont été fabriquées afin de solliciter l'interface en traction. Une grande différence de microstructure a été observée entre les deux matériaux. Néanmoins, l'interface n'a jamais été la zone de rupture lors d'essais de traction. De plus, une deformation homogène a été observée dans la partie tôle alors qu'une déformation hétérogène avec des pics de concentration au niveau de certaines intercouches a été remarquée dans la partie imprimée lors d'essais in situ. Enfin, une zone de faible déformation a été constatée de part et d'autres de l'interface, zone dans laquelle une plus grande dureté a été mesurée. Le dernier objectif a été d'évaluer les propriétés en fatigue par des essais d'autoéchauffement. Il a été montré que les difficultés liées à la faible épaisseurs de nos éprouvettes pouvaient être surmontées en maitrisant le protocole expérimental. Un comportement anisotrope a été observé durant ces essais cycliques avec des éprouvettes perpendiculaires au sens d'impression montrant une plus grande limite d'endurance par rapport aux éprouvettes sollicitées parallèlement. Pour ces dernières, des analyses post-mortem ont montré un scénario de fatigue classique avec une fissure dominante et donc une source de dissipation de chaleur localisée. À l'inverse, une multitude de fissures aux intercouches créant de nombreux sites de dissipation à été constatée pour les éprouvettes testées perpendiculairement.

Articles publiés ou en cours de publication

- Yanis Balit, Eric Charkaluk and Andrei constantinescu: *Digital image correlation for microstructural analysis of deformation pattern in additively manufactured 316L thin walls.* Accepted in **Additive Manufacturing**, september 2019

- Yanis Balit, Louis-Romain Joly, Fabien Szmytka, Sylvain Durbecq, Eric Charkaluk, Andrei Constantinescu: *Self-heating behavior during cyclic loadings of 316L stainless steel specimens manufactured or repaired by Directed Energy Deposition.* Submitted to **Materials Science and Engineering: A**, october 2019.

- Deux articles traitant respectivement de la réparations et de treillis sont en cours de finalisation. Ils seront soumis en 2019.

Bibliography

[1] Di Wang, Changhui Song, Yongqiang Yang, and Yuchao Bai. Investigation of crystal growth mechanism during selective laser melting and mechanical property characterization of 316l stainless steel parts. *Materials & Design*, 100:291 – 299, 2016.

[2] F. Bartolomeu, M. Buciumeanu, E. Pinto, N. Alves, O. Carvalho, F.S. Silva, and G. Miranda. 316l stainless steel mechanical and tribological behavior—a comparison between selective laser melting, hot pressing and conventional casting. *Additive Manufacturing*, 16:81 – 89, 2017.

[3] Aref Yadollahi, Nima Shamsaei, Scott M Thompson, and Denver W Seely. Effects of process time interval and heat treatment on the mechanical and microstructural properties of direct laser deposited 316l stainless steel. *Materials Science and Engineering: A*, 644:171 – 183, 2015.

[4] Beth E. Carroll, Todd A. Palmer, and Allison M. Beese. Anisotropic tensile behavior of ti–6al–4v components fabricated with directed energy deposition additive manufacturing. *Acta Materialia*, 87:309 – 320, 2015.

[5] Zhuqing Wang, Todd A. Palmer, and Allison M. Beese. Effect of processing parameters on microstructure and tensile properties of austenitic stainless steel 304l made by directed energy deposition additive manufacturing. *Acta Materialia*, 110:226 – 235, 2016.

[6] Kai Zhang, Shijie Wang, Weijun Liu, and Xiaofeng Shang. Characterization of stainless steel parts by laser metal deposition shaping. *Materials and Design*, 55:104 – 119, 2014.

[7] T. DebRoy, H.L. Wei, J.S. Zuback, T. Mukherjee, J.W. Elmer, J.O. Milewski, A.M. Beese, A. Wilson-Heid, A. De, and W. Zhang. Additive manufacturing of metallic components – process, structure and properties. *Progress in Materials Science*, 92:112 – 224, 2018.

[8] Olga Vayena, Charalabos Doumanidis, Rajesh Ranganathan, and Teiichi Ando. Welding methods for production of mmc coatings using particulate-cored wire precursors. *Journal of Manufacturing Processes*, 7(2):130 – 139, 2005.

[9] M.F. Morks, N.F. Fahim, and A. Kobayashi. Microstructure, corrosion behavior, and microhardness of plasma-sprayed w–ni composite coatings. *Journal of Manufacturing Processes*, 10(1):6 – 11, 2008.

[10] R.G. Bonora, H.J.C. Voorwald, M.O.H. Cioffi, G.S. Junior, and L.F.V. Santos. Fatigue in aisi 4340 steel thermal spray coating by hvof for aeronautic application. *Procedia Engineering*, 2(1):1617 – 1623, 2010. Fatigue 2010.

[11] W. Kaysser. Surface modifications in aerospace applications. *Surface Engineering*, 17(4):305–312, 2001.

[12] Shuo Yin, Pasquale Cavaliere, Barry Aldwell, Richard Jenkins, Hanlin Liao, Wenya Li, and Rocco Lupoi. Cold spray additive manufacturing and repair: Fundamentals and applications. *Additive Manufacturing*, 21:628 – 650, 2018.

[13] Y.T Pei and J.Th.M De Hosson. Functionally graded materials produced by laser cladding. *Acta Materialia*, 48(10):2617 – 2624, 2000.

[14] X. Lin, T.M. Yue, H.O. Yang, and W.D. Huang. Laser rapid forming of ss316l/rene88dt graded material. *Materials Science and Engineering: A*, 391(1):325 – 336, 2005.

[15] Shi Da Sun, Qianchu Liu, Milan Brandt, Vladimir Luzin, Ryan Cottam, Madabhushi Janardhana, and Graham Clark. Effect of laser clad repair on the fatigue behaviour of ultra-high strength aisi 4340 steel. *Materials Science and Engineering: A*, 606:46 – 57, 2014.

[16] Bonny Onuike and Amit Bandyopadhyay. Additive manufacturing in repair: Influence of processing parameters on properties of inconel 718. *Materials Letters*, 252:256 – 259, 2019.

[17] Lakshmi L. Parimi, G.A. Ravi, Daniel Clark, and Moataz M. Attallah. Microstructural and texture development in direct laser fabricated IN718. *Materials Characterization*, 89:102–111, 2014.

[18] David Foehring, Huck Beng Chew, and John Lambros. Characterizing the tensile behavior of additively manufactured ti-6al-4v using multiscale digital image correlation. *Materials Science and Engineering: A*, 724:536 – 546, 2018.

[19] Michael D. Sangid, Todd A. Book, Diwakar Naragani, John Rotella, Priya Ravi, Alexander Finch, Peter Kenesei, Jun-Sang Park, Hemant Sharma, Jonathan Almer, and Xianghui Xiao. Role of heat treatment and build orientation in the microstructure sensitive deformation characteristics of in718 produced via slm additive manufacturing. *Additive Manufacturing*, 22:479 – 496, 2018.

[20] Andrei constantinescu Yanis Balit, Eric Charkaluk. Sent to production: Digital image correlation for microstructural analysis of deformation pattern in additively manufactured 316l thin walls. *Additive Manufacturing*, Sent to production september 2019.

[21] Joseph Marae Djouda, Yazid Madi, Fabrice Gaslain, Jérémie Beal, Jérôme Crépin, Guillaume Montay, Léa Le Joncour, Naman Recho, Benoît Panicaud, and Thomas Maurer. Investigation of nanoscale strains at the austenitic

stainless steel 316l surface: Coupling between nanogauges gratings and ebsd technique during in situ tensile test. *Materials Science and Engineering: A*, 740-741:315 – 335, 2019.

[22] A. Constantinescu, K. Dang van, and M. H. Maitournam. A unified approach for high and low cycle fatigue based on shakedown concepts. *Fatigue & Fracture of Engineering Materials & Structures*, 26(6):561–568, 2003.

[23] Vincent Monchiet, Eric Charkaluk, and Djimedo Kondo. Plasticity-damage based micromechanical modelling in high cycle fatigue. *Comptes Rendus Mécanique*, 334(2):129–136, 2006.

[24] Aref Yadollahi and Nima Shamsaei. Additive manufacturing of fatigue resistant materials: Challenges and opportunities. *International Journal of Fatigue*, 98:14 – 31, 2017.

[25] Todd M. Mower and Michael J. Long. Mechanical behavior of additive manufactured, powder-bed laser-fused materials. *Materials Science and Engineering: A*, 651:198 – 213, 2016.

[26] Michał Ziętala, Tomasz Durejko, Marek Polanski, Izabela Kunce, Tomasz Płociński, Witold Zieliński, Magdalena Łazińska, Wojciech Stępniowski, Tomasz Czujko, K.J. Kurzydłowski, and Zbigniew Bojar. The microstructure, mechanical properties and corrosion resistance of 316l stainless steel fabricated using laser engineered net shaping. *Materials Science and Engineering: A*, 677:1–10, 11 2016.

[27] Jerard Gordon, Jacob Hochhalter, Christina Haden, and D. Gary Harlow. Enhancement in fatigue performance of metastable austenitic stainless steel through directed energy deposition additive manufacturing. *Materials & Design*, 168:107630, 2019.

[28] Yi Rye Choi, Shi D Sun, Qianchu Liu, Milan Brandt, and Ma Qian. Influence of deposition strategy on the microstructure and fatigue properties of laser metal deposited ti-6al-4v powder on ti-6al-4v substrate. *International Journal of Fatigue*, page 105236, 2019.

[29] C. E. Stromeyer and William Ernest Dalby. The determination of fatigue limits under alternating stress conditions. *Proceedings of the Royal Society of London. Series A, Containing Papers of a Mathematical and Physical Character*, 90(620):411–425, 1914.

[30] Rémi Munier, Cédric Doudard, Sylvain Calloch, and Bastien Weber. Determination of high cycle fatigue properties of a wide range of steel sheet grades from self-heating measurements. *International Journal of Fatigue*, 63:46 – 61, 2014.

[31] ASTM International. Standard terminology for additive manufacturing technologies. Technical report, ASTM International, 2012.

[32] R.M. Miranda, G. Lopes, L. Quintino, J.P. Rodrigues, and S. Williams. Rapid prototyping with high power fiber lasers. *Materials and Design*, 29(10):2072 – 2075, 2008.

[33] Nannan Guo and Ming C. Leu. Additive manufacturing: technology, applications and research needs. *Frontiers of Mechanical Engineering*, 8(3):215–243, Sep 2013.

[34] R. Liu, Z. Wang, T. Sparks, F. Liou, and J. Newkirk. 13 - aerospace applications of laser additive manufacturing. In Milan Brandt, editor, *Laser Additive Manufacturing*, Woodhead Publishing Series in Electronic and Optical Materials, pages 351 – 371. Woodhead Publishing, 2017.

[35] Sneha Prabha Narra, Peter N. Mittwede, Sandra DeVincent Wolf, and Kenneth L. Urish. Additive manufacturing in total joint arthroplasty. *Orthopedic Clinics of North America*, 50(1):13 – 20, 2019. New Technologies.

[36] https://www.ge.com/additive/blog/new-manufacturing-milestone-30000-additive-fuel nozzles.

[37] KC Wong. 3d-printed patient-specific applications in orthopedics. *Orthopedic Research and Reviews*, Volume 8:57–66, 10 2016.

[38] M.W Khaing, J.Y.H Fuh, and L Lu. Direct metal laser sintering for rapid tooling: processing and characterisation of eos parts. *Journal of Materials Processing Technology*, 113(1):269 – 272, 2001. 5th Asia Pacific conference on Materials processing.

[39] J.P. Kruth, L. Froyen, J. Van Vaerenbergh, P. Mercelis, M. Rombouts, and B. Lauwers. Selective laser melting of iron-based powder. *Journal of Materials Processing Technology*, 149(1):616 – 622, 2004. 14th Interntaional Symposium on Electromachining (ISEM XIV).

[40] Lawrence E. Murr, Sara M. Gaytan, Diana A. Ramirez, Edwin Martinez, Jennifer Hernandez, Krista N. Amato, Patrick W. Shindo, Francisco R. Medina, and Ryan B. Wicker. Metal fabrication by additive manufacturing using laser and electron beam melting technologies. *Journal of Materials Science Technology*, 28(1):1 – 14, 2012.

[41] S. Haeri. Optimisation of blade type spreaders for powder bed preparation in additive manufacturing using dem simulations. *Powder Technology*, 321:94 – 104, 2017.

[42] http://www.arcam.com.

[43] International Organization for Standardization. Iso/astm 52900, additive manufacturing - general principles - terminology. Technical report, ASTM International, 2015.

[44] G. P. Dinda, A. K. Dasgupta, and J. Mazumder. Laser aided direct metal deposition of Inconel 625 superalloy: Microstructural evolution and thermal stability. *Materials Science and Engineering A*, 509(1-2):98–104, 2009.

[45] L. Sexton, S. Lavin, G. Byrne, and A. Kennedy. Laser cladding of aerospace materials. *Journal of Materials Processing Technology*, 122(1):63 – 68, 2002.

[46] R.M. Mahamood and E.T. Akinlabi. Laser metal deposition of functionally graded ti6al4v/tic. *Materials Design*, 84:402 – 410, 2015.

[47] Chunlei Qiu, G.A. Ravi, Chris Dance, Andrew Ranson, Steve Dilworth, and Moataz M. Attallah. Fabrication of large ti–6al–4v structures by direct laser deposition. *Journal of Alloys and Compounds*, 629:351 – 361, 2015.

[48] Taewoo Hwang, Young Yun Woo, Sang Wook Han, and Young Hoon Moon. Functionally graded properties in directed-energy-deposition titanium parts. *Optics and Laser Technology*, 105:80 – 88, 2018.

[49] Niyanth Sridharan, Ercan Cakmak, and Ryan R. Dehoff. Microstructure evolution during laser direct energy deposition of a novel fe-cr-ni-w-b hardfacing coating. *Surface and Coatings Technology*, 358:362 – 370, 2019.

[50] J. Michael Wilson, Cecil Piya, Yung C. Shin, Fu Zhao, and Karthik Ramani. Remanufacturing of turbine blades by laser direct deposition with its energy and environmental impact analysis. *Journal of Cleaner Production*, 80:170 – 178, 2014.

[51] Ian Gibson, David Rosen, and Brent Stucker. *Directed Energy Deposition Processes*, pages 245–268. 01 2015.

[52] Donghong Ding, Zengxi Pan, Dominic Cuiuri, and Huijun Li. Wire-feed additive manufacturing of metal components: technologies, developments and future interests. *The International Journal of Advanced Manufacturing Technology*, 81(1):465–481, Oct 2015.

[53] P. Heinl, A. Rottmair, C. Körner, and R.F. Singer. Cellular titanium by selective electron beam melting. *Advanced Engineering Materials*, 9(5):360–364, 2007.

[54] Milewski JO et al. Directed light fabrication of a solid metal hemisphere using 5-axis powder deposition. *J Mater Process Technol 75:165–172*, 1998.

[55] Lijue Xue. Laser consolidation - a one-step manufacturing process for making net-shaped functional aerospace components. *SAE Technical Papers*, 09 2006.

[56] *Colegrove PA (2010) High deposition rate high quality metal additive manufacture using wire + are technology.*, 2010.

[57] Taminger KMB et al. Electron beam freeform fabrication for cost effective near-net shape manufacturing. nato avt 139:16–1. Technical report, ., 2006.

[58] Scott M. Thompson, Linkan Bian, Nima Shamsaei, and Aref Yadollahi. An overview of direct laser deposition for additive manufacturing; part i: Transport phenomena, modeling and diagnostics. *Additive Manufacturing*, 8:36 – 62, 2015.

[59] Franz-Josef Kahlen and Aravinda Kar. Tensile strengths for laser-fabricated parts and similarity parameters for rapid manufacturing. *Journal of Manufacturing Science and Engineering-transactions of The Asme - J MANUF SCI ENG*, 123, 02 2001.

[60] G.P. Dinda, A.K. Dasgupta, and J. Mazumder. Texture control during laser deposition of nickel-based superalloy. *Scripta Materialia*, 67(5):503 – 506, 2012.

[61] David Bourell, Jean Pierre Kruth, Ming Leu, Gideon Levy, David Rosen, Allison M. Beese, and Adam Clare. Materials for additive manufacturing. *CIRP Annals*, 66(2):659 – 681, 2017.

[62] John Milewski. *Additive Manufacturing of Metals*, volume 258. 01 2017.

[63] http://www.dierk-raabe.com/titanium alloys/.

[64] I Weiss and S.L Semiatin. Thermomechanical processing of alpha titanium alloys—an overview. *Materials Science and Engineering: A*, 263(2):243 – 256, 1999.

[65] Daisuke Kuroda, Mitsuo Niinomi, Masahiko Morinaga, Yosihisa Kato, and Toshiaki Yashiro. Design and mechanical properties of new type titanium alloys for implant materials. *Materials Science and Engineering: A*, 243(1):244 – 249, 1998.

[66] S. L. Semiatin, V. Seetharaman, and I. Weiss. The thermomechanical processing of alpha/beta titanium alloys. *JOM*, 49(6):33–39, Jun 1997.

[67] Yuwei Zhai, Diana A. Lados, Eric J. Brown, and Gregory N. Vigilante. Understanding the microstructure and mechanical properties of ti-6al-4v and inconel 718 alloys manufactured by laser engineered net shaping. *Additive Manufacturing*, 27:334 – 344, 2019.

[68] Qi Liu, Yudai Wang, Hang Zheng, Kang Tang, Li Ding, Huaixue Li, and Shuili Gong. Microstructure and mechanical properties of lmd–slm hybrid forming ti6al4v alloy. *Materials Science and Engineering: A*, 660:24 – 33, 2016.

[69] Xipeng Tan, Yihong Kok, Yu Jun Tan, Marion Descoins, Dominique Mangelinck, Shu Beng Tor, Kah Fai Leong, and Chee Kai Chua. Graded microstructure and mechanical properties of additive manufactured ti–6al–4v via electron beam melting. *Acta Materialia*, 97:1 – 16, 2015.

[70] S.M. Gaytan, L.E. Murr, E. Martinez, J.L. Martinez, B.I. Machado, D.A. Ramirez, F. Medina, S. Collins, and R.B. Wicker. Comparison of microstructures and mechanical properties for solid and mesh cobalt-base alloy prototypes fabricated by electron beam melting. *Metallurgical and Materials Transactions A*, 41(12):3216–3227, Dec 2010.

[71] Chengyun Cui, Zuoxing Guo, Yuhua Liu, Qiongqiong Xie, Zheng Wang, Jiandong Hu, and Yuan Yao. Characteristics of cobalt-based alloy coating on tool

steel prepared by powder feeding laser cladding. *Optics Laser Technology*, 39(8):1544 – 1550, 2007.

[72] D.P. Weston, P.H. Shipway, S.J. Harris, and M.K. Cheng. Friction and sliding wear behaviour of electrodeposited cobalt and cobalt–tungsten alloy coatings for replacement of electrodeposited chromium. *Wear*, 267(5):934 – 943, 2009. 17th International Conference on Wear of Materials.

[73] Pantcho Stoyanov, Kalissa Andre, Paul Prichard, Matthew Yao, and Christoph Gey. Microstructural and mechanical characterization of mo-containing stellite alloys produced by three dimensional printing. *Procedia CIRP*, 45:167 – 170, 2016. 3rd CIRP Conference on Surface Integrity.

[74] D. Klarstrom, P. Crook, and A. Sharif. Cobalt alloys: Alloying and thermo-mechanical processing. In *Reference Module in Materials Science and Materials Engineering*. Elsevier, 2017.

[75] http://www.dierk-raabe.com/cobalt alloys/.

[76] J. A. Goebel, F. S. Pettit, and G. W. Goward. Mechanisms for the hot corrosion of nickel-base alloys. *Metallurgical Transactions*, 4(1):261–278, Jan 1973.

[77] D. P. Pope and S. S. Ezz. Mechanical properties of ni3ai and nickel-base alloys with high volume fraction of '. *International Metals Reviews*, 29(1):136–167, 1984.

[78] Gerald R. Leverant and Bernard H. Kear. The mechanism of creep in gamma prime precipitation-hardened nickel-base alloys at intermediate temperatures. *Metallurgical and Materials Transactions B*, 1(2):491–498, Feb 1970.

[79] Matthew Donachie and Stephen Donachie. *Superalloys: A Technical Guide, 2nd Edition*. 01 2002.

[80] *Stainless steel*. American Society for Metals, 1986.

[81] K.H. Lo, C.H. Shek, and J.K.L. Lai. Recent developments in stainless steels. *Materials Science and Engineering: R: Reports*, 65(4):39 – 104, 2009.

[82] http://www.dierk-raabe.com/stainless steels/.

[83] A. Nasery Isfahany, H. Saghafian, and G. Borhani. The effect of heat treatment on mechanical properties and corrosion behavior of aisi420 martensitic stainless steel. *Journal of Alloys and Compounds*, 509(9):3931 – 3936, 2011.

[84] D. Raabe and K. Lüucke. Textures of ferritic stainless steels. *Materials Science and Technology*, 9(4):302–312, 1993.

[85] Y.S. Sato, T.W. Nelson, C.J. Sterling, R.J. Steel, and C.-O. Pettersson. Microstructure and mechanical properties of friction stir welded saf 2507 super duplex stainless steel. *Materials Science and Engineering: A*, 397(1):376 – 384, 2005.

[86] C.N. Hsiao, C.S. Chiou, and J.R. Yang. Aging reactions in a 17-4 ph stainless steel. *Materials Chemistry and Physics*, 74(2):134 – 142, 2002.

[87] M.F. McGuire. Austenitic stainless steels. In K.H. Jürgen Buschow, Robert W. Cahn, Merton C. Flemings, Bernhard Ilschner, Edward J. Kramer, Subhash Mahajan, and Patrick Veyssière, editors, *Encyclopedia of Materials: Science and Technology*, pages 406 – 410. Elsevier, Oxford, 2001.

[88] Y. Wang, Thomas Voisin, Joseph McKeown, Jianchao Ye, Nicholas Calta, Zan Li, Zhi Zeng, Yin Zhang, Wen Chen, Tien Roehling, Ryan Ott, Melissa Santala, Philip J Depond, Manyalibo Matthews, Alex Hamza, and Ting Zhu. Additively manufactured hierarchical stainless steels with high strength and ductility. *Nature Materials*, 17, 10 2017.

[89] Nesma T. Aboulkhair, Marco Simonelli, Luke Parry, Ian Ashcroft, Christopher Tuck, and Richard Hague. 3d printing of aluminium alloys: Additive manufacturing of aluminium alloys using selective laser melting. *Progress in Materials Science*, 106:100578, 2019.

[90] A Strondl, Ola Lyckfeldt, H Brodin, and Ulf Ackelid. Characterization and control of powder properties for additive manufacturing. *JOM*, 67:549–554, 03 2015.

[91] Joakim Karlsson, Anders Snis, Håkan Engqvist, and Jukka Lausmaa. Characterization and comparison of materials produced by electron beam melting (ebm) of two different ti–6al–4v powder fractions. *Journal of Materials Processing Technology*, 213(12):2109 – 2118, 2013.

[92] Xiaoming Zhao, Jing Chen, Xin Lin, and Weidong Huang. Study on microstructure and mechanical properties of laser rapid forming inconel 718. *Materials Science and Engineering: A*, 478(1):119 – 124, 2008.

[93] https://www.carpenteradditive.com.

[94] Berenika Hausnerova, Bhimasena Nagaraj Mukund, and Daniel Sanetrnik. Rheological properties of gas and water atomized 17-4ph stainless steel mim feedstocks: Effect of powder shape and size. *Powder Technology*, 312:152 – 158, 2017.

[95] Bourdeau RG. Rotary atomizing process. Technical report, US Patent 1983; No. 4415511, 1983.

[96] A Ozols, H.R Sirkin, and E.E Vicente. Segregation in stellite powders produced by the plasma rotating electrode process. *Materials Science and Engineering: A*, 262(1):64 – 69, 1999.

[97] W.J. Sames, F. Medina, W.H. Peter, S.S. Babu, and R.R. Dehoff. *Effect of Process Control and Powder Quality on Inconel 718 Produced Using Electron Beam Melting*, pages 409–423. John Wiley Sons, Ltd, 2014.

[98] Taminger K. Electron beam additive manufacturing: state-of-the-technology, challenges opportunities. In *Direct digital manufacturing workshop. Solomons (MD)*, 2010.

[99] J.S. Zuback, P. Moradifar, Z. Khayat, N. Alem, and T.A. Palmer. Impact of chemical composition on precipitate morphology in an additively manufactured nickel base superalloy. *Journal of Alloys and Compounds*, 798:446 – 457, 2019.

[100] Austin Sutton, Caitlin Kriewall, Ming Leu, and Joseph Newkirk. Powder characterisation techniques and effects of powder characteristics on part properties in powder-bed fusion processes. *Virtual and Physical Prototyping*, 12:1–27, 12 2016.

[101] Rustam Baitimerov, Pavel Lykov, Dmitry Zherebtsov, Lyudmila Radionova, Alexey Shultc, and Prashanth K G. Influence of powder characteristics on processability of alsi12 alloy fabricated by selective laser melting. *Materials*, 11:742, 05 2018.

[102] Yasuhiro Kakinuma, Masahiko Mori, Yohei Oda, Takanori Mori, Makoto Kashihara, Adam Hansel, and Makoto Fujishima. Influence of metal powder characteristics on product quality with directed energy deposition of inconel 625. *CIRP Annals*, 65(1):209 – 212, 2016.

[103] P.A.A. Khan and T. Debroy. Alloying element vaporization and weld pool temperature during laser welding of alsl 202 stainless steel. *Metallurgical Transactions B*, 15(4):641–644, 1984. cited By 50.

[104] O.V. Borisov, X.L. Mao, A. Fernandez, M. Caetano, and R.E. Russo. Inductively coupled plasma mass spectrometric study of non-linear calibration behavior during laser ablation of binary cu–zn alloys. *Spectrochimica Acta Part B: Atomic Spectroscopy*, 54(9):1351 – 1365, 1999.

[105] Richard Charles Barclay. Parameter optimization for controlling aluminum loss when laser depositing ti-6al-4v. Master's thesis, Missouri university of science and technology, 2013.

[106] Imade Koutiri, Etienne Pessard, Patrice Peyre, Ouafae Amlou, and Thibaut De Terris. Influence of slm process parameters on the surface finish, porosity rate and fatigue behavior of as-built inconel 625 parts. *Journal of Materials Processing Technology*, 255:536 – 546, 2018.

[107] D. Greitemeier, C. Dalle Donne, F. Syassen, J. Eufinger, and T. Melz. Effect of surface roughness on fatigue performance of additive manufactured ti–6al–4v. *Materials Science and Technology*, 32(7):629–634, 2016.

[108] Jason C. Fox, Shawn P. Moylan, and Brandon M. Lane. Effect of process parameters on the surface roughness of overhanging structures in laser powder bed fusion additive manufacturing. *Procedia CIRP*, 45:131 – 134, 2016. 3rd CIRP Conference on Surface Integrity.

[109] Grzegorz Pyka, Greet Kerckhofs, Ioannis Papantoniou, Mathew Speirs, Jan Schrooten, and Martine Wevers. Surface roughness and morphology customization of additive manufactured open porous ti6al4v structures. *Materials*, 6(10):4737–4757, 2013.

[110] Ali Fatemi, Reza Molaei, Shahriar Sharifimehr, Nima Shamsaei, and Nam Phan. Torsional fatigue behavior of wrought and additive manufactured ti-6al-4v by powder bed fusion including surface finish effect. *International Journal of Fatigue*, 99:187 – 201, 2017.

[111] Myriam Gharbi, Patrice Peyre, Cyril Gorny, Muriel Carin, Simon Morville, Philippe Le Masson, Denis Carron, and Rémy Fabbro. Influence of various process conditions on surface finishes induced by the direct metal deposition laser technique on a ti–6al–4v alloy. *Journal of Materials Processing Technology*, 213(5):791 – 800, 2013.

[112] K. Mumtaz and N. Hopkinson. Top surface and side roughness of inconel 625 parts processed using selective laser melting. *Rapid Prototyping Journal*, 2009.

[113] Andrew J. Pinkerton and Lin Li. The effect of laser pulse width on multiple-layer 316l steel clad microstructure and surface finish. *Applied Surface Science*, 208-209:411 – 416, 2003. Physics and Chemistry of Advanced Laser Materials Processing.

[114] Pascal Aubry, C. Colin, and J. Maisonneuve. Profil project: Direct manufacturing of aerospace components by laser cladding and laser sintering. *26th International Congress on Applications of Lasers and Electro-Optics, ICALEO 2007 - Congress Proceedings*, 01 2007.

[115] Sadegh Rahmati and Ebrahim Vahabli. Evaluation of analytical modeling for improvement of surface roughness of fdm test part using measurement results. *The International Journal of Advanced Manufacturing Technology*, 79(5):823–829, Jul 2015.

[116] Holly D. Carlton, Abdel Haboub, Gilbert F. Gallegos, Dilworth Y. Parkinson, and Alastair A. MacDowell. Damage evolution and failure mechanisms in additively manufactured stainless steel. *Materials Science and Engineering: A*, 651:406 – 414, 2016.

[117] Wayne E. King, Holly D. Barth, Victor M. Castillo, Gilbert F. Gallegos, John W. Gibbs, Douglas E. Hahn, Chandrika Kamath, and Alexander M. Rubenchik. Observation of keyhole-mode laser melting in laser powder-bed fusion additive manufacturing. *Journal of Materials Processing Technology*, 214(12):2915 – 2925, 2014.

[118] D.F. Susan, J.D. Puskar, J.A. Brooks, and C.V. Robino. Quantitative characterization of porosity in stainless steel lens powders and deposits. *Materials Characterization*, 57(1):36 – 43, 2006.

[119] P A. Kobryn, E H. Moore, and S Semiatin. Effect of laser power and traverse speed on microstructure, porosity, and build height in laser-deposited ti-6al-4v. *Scripta Materialia - SCRIPTA MATER*, 43:299–305, 07 2000.

[120] P Monson W M Steen, V M. Weerasinghe. Some aspects of the formation of laser clad tracks, 1986.

[121] Marcel Schneider. *Laser cladding with powder - effect of some machining parameters on clad properties*. PhD thesis, 1998.

[122] T. Mukherjee, W. Zhang, and T. DebRoy. An improved prediction of residual stresses and distortion in additive manufacturing. *Computational Materials Science*, 126:360 – 372, 2017.

[123] K. Kempene tal. Producing crack-free, high density m2 hss parts by selective laser melting: Pre-heating the baseplate. In *24th International SFF Symposium - An Additive Manufacturing Conference,*, 2013.

[124] *Weld Metal Solidification Cracking*, chapter 11, pages 263–300. John Wiley Sons, Ltd, 2003.

[125] Pulin Nie, O.A. Ojo, and ZhuGuo Li. Numerical modeling of microstructure evolution during laser additive manufacturing of a nickel-based superalloy. *Acta Materialia*, 77:85–95, 09 2014.

[126] Yuan Chen, Fenggui Lu, Ke Zhang, Pulin Nie, Seyed Reza Elmi Hosseini, Kai Feng, and Zhuguo Li. Dendritic microstructure and hot cracking of laser additive manufactured inconel 718 under improved base cooling. *Journal of Alloys and Compounds*, 670:312 – 321, 2016.

[127] Michael F. Zaeh and Gregor Branner. Investigations on residual stresses and deformations in selective laser melting. *Production Engineering*, 4(1):35–45, Feb 2010.

[128] Damien Buchbinder, Wilhelm Meiners, Norbert Pirch, Konrad Wissenbach, and Johannes Schrage. Investigation on reducing distortion by preheating during manufacture of aluminum components using selective laser melting. *Journal of Laser Applications*, 26:2004–, 02 2014.

[129] M. Shiomi, K. Osakada, K. Nakamura, T. Yamashita, and F. Abe. Residual stress within metallic model made by selective laser melting process. *CIRP Annals*, 53(1):195 – 198, 2004.

[130] Qianchu Liu, Shi Sun, K. Walker, Yi rye Choi, and Milan Brandt. Repair and manufacturing of military aircraft components by additive manufacturing technology. 02 2017.

[131] D. Tejero-Martin, M. Rezvani Rad, A. McDonald, and T. Hussain. Beyond traditional coatings: A review on thermal-sprayed functional and smart coatings. *Journal of Thermal Spray Technology*, 28(4):598–644, Apr 2019.

[132] Victor Champagne Jr. *The cold spray materials deposition process: Fundamentals and applications*. 09 2007.

[133] Nicholas Curry, Nicolaie Markocsan, Lars Östergren, Xin-Hai Li, and Mitch Dorfman. Evaluation of the lifetime and thermal conductivity of dysprosia-stabilized thermal barrier coating systems. *Journal of Thermal Spray Technology*, 22, 08 2013.

[134] S Deshpande, A Kulkarni, S Sampath, and H Herman. Application of image analysis for characterization of porosity in thermal spray coatings and correlation with small angle neutron scattering. *Surface and Coatings Technology*, 187(1):6 – 16, 2004.

[135] N. Matthews, R. Jones, and G. C. Sih. Application of supersonic particle deposition to enhance the structural integrity of aircraft structures. *Science China Physics, Mechanics and Astronomy*, 57(1):12–18, Jan 2014.

[136] R. Jones, L. Molent, S. Barter, N. Matthews, and D. Tamboli. Supersonic particle deposition as a means for enhancing the structural integrity of aircraft structures. *International Journal of Fatigue*, 68:260 – 268, 2014.

[137] Kevin Edwards. Materials enabled designs: The materials engineering perspective to product design and manufacturing, m. pfeifer. butterworth–heinemann (2009). 306 pp., isbn: 978-0-7506-8287-9. *Materials Design - MATER DESIGN*, 31:654–654, 01 2010.

[138] T. Álvarez Tejedor, R. Singh, and P. Pilidis. 13 - maintenance and repair of gas turbine components. In Peter Jansohn, editor, *Modern Gas Turbine Systems*, Woodhead Publishing Series in Energy, pages 565 – 634. Woodhead Publishing, 2013.

[139] http://www.wermac.org/others/welding$_t ig_g as - tungsten - arc - weldingprocess_g taw$,*html*,

[140] Marcin Hojny. Thermo-mechanical model of a tig welding process for the aircraft industry. *Archives of Metallurgy and Materials*, 58, 12 2013.

[141] www.beam-machines.com.

[142] https://www.irepa laser.com.

[143] www.hoganas.com.

[144] Cunat. Aciers inoxydables : critères de choix et structure. Technical report, Les techniques de l'ingénieur, 2003.

[145] DJ Kotecki and TA Siewert. Wrc-1992 constitution diagram for stainless steel weld metals: a modification of the wrc-1988 diagram. *Welding Journal*, 71(5):171–178, 1992.

[146] Zachary Ryan Francis. The Effects of Laser and Electron Beam Spot Size in Additive Manufacturing Processes. 5 2017.

[147] Alexander Metel, Michael Stebulyanin, Sergey Fedorov, and Anna Okunkova. Power density distribution for laser additive manufacturing (slm): Potential, fundamentals and advanced applications. *Technologies*, 7:5, 12 2018.

[148] B. Ferrar, L. Mullen, E. Jones, R. Stamp, and C.J. Sutcliffe. Gas flow effects on selective laser melting (slm) manufacturing performance. *Journal of Materials Processing Technology*, 212(2):355 – 364, 2012.

[149] J. M. Pelletier, M. C. Sahour, M. Pilloz, and A. B. Vannes. Influence of processing conditions on geometrical features of laser claddings obtained by powder injection. *Journal of Materials Science*, 28(19):5184–5188, Jan 1993.

[150] Lino Costa, Imre Felde, Tamás Réti, Zoltán Kálazi, Rogerio Colaço, Rui Vilar, and Balázs Verő. A simplified semi-empirical method to select the processing parameters for laser clad coatings. In *Materials Science, Testing and Informatics I*, volume 414 of *Materials Science Forum*, pages 385–394. Trans Tech Publications Ltd, 12 2002.

[151] U. de Oliveira, V. Ocelík, and J.Th.M. De Hosson. Analysis of coaxial laser cladding processing conditions. *Surface and Coatings Technology*, 197(2):127 – 136, 2005.

[152] Shengfeng Zhou, Xiaoguang Dai, and Xiaoyan Zeng. Effects of processing parameters on structure of ni-based wc composite coatings during laser induction hybrid rapid cladding. *Applied Surface Science*, 255(20):8494 – 8500, 2009.

[153] Hussam El Cheikh, Bruno Courant, Samuel Branchu, Jean-Yves Hascoët, and Ronald Guillén. Analysis and prediction of single laser tracks geometrical characteristics in coaxial laser cladding process. *Optics and Lasers in Engineering*, 50(3):413 – 422, 2012.

[154] M. Ansari, R. Shoja Razavi, and M. Barekat. An empirical-statistical model for coaxial laser cladding of nicraly powder on inconel 738 superalloy. *Optics & Laser Technology*, 86:136 – 144, 2016.

[155] Benjamin Bax, Rohan Rajput, Richard Kellet, and Martin Reisacher. Systematic evaluation of process parameter maps for laser cladding and directed energy deposition. *Additive Manufacturing*, 21:487 – 494, 2018.

[156] V. Ocelík, U. de Oliveira, M. de Boer, and J. Th M de Hosson. Thick Co-based coating on cast iron by side laser cladding: Analysis of processing conditions and coating properties. *Surface and Coatings Technology*, 201(12):5875–5883, 2007.

[157] G. J. Bruck. High-power laser beam cladding. *JOM*, 39(2):10–13, Feb 1987.

[158] I. Hemmati, V. Ocelík, and J. Th M De Hosson. Dilution effects in laser cladding of Ni-Cr-B-Si-C hardfacing alloys. *Materials Letters*, 84:69–72, 2012.

[159] Hussam El Cheikh, Bruno Courant, Samuel Branchu, Xiaowei Huang, Jean Yves Hascot, and Ronald Guilln. Direct Laser Fabrication process with coaxial powder projection of 316L steel. Geometrical characteristics and microstructure characterization of wall structures. *Optics and Lasers in Engineering*, 50(12):1779–1784, 2012.

[160] https://www.struers.com.

[161] Hussam El Cheikh. *Fabrication directe par laser. Analyse experimentale de depots d'acier 316l sur acier bas carbone. Modelisation et simulation de la geometrie des depots et des champs thermiques induits.* PhD thesis, Université de Nantes, 2012.

[162] Jehnming Lin. A simple model of powder catchment in coaxial laser cladding. *Optics & Laser Technology*, 31(3):233 – 238, 1999.

[163] Stocker H Harris JW. *Handbook of mathematics and computational science*. New York: Springer-Verlag, 1998.

[164] S. Atamert and H. K. D. H. Bhadeshia. Comparison of the microstructures and abrasive wear properties of stellite hardfacing alloys deposited by arc welding and laser cladding. *Metallurgical Transactions A*, 20(6):1037–1054, Jun 1989.

[165] T. Wang, Y.Y. Zhu, S.Q. Zhang, H.B. Tang, and H.M. Wang. Grain morphology evolution behavior of titanium alloy components during laser melting deposition additive manufacturing. *Journal of Alloys and Compounds*, 632:505 – 513, 2015.

[166] Alexandre Charles Eric Charkaluk Camille Guévenoux, Simon Hallais and Andrei Constantinescu. Influence of interlayer dwell time on the microstructure of inconel 718 laser cladded components. *Journal of Optics and Laser Technology*, Submitted in 2019.

[167] Y Morris Wang, Thomas Voisin, Joseph T McKeown, Jianchao Ye, Nicholas P Calta, Zan Li, Zhi Zeng, Yin Zhang, Wen Chen, Tien Tran Roehling, Ryan T Ott, Melissa K Santala, Philip J. Depond, Manyalibo J Matthews, Alex V Hamza, and Ting Zhu. Additively manufactured hierarchical stainless steels with high strength and ductility. *Nature Materials*, 17:63, oct 2017.

[168] K. Saeidi, X. Gao, F. Lofaj, L. Kvetková, and Z.J. Shen. Transformation of austenite to duplex austenite-ferrite assembly in annealed stainless steel 316l consolidated by laser melting. *Journal of Alloys and Compounds*, 633:463 – 469, 2015.

[169] Leifeng Liu, Qingqing Ding, Yuan Zhong, Ji Zou, Jing Wu, Yu-Lung Chiu, Jixue Li, Ze Zhang, Qian Yu, and Zhijian Shen. Dislocation network in additive manufactured steel breaks strength–ductility trade-off. *Materials Today*, 21(4):354 – 361, 2018.

[170] Andrew Pinkerton and K Mahmood. Direct laser deposition with different types of 316l steel particle: A comparative study of final part properties. *Proceedings of the Institution of Mechanical Engineers Part B Journal of Engineering Manufacture*, 227:520–531, 04 2013.

[171] I. Yadroitsev, P. Krakhmalev, I. Yadroitsava, S. Johansson, and I. Smurov. Energy input effect on morphology and microstructure of selective laser melting single track from metallic powder. *Journal of Materials Processing Technology*, 213(4):606 – 613, 2013.

[172] Mingming Ma, Zemin Wang, Dengzhi Wang, and Xiaoyan Zeng. Control of shape and performance for direct laser fabrication of precision large-scale metal parts with 316l stainless steel. *Optics and Laser Technology*, 45:209 – 216, 2013.

[173] Masoud Alimardani, Vahid Fallah, Mehrdad Iravani-Tabrizipour, and Amir Khajepour. Surface finish in laser solid freeform fabrication of an aisi 303l stainless steel thin wall. *Journal of Materials Processing Technology*, 212(1):113 – 119, 2012.

[174] H.Y. Wan, Z.J. Zhou, C.P. Li, G.F. Chen, and G.P. Zhang. Effect of scanning strategy on mechanical properties of selective laser melted inconel 718. *Materials Science and Engineering: A*, 753:42 – 48, 2019.

[175] Xianglong Wang, Jose Alberto Muñiz-Lerma, Oscar Sánchez-Mata, Mohammad Attarian Shandiz, and Mathieu Brochu. Microstructure and mechanical properties of stainless steel 316l vertical struts manufactured by laser powder bed fusion process. *Materials Science and Engineering: A*, 736:27 – 40, 2018.

[176] E. Héripré, M. Dexet, J. Crépin, L. Gélébart, A. Roos, M. Bornert, and D. Caldemaison. Coupling between experimental measurements and polycrystal finite element calculations for micromechanical study of metallic materials. *International Journal of Plasticity*, 23(9):1512 – 1539, 2007.

[177] M Sachtleber, Z Zhao, and D Raabe. Experimental investigation of plastic grain interaction. *Materials Science and Engineering: A*, 336(1):81 – 87, 2002.

[178] Michael D. Sangid. The physics of fatigue crack initiation. *International Journal of Fatigue*, 57:58 – 72, 2013. Fatigue and Microstructure: A special issue on recent advances.

[179] Stephen D. Antolovich and Ronald W. Armstrong. Plastic strain localization in metals: origins and consequences. *Progress in Materials Science*, 59:1 – 160, 2014.

[180] Alberto W. Mello, Andrea Nicolas, and Michael D. Sangid. Fatigue strain mapping via digital image correlation for ni-based superalloys: The role of thermal activation on cube slip. *Materials Science and Engineering: A*, 695:332 – 341, 2017.

[181] www.flowwaterjet.com.

[182] http://www.gatan.com/products/sem-specimen-preparation/pecs-ii-system.

[183] Bing Pan, Kemao Qian, Huimin Xie, and Anand Asundi. Two-dimensional digital image correlation for in-plane displacement and strain measurement: a review. *Measurement Science and Technology*, 20(6):062001, apr 2009.

[184] F. Hild and S. Roux. Digital image correlation: from displacement measurement to identification of elastic properties – a review. *Strain*, 42(2):69–80, 2006.

[185] L. Allais, M. Bornert, T. Bretheau, and D. Caldemaison. Experimental characterization of the local strain field in a heterogeneous elastoplastic material. *Acta Metallurgica et Materialia*, 42(11):3865 – 3880, 1994.

[186] M. Bornert, F. Brémand, P. Doumalin, J.-C. Dupré, M. Fazzini, M. Grédiac, F. Hild, S. Mistou, J. Molimard, J.-J. Orteu, L. Robert, Y. Surrel, P. Vacher, and B. Wattrisse. Assessment of digital image correlation measurement errors: Methodology and results. *Experimental Mechanics*, 49(3):353–370, Jun 2009.

[187] Pascal Doumalin. Microextensometrie locale par correlation d'images numeriques application aux etudes micromecaniques par microscopie electronique a balayage. *PhD*, 2000.

[188] H L Wei, J Mazumder, and T DebRoy. Evolution of solidification texture during additive manufacturing. *Sci Rep*, 5:16446, 2015.

[189] Eric W Weisstein. Probability density function.

[190] Atasi Ghosh and N.P. Gurao. Effect of crystallographic texture on the planar anisotropy of ratcheting response in 316 stainless steel sheet. *Materials and Design*, 109:186 – 196, 2016.

[191] J. Yu, M. Rombouts, and G. Maes. Cracking behavior and mechanical properties of austenitic stainless steel parts produced by laser metal deposition. *Materials and Design*, 45:228 – 235, 2013.

[192] M.L. Griffith, D.M. Keicher, and J.T. Atwood. Free form fabrication of metallic components using laser engineering net shaping (lens). *Proceedings of the Solid Freeform Fabrication Symposium*, pages 125–132, 1996. cited By 1.

[193] Jorge Jorge. Influence of chemical composition on the mechanical properties of high strength steel weld metals for application in mooring components. *International Journal of Engineering and Technical Research*, 4:71–76, 02 2016.

[194] J.E. MacDonald, R.H.U. Khan, M. Aristizabal, K.E.A. Essa, M.J. Lunt, and M.M. Attallah. Influence of powder characteristics on the microstructure and mechanical properties of hipped cm247lc ni superalloy. *Materials Design*, 174:107796, 2019.

[195] Y.B. Zhang, A. Elbrønd, and F.X. Lin. A method to correct coordinate distortion in ebsd maps. *Materials Characterization*, 96:158 – 165, 2014.

[196] Fitzgerald Archibald Copyright (c) 2009.

[197] Sébastien Jean François RIX Yanis BALIT Eric CHARKALUK Camille GUEVENOUX, Alexandre CHARLES and Andrei CONSTANTINESC. Eprouvette representative du rechargement des sommets de pale par laser metal deposition eprouvette representative du rechargement des sommets de pale par laser metal deposition. *Brevet en cours de validation*.

[198] G.P. Dinda, A.K. Dasgupta, and J. Mazumder. Evolution of microstructure in laser deposited al–11.28 *Surface and Coatings Technology*, 206(8):2152 – 2160, 2012.

[199] V. Ocelík, I. Furár, and J.Th.M. De Hosson. Microstructure and properties of laser clad coatings studied by orientation imaging microscopy. *Acta Materialia*, 58(20):6763 – 6772, 2010.

[200] Yanis Balit Alexandre Charles Eric Charkaluk Andrei Constantinescu Camille Guévenoux, Simon Hallais. Plastic strain localization induced by microstructure gradient in laser cladding repaired structures. *Theoretical and Applied Fracture Mechanics*, Submitted october 2019.

[201] Yanyan Zhu, Jia Li, Xiangjun Tian, Huaming Wang, and Dong Liu. Microstructure and mechanical properties of hybrid fabricated ti–6.5al–3.5mo–1.5zr–0.3si titanium alloy by laser additive manufacturing. *Materials Science and Engineering: A*, 607:427 – 434, 2014.

[202] Zhuang Zhao, Jing Chen, Hua Tan, Xin Lin, and Weidong Huang. Evolution of plastic deformation and its effect on mechanical properties of laser additive repaired ti64eli titanium alloy. *Optics & Laser Technology*, 92:36 – 43, 2017.

[203] Wook Jin Oh, Wook Jin Lee, Min Seob Kim, Jong Bae Jeon, and Do Sik Shim. Repairing additive-manufactured 316l stainless steel using direct energy deposition. *Optics & Laser Technology*, 117:6 – 17, 2019.

[204] MyoungGuk Park, SeJin Ahn, Jae Ho Yun, Jihye Gwak, Ara Cho, SeoungKyu Ahn, Keeshik Shin, Dahyun Nam, Hyeonsik Cheong, and Kyunghoon Yoon. Characteristics of cu(in,ga)se2 (cigs) thin films deposited by a direct solution coating process. *Journal of Alloys and Compounds*, 513:68 – 74, 2012.

[205] A J Pinkerton, W Wang, and L Li. Component repair using laser direct metal deposition. *Proceedings of the Institution of Mechanical Engineers, Part B: Journal of Engineering Manufacture*, 222(7):827–836, 2008.

[206] Chunlei Qiu, Sheng Yue, Nicholas J.E. Adkins, Mark Ward, Hany Hassanin, Peter D. Lee, Philip J. Withers, and Moataz M. Attallah. Influence of processing conditions on strut structure and compressive properties of cellular lattice structures fabricated by selective laser melting. *Materials Science and Engineering: A*, 628:188 – 197, 2015.

[207] J. Nguejio, F. Szmytka, S. Hallais, A. Tanguy, S. Nardone, and M. Godino Martinez. Comparison of microstructure features and mechanical properties for additive manufactured and wrought nickel alloys 625. *Materials Science and Engineering: A*, 764:138214, 2019.

[208] J. Leunda, C. Soriano, C. Sanz, and V. García Navas. Laser cladding of vanadium-carbide tool steels for die repair. *Physics Procedia*, 12:345 – 352, 2011. Lasers in Manufacturing 2011 - Proceedings of the Sixth International WLT Conference on Lasers in Manufacturing.

[209] S. Mokadem, C. Bezençon, A. Hauert, A. Jacot, and W. Kurz. Laser repair of superalloy single crystals with varying substrate orientations. *Metallurgical and Materials Transactions A*, 38(7):1500–1510, Jul 2007.

[210] H. Paydas, A. Mertens, R. Carrus, J. Lecomte-Beckers, and J. Tchoufang Tchuindjang. Laser cladding as repair technology for ti–6al–4v alloy: Influence of building strategy on microstructure and hardness. *Materials & Design*, 85:497 – 510, 2015.

[211] Jae-Hyun Yu, Yoon-Suk Choi, Do-Sik Shim, and Sang-Hu Park. Repairing casting part using laser assisted additive metal-layer deposition and its mechanical properties. *Optics & Laser Technology*, 106:87 – 93, 2018.

[212] Cédric Doudard and Sylvain Calloch. Influence of hardening type on self-heating of metallic materials under cyclic loadings at low amplitude. *European Journal of Mechanics - A/Solids*, 28(2):233 – 240, 2009.

[213] Anthony Ezanno, Cédric Doudard, Sylvain Calloch, and Jean-Loup Heuzé. A new approach to characterizing and modeling the high cycle fatigue properties of cast materials based on self-heating measurements under cyclic loadings. *International Journal of Fatigue*, 47:232 – 243, 2013.

[214] C. Doudard, M. Poncelet, S. Calloch, C. Boue, F. Hild, and A. Galtier. Determination

of an hcf criterion by thermal measurements under biaxial cyclic loading. *International Journal of Fatigue*, 29(4):748 – 757, 2007.

[215] L. Zhang, X.S. Liu, S.H. Wu, Z.Q. Ma, and H.Y. Fang. Rapid determination of fatigue life based on temperature evolution. *International Journal of Fatigue*, 54:1 – 6, 2013.

[216] Eric Charkaluk and Andrei Constantinescu. Dissipative aspects in high cycle fatigue. *Mechanics of Materials*, 41(5):483 – 494, 2009.

[217] Etienne Pessard, Franck Morel, Catherine Verdu, Laurent Flacelière, and Gilles Baudry. Microstructural heterogeneities and fatigue anisotropy of forged steels. *Materials Science and Engineering: A*, 529:289 – 299, 2011.

[218] Charles Mareau, Véronique Favier, Bastien Weber, André Galtier, and Marcel Berveiller. Micromechanical modeling of the interactions between the microstructure and the dissipative deformation mechanisms in steels under cyclic loading. *International Journal of Plasticity*, 32-33:106 – 120, 2012.

[219] https://www.instron.us/.

[220] Michel Bornert, F. Vales, H. Gharbi, and D. Nguyen Minh. Multiscale Full-Field Strain Measurements for Micromechanical Investigations of the Hydromechanical Behaviour of Clayey Rocks. *Strain*, 46(1):33–46, 2010.

[221] Cédric Doudard, Sylvain Calloch, François Hild, and Stéphane Roux. Identification of heat source fields from infrared thermography: Determination of 'self-heating' in a dual-phase steel by using a dog bone sample. *Mechanics of Materials*, 42(1):55 – 62, 2010.

[222] www.flir.com.

[223] Remi Munier. *Study of fatigue properties of rolled steels from self-heating measurements under cyclic loading : tests, observations, model and influence of a plastic pre-strain.* Theses, Université de Bretagne occidentale - Brest, February 2012.

[224] H L Wei, J Mazumder, and T DebRoy. Evolution of solidification texture during additive manufacturing. *Sci Rep*, 5:16446, Nov 2015.

[225] Hasse Fredriksson and Ulla Åkerlind. *Solidification and Crystalisation Processing in Metals and Alloys*. John Wiley & Sons, 01 2012.

[226] Xin Zhou, Kailun Li, Dandan Zhang, Xihe Liu, Jing Ma, Wei Liu, and Zhijian Shen. Textures formed in a cocrmo alloy by selective laser melting. *Journal of Alloys and Compounds*, 631:153 – 164, 2015.

[227] Olivier Andreau, Imade Koutiri, Patrice Peyre, Jean-Daniel Penot, Nicolas Saintier, Etienne Pessard, Thibaut De Terris, Corinne Dupuy, and Thierry Baudin. Texture control of 316l parts by modulation of the melt pool morphology in selective laser melting. *Journal of Materials Processing Technology*, 264:21 – 31, 2019.

[228] Thale R Smith, Joshua D Sugar, Chris San Marchi, and Julie M Schoenung. Orientation Effects on Fatigue Behavior of Additively Manufactured Stainless Steel, 2017.

[229] Zhuqing Wang, Todd A. Palmer, and Allison M. Beese. Effect of processing parameters on microstructure and tensile properties of austenitic stainless steel 304L made by directed energy deposition additive manufacturing. *Acta Materialia*, 110:226–235, 2016.

[230] Pierrick Florin, Matteo Facchinetti, Cédric Doudard, and Sylvain Calloch. Fast fatigue properties identification by "self-heating" method: Application to automotive welded joints. *Procedia Engineering*, 66:676 – 683, 2013. Fatigue Design 2013, International Conference Proceedings.

[231] Catherine Peyrac, Thomas Jollivet, Nolwenn Leray, Fabien Lefebvre, Ophélie Westphal, and Laurent Gornet. Self-heating method for fatigue limit determination on thermoplastic composites. *Procedia Engineering*, 133:129 – 135, 2015. Fatigue Design 2015, International Conference Proceedings, 6th Edition.

[232] Parham Mostofizadeh, Mahmoud Kadkhodaei, Shabnam Arbab Chirani, Luc Saint-Sulpice, Maha Rokbani, Tarak Bouraoui, and Sylvain Calloch. Fatigue analysis of shape memory alloys by self-heating method. *International Journal of Mechanical Sciences*, 156:329 – 341, 2019.

[233] Bastian Blinn, Maximilian Ley, Nils Buschhorn, Roman Teutsch, and Tilmann Beck. Investigation of the anisotropic fatigue behavior of additively manufactured structures made of aisi 316l with short-time procedures phyballit and phybalcht. *International Journal of Fatigue*, 124:389 – 399, 2019.

[234] A. Riemer, S. Leuders, M. Thöne, H.A. Richard, T. Tröster, and T. Niendorf. On the fatigue crack growth behavior in 316l stainless steel manufactured by selective laser melting. *Engineering Fracture Mechanics*, 120:15 – 25, 2014.

[235] J.V. Gordon, C.V. Haden, H.F. Nied, R.P. Vinci, and D.G. Harlow. Fatigue crack growth anisotropy, texture and residual stress in austenitic steel made by wire and arc additive manufacturing. *Materials Science and Engineering: A*, 724:431 – 438, 2018.

[236] Nicolas Malésys, Ludovic Vincent, and François Hild. A probabilistic model to predict the formation and propagation of crack networks in thermal fatigue. *International Journal of Fatigue*, 31(3):565 – 574, 2009.

Titre : Propriétés mécaniques de pièces élancées fabriquées ou réparées par Directed Energy Deposition.

Mots clés : Microstructure, fatigue, essai in situ sous MEB, EBSD, corrélation d'images, auto-échauffement

Résumé : Les travaux de cette thèse ont été dédiés à l'étude de pièces minces en acier inoxydable 316L fabriquées ou réparées par Directed Energy Deposition (DED). La nouveauté princpale est l'observation de la déformation à l'échelle de la microstructure. Pour ce faire, une expérience associant un essai de traction in situ dans un microscope électronique à balayage, de la corrélation d'images à haute résolution et une carte EBSD de la microstructure ont été réalisés. Les résultats obtenus permettent alors de mieux appréhender les différentes propriétés en traction ainsi que les comportements d'autoéchauffement lors d'essais cycliques. Le premier objectif a été de qualifier et quantifier les mécanismes de déformation à l'échelle de la microstructure pour expliquer le comportent anisotrope révélé lors d'essais de traction. Par conséquent, deux orientations de sollicitation permettant d'effectuer un chargement perpendiculaire ou parallèle à la direction d'impression ont été définies. Dans le premier cas, la localisation de deformation s'effectue au niveau de certaines intercouches. Pour le second, une localisation dans certaines régions correspondant à de gros grains particuliers a été observée. Le deuxième objectif a été d'évaluer la capacité du DED à réparer. Pour ce faire, des éprouvettes moitié tôle / moitié imprimées ont été fabriquées afin de solliciter l'interface en traction. Une grande différence de microstructure a été observée entre les deux matériaux. Néanmoins, l'interface n'a jamais été la zone de rupture lors d'essais de traction. De plus, une deformation homogène a été observée dans la partie tôle alors qu'une déformation hétérogène avec des pics de concentration au niveau de certaines intercouches a été remarquée dans la partie imprimée lors d'essais in situ. Enfin, une zone de faible déformation a été constatée de part et d'autres de l'interface, zone dans laquelle une plus grande dureté a été mesurée. Le dernier objectif a été d'évaluer les propriétés en fatigue par des essais d'autoéchauffement. Il a été montré que les difficultés liées à la faible épaisseurs de nos éprouvettes pouvaient être surmontées en maitrisant le protocole expérimental. Un comportement anisotrope a été observé durant ces essais cycliques avec des éprouvettes perpendiculaires au sens d'impression montrant une plus grande limite d'endurance par rapport aux éprouvettes sollicitées parallèlement. Pour ces dernières, des analyses post-mortem ont montré un scénario de fatigue classique avec une fissure dominante et donc une source de dissipation de chaleur localisée. À l'inverse, une multitude de fissures aux intercouches créant de nombreux sites de dissipation à été constatée pour les éprouvettes testées perpendiculairement.

Title : Mechanical properties of additively manufactured or repaired single-track thickness structures by Directed Energy Deposition.

Keywords : Microstructure, fatigue, SEM in situ tests, EBSD, digital image correlation, self-heating

Abstract : This thesis was dedicated to the study of 316L stainless steel additively manufactured or repaired specimens by Directed Energy Deposition (DED). Different configurations were manufactured under optimal process parameters. The novelty of this work is the observation of the microstructural strain localization. This experiment combined an in situ tensile test inside a scanning electron microscope with high resolution digital image correlation and an electron backscatter diffraction map. These results allowed for a fresh interpretation of monotonic tensile tests as well as of self-heating experiments under cyclic loading and the failure patterns observed at the surface of specimens. The first objective was to understand the deformation mechanisms at the grain scale which could explain the observed macroscopic anisotropy of the tensile properties as reported in literature. Two loading directions, along and perpendicular, were considered with respect to the printing direction for fully printed specimens. We observed that for a tensile load perpendicular to the printing direction, the strain localization is mainly situated at some interlayers. For a tensile load along the printing direction, the strain localization was observed in some particular regions of large grains. The second objective was the assessment of DED as a repair technology. Dog bone shaped repaired specimens (half hot rolled sheet and half printed) were designed and they exhibited an important hierarchical microstructural gradient. We noticed that the interface is not a weak area during a monotonic tensile test. Moreover, while homogeneous strain was observed in the substrate half, the printed half showed a strain heterogeneity, with the highest localization found at some interlayers. An unstrained zone was observed at both sides of the interface and was associated with higher hardness. The last objective was to evaluate the fatigue properties by self-heating tests. The experiment has proven that the difficulties due to the small dimensions of the single-track thickness specimens can be overcome by careful construction of the experimental set-up. The results revealed a certain correlation between the pattern of the microstructure, the deformation pattern at this scale and the self-heating results. Anisotropy was highlighted during these cyclic tests where specimens tested perpendicularly to the printing direction showed higher fatigue limits in comparison to the ones tested along the printing direction. Post mortem analysis revealed a multitude of cracks at interlayers for the specimens tested perpendicularly to the printing direction creating several sites of heat diffusion. For the specimens tested along the printing direction, a more classical fatigue scenario was observed with one dominating crack and thus a localized heat dissipation.

Institut Polytechnique de Paris
91120 Palaiseau, France